UNIVERSITAT AUTÒNOMA DE BARCELONA
POSTGRADUATE SCHOOL
PHYSICS DEPARTMENT

Ph. D. THESIS

Epitaxial Thin Film Growth and Study of Charge and Mass Transport Properties of Mixed Ionic Electronic Conducting $GdBaCo_2O_{5+\delta}$ (GBCO)

Thesis submitted by
James Arturo Zapata Correa

to apply for the Degree of Doctor at the Universitat Autonòma of Barcelona in the Materials Science Program

Thesis Advisor: José Santiso Lopéz
Thesis Tutor: Javier Rodriguez Viejo

prepared at Institut Català de Nanociència i Nanotecnologia (ICN2)
Consejo Superior de Investigaciones Científicas (CSIC)

defended on:
2016

Institut Català de Nanociència i Nanotecnologia

Nano-Materials Grown Division
Campus UAB,Edifici ICN2
E-08193, Bellaterra, Spain
Tel.: (+34) 93 737 2649
Fax: (+34) 93 737 2648

Bellaterra, December de 2014

El Dr José Santiso Lopéz, científico titular y lider de la Nano-Materials Grown Division del **Institut Català de Nanociència i Nanotecnologia (ICN2 - CSIC)**, en calidad de director de tesis y el Dr Javier Rodríguez Viejo, profesor titular del Departamento de Física de la **Universitat Autònoma de Barcelona**, en calidad de tutor de tesis.

CERTIFICAN:

Que el presente trabajo titulado ***Epitaxial Thin Film Growth and Study of Charge and Mass Transport Properties of Mixed Ionic Electronic Conducting*** $GdBaCo_2O_{5+\delta}$ ***(GBCO)*** ha sido llevado a cabo en el Institut Català de Nanociència i Nanotecnologia (ICN2-CSIC) por James Arturo Zapata Correa y constituye su memoria de tesis doctoral.

Dr. José Santiso Lopéz
Nanomaterials Growth Division Leader
ICN2 - CSIC

Javier Rodriguez Viejo
Profesor Titular Dpto. Física
UAB

Jury :

Presidente :	Dr. Alberto Tarancón Rubio	Dep. Materiales Avanzados Institut de Recerca en Energia de Catalunya (IREC) Barcelona, España
Secretario :	Dr. Jose Ángel Pardo Gracia	Dep. Ciencia de Materiales e Ingenieria Universidad de Zaragoza Zaragoza, España
Vocal :	Dra. Ainara Aguadero	Dep. Materials Imperial College London Londres, Reino Unido
Suplente :	Dr. Carlos Frontera Beccaria	Dep. Materiales Magnéticos y Óxidos Funcionales Instituto de Ciencia de Materiales de Barcelona ICMAB/CSIC Cerdanyola del Valles, España)
Suplente :	Dr. Andrea Cavallaro	Dep. Materials Imperial College London Londres, Reino Unido

Abstract

The general trend in solid oxide fuel cell research leads to lower operating temperatures in order to reduce degradation phenomena due to reactions between adjacent cell components and sealing problems. Since the system kinetics are mostly thermally activated lower temperatures introduce severe problems regarding the overall efficiency of the SOFC system.The cathode material is known to limit the overall system performance and therefore research focuses on the development of new cathode materials with similar or even superior properties such as electrical conductivity, electrochemical activity, and oxygen exchange properties even at lower temperatures. Thus the high efficiency compared to standard thermo-mechanical energy conversion processes could be kept or even be improved. This would be a small step towards sustainable and highly efficient energy conversion systems which are quiet and pollution-free.

Research on new oxide materials with both high mixed ionic and electronic conductivity (MIEC) is of great importance in order to achieve optimum performance in a wide range of devices that have considerable potential for clean, low carbon, electrochemical energy conversion. In the case of solid oxide fuel cells (SOFCs), in order to reduce the working temperature to the intermediate range (500-750$°C$), more active cathode materials are needed, and conventional electronic conductors such as $La_{1-x}Sr_xMnO_{3-\delta}$ (LSM) should be replaced by materials with high electronic and ionic conductivity, as well as good catalytic activity. In the past decade several reports on layered $LnBaCo_2O_{5+\delta}$ ($Ln-BCO$) cobaltites (with Ln = Rare Earth, such as La, Y, Gd, Nd, or Pr) of the so-called "112" phase have evidenced a large variety of transport and magnetic properties, which makes their study a very active area in solid-state physics. Previous studies have highlighted the great potential of GBCO, as a cathode in SOFC, with a high reported electronic conductivity above the metal-insulator transition temperature, outstanding oxygen transport properties and enhanced surface exchange, as well as excellent stability for both structural and electrochemical performance. However, to date there is an absence of information about intrinsic ionic conductivity of this $GdBaCo_2O_{5+\delta}$ compound. To enable measurement of intrinsic electronic and particularly ionic transport properties, the greatest challenge is to synthesise dense, continuous or ideally epitaxial specimens of GBCO.

The aim of this work is to achieve well-defined epitaxial $GdBaCo_2O_{5+\delta}$ deposited by the pulsed laser deposition (PLD) technique in order to fundamentally investigate their intrinsic anisotropic properties for SOFC applications. This research involved PLD target synthesis and PLD deposition for these materials. The obtained films were evaluated through crystallographic, compositional, surface morphological and microstructural characterisation. Finally electrical, oxygen diffusion and surface exchange properties were characterised by

Electrochemical impedance and the isotopic exchange depth profile (IEDP) with secondary ion mass spectrometry (SIMS) method.

After a long process of optimization, high-quality epitaxial GBCO films mainly consisting a double-perovskite regions were obtained by pulsed laser deposition. The nature of the ablation process from stoichiometric $GdBaCo_2O_{5+\delta}$ target generates a deviation in the composition of the films which basically consists in a Co depletion. This composition deviation induces the appearance of characteristic stacking faults with supplementary GdO planes without affecting the overall epitaxial arrangement of the films. Despite the observed changes in the film orientation from $c_{\parallel}$ to $c_{\perp}$ upon deposition temperature increase, the film electronic conductivities seem to be mainly correlated with the cation composition. So, the larger the deviation from stoichiometric ideal composition, the lower the conductivity. This effect has been mainly ascribed to the role of defects in impeding the achievement of a long-range order of the highly conducting $Pmmm$ structure in the films. Despite the presence of defects, the conductivities in our films, which are considered very promising for their application as cathodes in intermediate temperature SOFCs, attain values as high as 800 S/cm at temperatures between 300 and $400°C$.

It also demonstrates that the appropriate choice of substrate mismatch allows growing films with either pure c-axis or a-axis orientation. This has allowed exploration of the potential anisotropy in the oxygen transport and has proven that indeed the oxygen diffusion at low temperatures is almost one order of magnitude larger along the a-axis compared to the c-axis. This has been related to the arrangement of oxygen vacancies preferentially in the GdO planes forming channels along the a-axis, and therefore providing a path for oxygen migration. However, no influence of the structure anisotropy was observed in the oxygen surface exchange rates, which were of similar values regardless of the film orientation or measuring geometry. The method described here provides a very powerful tool to explore intrinsic oxygen transport properties in complex anisotropic oxide materials otherwise dominated by the mixture of all orientations and grain boundary contributions in polycrystalline samples.

Contents

List of Figures

Part I

General

CHAPTER 1

Introduction

The purpose of this chapter is to introduce the general background of the research detailed in the thesis. Initially, the general concepts of fuel cells will be described, then the attention is focused on solid oxide fuel cells (SOFC), followed by a description of the cathodes typically used in SOFCs and a brief introduction to mixed ionic electronic conductors (MIEC). The $Ln - BaCo_2O_{5+\delta}$ ($Ln - BCO$) family is analyzed in detail and particular attention is given to $GdBaCo_2O_{5+\delta}$ ($GBCO$) state of the art. Finally, the motivation and objectives of the thesis will be described.

1.1 Fuel Cells

According to the International Energy Outlook 2013 [1], the world energy consumption will grow by 56 percent between 2010 and 2040. Renewable energy and nuclear power are the world's fastest-growing energy sources, each increasing by 2.5 percent per year. However, fossil fuels are expected to continue supplying almost 80 percent of world energy consumption through 2040. This will generate large environmental cost in the short and long term because of greenhouse effect of byproducts from the combustion process. Worldwide energy-related carbon dioxide emissions will rise from about 31 billion metric tons in 2010 to 36 billion metric tons in 2020 and then to 45 billion metric tons in 2040, a 46-percent increase. Furthermore, most of the people and industries who consume fossil fuels do not live where fuels are extracted. This situation creates enormous economic motivation for the consuming nations to try to exert control over the regions that supply the fuels, thus generating international conflicts with the intrinsic negative social and geopolitic consequences. In this context, it is therefore necessary to implement policies and regulations that limit the use of fossil fuels and to provide support for renewable energy sources and development of new technologies. Fuel cells may help to reduce our dependence on fossil fuels and diminish poisonous emissions into the atmosphere (main cause of climate change due to greenhouse effect), since fuel cells have higher energy conversion efficiencies

compared to thermal powered engines. Using pure hydrogen, fuel cells only produce pure water, thus eliminating locally all emissions otherwise caused by electricity production from fossil fuels. The share of renewable energy from wind, water and sun will increase further but these sources are not suited to cover the electrical base load due to their irregular availability. The combination of these sources, however, to produce hydrogen during low demand periods in cooperation with fuel cells producing additional electricity from stored hydrogen during high demand hours may well be an option for future power generation. Furthermore, in comparison with other energy storage devices (like lithium ion batteries, or supercapacitors) the use of stored hydrogen in combination of fuel cells is largely more efficient in terms of specific power density (power per unit volume or weight). Fuel cells are electrochemical devices that convert the chemical energy of a chemical reaction directly into electrical energy and heat [3]. The conventional power generators involving the conversion of chemical energy successively into heat, kinetic energy and finally electricity are limited by the Carnot-cycle with efficiency of around 30%. Interestingly, fuel cells eliminate the intermediate fuel-to-heat-to-mechanical energy conversion losses, offering efficiencies above 50%. Hydrogen is the most common fuel used in fuel cells and is also the least harmful to the environment. The only by-products of the reaction between hydrogen and oxygen are electricity, heat (it is partially used to maintain the high temperature necessary for the reaction) and water vapor. In many cases, part of this waste heat can be recaptured for use in industrial or residential applications, greatly increasing the system's total efficiency. In practice, however, lost in chemical reactions due to non complete usage of fuels, mass transport energy and steric barriers will always be present. From an engineering point of view, the challenge is to understand and reduce these energy losses as much as possible.The basic physical structure or building block of most fuel cells consists of a dense layer of a pure ionic conducting electrolyte material in contact with anode and cathode electrodes (normally porous) on either side [4]. In the dual chamber fuel cell, a fuel enters the anode and an oxidant enters the cathode. Ion conduction through the electrolyte can occur in either direction – anode to cathode or cathode to

Figure 1.1: *Five main types of fuel cells and their working temperatures and reaction mechanisms [2].*

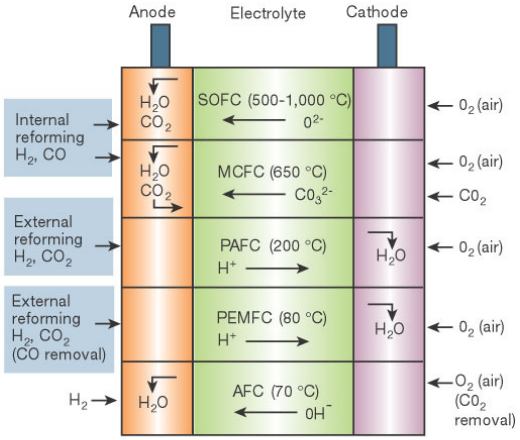

anode – depending on the fuel cell type. A schematic representation of a single cell with the reactant/product gases and the ion conduction flow directions through the cell is shown in Fig. 1.1. While there are different fuel cell types, all fuel cells work similarly and can be classified by the type of electrolyte, by the temperature of operation or by whether the fuel is processed outside (externally reformed) or inside (internally reformed) [1]. A brief description of the major types of fuel cells characterized by the type of electrolyte employed is presented in the Table 1.1. They differ in their operating temperatures, power outputs, electrical efficiencies, and typical applications. Polymer electrolyte membrane fuel cells (PEMFCs) have wide range of applications and they are promising candidates for transport applications due to their high power density, fast start-up time, high efficiency, low operating temperature, and easy and safe handling. However, PEMFCs are still too expensive (because they need noble metal electrodes like platinum) to be competitive or economically-feasible. Alkaline fuel cells (AFCs) have the best performance when operating on pure hydrogen and oxygen, yet their intolerance to impurities (especially carbon monoxide) and short life times hinder their use for terrestrial applications (they are predominantly used for extraterrestrial purposes). Phosphoric acid fuel cells (PAFCs) are possibly the most commercially-developed fuel cells operating at intermediate temperatures $(160-220°C)$. PAFCs are currently used for combined-heat-and-power (CHP) applications with high energy efficiencies. Molten carbonate fuel cells (MCFCs) and solid oxide fuel cells (SOFCs) are high-temperature fuel cells appropriate for cogeneration and combined cycle systems (the high operation temperature allows reforming reactions directly on the anode surface). At present MCFCs have the highest energy efficiency attainable from methane-to- electricity conversion in the power range from 250kW to 20MW, while SOFCs are best suited for base-load utility applications operating on coal-based gasses. Although there has been tremendous advances in the application of fuel cells, there are still some limitations that prevent their full expansion such as the high cost of the materials involved and the limited life span of the cells, especially those working at elevated temperatures. This has promoted an effort to reduce the operating temperature of the cell which require improvements in catalytic activity of the materials used for the reduction of oxygen at the cathodes as main element. This has encouraged the search for new cathode material with better performance. The work in this thesis will focus on new cathode materials for application in SOFC technology, for more detailed reviews of these other fuel cell types refer to handbook published by U.S. Department of Energy [3] or the books published by Shekhawat et. al [4] and O'Hayre et al.[5]. The paper of Sharaf *et. al.* [6] provides a concise, up-to-date review of the fuel cell fundamentals with a complete summary table.

[1] *Certain electrodes are not capable of producing the hydrocarbon fuel oxidation unless a preliminary forming reaction (reforming) breaks the hydrocarbon molecules into more reactives species*

Type	Electrolyte	Charge Carrier	Operating Temperature [$^{\circ}C$]	Typical Fuel	Electrical Efficiency (%)	Electrochemical reactions	
PEMFC	Hydrated Polymeric Ion Membrane Exchange	H^+	60 - 80	Hydrogen	40 - 60	Anode:	$H_2 \rightarrow 2H^+ + 2e^-$
						Cathode:	$\frac{1}{2}O_2 + 2H^+ + 2e^- \rightarrow H_2O$
						Cell:	$H_2 + \frac{1}{2}O_2 \rightarrow H_2O$
AFC	KOH solution in a Matrix	OH^-	Below Zero - 230	Hydrogen	60 - 70	Anode:	$H_2 + 2(OH)^- \rightarrow 2H_2O + 2e^-$
						Cathode:	$\frac{1}{2}O_2 + H_2O + 2e^- \rightarrow 2(OH)^-$
						Cell:	$H_2 + \frac{1}{2}O_2 \rightarrow H_2O$
PAFC	H_3PO_4 soaked in a matrix	H^+	160-220	Hydrogen	36 - 45	Anode:	$H_2 \rightarrow 2H^+ + 2e^-$
						Cathode:	$\frac{1}{2}O_2 + 2H^+ + 2e^- \rightarrow H_2O$
						Cell:	$H_2 + \frac{1}{2}O_2 \rightarrow H_2O$
MCFC	Li_2CO_3 K_2CO_3 $LiAlO_2$	CO_3^{2-}	600-700	Methane	55-65	Anode:	$H_2 + CO_3^{2-} \rightarrow H_2O + CO_2 + 2e^-$
						Cathode:	$\frac{1}{2}O_2 + CO_2 + 2e^- \rightarrow CO_3^{2-}$
						Cell:	$H_2 + \frac{1}{2}O_2 + CO_2 \rightarrow H_2O + CO_2$
SOFC	Ceramic Ionic Conductor	O^{2-}	500 - 1000	Hydrogen, Methane	55 - 65	Anode:	$H_2 + O^{2-} \rightarrow H_2O + 2e^-$
						Cathode:	$\frac{1}{2}O_2 + 2e^- \rightarrow O^{2-}$
						Cell:	$H_2 + \frac{1}{2}O_2 \rightarrow H_2O$

Table 1.1: *Summary of fuel cell types according to electrolyte, adapted from [6] and [7].*

1.2 Solid Oxide Fuel Cells

This section will briefly discuss different components and materials aspects of SOFCs. For further insight into the SOFCs technology and its components the reader is referred to review articles of Stamboul & Traversa [7], Ormerod [8] and Kilner & Burriel [9] and references therein. Other components such as interconnects and sealings are also of great importance for the operation of an SOFC cell stack but are out of the scope of this thesis. An SOFC is produced from oxide materials, which become active for transportation of oxide ions and electro-catalysis at high temperatures. The oxide ions are created at the cathode side via electrochemical reduction of gaseous oxygen in the presence of an electrocatalytically active ceramic oxide (e.g., mixed ion-electron conductors based on transition metal oxide perovskites such as Strontium-doped lanthanum manganite ($La_{1-x}Sr_xMnO_3$) (LSM)). The cathode reaction in the case where only oxygen vacancies are the active defects (it may be different in the case of interstitial oxygen ions) and using

Kröger-Vink notation[2] [10] is given by the following equation

$$\frac{1}{2}O_2^{(gas)} + V_O^{\bullet\bullet} + 2e' \longrightarrow O_O^{\times} \tag{1.1}$$

The formed oxide ions (vacancies in this case) diffuse, driven by a gradient in the electrochemical potential, through the electrolyte membrane (for example, $Y_2O_3 - doped\ ZrO_2$ (YSZ)) and react with the molecular hydrogen H_2 (or any other fuel, here only H_2 is expressed for simplicity of the reactions) at the anode side (e.g., a Ni/YSZ cermet) for the formation of water, while at the same time, a flow of electrons through the outer electrical circuit is generated. The oxidation at the anode proceeds according to

$$H_2 + O_O^x \longrightarrow H_2O + V_O^{\bullet\bullet} + 2e' \tag{1.2}$$

The overall reaction in the fuel cell produces water, heat, and electrical work as follows:

$$\frac{1}{2}O_2 + H_2 \longrightarrow H_2O + W_{elec} + Q_{heat} \tag{1.3}$$

Figure 1.2 is a schematic diagram briefly describing the transport and reaction mechanism in a SOFC system. The heat and water by-products must be continuously removed in order to maintain continuous isothermal operation for ideal electric power generation. Hence, water and thermal management are key areas in the efficient design and operation of SOFCs. Unlike other types of fuel cells operated at lower temperatures, SOFCs exhibit a high tolerance towards CO and also sufficiently fast electrode kinetics to directly oxidize complex hydrocarbon gases. Therefore, natural gas can directly be used as fuel without any further elaborate purification or prereforming steps. SOFCs are probably intended for larger scale production, for the on-site cogeneration of heat and power on a small scale (1-5 kW electrical power output) and as auxiliary power units in motor vehicles running on the respective vehicle fuel.

[2] *$M_S^C \rightsquigarrow M$ corresponds to the species. These can be atoms (e.g., Si, Ni, O, Cl), vacancies V, interstitials i, electrons e or electron holes h. S index indicates the lattice site that the species occupies (the site may be a atom side or a lattice interstice). C index corresponds to the electronic charge of the species relative to the site that it occupies. The charge of the species is calculated by the charge on the current site minus the charge on the original site (To indicate null charge, $\times$ is used. A single $\bullet$ indicates a single positive charge and $'$ signifies a single negative charge).*

Figure 1.2: *Schematic of an Individual Fuel Cell.*

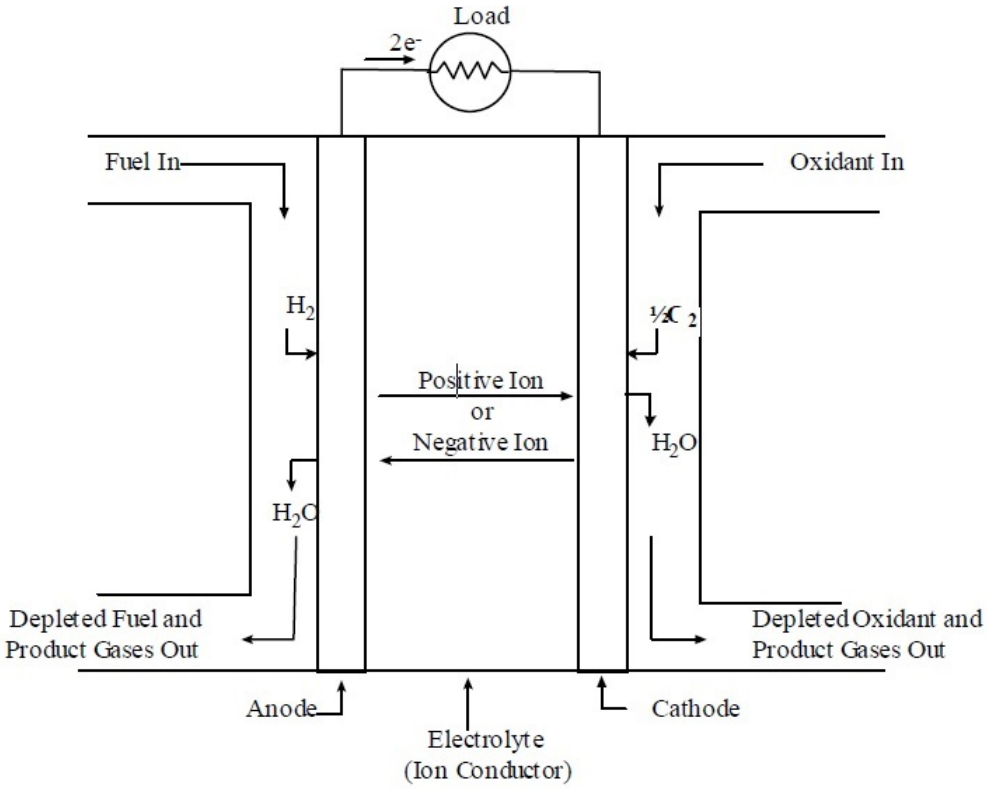

1.2.1 Thermodynamics of SOFCs

Considering the basic SOFC chemical reaction described by Eq. 1.3, the difference in the Gibbs free energy of formation ΔG_f during the reaction can be given as

$$\Delta G_f = \frac{G_{H_2O} - G_{H_2}}{1/2 G_{O_2}} \tag{1.4}$$

where G_{H_2O} , G_{H_2} , and G_{O_2} refer, respectively, to the free energies of water, hydrogen, and oxygen. If all the Gibbs free energy is converted into electrical work (*If the system is reversible - or has no losses* -), then

$$\Delta G_f = -nFE$$

Thus

$$E = -\frac{\Delta G_f}{nF} \tag{1.5}$$

where n is number of electrons involved in the chemical reaction, F is the Faraday constant and E the electromotive force (EMF) or reversible open circuit voltage (OCV) of the hydrogen fuel cell. Here, the Gibbs free energy is dependent on the temperature by the relation

$$\Delta G_f = \Delta H_f - T\Delta S_f \tag{1.6}$$

where ΔH_f is the enthalpy change for the reaction, T is the absolute temperature, and ΔS_f is the entropy change for the reaction. The different ΔG_f values at different temperatures are available in the literature [11]. If the reactants and products are all in their standard conditions, the reversible standard potential E^0 of the electrochemical reaction using Eq. 1.5 is gives by

$$E^0 = -\frac{(-237300\ J/mol)}{2(96485\ C/mol)} = 1.23V \tag{1.7}$$

Beyond the standard condition, the theoretical reversible potential E_{Th} can be expressed by the Nernst equation [12], which in the case of hydrogen as fuel can be written:

$$E_{Th} = E^0 - \frac{RT}{nF} ln\left(\frac{P_{H_2O}}{P_{H_2} \cdot P_{O_2}^{1/2}}\right) \tag{1.8}$$

where R is the gas constant, and P is the partial pressure of each gas. Equation 1.8 implies that the theoretical voltage that can be gained decreases with increasing temperature. The cells are on the other hand more efficient at higher T due to thermally activated reactions as well as higher oxide ion conductivities, which decreases the polarization losses of the cell. The characteristic shape of the voltage/current density shown in Fig. 1.3 results from four major irreversibilities. These will be outlined very briefly here. For more detailed information you can refer to the book by Larminie [11] or any of the fuel cell handbooks [3, 13].

1. *Activation losses*(ΔV_{act}). These are caused by the slow kinetics of the reactions taking place on the surface of the electrodes. A proportion of the voltage generated is lost in driving the chemical reaction that transfers the electrons to or from the electrode. This voltage drop is highly non-linear.

2. *Fuel crossover and internal currents.* This energy loss results from the waste of fuel passing through the electrolyte, and, to a lesser extent, from electron conduction through the electrolyte. The electrolyte should only transport ions through the cell, as in Fig. 1.3. However, a certain amount of fuel diffusion and electron flow will always be possible. Except in the case of direct methanol cells the fuel loss and current is small, and its effect is usually not very important. However, it does have a marked effect on the OCV of low-temperature cells.

3. *Ohmic losses*(ΔV_{ohm}). This voltage drop is the straightforward resistance to the flow of electrons through the material of the electrodes and the various interconnections, as well as the resistance to the flow of ions through the electrolyte. This voltage drop is essentially proportional to current density, linear, and so is called ohmic losses, or sometimes as resistive losses.

4. *Mass transport or concentration losses*(ΔV_{trans}). These result from the change in concentration of the reactants at the surface of the electrodes as the fuel is used. That concentration affects voltage, and so this type of irreversibility is sometimes called concentration loss. Because the reduction in concentration is the result of a failure to transport sufficient reactant to the electrode surface, this type of loss is also often called mass transport loss. This type of loss has a third name "Nernstian", this is because of its connections with concentration, and the effects of concentration are modelled by the Nernst equation.

It is useful to construct an equation that brings together all these irreversibilities. We can do so and arrive at the following equation for the operating voltage of a fuel cell at a current density i.

$$V = E - \Delta V_{act} - \Delta V_{ohm} - \Delta V_{trans}$$

$$V = E - i \cdot r - \eta_a - \eta_c - \Delta V_{trans} \tag{1.9}$$

In this equation, E is the reversible OCV, r is the area-specific resistance and η_c and η_a the polarization losses associated with the cathode and the anode, respectively. With this picture in mind it is obvious that a number of aspects must be improved in order to increase the efficiency including better electro-catalysts (activation), better electronic and ionic conducting materials (ohmic) and better flow designs (gas transport). An improved microstructure has the potential of decreasing all kinds of losses and is thus also of great importance.

1.2.2 Mixed Ionic-Electronic Conductor (MIEC)

As indicated by the Eq. 1.1 for the case of vacancy ionic conductivity mechanisms, the overall reaction occurring at the cathode involves the absorption of gaseous O_2 and ultimate incorporation into oxygen ion vacancies in the electrolyte. This reaction can be further broken down into several different steps, each representing a different step involved in the overall oxygen reduction reaction occurring on the cathode. For SOFC cathodes with electronic conductivity (202 $S\ cm^{-1}$ at 900 $^{\circ}C$ [14]) but little ionic conductivity ($10^{-7} S\ cm^{-1}$ at 900 $^{\circ}C$[15]), such as $La_{1-x}Sr_xMnO_3$ (LSM), ionic diffusion will be limited, and the reaction must take place at the triple phase boundary (TPB) between gas, cathode,

Figure 1.3: *Cell voltage as function of current density of a fuel cell. The regions where the different losses are dominating are also marked. Close to open circuit voltage the resistance is mainly associated with the electrode reactions. At higher current densities ohmic losses become significant and at even higher current densities (and thus high fuel utilizations) gas transport limitations start contributing to the total voltage drop of the cell.*

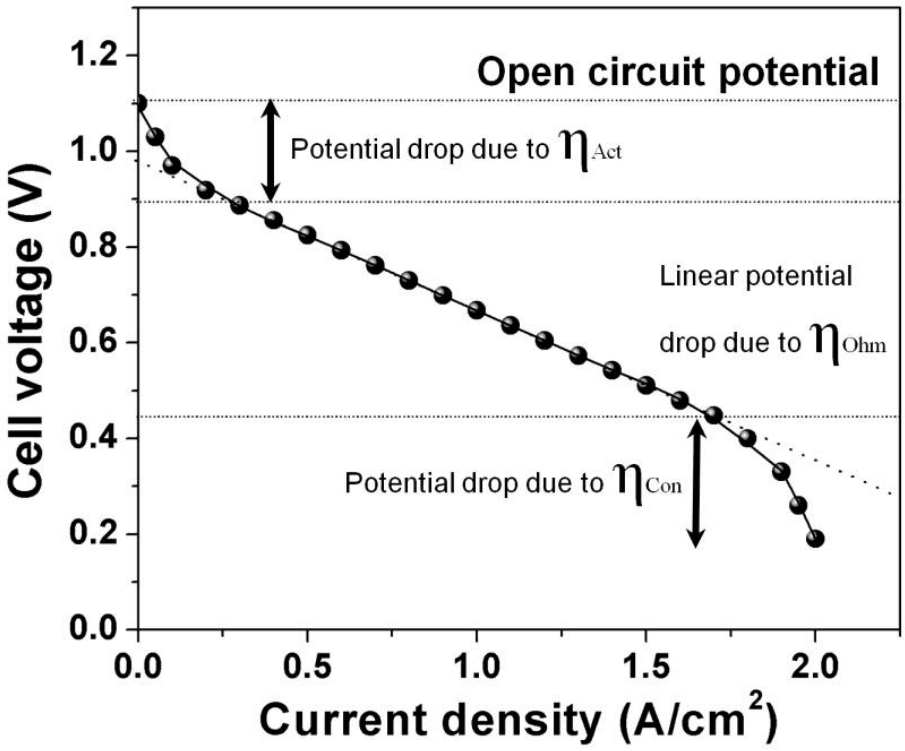

and electrolyte. If the material has substantial ionic diffusion, however, the reaction can occur further away from the TPB, opening up more potential reaction sites. Materials which have high electronic and high ionic conductivity are called mixed ionic electronic conductors (MIEC)

The oxygen reduction reaction on a MIEC cathode consists of four general processes: dissociation of the oxygen molecule, surface oxygen exchange, diffusion through the cathode (bulk or surface), and electrochemical charge transfer at the cathode-electrolyte interface (see Fig. 1.4). The two important material properties which describe the aforementioned steps are the oxygen surface exchange coefficient $k[cm \cdot s^{-1}]$ and the oxygen diffusion coefficient $D[cm^2 s^{-1}]$, respectively. It is known that both of them exhibit different activation energies, *i.e.* within certain temperature ranges one of them is determining the performance of the material. For membranes often the surface exchange shows higher activation energies compared to the oxygen diffusion. Therefore the oxygen exchange is likely to be rate limiting in lower temperature regions whereas the diffusion process limits the performance at elevated temperatures [16]. On the other hand, Kilner et. al

Figure 1.4: *Processes involved in the oxygen reduction reaction on a mixed ionic-electronic conducting electrode*

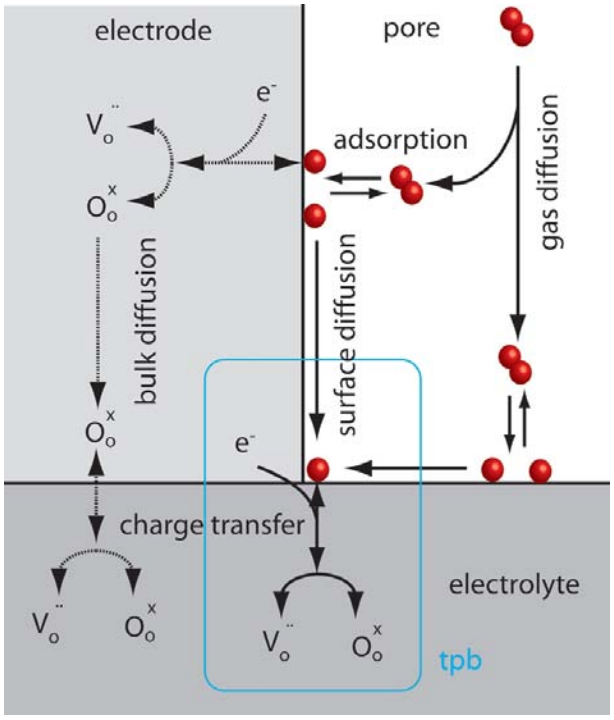

[17] found the activation enthalpy of the surface exchange coefficient to be lower than that one for the self-diffusion coefficient. This contradiction shows that the processes are not yet well understood. They also reported a strong correlation between k and D. This leads to the suggestion, that good oxygen ion conductors also have good oxygen exchange properties. Another investigation on perovskites revealed a dependence of k on the oxygen nonstoichiometry [18]. This implies that both the surface exchange and the diffusion are dependent on the presence of vacancies in the oxygen sublattice. However, in order to obtain well performing cathode materials the compositions should exhibit high oxygen exchange capacities for an easy incorporation of oxygen ions in their lattices and additionally high oxygen diffusivity in order to ensure fast transport of the oxygen ions through their lattice.

Based on the experimental findings and hypotheses presented in literature, the exchange of oxygen on the surface of a MIEC can be divided tentatively into a number of elementary steps according to the following scheme

$$O_2^{(gas)} + M_M^X \leftrightharpoons O'_{2,Ad} + M_M^\bullet$$

$$O'_{2,Ad} + M_M^X \leftrightharpoons O''_{2,Ad} + M_M^\bullet$$

$$O''_{2,Ad} \leftrightharpoons 2O'_{Ad}$$

$$O'_{Ad} + V_O^{\bullet\bullet} \leftrightharpoons O_O^{\bullet}$$

$$O_O^{\bullet} + M_M^X \leftrightharpoons O_O^x + M_M^{\bullet}$$

The subscript "ad" refers to "adsorbed". Here, electronic defects are supposed to be localized on the transition metal M site in accordance with small polaron hopping being the dominant conduction mechanism in most mixed-conducting perovskites in the relevant temperature and oxygen partial pressure range [19–23]. The scheme comprises the adsorption, dissociation, and incorporation of oxygen species as well as charge transfer steps from the solid oxide to the respective species. In order to create a starting point for any investigation of the actual oxygen exchange mechanism, it is commonly assumed that one of the above mentioned steps is significantly slower than the other steps and hence determining the rate of the overall reaction.
To gather information about this rate-determining step (rds), attempts have been made to identify and quantify the oxygen species and crystal defects such as oxygen vacancies present on the electrode surface using in situ surface analytical techniques. However, up to date many of the available surface analytical tools are applied successfully only to systems under vacuum conditions, which are far apart from the conditions typically prevailing in a SOFC. A phenomenological approach to an elucidation of the rds consists in determining the effective rate constant of surface oxygen exchange. In fact, three different rate constants need to be distinguished depending on the applied experimental technique: k^q from electrical measurements, k^δ from chemical experiments, and k^* from isotope exchange experiments with (this part will be explained in more detail in subsection 3.1.3)

$$k^q \approx k^*$$

and

$$k^\delta = \omega_O k^*$$

where

$$\omega_O = \frac{c_O}{RT}\frac{\partial \mu_O}{\partial c_O} = \frac{1}{2}\frac{\partial \ln P_{O_2}}{\partial \ln C_O}$$

ω_O is call the thermodynamic factor, c the concentration, R the gas constant, T the temperature, μ the chemical potential, P_{O_2} the oxygen partial pressure and the subscript "O" refers to regular oxide ions $O_O^\times$ [24].

Theory of Ionic Conduction in Solids: The total electrical conductivity (σ) of a solid is the sum of the partial conductivities of the ionic and electronic charge carriers:

$$\sigma = \sum_i q_i \mu_i c_i \tag{1.10}$$

where c_i is the carrier density, q_i the charge, and μ_i the mobility. It is thus apparent that two parameters can be modified to increase the conductivity of a solid: the carrier concentration and/or the mobility

The concentration of ionic defects can be increased in one of several ways: (1) by substitution, *i.e.*, the addition of aliovalent impurities requires the generation of ionic defects with opposite charge to maintain electrical neutrality; and (2) by deviation from stoichiometry, *i.e.*, reaction with the gas phase results in a reduction or oxidation of the compound and a formation of excess oxygen vacancies or interstitials. However, the latter process simultaneously produces electronic species, thereby leading to mixed conduction. The ionic mobility depends on several factors, the most important being the height of the potential barrier that the ion must overcome to pass from one well to an adjacent well. In general, the barrier height depends on several factors, including the strain energy that needs to be expended for the ion to squeeze through the bottleneck, the polarizability of the lattice, and the electrostatic interactions between the ion and its surroundings [25].

The materials used to construct SOFC device need to have high oxygen ion conductivity at the operating temperature of the device. This ionic conductivity consists of two components: bulk, or lattice, conductivity and grain boundary conductivity (this could have two components, conductivity through or along the boundary). Both components are involved in dc devices in which the total conductivity (bulk plus grain boundary conductivity) is important [9]. The lattice conductivity σ is determined by an empirical Arrhenius-type equation,

$$\sigma T = \sigma_0 \, e^{\frac{-E_a}{kT}} \tag{1.11}$$

where T is the absolute temperature, k is Boltzmann's constant, E_a is the activation energy for the conduction process, and σ_0 is the preexponential constant. To obtain high values of lattice conductivity at low temperatures, the E_a for the conduction process needs to be as small as possible.

1.2.3 Materials for Solid Oxide Fuel Cells

As already mentioned, the transport and reaction processes occurring in a SOFC require thermal activation to proceed at a noticeable rate. For this reason, SOFCs are normally operated at temperatures as high as 800-1000 $°C$ (HT-SOFC). At these temperatures, however, undesired reactivity of the individual cell components towards each other is significantly increased. In addition, thermochemical expansion mismatch can cause cracks and sealing leaks upon (intended or unintended) thermal cycling further reducing the lifetime of the cell. Consequently, one main aim of current SOFC research lies in lowering the operating temperature to the intermediate range of 500-700 $°C$ (IT-SOFC). This makes a further optimization of the different components necessary. Regarding the electrolyte, ohmic losses might be lowered to a reasonable degree by reducing its thickness. The greater challenge resides in the reduction of polarization losses at the cathode, since the cathode reaction typically exhibits a higher activation energy than the electrolyte conductivity and anode reaction [26, 27].

1. *Electrolyte Materials*
   The conventional electrolyte is made of Yttria (Y_2O_3) Stabilised Zirconia (ZrO_2), abbreviated YSZ (typically 8 or 10 % Y_2O_3). YSZ is an electronically insulating oxide with high stability both in oxidizing and reducing atmospheres presents at the cathode and anode of the fuel cell, respectively. The ability to conduct O^{2-} ions is brought about by the fluorite crystal structure of zirconia in which some of the Zr^{4+} ions are replaced with Y^{3+} ions. When this ion substitution occurs, one every two Y^{3+} substituted become vacant ($V_O^{\bullet\bullet}$) because of three O^{2-} ions replacing four O^{2-} ions for the material to remain neutral. Oxide-ion transport occurs between vacancies located at tetrahedral sites in the fluorite lattice, and the process is now well understood at the atomic and molecular level [28]. The ionic conductivity of YSZ ($0.02\ S \cdot cm^{-1}$ *at* $800\ °C$ *and* $0.1\ S \cdot cm^{-1}$ *at* $1000\ °C$) is comparable with that of liquid electrolytes, and it can be made very thin (in the order of μm) ensuring that the ohmic loss in SOFC is comparable with other fuel cell types. Gadolinium doped Ceria (CGO) is an alternative oxide ionic conductor, which is well studied within the field of SOFC. It has a substantially higher ionic conductivity than YSZ which allows for reducing the working temperature while keeping reasonable conductance but on the other hand, shows also an electronic conductivity in reducing atmospheres (H_2) at high operating temperatures, which gives rise to leak currents because of partial reduction of Ce^{4+} to Ce^{3+}. Gd substitution confers the material a larger stability avoiding Cerium reduction. In state-of-the-art cells CGO does however fill an important purpose as a barrier layer between the YSZ-electrolyte

and the cathode to prevent reactions between these two components. The CGO has become nowadays a standard electrolyte and it is used by companies as Kyocera, CeresPower, BloomEnergy for applications in new domestic power generators. Materials aspects of different electrolyte are summarised in Tsipis *et. al.* reviews [29–31].

Based on the layer that mechanically supports the fuel cells, SOFCs can be commonly divided into five categories, as shown in Fig. 1.5. A comprehensive study has determined that, the area specific resistance (ASR) of an appropriate solid-oxide electrolyte should be less than 0.15 $\Omega \cdot cm^2$ whatever the types of SOFCs are [32]. If for instance, the thinnest dense gas-tight electrolyte layer that can be reliably produced using low cost processing routes is 15 μm, then the acceptable ASR can be achieved once the electrolyte conductivity reaches $\sigma = thickness/ASR = 1 \times 10^{-2}\ S \cdot cm^{-1}$. The need of thin electrolytes to fulfill the above criteria has made anode or cathode supported cells the most interesting choice. There is another type of cells based on proton conductors which have been receiving much attention in recent years due to the advantage of producing steam in the combustion zone and not in the fuel zone, in addition to its possible reversible operation mode as high temperature electrolyzer, however this type of cells are not studied in this thesis. Oxide-ion and proton conducting oxide materials, classified by the conduction of their different types of ions, have been widely exploited for use as electrolytes of SOFCs [27].

Figure 1.5: *Illustration of the different types of cell support architectures for SOFCs.*

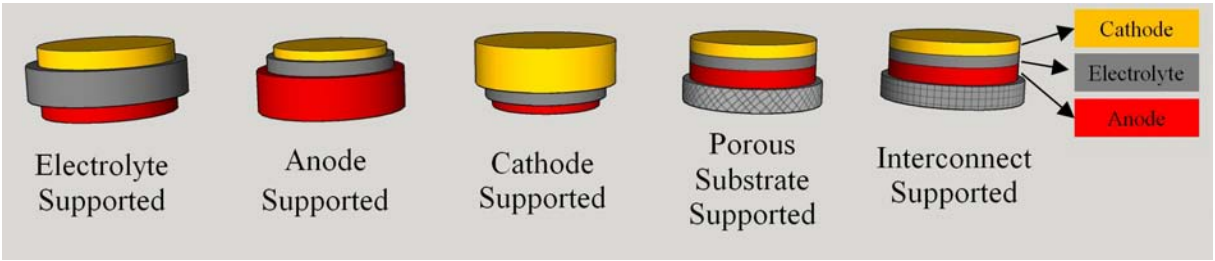

2. *Anode Materials*

   A commonly used anode material is Ni/YSZ cermet (ceramic-metal composite), which does not react with typical electrolyte materials; for example, YSZ and CGO. The material also possesses excellent catalytic properties for fuel oxidation (because of Ni metal particles, while YSZ provides the necessary oxide ionic conductivity to reach the fuel oxidation reaction sites) and its highly porous structure facilitate the

mass transport of reactant and product gas. Ni/YSZ has an appropriate thermal expansion coefficient (TEC) which makes it compatible with the most common electrolytes, while providing a high level of electronic conductivity. Depending on the geometry of the anode, the required electronic conductivity could vary from 1 to $10^2\ S \cdot cm^{-1}$ [33], with the higher conductivities required for anode-supported cells in which the anode is thicker [34]. The ionic conductivity of the anode should be greater than $0.1\ S \cdot cm^{-1}$ [35].

There are some drawbacks for the Ni/YSZ-based anode; for instance, sulphur poisoning and carbon deposition when using natural gas as fuel due to the cracking of methane at low temperatures. The main strategies that have been used to prevent carbon accumulation include complete replacement of the Ni with ceramic materials, promotion of the Ni with other species, and redesign of the anode to use non-Ni containing materials in the conduction layer. More details can be found in a review article regarding the development of anode materials [36] and articles of Boukamp *et. al.* [37] and Tao *et. al.* [33].

3. *Perovskite Structure and Cathode Materials*

The vast majority of oxide ceramics considered as potential cathodes for SOFCs are perovskites or exhibit a perovskite-related structure. In order to better design and optimize the cathode materials, it is necessary to first understand the fundamentals of the perovskite structure. A perovskite-type oxide has the general formula ABO_3. This oxide consists of three elements, namely the large cations, A^{n+} (typically Rare earth or alkaline earth cations of a large ionic radius), the small cations $B^{(6-n)+}$ (transition metal oxides of smaller size), and the oxide anions, O^{2-}, where n is the positive charge on the A ions[3]. Cations $B^{(6-n)+}$ are coordinatted with 6 oxide ions forming octahedral units connected by their corners. Whereas cations A^{n+} are positioned in the sites between the octahedral have 12 oxide ion coordinates. Perovskite is a very versatile structure and full or partial substitution of A or B cations with cations of different size or valence is possible. When the overall valence of the $A-site$ and $B-site$ cations $(n+m)$ adds up to less than six, the missing charge is compensated by introducing vacancies at the oxygen lattice sites [33, 37]. In other words, in aliovalent substitution there should be a charge compensation mechanism for the material to remain neutral, this can be either electronically compensating the concentration of electron carries, for instance when substituting Nb^{5+} in Ti^{3+}

[3]We assume here a full occupancy of the A and B sites. there are some oxides with perovskite structure with a large concentration of cation vacancies and therefore the oxidation state of the cations may vary from what is written here. There are even some perovskites with no A site cations (in this case we can say that n=0)

sites in $SrTi_{1-x}Nb_xO_3$ the material becomes highly conducting. Or generating oxygen vacancies in the oxygen sublattice, for instance when substituting Fe^{3+} for Ti^{4+} in $SrTi_{1-x}Fe_xO_{3-\delta}$ there is one oxygen vacancy each 2Fe ions substituting Ti. Figure 1.6 shows the typical structure of the cubic perovskite.

Figure 1.6: *Perovskite structure.*

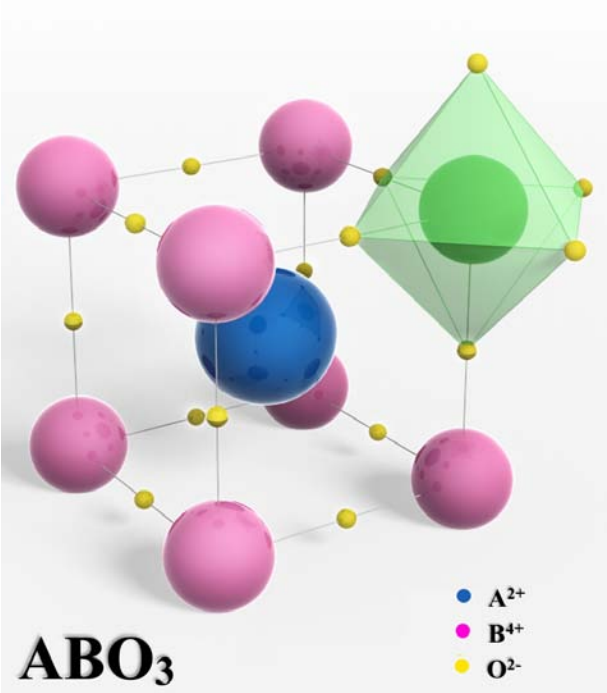

Many perovskite structures are distorted and do not have cubic symmetry. Common distortions such as cation displacements within the octahedra and tilting of the octahedra are related to the properties of the A and B substituted atoms. The degree of distortion in ABO_3 perovskites can be determined according to the Goldschmidt tolerance factor t as follows:

$$t = \frac{r_A + r_O}{\sqrt{2}(r_O + r_B)} \tag{1.12}$$

Where r_A, r_B, and r_O are the effective ionic radii of A, B, and O ions, respectively. Stable perovskite structures are predicted for $0.77 \leq t \leq 1.00$ [38]. Designing t close to unity leads to higher symmetry and smaller unit cell volumes [39]. The perfect cubic structure ($t = 1$) is achieved when the $A - site$ cation has the same size as the oxygen ion (1.40) Å [40]. These form cubic closest packing and the $B - site$ cations are located in the octahedral cavities formed by oxygen [41]. In a perfect cubic perovskite structure the $B - O - B$ chains are linear, *i.e.* the bond angle is

180°. Deviation from cubic symmetry results in tilting of the BO_6 octahedra and, therefore, in reduced $B-O-B$ bond angles. For $t > 1$ the hexagonal structures tend to be stable [38] whereas for $t < 1 - 0.9$ the lattice structure changes from cubic to rhombohedral and then to orthorhombic [42], $t < 0.7$ generally form other structures. Those are not strict rules and are only taken as a guide.

For most of the perovskite materials used as cathodes in SOFCs, the A-site cation is a mixture of rare and alkaline earths (such as La and Sr, Ca or Ba), while the B-site cation is a reducible transition metal such as Mn, Fe, Co, or Ni (or a mixture thereof)[43]. Therefore, in most cases, a redox catalytic mechanism is usually provided by the mixed valence of the B-site cations [44]. The octahedral symmetry around the transition metal often promotes a metallic or semiconducting band structure leading to high electronic conduction at high temperatures . With a rational choice of A- and B-site cations, a large and stable number of oxygen ion vacancies can be introduced at SOFC operating conditions, thus facilitating significant bulk ionic oxygen transport [45] and according to the involved cations (their size, valence state, electronic configuration, etc.) much more complex compositions compared with the simple ABO_3 compounds can be obtained, for example the Ruddlesden-Popper series (R-P) $A_{n+1}B_nO_{3n+1}$ or layered double perovskite $AA'B_2O_6$ compounds. We will discuss in more detail about these compounds below.

Similar to the anode, the cathode is normally a porous structure that must allow rapid mass transport of reactant and product gases. Strontium-doped lanthanum manganite ($La_{1-x}Sr_xMnO_3$) (LSM), a *p-type* semiconductor with high electronic conductivity (202 $S\ cm^{-1}$ at 900 $°C$ for $x = 0.16$ [14]), has been the most commonly used material for cathodes in high temperature SOFCs. An advantage of LSM compared to other cathode materials is the low thermal expansion coefficient (TEC) of $11 \times 10^{-6} - 13 \times 10^{-6}\ °C^{-1}$ in a temperature range of $35 - 1000°C$ [14, 47]. These low TEC values show good compatibility with YSZ (TEC: $10.5 \times 10^{-6}\ °C^{-1}$) [48, 49]. Although LSM shows acceptable electronic conductivity, it shows poor oxide ion conductivity and inadequate catalytic activity at intermediate temperatures because of the stability of Mn^{4+} ions and the difficulty of creating oxygen vacancies in the lattice [32, 50]. Due to its sluggish oxygen diffusion rate [50, 51], the oxygen reduction reaction in LSM mainly occurs at the triple phase boundary (TPB)(cathode-electrolyte-gas Figure 1.4). To increase the TPB area or length, LSM + YSZ composite cathode has been adopted, which provides improved cathode performances compared to the single LSM cathode [52, 53]. However, LSM and YSZ react forming a $La_2Zr_2O_7$ impurity phase at the interface [54]. This electronic and oxide ionic insulator phase in between LSM and YSZ decreases the TPB area and finally

Figure 1.7: *Ruddlesden–Popper phases, $A_{n+1}B_nO_{3n+1}$, where A and B are cations, and O an oxygen anion. The $n = 1$, 2 and 3 members of the series are shown [46].*

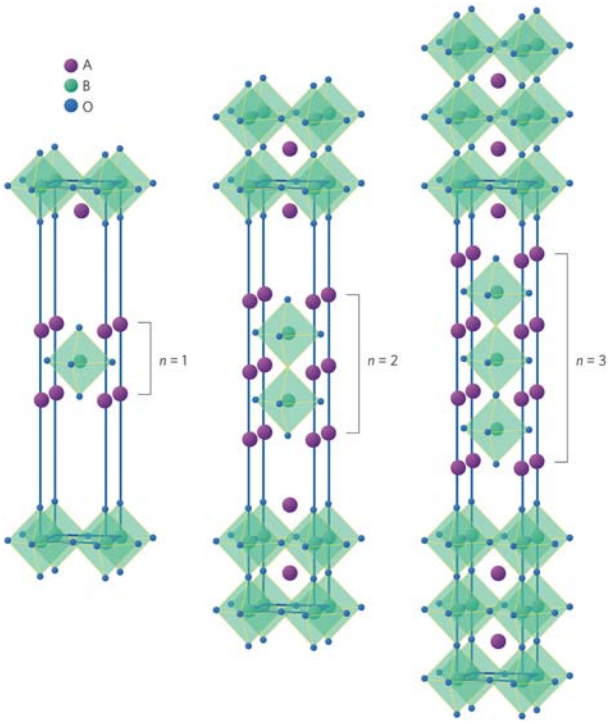

deteriorates the cathode performance. The side reaction between LSM and YSZ can, however, be suppressed by adopting A-site deficient LSM [55]. Recent papers shows outstanding surface exchange coefficients in LSM films with columnar structure being the enhanced performance associated to the exchange rate at the grain boundary regions at the surface [56, 57].

The polarization of the cathode increases significantly as the SOFC temperature is lowered due to the high activation energies of the oxygen reduction reaction (It is found that the overall cell loss is dominated by the cathode process [58], which can be 65% of the total voltage loss [59]), therefore, reducing the operation temperature for IT-SOFC requires cathode materials with a high catalytic activity. In this regard, alternative cathode materials with a mixed valence transition metal oxide provide higher activities for oxygen reduction. At the same time most of these compounds are mixed ionic-electronic conductors (MIEC) which extends the TPB to the whole surface of the cathode decreasing the ASR at intermediate working temperature. It is in cells operating at around 650 $^{\circ}C$ that the advantages of using mixed conducting oxides become apparent. One such material is Lanthanum cobaltite, $LaCoO_3$. This has a perovskite structure with significant *p-type* electronic conductivity (8×10^2 $S\ cm^{-1}$ at 800 $^{\circ}C$); higher than LSM under similar conditions [60]. However, it is less stable than LSM at HT-SOFC temperatures [61]. Substituting

strontium onto the A site forms $La_{1-x}Sr_xCoO_{3-\delta}$ (LSC), improving stability and maintaining good electronic conductivity, above 1300 $S \cdot cm^{-1}$ (for $0.1 < x < 0.8$ at 600 $°C$ [62]) increasing the oxygen vacancy concentration in the intermediate-temperature range. A drawback to LSC is its unacceptably-high TEC of the order of 20×10^{-6} $°C^{-1}$ [20]. This can be attenuated by replacing some of the cobalt with iron, forming $La_{1-x}Sr_xCo_{1-y}Fe_yO_{3-\delta}$ (LSCF). The properties of this material are remarkably attractive; electronic conductivity is high: 350 and 250 $S \cdot cm^{-1}$ at 600 and 800$°C$ [63]; ionic conductivity is significant: $> 10^{-2}$ $S \cdot cm^{-1}$ at 800$°C$ ($La_{0.8}Sr_{0.2}Co_{0.2}Fe_{0.8}O_3$) [64]; TEC is adequate: $\approx 15 \times 10^{-6}$ $°C^{-1}$ [63]. Deleterious reactivity does occur with YSZ but not with CGO [65] meaning that LSCF is typically studied using the latter as the electrolyte, or with a doped ceria barrier layer if the use of YSZ is required or if YSZ is used as electrolyte [66–68]. This solution is complicated by the possibility of reactivity between YSZ and CGO forming $(Ce, Zr, Gd, Y)O_{2-\delta}$ phases of lower ionic conductivity [69]. Shao et al [70] used Ba instead of La into the LSCF structure to obtain $Ba_{0.5}Sr_{0.5}Co_{0.8}Fe_{0.2}O_{3-\delta}$ (BSCF) cathode and reported high conductivity, excellent oxygen transport and catalytic activity. In fact, it is considered among the most active MIEC material but very unstable degrading very quickly with a phase transformation into the hexagonal phase. Here it is important mentioning that the degradation process associated with segregation toward the surface (Sr in LSCF and Ba in BSCF) cause serious deactivation. Therefore the use of more stable materials avoiding or minimizing A-cation migration is very interesting.

In addition to perovskite-type cathode materials, there are a number of other new, promising candidates that have been intensively focused recently. These materials include perovskite-related Ruddlesden-Popper (R-P) phases and layered double perovskite. As we mentioned above, R-P phases have the generic formula $A_{n+1}B_nO_{3n+1}$. These phases are related to the perovskite structure as they consist of n perovskite-like layers; ABO_3, separated by single rock salt-like layers; AO. Typically phases with $n = 1, 2$, and 3 can be synthesised by traditional ceramic techniques [71]. These structures are shown in Fig. 1.7. Higher-order phases can be reached via layer-by-layer deposition methods[72, 73] ($n = \infty$ corresponds to infinitely thick perovskite layers, *i.e.* the perovskite structure itself). Interest in these phases was motivated by the discovery of MIEC in the $n = 1$ phase $La_2NiO_{4+\delta}$ (LNO) at temperatures relevant to IT-SOFCs [74, 75]. The ionic conductivity in this case it is mediated by a very effective diffusion mechanism involving interstitial oxygen (not oxygen vacancies as in common perovskites). Before that time R-P phases had predominantly been studied at low temperatures for interesting magnetic

Table 1.2: *The most relevant materials properties for the main state-of-the-art SOFC cathodes [9]*

Family	Composition	TEC (K^{-1})	σ (S cm^{-1}) 500–750°C	D^*(cm^2 s^{-1}) 600°C	k^* (cm s^{-1}) 600°C	Reference(s)
Perovskites	$La_{0.8}Sr_{0.2}MnO_{3-\delta}$	12.0×10^{-6}	120–130	$5.2 \times 10^{-18(a)}$	$1.5 \times 10^{-11(a)}$	175–177
	$La_{0.5}Sr_{0.5}CoO_{3-\delta}$	21.3×10^{-6}	1,300–1,800	2.6×10^{-9}	1.3×10^{-6}	93, 177, 178
	$La_{0.6}Sr_{0.4}Co_{0.2}Fe_{0.8}O_{3-\delta}$	15.3×10^{-6}	300–330	1.7×10^{-10}	1.1×10^{-7}	95, 179
	$Ba_{0.5}Sr_{0.5}Co_{0.8}Fe_{0.2}O_{3-\delta}$	24×10^{-6}	30–35	3.3×10^{-7}	1.4×10^{-5}	99, 180, 181
Double perovskites	$GdBaCo_2O_{5+\delta}$	16.4×10^{-6}	550–925	7.0×10^{-10}	3.1×10^{-7}	125, 126
	$PrBaCo_2O_{5+\delta}$	24.6×10^{-6}	400–700	6.4×10^{-9}	2.8×10^{-7}	122, 127, 132
RP K_2NiF_4 type	$La_2NiO_{4+\delta}$	13.0×10^{-6}	55–65	8.7×10^{-9}	1.7×10^{-8}	182, 183
	$Pr_2NiO_{4+\delta}$	13.6×10^{-6}	100–120	2.5×10^{-8}	5.1×10^{-7}	183
	$Nd_2NiO_{4+\delta}$	12.7×10^{-6}	35–45	9.7×10^{-9}	1.1×10^{-7}	183

Abbreviations: σ, overall conductivity; D^*, oxygen self-diffusion coefficient; k^*, oxygen surface exchange coefficient; RP, Ruddlesden-Popper; TEC, thermal expansion coefficient.
[a]For $La_{0.8}Sr_{0.2}MnO_{3-\delta}$, D^* and k^* were extrapolated from high-temperature values.

effects [76, 77], as well as superconductivity[78]. The interstitial ionic conductivity in LNO was found to be greater than in LSCF [75]; 0.02 *vs.* 0.003 $S \cdot cm^{-1}$ at 700°C [79] and this boosted research into R-P phases as SOFC materials. The Table 1.2 show a summary of the most relevant materials properties for the main state-of-the-art SOFC Cathodes[9].

More detailed information on cathodes can be found in the reviews of Tarancon *et. al.* [80], Santiso and Burriel [81] and Kilner and Burriel [9]. The current development and properties related to double perovskite materials associated with the work of this thesis will be reviewed in the sections below.

1.3 Family $LnBaCo_2O_{5+\delta}$ $(Ln - BCO)$: State of the Art

The double perovskite materials are derived from 50% lower valent substitution on the *A-site* of a normal perovskite oxide such that the general formula ABO_3 can be written as; $A_{0.5}A'_{0.5}BO_{3+\delta}$. This is the format used when the two cations are disordered over the available *A sites*. However when the size difference between the two cations is significant they tend to order and the formula for the material is rewritten in the following; $AA'B_2O_{5+\delta}$. These layered perovskite have been extensively studied in the past because of their extraordinary magnetic and transport properties at low temperatures, in particular, layered cobaltites with the general formula $LnBaCo_2O_{5+\delta}$ (Ln=Gd, Pr, Y, La, etc.) have been the object of growing research activity in recent years [80, 82–88]. These materials possess an ordered structure in which lanthanide and alkali earth ions occupy the $A - site$ sublattice, barium the $A' - site$, and cobalt the $B - site$. The crystal structure of these oxides can be regarded as a layered crystal consisting of consecutive layers of

$[BO]_2-[A'O]-[BO]_2-[AO]_\delta$ stacked along the c-axis [89]. The transformation of a cubic perovskite to such a layered structure reduces the oxygen bonding strength in the $[AO]_\delta$ layer and provides disorder-free channels for ion motion [86], which remarkably enhances oxygen diffusivity and opens the possibility for developing a new class of materials suitable for application as IT-SOFC cathodes. High electronic conductivity was observed by Maignan *et al.*[82] for these layered perovskites above the metal-insulator transition temperature, $T_{M-I} \sim 300-400K$. In addition, for a certain range of oxygen stoichiometry, these materials possess an ordered structure in which lanthanide and alkali-earth ions occupy alternate (0 0 1) layers and oxygen vacancies are mainly located in the rare earth planes $[AO]_\delta$ forming channels along the *a axis* [82, 87, 90] that enhance the oxygen transport properties. Zhang *et al.* [83] systematically studied the phase structure/stability, oxygen content, electrical conductivity, and cathode performance of Ln-BCO (Ln=La, Pr, Nd, Sm, Gd, and Y) oxides. Stability of the double-layered perovskite structure of Ln-BCO oxides is closely related to the ionic radius of the Ln^{3+} cation. A stable layered structure was observed for Ln=Pr, Nd, Sm, and Gd, while it was in a metastable state for Ln=Y and La. The oxygen content and the nominal oxidation state of cobalt ions in the oxide increases with the ionic radius of Ln^{3+}. In addition, larger ionic radii for the Ln^{3+} cation translated into higher oxygen mobility in the $[LnO]_\delta$ layer. Figure 1.8 shows the structure of double-perovskite oxide. The oxygen permeability test shows that the rate of oxygen diffusion through thick $LnBaCo_2O_{5+\delta}$ membrane bulk is much slower than that in BSCF. This was attributed to the oxides' polycrystalline structure and to the fact that oxygen diffusion was limited to the $[LnO]_\delta$ layers only.

However, attractive electrode performance was still observed for Ln-BCO, especially $PrBaCo_2O_{5+\delta}$ (PBCO), which gave a relatively low ASR of 0.213 $\Omega\ cm^2$ at 600 $^\circ C$, because of the fast exchange kinetics across the oxides' surfaces. These results suggest that these layer-structured Ln-BCO oxides have more promising application as materials of reduced temperature SOFC electrodes rather than as materials of ceramic oxygen-separation membranes. Recent studies also demonstrated that layered cobaltites, with Ln=Gd [87, 92] and Pr [93], could be one of the aforementioned potential materials for IT-SOFC applications due to their excellent oxygen transport properties at low temperatures, that is, high oxygen surface exchange coefficient and reasonable oxide ionic diffusivity, in combination with their high electronic conductivity. Tarancón *et al.* [92] obtained the oxygen surface exchange and oxygen tracer diffusion coefficients yielding optimum values for GBCO ($k^* = 2.8\times10^{-7}\ cms^{-1}$ and $D^* = 4.8\times10^{-10}\ cm^2s^{-1}$ at 575 $^\circ C$) by $^{18}O/^{16}O$ isotope exchange depth profile (IEDP) method. Zhu *et al.* [94] reported that a fuel cell with a porous layer of PBCO deposited on a $42\mu m$ thick SDC electrolyte provided a maximum power density of 583 $mWcm^{-2}$ at 600 $^\circ C$, using hydrogen as the fuel and

Figure 1.8: ***(a)*** *Schematic representation of $LnBaCo_2O_{5+\delta}$ double perovskites showing the ordering of Ln and Ba cations and the formation of oxygen deficiency in the $[LnO]_\delta$ planes. This ordering is reflected by the doubling of the c parameter compared with ideal cubic perovskites, resulting in $ap \times ap \times 2ap$ lattice parameters (ap being the lattice parameter of cubic perovskite indexed in Pm-3m space group). The structure has* ***(b)*** *octahedral (O_h) and* ***(c)*** *square pyramidal (C_{4v}) symmetry for Co ions, with different crystal-field splitting of d-electron states for the different coordination symmetries [91].*

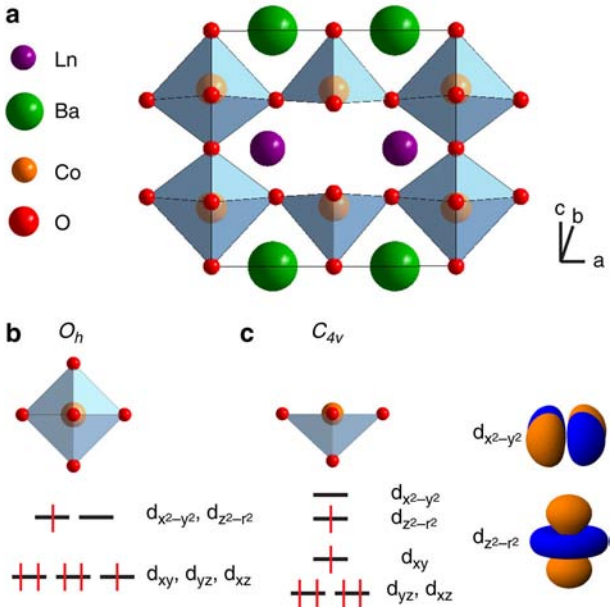

stationary air as the oxidant. Chen *et al.* [95] showed that the phase reaction between PBCO and SDC is weak even at 1100 $°C$. It was found that the electrode's polarization resistance was mainly due to oxygen-ion transfer through the electrode–electrolyte interface and electron charge transfer over the electrode surface over the intermediate-temperature range $450 - 700\ °C$.

Kim and Manthiram [85] observed an increase in TEC with increase in the cation size of the rare earth metal in Ln-BCO. From the viewpoint of stability of SOFCs, they proposed samples with the intermediate rare earth metals, for example, $Ln = Sm$, as the best candidates. The ASR of a composite cathode (50 $wt\%$ $SmBaCo_2O_{5+\delta}$ $(SBCO)$ and 50 $wt\%$ GDC) on a GDC electrolyte is only 0.05 Ωcm^2 at 700 $°C$. Moreover, by using this composite material, the TEC of the electrode was decreased to $12.5 \times 10^{-6}\ K^{-1}$ as compared to the TEC of $20 \times 10^{-6}\ K^{-1}$ for the single-phase SBCO [96].

Since the presence of Ba with a large ionic radius (1.6 Å) is beneficial to form large lattice spacing and higher freedom of oxygen ionic movement, higher Ba content in perovskite has been associated with enhanced ORR rate [97]. Most recently, Deng *et al.* [98] reported a $B - site - ordered$ double perovskite with the $A - site$ fully occupied by Ba, for example, $Ba_2CoMo_{0.5}Nb_{0.5}O_{6-\delta}(BCMN)$ as the promising cathode for SOFCs operated at 700$°C$.

The Co concentration in BCMN, however, is not optimum, for example, only 50% on its $B-site$ cation, resulting in its low electrical conductivity and electrocatalytic activity. Zhou *et al.* [99] reported on $Ba_2Bi_{0.1}Sc_{0.2}Co_{1.7}O_{6-x}(BBSC)$ high oxygen vacancy bulk diffusion and surface exchange rates, as well as high electrical conductivity, of BBSC translate into its extraordinary electrochemical performance at $600°C$ ($0.22\Omega cm^2$). BBSC is also attractive in terms of its low TEC ($17.9 \times 10^{-6}K^{-1}$) due to the absence of Co^{4+}. Despite these encouraging results, possible detrimental effects associated with the phase transition, as reported recently by Streule *et al.* [100, 101] for PBCO at about 500 $°C$, could compromise the applicability of this, and other compounds of the same family, as cathodes for IT-SOFCs. According to Streule *et al.*, apart from the extensively reported lattice distortion observed at low temperatures ($T \sim 75\ °C$) [102, 103], PBCO shows an order–disorder phase transition at 503 $°C$. This phase transition involves a rearrangement of oxygen vacancies from the low-temperature one-dimensional distribution alternating filled and empty chains of oxygen along the a-axis (orthorhombic symmetry, $Pmmm$ space group) to the high-temperature two-dimensional distribution of vacancies in (001) layers, that is, in the $[PrO]_\delta$ plane (tetragonal symmetry, $P4/mmm$ space group). Owing to the importance of oxygen transport properties for electrode applications, strong effects on the electrical and electrochemical performance would originate from the phase transition. Therefore, it is essential to dedicate some efforts to clarify possible problems associated with this particular feature. Tarancón *et al.* [104] demonstrated the significant effect of phase transition on high-temperature electrical properties of layered GBCO perovskite. The phase transition from orthorhombic to tetragonal symmetry takes place for values of $\delta < 0.45$, and an electronic conductivity decrease starts for values of $\delta < 0.25$. In addition, the electrochemical performance of GBCO decreases probably due to an excessive reduction of the oxygen content in the $[GdO]_\delta$ plane. In the review of Pelosato *et. al.* there is an excellent compendium of tables with the most important values for cobalt based layered perovskites. In the sections below the GBCO compound will be reviewed in detail.

1.4 $GdBaCo_2O_{5+\delta}$ (GBCO): State of the Art

Recent work has attracted attention the double perovskite $GdBaCo_2O_{5+\delta}$ (GBCO), which has shown very high oxygen diffusion coefficients D^* (similar to those of pure ionic conducting materials such as YSZ) and large oxygen surface exchange rates k^* [92], along with superior chemical stability against the typical CeO_2 electrolytes [105]. In this compound Gd and Ba cations alternate in sequential A-site layers along the c-axis of the structure, whereas Co ions occupy the B-sites. The stoichiometric material under

standard conditions of P_{O_2} and T holds a substantial oxygen deficiency with oxygen vacancies located mostly on the GdO layers of the structure, parallel to the a–b plane, and arranged forming channels along the crystallographic a-axis [82, 90] and δ changing from 0 to 1. This gives rise to a superstructure that doubles along the c- and b-axis and forms a double perovskite $a \times 2a \times 2a$ cell. The structure of the GBCO material is reported to be orthorhombic Pmmm with a=3.862 Å, b/2=3.934 Å and c/2=3.786 Å [90]. The mechanism for the fast oxygen diffusion in this material is reported to involve mainly those oxygen vacancy sites arranged forming parallel channels along the a-axis, and is therefore expected to be highly anisotropic, as it has been inferred from molecular dynamics calculations [106], the oxygen diffusivity being much larger in the a–b planes of the structure when compared to the diffusivity along the c-axis.

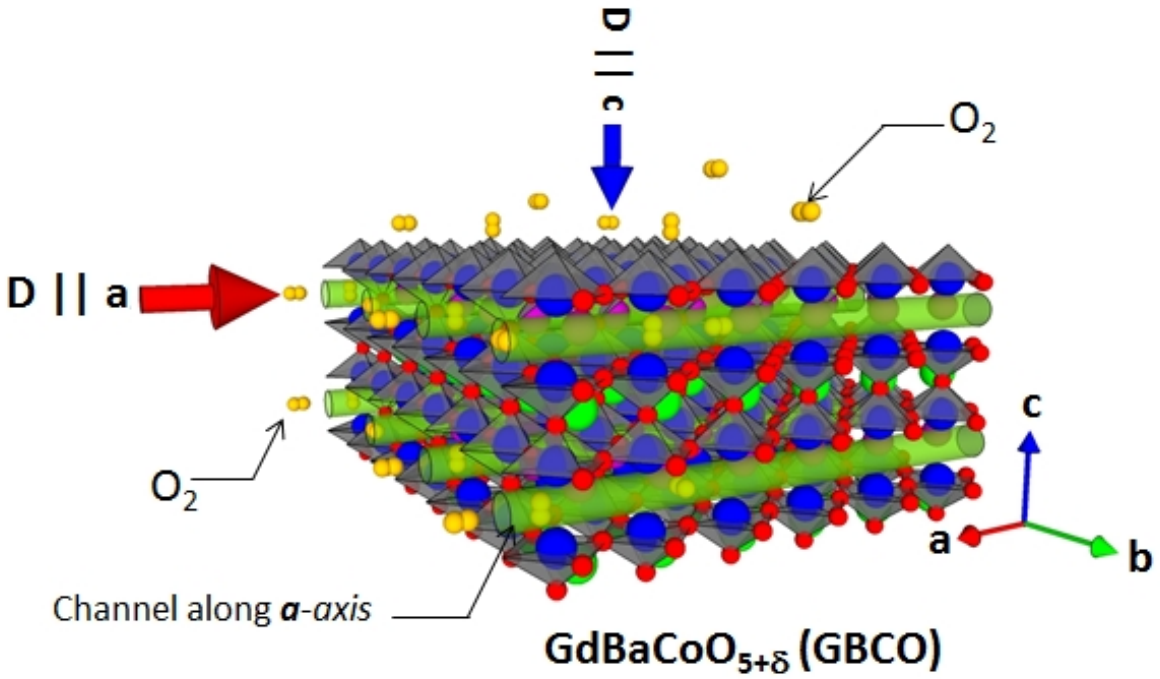

Figure 1.9: *The layered structure of the orthorhombic $GdBaCo_2O_{5+\delta}$ (GBCO) double perovskite compound, currently considered as a promising cathode material in SOFCs, is believed to induce a high degree of anisotropy in the oxygen diffusion coefficient, being maximum along the a–b plane in comparison to the diffusion along the c-axis direction.*

Therefore, in order to experimentally explore the anisotropic diffusion along different crystallographic directions it is necessary to study either single crystals [113] or highly textured (epitaxial) thin films. Recent studies on polycrystalline ceramic samples of the praseodymium double perovskite compound $PrBaCo_2O_{5.5}$ have been able to experimentally probe the anisotropy in the oxygen diffusion which is at least four times larger in crystallites with [100] or [010] orientation than in those with [001] orientation [114]. The intrinsic

anisotropy might be even larger, as the measurements were performed on polycrystalline samples with small grain size, and therefore there were experimental limitations associated to inter-grain diffusion and to the random orientation of the grains. Previous attempts to grow epitaxial GBCO films by Pulsed Laser Deposition (PLD) from stoichiometric targets showed a tendency to form Co-deficient films. This induced the generation of planar defects consisting of supplementary GdO layers, which had an important impact on the charge transport in the films [115]. One purpose of this study is to analyse the oxygen surface exchange and diffusion process on epitaxially grown stoichiometric GBCO films with different orientations. With this aim the composition of the PLD target was varied to obtain stoichiometric films. We make use of the ^{18}O tracer diffusion experiments in both longitudinal and transverse directions, using the same methodology as previously described for La_2NiO_4 epitaxial films [107, 108, 116]. This technique gives us information about the oxygen surface exchange and diffusion kinetics in solids and has been successfully used for the characterisation of thin epitaxial films of different cathode materials like $La_2NiO_{4+\delta}$ [109], $Ba_{0.5}Sr_{0.5}Co_{0.8}Fe_{0.2}O_{3-\delta}$ [110], $La_{0.7}Sr_{0.3}MnO_3$ [111] as well as $La_{1-x}Sr_xCoO_{3-\delta}$ [112].

1.5 Research Motivation and Aim

The general trend in solid oxide fuel cell research leads to lower operating temperatures in order to reduce degradation phenomena due to reactions between adjacent cell components and sealing problems. Since the system kinetics are mostly thermally activated lower temperatures introduce severe problems regarding the overall efficiency of the SOFC system. The cathode material is known to limit the overall system performance and therefore research focuses on the development of new cathode materials with similar or even superior properties such as electrical conductivity, electrochemical activity, and oxygen exchange properties even at lower temperatures. Thus the high efficiency compared to standard thermo-mechanical energy conversion processes could be kept or even be improved. This would be a small step towards sustainable and highly efficient energy conversion systems which are quiet and pollution-free.

Research on new oxide materials with both high mixed ionic and electronic conductivity (MIEC) is of great importance in order to achieve optimum performance in a wide range of devices that have considerable potential for clean, low carbon, electrochemical energy conversion. In the case of solid oxide fuel cells (SOFCs), in order to reduce the working temperature to the intermediate range (500-750°C), more active cathode materials are needed, and conventional electronic conductors such as $La_{1-x}Sr_xMnO_{3-\delta}$ (LSM) should be replaced by materials with high electronic and ionic conductivity, as well as good catalytic

activity. In the past decade several reports on layered $LnBaCo_2O_{5+\delta}$ $(Ln - BCO)$ cobaltites (with Ln = Rare Earth, such as La, Y, Gd, Nd, or Pr) of the so-called "112" phase have evidenced a large variety of transport and magnetic properties, which makes their study a very active area in solid-state physics[82, 87, 90, 117, 118].

The aim of this thesis is to find new SOFC cathode materials in the system $GdBaCo_2O_{5+\delta}$ and to characterize these compounds by structural, electrical, and electrochemical means for their suitability in SOFC application. Some of previous studies have highlighted the great potential of GBCO, as a cathode in SOFC [80], with a high reported electronic conductivity above the metal-insulator transition temperature [82, 90], outstanding oxygen transport properties and enhanced surface exchange [80, 87, 92, 118, 119], as well as excellent stability for both structural and electrochemical performance moving across the phase transition[104]. However, to date there is an absence of information about intrinsic ionic conductivity of these higher order $GdBaCo_2O_{5+\delta}$ compounds. To enable measurement of intrinsic electronic and particularly ionic transport properties, the greatest challenge is to synthesise dense, continuous or ideally epitaxial specimens of GBCO through the pulsed laser deposition (PLD) technique. Furthermore, earlier studies on GBCO have theoretically [106] confirmed their anisotropic transport properties (electronic and ionic). These studies also revealed that the anisotropy of oxygen diffusion and electrical conduction appears to improve the transport properties in comparison with non-layered compounds. Based on these earlier findings, both higher order GBCO compounds are also expected to naturally have anisotropic transport properties because of their layered structures. Therefore, growing epitaxial films of the higher order compounds may facilitate the investigation of their intrinsic anisotropic properties.

1.6 Outline of Thesis

This thesis explores deposition and characterisation of the Mixed Ionic Electronic Conducting $GdBaCo_2O_{5+\delta}$ (GBCO). The organisation of the thesis is as follows.

The first chapter has briefly introduced the background, motivation and aims of the research. The second chapter present an overview of the technique, methods and processes involved in the preparation of the layers. The pulsed laser deposition (PLD) technique is described briefly, including background, principles and setup used. Next, the synthesis process for obtaining the PLD targets is shown and finally the general deposition procedure adopted for the growth of the films is described.

The following chapter (Ch.3) to introduce briefly the main techniques used in the characterization of thin film obtained by PLD. Initially, a series of material characterization techniques for structural, morphological and compositional analysis of the films are

described. Then, special attention is devoted to unconventional techniques to study transport properties, surface exchange and diffusion of oxygen in thin films.

There are 2 results chapters. The first one (Ch.4) is with regard to the synthesis and characterisation of the utilised $GdBaCo_2O_{5+\delta}$ PLD targets, followed by the description of the substrate requirements for PLD. The phenomena of target degradation is also highlighted. After the preparation of PLD targets, the chapter continue with the growth and characterization of GBCO in order to primarily determine the appropriate deposition conditions and substrate in order to obtain high-quality epitaxial GBCO films and relate the influence on film microstructure caused by different deposition conditions. in Ch.5. The transport properties of these obtained films are provided and the surface and interface information for these films are investigated. In particular, films with different orientation: pure c-axis and a-axis orientation on SrTiO3(001) and NdGaO3(110) single crystals are studied and the oxygen diffusion analysed by isotopic ^{18}O exchange depth profiling (IEDP) and Time-of-flight Secondary Ion Mass Spectrometry (ToF-SIMS) in the films along the longitudinal and transverse directions at different exchange temperatures and exposure times. The last chapter (Ch.6) summarises the conclusions with respect to the obtained results in this work. Future work about the doubles perovskites materials is also suggested.

CHAPTER 2

Technique, Methods and Processes Involved in the GBCO Preparation

The purpose of this chapter is to present an overview of the technique, methods and processes involved in the preparation of the layers studied in this thesis. The pulsed laser deposition (PLD) technique will be described briefly, including background, principles and setup used. Next, the synthesis process for obtaining the PLD targets is shown and finally will be described the general deposition procedure adopted for the growth of the films.

2.1 Pulsed Laser Deposition (PLD)

The pulsed laser deposition (PLD) is a type of physical vapour deposition (PVD) technique, it is intensively used in material research, as well as the industry, for developing thin films and coatings of special materials, such as: ferroelectrics, superconductors, oxides, polymers, complex hybrid metal-organics, etc. This simple, yet versatile thin film deposition method can be applied to such materials that are not suitable to process by other techniques. PLD technique was utilized to grow $Ln - BaCo_2O_{5+\delta}$ epitaxial films in this work. Prior to describing the experimental procedure, a brief background and basic principles of PLD will be described.

2.1.1 Introduction to Pulsed Laser Deposition (PLD)

Soon after the availability of high power lasers in the 1960's their application to the evaporation of solids and the potential of film growth by re-condensation was realized [120]. However, the breakthrough of this technique, nowadays known as pulsed laser deposition (PLD), came only in 1987 with the successful growth of high T_c superconducting films [121] and later, in 1994, with the discovery of colossal magnetoresistance in PLD-grown $La_{1-x}Ca_xMnO_3$ layers [122]. This was as well only possible after progress in the laser technology has been made and pulsed ultra violet (UV) excimer lasers became available

in the 1970's and 1980's. Great attraction in PLD technique is because of its primary characteristics - the complex stoichiometric transfer from a single target to deposited films, allowing for precise stoichiometric control -. Since these successful developments, this technique has been widely applied to deposit a very widespread range of materials such as superconductors, semiconductors, insulators, oxides, nitrides, carbides, metals, polymers, and even bio-materials throughout various research fields [123]. In addition, this technique has presented remarkably effective fabrication of epitaxial films, superlattices, and electronic devices in the past few decades [123, 124]. Recently, PLD is also gathering increasing attention in the current development of electrochemical applications [125].

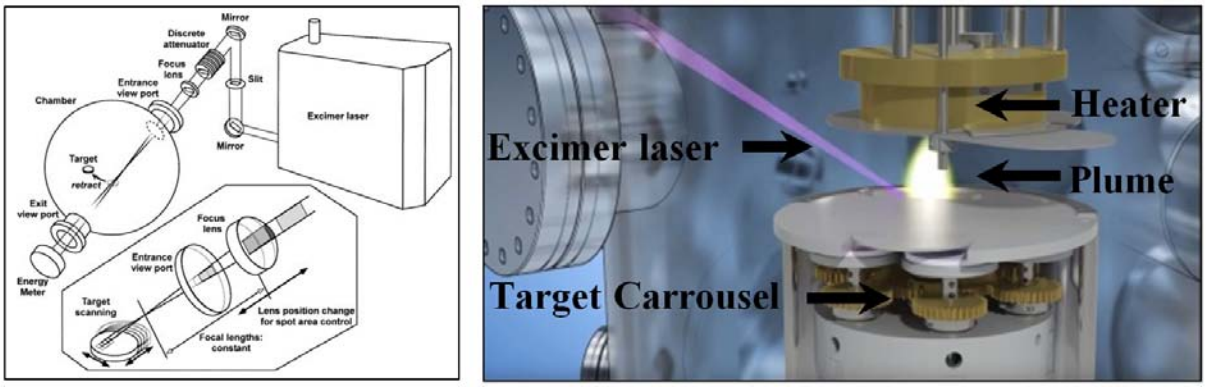

Figure 2.1: *Schematic illustration of PLD system setup: Although conceptually simple, the chemical-physical processes involved in pulsed laser deposition are complex and involve three stages, (i) the laser-material interaction resulting in plasma formation, (ii) the subsequent plasma expansion, and (iii) film growth from the supersaturated gas phase.*

The basic operational principle is depicted in Fig. 2.1. A pulsed high power laser beam, most frequently an UV excimer laser emitting pulses on the order of 20 ns, is focused through an entrance window into a vacuum chamber on a solid target. The focused laser pulses are absorbed at the target surface in a small volume. The absorbed energy density is sufficient to break any chemical bonds of the molecules within that volume. What essentially happens is that high-pressure gas is produced in the surface layer. As a result of the pressure gradient, a supersonic jet of particles is ejected normal to the target surface. In practice, the process is far more complicated than the idealized model discussed above [126]. The particle cloud absorbs a large amount of energy from the laser beam producing an expansion of hot plasma (including atoms, electrons, molecules, ions, clusters etc.) through the deposition chamber. The resulting plasma, also called the plume, is directed towards a substrate, typically positioned in a distance of $30 - 80$ mm from the target, where material re-condenses. The chemistry and energetics of the film growth process can be modified by introducing a background gas into the vacuum chamber (*e.g.* Ar or reactive gas like O_2, N_2, etc.). For example, performing PLD in an O_2 background gas

aids the maintenance of the oxygen stoichiometry of the deposited oxide films.

The technique is inherently very flexible and practically every material can be ablated as the external laser source may easily be exchanged. In addition, various modifications of PLD have been developed for certain deposition requirements. The chemical reactivity may for instance be enhanced by a supplementary ion or plasma beam (ion or plasma beam assisted PLD), the confinement of the plasma in a magnetic field (Aurora PLD), or a synchronized reactive gas pulse (pulsed reactive crossed-beam laser ablation, PRCLA) [127]. PLD can be performed in high vacuum or in low pressure of ambient gases. Due to high deposition rate a single layer can be made in a relatively short period of time with quick turn to next one. Combination of PLD with reflection high-energy electron diffraction (RHEED) allows control deposition of materials not only by number of pulses but also by monitoring intensity of RHEED oscillations (For more information, Ichimiya and Cohen book covering various aspects of theory and application of RHEED for surface analysis [128]). One can control the growth of thin films at an atomic layer level, and by incorporating this layer-by-layer deposition technique; one can design and explore novel materials systems that do not exist in present in any form (the Fig. 2.2 show a 3-D sketch of the elastically scattered electrons in real space). PLD successfully fulfils the requirement in performing of fabrication of combinatorial materials that is to facilitate deposition of number of different materials in a single series of deposition sequence. Segmented targets or multi-target carousels facilitate the deposition of film alloys, heterostructures, new compounds in a single run [129]. The growth conditions in PLD are far from thermal equilibrium and involve kinetic energies typically in the range of $1 - 100\ eV$ as well as electronically excited species, which promote surface mobility. This enables the deposition of high quality films at comparatively low substrate temperatures and yields the potential

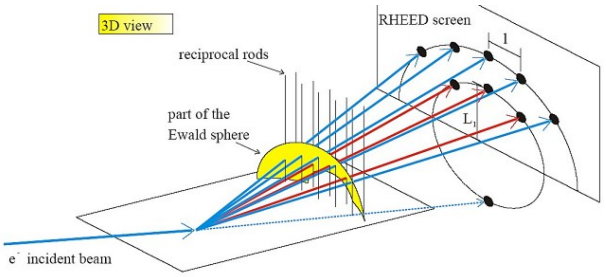

Figure 2.2: *The 3D sketch shows the directions of the elastically scattered electrons in real space. These scattered electron beams hit a fluorescent RHEED screen in certain RHEED spots, lying on so-called Laue circles which are numbered starting from zero. The figure shows the Laue circles n_o.0 in red and n_o.1 in cyan. The spots form a characteristic RHEED pattern depend on the morphology and roughness of the sample surface. As the RHEED intensity depends on the film roughness, the growth process leads to characteristic intensity oscillations of the RHEED spots during the growth process with a single oscillation usually corresponding to the completion of a single monolayer.(Figures taken from: Jürgen Klein, Epitaktische Heterostrukturen aus dotierten Manganaten, PhD Thesis, University of Cologne (2001))*

to synthesize metastable materials unattainable for thermal equilibrium conditions ($E_{Kinetic} \sim 0.1\ eV$)[127].

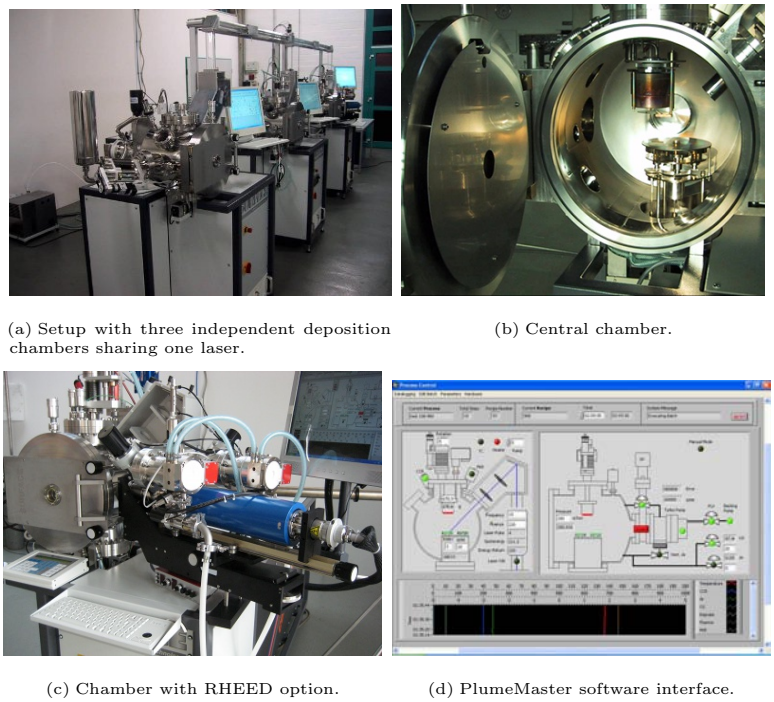

(a) Setup with three independent deposition chambers sharing one laser.

(b) Central chamber.

(c) Chamber with RHEED option.

(d) PlumeMaster software interface.

Figure 2.3: *PLD-Workstation setup.*

Our PLD-Workstation was manufactured by SURFACE systems+technology GmbH & Co. KG. The standard configuration provides a 2" substrate heater and a 4×2" indexed target manipulator. To adjust the process conditions, two mass flow controller (MFC) channels for process gas supply into the chamber are standard. They enable automated control of the process atmosphere and pressure. By the design of the target manipulator in connection with the control software, cone formation on the target surface is avoided and even wear of the target is guaranteed. To achieve even target wear, two different modes of target movement during deposition are available: *Toggling* – The target carousel moves back and forth in a continuous motion so that the laser beam hits the target at any radius from the target center. This mode is easy to set up, only the target diameter needs to be known. *Rotation* – Target rotation speed can be adjusted in order to achieves a very even wear of the target surface. All SURFACE PLD systems are highly automated to control the whole deposition process, this ensures easy operation of the system. The PlumeMaster® software is based on the proven Windows XP Professional operating system. Several process steps with individual settings can be combined into one deposition program. Intuitive process visualization, highly flexible data logging with data export, and self-test capability are additional features. PLD-Workstations is combined into a system sharing

one laser. An extended beamline with automated mirrors then guides the laser beam to the required PLD-Workstation chamber. A laser server computer controls the laser and the beam lines automatically based on a request table, and deposition processes in the PLD chambers are delayed until the laser is available for the particular chamber. The Fig. 2.3 show our PLD-Workstation setup with three independent deposition chambers sharing one laser.

In excimer lasers, the output wavelength is a function of the rare gas/halogen combination. Excimer is the name of the rare gas / halide molecule. There are four wavelengths (spectral lines) that can be generated from fluorine mixtures (ArF, F_2, KrF, XeF). Our system work with a premix KrF radiation (wavelength 248 nm, pulse duration around $20ns$). The Table 2.1 contains the more relevant system specifications.

Laser:	Coherent COMPex Pro 201F, $0.7J$ max. pulse energy
Wavelength:	KF (248 nm)
Laser gases:	20 liters premix, 10 liters He, built-in gas cabinet
Process gases:	2 MFC channels, automated pressure control
Substrate heater:	1" or 2" diameter, 1000 $°C$
Substrate rotation:	0 to 50 rpm
Targets:	4×2", target rotation (0-50 rpm) and position with track control for even wear
Control system:	PC based control, integrated TFT monitor
IT features:	LAN connectivity, SURFWARE support software
Power supply:	3×400 VAC/50 Hz or 3×208 VAC/60 Hz
Water cooling:	Included chiller (201F)

Table 2.1: *PLD-WorkStation System Specifications*

2.1.2 Synthesis of PLD Targets

For the deposition of multication materials, target selection can have significant impact on film growth properties, including particulate density, epitaxy, phase formation, and deposition rate. As a minimum requirement, ablation requires a target material possessing a high optical absorption coefficient at the selected laser wavelength. In general, the phase of the target does not need to be the same as that of the desired film. Only the cation stoichiometry need be "identical"to that of the films, assuming stoichiometric transfer and negligible evaporation from the film surface. For ceramic targets, one prefers target materials that are highly dense, as this will reduce particulate formation during the ablation process. The PLD technique is also flexible, because the spot size of the focused laser beam is small and, therefore, the target area may even be less than 1 cm^2.

This allows to prepare complex samples with enrichments of isotopes or isotopic markers within the deposited film. Being able to easily prepare samples for research purposes or for application tests is especially interesting if the sample or one component is extremely expensive or impossible to prepare with other techniques. Here, the flexibility of the PLD technique pays off, due to the possibility of easily exchanging and adjusting the targets.

The various cathode materials presented in this dissertation were synthesized by conventional solid-state reactions. The conditions and procedures employed varied depending on the material system. While the general procedures are given in this section, more details of the characterization will be given in the relevant chapters. The solid-state reaction route is the most widely used method for the preparation of polycrystalline solids from a mixture of solid starting materials. Solids do not react together at room temperature over normal time scales and it is necessary to heat them to much higher temperatures, often to $1000 - 1500\ ^{\circ}C$ in order for the reaction to occur at an appreciable rate. The factors on which the feasibility and rate of a solid state reaction depend include, reaction conditions, structural properties of the reactants, surface area of the solids, their reactivity and the thermodynamic free energy change associated with the reaction [130, 131]. Fine grained materials should be used if possible in order to increase surface area and enhance the reaction rate. We used high purity commercial (Alfa Aesar) oxides and carbonates as precursor materials (Gd_2O_3, Pr_6O_{11}, Nd_2O_3, $BaCO_3$, Co_3O_4). The reactants are dried thoroughly prior to weighing and the amount of each reactant is calculated depending on the desired stoichiometric ratio (target with excess of specific ions can be obtained in order to compensate deficiencies of such species in the thin films [115]). The powder are manually mixed using an agate and pestle. Sufficient amount of some volatile organic liquid (Methanol in our case) is added to the mixture to aid homogenization. This forms a paste which is mixed thoroughly. During the process of grinding and mixing, the organic liquid gradually volatilizes and has usually evaporated completely after 10 to 15 minutes. The mixtures are successively calcined at 900 $^{\circ}C$ for 20 h, with careful regrinding before and after heat treatment (de-carbonation process). The powder was pressed into a circular pellet (using the uniaxial press of $1''$ of diameter and applying 2 tons for 5 min) and

Figure 2.4: *Heat Treatment following in the target fabrication*

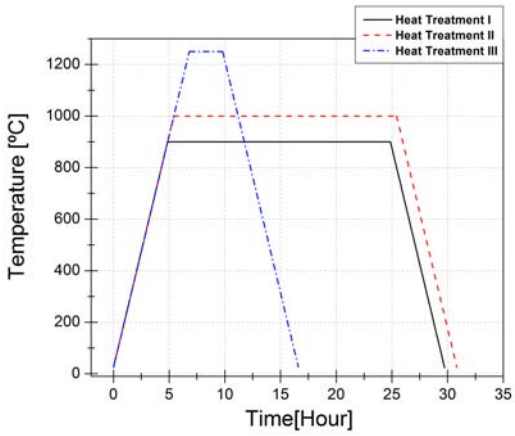

annealed over 20 h at 1000 $°C$ with a final heat treatment at 1250 $°C$ for 3 h to densify it [92, 132] (Fig. 2.4 show the heat treatment curves following in the targets fabrication). The heating and cooling rate of each heat treatment was 3 $°C/min$. Balanced equations for different targets produced are given below;

$$3Gd_2O_3 + 6BaCO_3 + 4Co_3O_4 \Longleftrightarrow 6GdBaCo_2O_{5.5} + 6CO + 2O_2 \quad (2.1)$$

$$Pr_6O_{11} + 6BaCO_3 + 4Co_3O4 \Longleftrightarrow 6PrBaCo_2O_{5.5} + 6CO \quad (2.2)$$

$$3Nd_2O_3 + 6BaCO_3 + 4Co_3O4 \Longleftrightarrow 6NdBaCo_2O_{5.5} + 6CO + 2O_2 \quad (2.3)$$

	Purity %	atomic weight $[g/mol]$	GBCO 10 g	PBCO 10g	NBCO 10g
Gd_2O_3	99.99+	362.50	3.622	– ∘ –	– ∘ –
Pr_6O_{11}	99.99	1021.49	– ∘ –	3.515	– ∘ –
Nd_2O_3	99.997	336.48	– ∘ –	– ∘ –	3.452
$BaCO_3$	99.997	197.33	3.943	4.076	4.048
Co_3O_4	99.9985	240,80	3.208	3.316	3.293
$GdBaCo_2O_{5.5}$	– ∘ –	500.45	$\rho_{theo} = 7,28\ g/cm^3$		
$PrBaCo_2O_{5.5}$	– ∘ –	484.10	$\rho_{theo} =\ g/cm^3$		
$NdBaCo_2O_{5.5}$	– ∘ –	487.44	$\rho_{theo} =\ g/cm^3$		

Table 2.2: *Atomic weights and amount of powder required to prepare 10 g of material (Targets with cobalt excess were obtained increasing by 5% the required weight of Co_3O_4 in the initial stoichiometric mixture)*

In Table 2.2, the atomic weights and the amount of powder required to prepare 10 g of the desired material are listed. The density of the final PLD targets (GBCO, PBCO and NBCO) was determined measuring the final volume of targets and their respective mass. The theoretical density of the oxide materials can be determined by the formula:

$$\rho_{theo} = \frac{\sum_i n_i M_i}{V_c N_A} \quad (2.4)$$

where n is the ions/unit cell (*e.g.* fcc packing n = 4 and for bcc packing n = 2), M is the atomic mass of the ions in the unit cell (g/mol), $V_c = a^3$ is the volume of unit cell (cm^3), where a can be found by the radius of the ions and the packing used. (*e.g* in bcc packing it is "$a = 2r$". In fcc packing it is "$a = sin(4r)$" or "$a = cos(4r)$") and N_A is

avorgados constant ($6.023 \times 10^{23} mol^{-1}$). The related lattice parameters of the materials for calculating their theoretical density can be obtained from crystallographic data, that is, the Inorganic Crystal Structure Database (ICSD) from the Chemical Database Service (CDS). The phases present in the targets were studied using x-ray powder diffraction (XRD) and compared with those obtained from ICSD databases, this technique and the results obtained will be described in later sections.

2.1.3 Film Deposition Process

For any deposition technique, there is a set of fundamental parameters which can be controlled. The most important of these are *(i)* the substrate temperature T_s, *(ii)* the deposition rate $\boldsymbol{R}$, *(iii)* the ambient pressure in the chamber $\boldsymbol{P}$, and *(iv)* the energy of the deposition flux E_f [129, 133]. In thermal deposition techniques, the contribution to the surface dynamics from $E_f \sim 0.1 eV/Particle$ is insignificant as it is one to two orders of magnitude lower than the bond strengths of the surface species. In nonthermal techniques, however, E_f is an important new control parameter that can critically influence the film properties. There are of course other parameters such as the thermodynamic properties of the system (though there is little control of these once the system has been chosen), the substrate crystallinity, orientation, chemistry [134] and lattice constants. The influence of the substrate type is also critical [135] and has been comprehensively reviewed by Li for the growth of ferroelectric/superconductor heterostructures, with emphasis on the problems of crystallinity and morphology in the growth of $YBa_2Cu_3O_{7-x}$ [136]. He makes the salutary point that, even using PLD in conjunction with RHEED (which he calls "laser MBE" and claims is the best method for research into complex metal oxide growth), the film quality depends critically on the details of the substrate surface. Only by carefully choosing the substrate's miscut angle (vicinality[1]), can step-flow growth be promoted, resulting in atomically smooth film surfaces. In general, optimization of each of these process parameters cannot be considered independently of one another. This interdependence has consequences on the choice of the most suitable deposition technique for any given chemical system.

2.1.3.1 Substrate Requirements

Two different types of single crystal substrates with perovskite structure have been used to epitaxially grow the films: $SrTiO_3$ (STO) with (100) orientation and $NdGaO_3$ (NGO) with (110) orientation. The STO crystal has a cubic crystal structure with a

[1]The miscut between the substrate surface and the ideal crystallographic plane

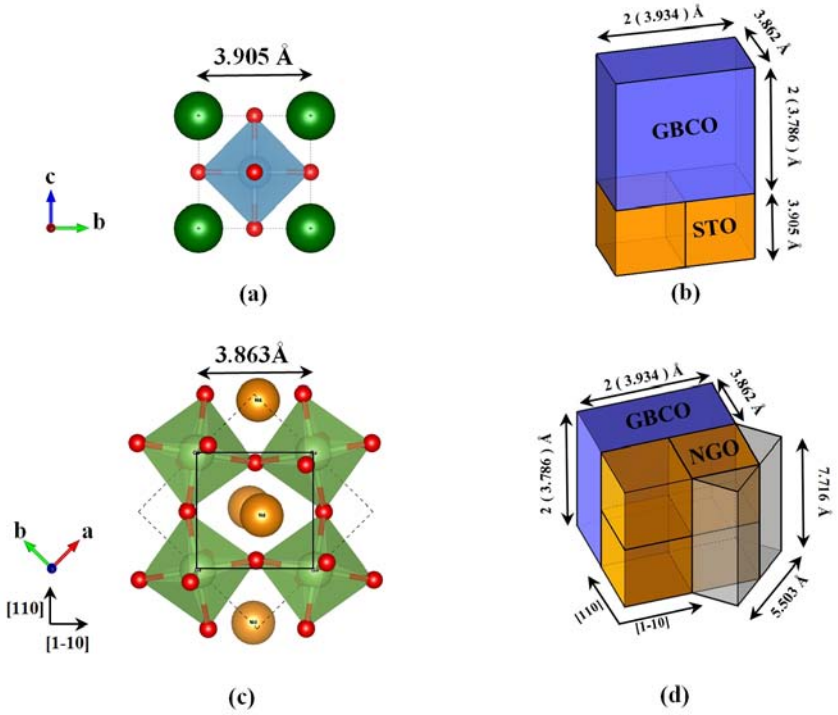

Figure 2.5: *(a) The projection of the STO along a-axis and (c) NGO along c-axis. (b) and (c) are a schematic view of the match of c-axis GBCO oriented on STO(100) and a-axis GBCO oriented on NGO(110) substrates respectively.*

tolerance factor of $t \sim 1.01$, in which the Ti atom is embedded in the octahedron oxygen box and the Sr atoms occupy the cubic corners. The STO compound is often chosen as the substrate material in oxides thin films deposition, mainly for its chemical and compositional stability and for its lattice constant 3.905Å, well matched with the lattices parameters of a wide class of perovskites oxides compounds. The NGO is orthorhombic with pseudo-cubic in-plane parameters of 3.863 and 3.854Å out-of-plane[2]. These substrates and orientations were chosen in order to promote the growth of highly textured thin films allowing experimentally explore the anisotropic properties of the material along different crystallographic directions (see Fig. 2.5). If we consider the GBCO structure reported by Frontera *et. al.* corresponding to ICSD Collection Code 154018 [90] (orthorhombic with $a = 3.862$, $b/2 = 3.934$ and $c/2 = 3.786$Å cell parameters), the corresponding mismatch[3]

[2]One useful tranformation from the pseudo-cubic to the orthorhombic cell is $a' = \sqrt{2}a, b' = \sqrt{2}b, c' = 2c$. In perovskites this transformation almost always needed. This phase is the Pbnm orthorhombic phase of the cubic perovskite cell [137].

[3]In case of heteroepitaxy, the materials of film and substrate are different, with different lattice parameters. Such lattice mismatch gives rise to a strain, tensile or compressive, that can be calculated as the ratio between the lattice parameters of the substrate and bulk/film $m = \frac{a_s - a_l}{a_s}$, where a_l and a_s are the unstrained layer and substrate in-plane lattice constants, respectively. In general the strain can be elastic, and in this case a deformation of the in-plane lattice parameters produce an out-of-plane deformation of the cell in order to conserve the volume. If $a_s > a_l$, $m > 0$ imply tensile strain on the deposited film in-plane, and out-of-plane compressed, while for $m < 0$ the strain is compressive and in-plane lattice is

on STO and NGO substrates can be easily calculated. The Table 2.3 contains the cell parameters of STO, NGO, GBCO, PBCO, NBCO structures and the mismattch calculated from the difference between the area of the corresponding plane of the primitive $Ln-BCO$ cell and the corresponding substrate. The mismatch values indicate the most probable growth directions. The X-ray patterns and reciprocal space maps indicate that indeed this growth trend is maintained at high temperatures and effectively for example GBCO grows c-oriented on STO(100) substrates and a-oriented on NGO(110) substrates. These aspects will be extensively detailed in the results section.

	STO Cubic [Å]	NGO Orthorhombic [Å]	NGO Pseudo-cubic [Å]	GBCO Orthorhombic[90] [Å]	PBCO Tetragonal[82] [Å]	NBCO Tetragonal[82] [Å]
a	3.905	5.463	3.863	3.862	3.9019	3.8969
b	3.905	5.563	3.863	2×(3.934)	3.9061	3.9015
c	3.905	7.708	3.854	2×(3.786)	7.6306	7.6115
STO				**ab: +0.37%** bc: +2.35% ac: +4.13%	ab: bc: ac:	ab: bc: ac:
NGO				ab: -1.99% **bc: -0.02%** ac: +1.85%	ab: bc: ac:	ab: bc: cd:

Table 2.3: *Cell parameters of STO, NGO, GBCO, PBCO and NBCO structures along with calculated mismatch for the different orientations*

2.1.3.2 Thin Film Growth

Films deposited on room temperature substrates are usually amorphous; their crystallinity can often be improved by deposition at higher substrate temperature (T_S). This can be understood by considering the microscopic detail of film growth by PLD in vacuum. The substrate is typically exposed to an incident flux of ablated ions and neutrals for a brief period ($\sim 1ms$) and then enters a quiescent interlude of $\sim 100ms$ (assuming a 10 Hz laser repetition rate) before receiving the next dose of ablated material [126]. We start by considering the evolution of the film during the brief periods when the substrate is being bombarded by ablated flux. Incident atoms may simply reevaporate. They could also sputter pre-deposited atoms. For film growth, however, some must accommodate. Depending on the particles kinetic energy, this may involve 'gentle' adsorption onto the surface, or more violent embedding and damage of the preexisting film. Larger incident particles may fragment on impact. Once on the surface, adsorbed particles may diffuse,

compressed, but expanded out-of-plane.

nucleate with pre-existing surface atoms and clusters, or induce fragmentation of pre-existing clusters. Given the assumption of such mobility on the surface, we can anticipate that models analogous to those used to explain the initial stages of film deposition by electron beam or thermal sputtering will be equally applicable to PLD. Three principal modes of film growth are generally distinguished [138] (see Fig. 2.6). These modes named after their original investigator and are as follow:

1. *Layer-by-layer, or Frank-van der Merve (FM)*, growth mode refer to the case when the film atoms strongly bound to the substrate than to each other. As a result, each layer is fully completed before the next layer start to grow, *i.e.*, strictly two-dimensional (2-D) growth takes place.

2. *Island, or Volmer-Weber (VW)*, growth mode correspond to the situation when film atoms are more strongly bound to each other than to the substrate. In this case, Three-dimensional (3-D) islands nucleate and grow directly on the substrate surface. This island mode results in the effects of more crystallographic disorder and less consummate layers in the films, leading to the formation of defects and grain boundaries.

3. *Layer-plus-Island, or Stranski-Krastanov (SK)*, growth mode represents the intermediate case between FM and VW growth. Here a crucial role is played by the mismatch between film and substrate, inducing a strain on the growing film. A layer-by-layer growth take place in the first stage. Then, the thicker become the film, the higher is the elastic energy due to the strain. Such large strain energy can be lowered by forming islands in which strain is relaxed. This mechanism results in a continuous film of one or two monolayers onto which successively discrete islands are formed.

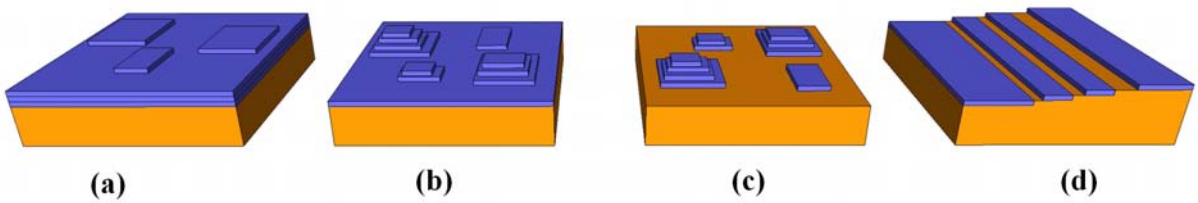

Figure 2.6: *(a) is layer-by-layer growth mode (Frank-van der Merwe), (b) is layer-island growth mode (Stranski-Krastanov), (c) island growth mode (Volmer-Weber) and (d) step-flow growth mode.*

The previous approach does not take into account the effect on the growth kinetic of the deposition parameters, such as the value of supersaturation in the gas phase, the substrate

vicinality and the crystallographic misfit between the film and substrate unit cells. For the effect of such parameters, different growth modes have been observed for the same film-substrate system, thus clearly indicating that growth techniques and parameters are crucial to determine the final film morphology. The substrate vicinality provides terrace surface, separated by steps. The steps heights and the terraces length depend on the angle and the direction of the miscut. On a vicinal substrate, beside the growth modes described above, a fourth way of growth can occur: the step-flow mode ((d) in Fig. 2.6). This growth mode takes place on vicinal surface with high steps density and small terraces, in some deposition condition. In this case, the steps act as a sink: the adatoms diffuse towards the substrate steps preventing the nucleation on the terraces. As result, steps will propagate during the growth. Since the diffusing adatoms attach to the step edges, the result is the advancement of the steps of the substrate surface. This growing mode will go on indefinitely, with no changes in the starting substrate surface morphology, if both the terraces will keep the same width and the step ledges remain straight. Otherwise, step bunching can occur: in this case a high density of steps moves with large velocities over the growth surface.
on the other hand, though the film growth rate may be relatively independent of (T_S), it is reasonable to expect that the film microstructure and morphology may be very sensitive to this temperature [123]. The discussion thus far has implicitly assumed that adatom adsorption and nucleation occurs homogeneously, and at randomly located sites on the substrate surface. In reality, most substrate surfaces will be defective, displaying steps, dislocations, point defects, etc. that can serve as low energy nucleation sites. Similarly, there are situations where epitaxial growth is possible – most generally when the lattice mismatch between the material of the film and the substrate is small. The growth modes can be identified by RHEED technique monitoring the intensity and spot form in the course of deposition.
One major problem in PLD is the presence of particulates on the film surface. Particulates can originate from liquid droplets that are expelled from the target during irradiation, from ejected protruding surface features that are mechanically removed from the target by laser induced thermal and mechanical shock, or from cluster condensation from vapour species due to supersaturation. The first particulate type is typically observed at laser power densities above 10^7 W/cm^2, and the latter type is most likely observed in the presence of a background gas during film deposition [139]. Typical particulate sizes are in the micron and submicron ranges, however, for particulates formed from the vapour state the size tends to be in the nanometer range. In general, the density and the size of particulates on the deposited film surface tend to increase with increasing laser fluence and with increasing laser wavelength [140]. However, other process parameters such as

laser spot size and ambient gas pressure are important as well.

General Deposition Procedure and "Optimum" Growth Parameters

As it mentioned in this and previous sections, PLD is a relatively simple experimental deposition technique. However, the deposition process is in fact rather complex and in order to deposit films of optimum quality, the process parameters must be controlled in an adequate manner. Process parameters such as the deposition rate, the kinetic energy of ablated particles and the mobility of adsorbed particles may be controlled by experimental parameters such as the laser fluence, the background gas pressure and the substrate temperature. The optimum process parameters, however, vary from one material to another. Next will be described the overall process carried out for the deposit of films and the "optimal" parameters found to grow GBCO epitaxial thin films.

Prior to deposition, all the substrates were ultrasonically cleaned with acetone, Ethanol absolute dry (0.02% of water) and deionized water for 10 minutes for each solvent and dried with a air gas gun in order to remove contamination (*e.g.* organics or impurities introduced during substrate preparation) on the sample surface. Furthermore, prior to deposition, a laser calibration process is required in order to ensure that the laser beam is properly aligned on the target with an appropriate spot size and energy. The laser energy was always measured just at the entrance of the chamber through a laser energy detector (LabMax-TOP sensor, COHERENT, INC.) and the beam spot was measured on the surface of target using thermal paper to print the beam mark[4]. The spot size depends on laser energy, the more crystalline quality films were obtained for energies of $100mJ$, which generated a spot about $\sim 0.03cm^2$ or more specifically a fluence of $\sim 3.3mJ/cm^2$. After the cleaning and laser calibration process, the substrates were mounted on the substrate holder using conductive silver paste for providing good thermal contact. The working distance between the substrate and the target was 55 mm. The substrates were heated to deposition temperature with $15°C/min$ under vacuum condition ($\sim 10^3 mTorr$). When reaching the deposition temperature, then the oxygen pressure was manipulated by the MFC to the deposition pressure ($60mTorr$). Before deposition, with a closed shutter on the substrate, a pre-ablation process with ~ 500 pulses is required to remove any accumulated layers of contamination, followed by the deposition process. During deposition, a spinning movement (15rpm) and toggling was applied to the target in order to keep an even ablation, and a homogeneous deposition. The pulse frequency used was 10 Hz. After deposition, the sample was cooled down to room temperature (RT) with

[4]The measurement of the energy laser (position where the energy is measured and calibrated sensor) and size of sopt (material upon which the beam is incident to generate the spot mark and the position in which it is measured) are very susceptible to the technique of measurement used. Once you have chosen a method of measurement, this should be maintained to avoid mistakes estimating the fluence

a rate of $10°C/min$ under a O_2 atmosphere of $(60mTorr)$. In the Table 2.4 the more favorable growth parameters for obtaining GBCO layers with a high crystal quality are listed. The process to determine these optimal growth conditions will be described in detail in chapter 4.

Substrate Temperature	Laser Energy	Fluence	Distance Target-Substrate	Pulse Frequency	O_2 Pressure
$850°C$	100 mJ	$\sim 3.3\ J/cm^2$	55 mm	10 Hz	60 mTorr

Table 2.4: *Favorable growth parameters for obtaining GBCO layers with a high crystal quality on STO(100) and NGO(110) substrates*

CHAPTER 3

Characterization Techniques

The aim of this chapter is to introduce briefly the main techniques used in the characterization of thin film obtained by PLD. Initially, a series of material characterization techniques used for structural, morphological and compositional analysis of the films will be described. Then, special attention is devoted to unconventional techniques to study transport properties, surface exchange and diffusion of oxygen in thin films.

3.1 Film Characterization Techniques

Characterization is an important step in the development of exotic materials. The complete characterization of any material consists of phase analysis, compositional characterization, structural elucidation, micro-structural analysis and surface characterization, which have strong bearing on the properties of materials. This has led to the emergence of variety of advanced techniques in the filed of materials science.

Thin film analysis covers a range of possible scenarios which strongly influence the choice of technique: film thickness can range from a few Å, through the μm range up to mm. Measurement sensitivity varies between techniques, from the atomic percent (at%) range down to parts-per-billion (ppm). The lateral analytical area could be unlimited in size or could be very restricted.

Films can generally be analyzed in two ways: vertically, from the top down or bottom up; or horizontally as a cross-section. Top-down analysis at the surface provides roughness, morphology, and surface composition and contaminant information. Subsequent sputtering can uncover additional information, such as thickness, composition, and dopant and contaminant levels. Cross-sectional analyses can reveal thickness, grain size, and crystallinity. Figure 3.1 shows the approximate length of penetration of some of the most used techniques in the characterization of thin films.

The chemical composition controls the intrinsic properties, such as the electrical nature of the material or phase transitions, which are not susceptible to significant change by modi-

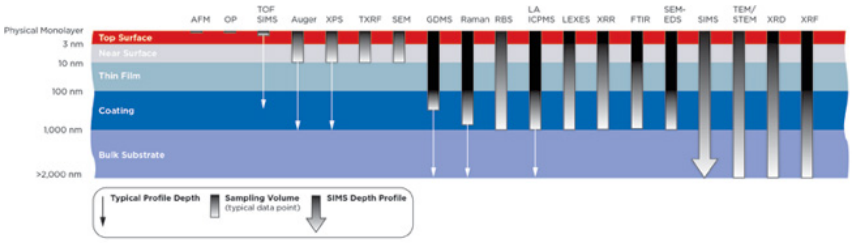

Figure 3.1: *Approximate penetration length of some characterization Techniques.*

fication of the microstructure. In contrast, other critical properties are strongly dependent on the microstructure, *e.g.* electrical conductivity or chemical reactivity. Technological aspects for controlling the chemical composition and microstructure of the thin films are then fundamental in order to optimize the performance of the SOFC cathodes. In this section different analytical instrumental techniques used to characterize our thin films are described briefly with relevant principles of their operation and working. The discussion will address to structural, microstructural, surface, compositional and transport analysis. Special attention is devote to unconventional techniques for transport properties and exchange and diffusion of oxygen in thin films.

3.1.1 Structural and Microstructural Characterization

3.1.1.1 X-ray Diffraction (XRD)

Part of the structural characterization of the films has been performed by X-ray diffraction. XRD is a fundamental technique in crystallography in which the pattern produced by the exposition to X-rays of a crystal is recorded and analyzed. The used X-ray wavelength is of the order of magnitude of the interatomic distances in the crystal in such a way that it acts as diffraction net, *i.e.* the X-rays are diffracted with specific directions and intensities. The better visual representation of the phenomenon of diffraction has been given by Ewald[1], he introduced the concept of a reciprocal lattice and it quickly became an important tool in the illustrating and understanding of both the diffraction geometry and relevant mathematical relationships. The Ewald's sphere and the reciprocal lattice are essential tools in the visualization of the three-dimensional diffraction patterns from single crystals and thin films. Diffraction can only be observed when a reciprocal lattice point intersects with the surface of the Ewald's sphere, depending on the structure and arrangement of the material (powder, micro samples, textured materials, single cristal, etc) a different situation is observed, *i.e.* when multiple single crystals (crystallites or

[1]Peter Paul Ewald (1888-1985). German physicist, whose work [P.P. Ewald, Das reziproke Gitter in der Strukturtheorie, Z. Kristallogr. 56, 129 (1921)][141] is considered a landmark in using reciprocal lattice in x-ray diffraction.

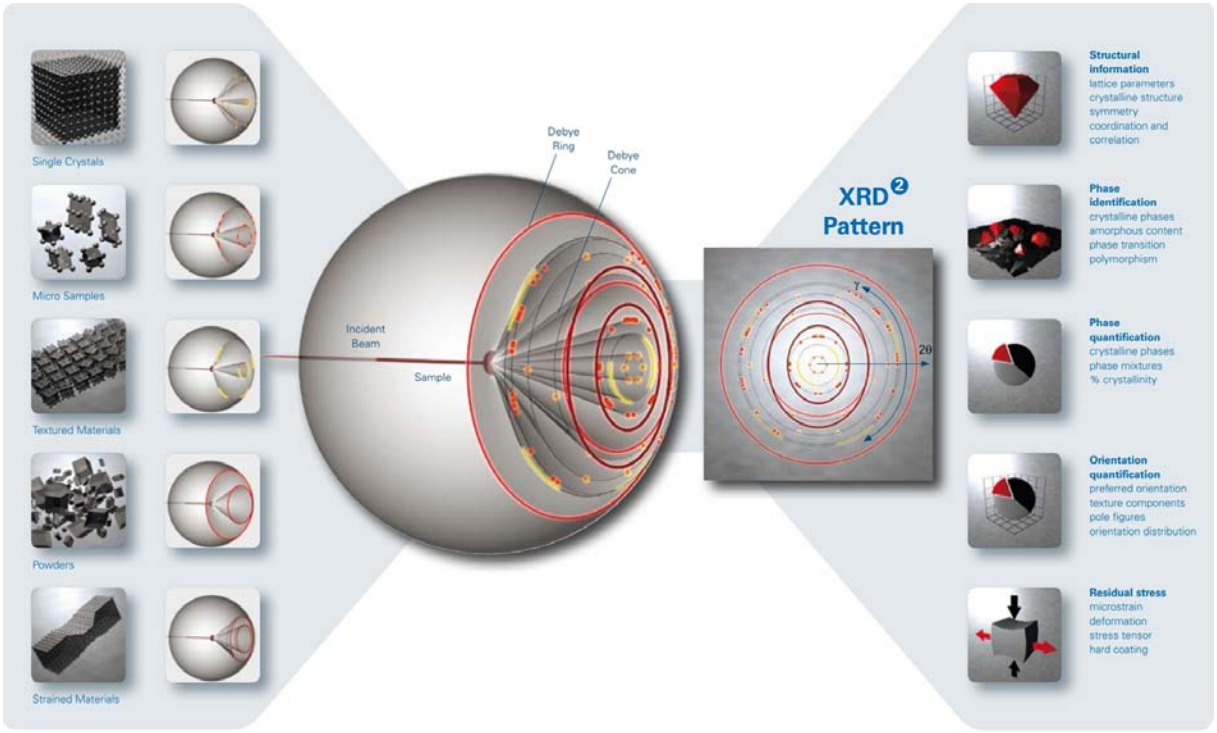

Figure 3.2: *Depending on the crystal structure and the arrangement of the material, the diffracted beam intersects the Ewald's sphere creating different diffraction patterns, these are measured by the sensor giving an image of the structure of the sample. All you have to do is decipher this "fingerprint" and extract the relevant parameters and information (adapted from D8 DISCOVER with GADDS)*

grains) are irradiated simultaneously by a monochromatic incident beam and the number of grains in the irradiated volume is large and their orientations are completely random, the same is true for the reciprocal lattices associated with each crystallite. Thus, the ends of the identical reciprocal lattice vectors, d^*_{hkl} (Where hkl are the Miller indices of the appropriate lattice planes), become arranged on the surface of the Ewald's sphere in a circle perpendicular to the incident wavevector, K_0. The corresponding scattered wavevectors, K_d, will be aligned along the surface of the cone, as shown schematically in Fig. 3.2. The apex of the cone coincides with the center of the Ewald's sphere, the cone axis is parallel to K_0, and the solid cone angle is 4θ. Diffraction principles are well covered in many books [142–145], here we will mention only the most relevant aspects for this thesis.

For a crystalline solid, the x ray are scattered from lattice planes separated by the interplanar distance d_{hkl} . When the scattered waves interfere constructively, they remain in phase since the path length of each wave is equal to an integer multiple of the wavelength [142, 144]. This condition is the well known Bragg's law, which is:

$$n\lambda = 2d_{hkl}\sin\theta \tag{3.1}$$

where n is an integer of the order of the reflection, λ is the wavelength of the incident X-ray (typically Cu K_α radiation ($\lambda = 1.5418$Å)), d_{hkl} is the lattice interplanar spacing between Miller planes passing through the crystal structure, and θ is the angle of incidence to the planes.

Diffractometers come in two basic varieties: $\theta - \theta$ in which the X-ray tube and detector move simultaneously (Bragg-Brentano geometry) or a $\theta - 2\theta$ in which the X-ray tube is fixed, and the specimen moves at 1/2 the rate of the detector to maintain the $\theta - 2\theta$ geometry. If λ is known and the intensity of the diffracted beam is obtained by a scan over a range of θ, then the interplanar spacing can be determined as shown in Fig. 3.3.

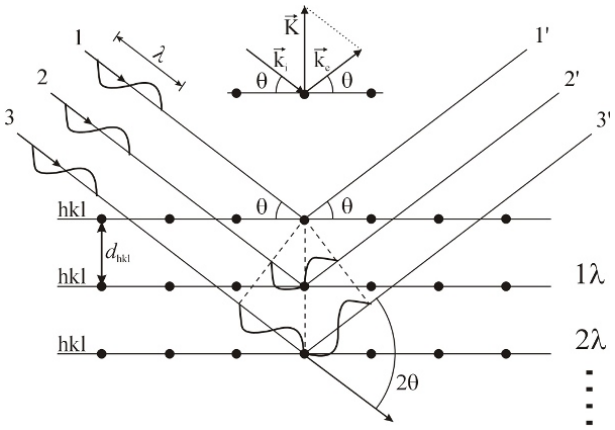

Figure 3.3: *Schematic description of Bragg's law.*

This technique was routinely used in order to identify the crystallographic structure and phase purity of the obtained PLD targets (including powders) and thin-films:

1. *Target Materials*; For PLD target materials the measurements were carried out using PANalytical X'Pert Pro MPD with vertical goniometer ($\theta - \theta$), X'Celerator detector, Ni filtered Cu K_α radiation ($\lambda = 1.541874$Å), and tube voltage/current at 45 kV/40 mA. The diffraction scans were measured between 10° to 100° with a step size of 0.084° and counting rate of 10.15 seconds per step.

2. *Thin films*; Two different equipment were used in the characterization of thin films. PANalytical X'Pert Pro MRD (4-angle ($2\theta, \omega, \varphi$ and ψ scan axes) goniometer – see Fig. 3.4) is a highly advanced and versatile materials characterization system. Interchangeable PreFIX incident and diffracted beam optics can be configured for optimal measurement of high resolution scans, reflectivity experiments, or for in-plane diffraction. This system can also map regions in reciprocal space around the Bragg reflections which can be useful to characterization relaxation of strained epitaxial films. For simple scan with $\theta - 2\theta$ geometry, Cu K_α ($\lambda = 1.541874$Å) radiation was used with tube voltage/current at 45 kV/40 mA, parabolic mirror in the incident beam with Ni filter and Pixel detector with Rocking Curve optic in the diffracted beam. The diffraction scans were measured usually between 5° to 120° with a step size of 0.03° and counting rate of 3 seconds per step. The

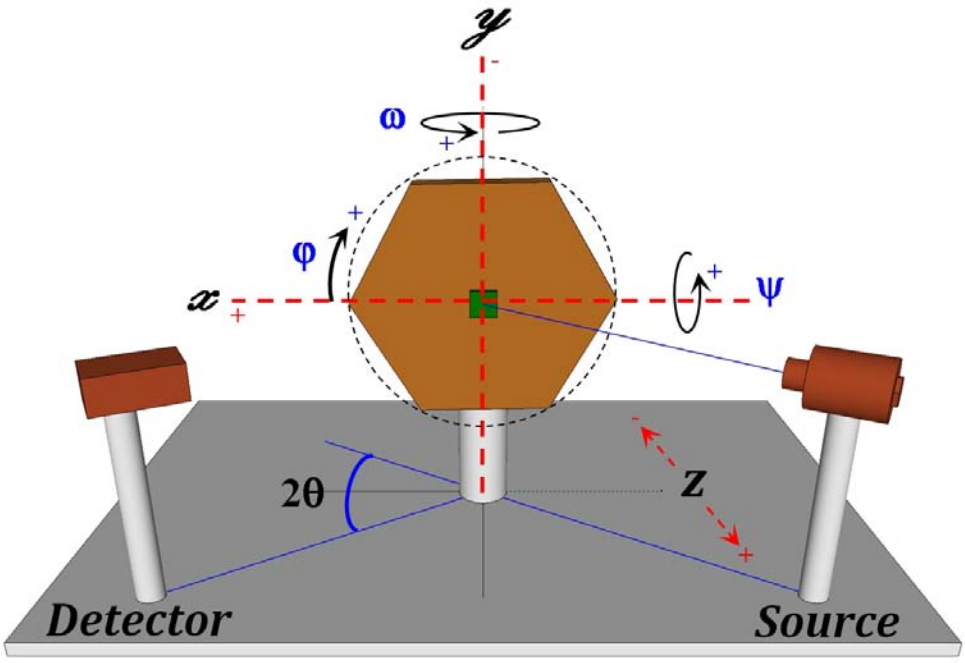

Figure 3.4: *Schematic diagram showing the X'pert MRD system, indicating the $2\theta, \omega, \varphi$ and ψ scan axes.*

equipment was also used to measure the film thickness by reflectometry technique and analyze the orientations and crystallinity of the epitaxial films through reciprocal space mapping (RSM) measurements, which will be described below. In some cases, a Bruker D8 DISCOVER diffractometer with a 4-angle goniometer and GADDS detector was also used. With this type of goniometer the angles $2\theta, \omega, \varphi$ and ψ can be independetly controlled. The GADDS is an area detector which allows the simultaneous data collection of a large 2θ and ω, range without sample or detector movement. Both Panalitical diffractometers are located in the Catalan Institute of Nanoscience and Nanotechnology (ICN2) and the Bruker D8 DISCOVER diffractometer in the Institute of Material Science of Barcelona (ICMAB-CSIC).

The diffraction peaks were identified using X'pert Highscore software[2], and ICSD, provided by the Chemical Database Service. In the case of films with a preferential orientation, the relationship between the intensity of the peaks of a diffraction diagram is very different from that of the databases, which correspond to powder samples, and therefore, with random orientation. The Highscore software allow incorporate new patterns to the database with desired structures and thus be able compare with the measured patterns.

[2]HighScore (Plus) is a powerful software package that allows for peak search and easy phase identification, even in complex phase mixtures. HighScore (Plus) allows simultaneous searching across multiple reference databases and offers many options for automation and reporting. Cluster analysis for grouping samples with a similar phase composition is also supported.

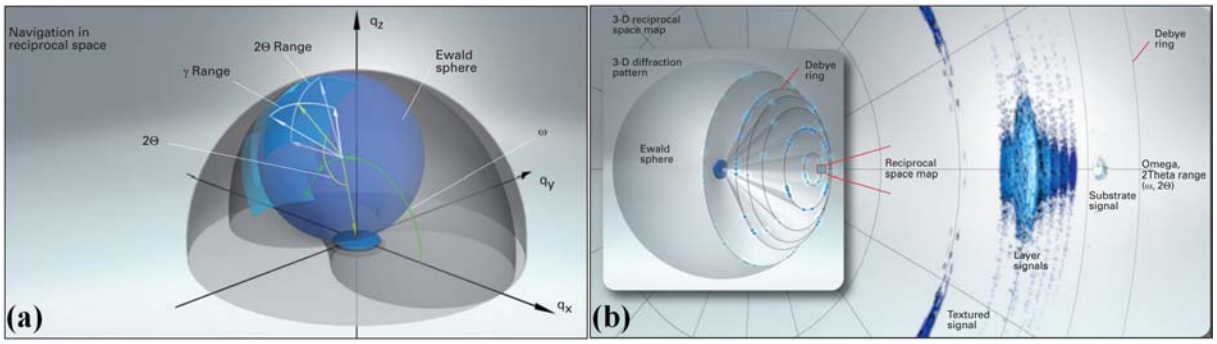

Figure 3.5: ***a.*** *Schematic diagram showing the geometric relationship between the reciprocal lattice vectors and ω and θ.* ***b.*** *Schematic diagram showing the 2D-RSM representation of a scattering experiment. The only peaks that are observed on the detector are those that intersect the Ewald sphere.(adapted from D8 DISCOVER with GADDS)*

3.1.1.2 Reciprocal Space Map (RSM)

The reciprocal lattice is an alternative description for the crystal, showing the same symmetry as the direct lattice. In the case of epitaxial materials, the relationship between the different layers is easily seen in reciprocal space. Most information can be extracted from RSM. Depending on the detector dimensionality, different volume elements are probed. A 0-dimensional point detector sees only a small point in reciprocal space. Consequently, a large number of $\omega - 2\theta$ positions are required to construct the RSM. A 1-dimensional detector collects a large number of 2θ-positions simultaneously, which means the interaction volume represents a line in reciprocal space. Therefore, a scan in one direction of reciprocal space is sufficient. With a 2-dimensional area detector, information in the γ direction is also gathered, which represents a slice through the reciprocal space. Combining a few of these detector slices in fact creates a 3-dimensional RSM (See Fig. 3.5).

RSM measurements of asymmetric reflections of the layers were used in an attempt to determine the *in-plane* and *out-of-plane* lattice parameters and investigate the influence of strain as a function of substrate ans thickness through the relative positions of the reciprocal lattice points. These measurements were conducted mostly using point-focus mode of X'pert MRD driffratometer with a Hybrid monochromator, soller slit (0.04 rad), mask fixed (2 mm) and divergence sit (1/2°) at incident side. Pixel detector at diffraction side with 7.5 mm anti-scatter slit. After the alignment calibration, the measurements were performed by successive $\omega - 2\theta$ scans over a range of $\sim 14°$ with a step size of $\sim 0.0492°$ of around the selected diffraction peaks by varying ω angle over a range and plotting the recorded intensities in a 2D frame.

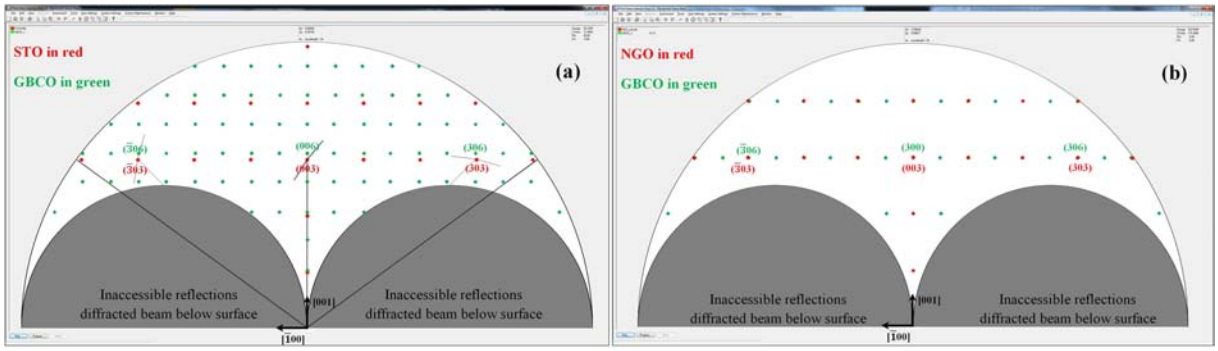

Figure 3.6: *(a) show the reciprocal space representation of c-oriented GBCO and STO(100), and (b) GBCO a-oriented and NGO pseudocubic. We can observe the presence of reflections in the intermediate positions between the main substrate reflection, characteristic of the GBCO double perovskite superstructure arising from the Gd/Ba sequential A-site arrangement in the [001] direction on STO and [100] on NGO.*

The reciprocal space interface of the X'Pert Data Collector[3] is shown in Fig. 3.6 for a c-oriented GBCO on STO(100) and a-oriented GBCO on NGO(110). The unit cell data introduced to generate the patterns are listed in Table 2.3. Primary vector = 0 0 1 and Secondary vector = 1 0 0 are show for STO and NGO pseudocubic. The reciprocal lattice points lying in the diffraction plane are shown as crosses. In STO for example, the mouse pointer has been moved to the 003 reciprocal lattice point using the Show Ewald Vectors mode. This mode shows the incident beam, diffracted beam and diffraction vector (or $1/d$ vector) on the map. The arc at the end of the diffraction vector shows a part of the Ewald sphere. The 003 reflection is referred to as a symmetrical reflection because the incident and diffracted beams are at equal angles to the sample surface. The reciprocal lattice points for symmetrical reflections lie along a line from the origin of reciprocal space which is normal to the sample surface. The $\bar{3}03$ and 303 reflections marked in the figure are referred to as asymmetrical reflections as the planes are inclined to the sample surface. Reflections which are accessible for a flat sample are shown in the white area of Fig. 3.6. These reflections all lie within an Ewald sphere diameter of the origin of reciprocal space. There are two inaccessible semicircular regions which correspond to areas where either the incident beam or the diffracted beam lies below the surface of the sample. Reflections very close to the half-spheres have grazing exit geometry (surface sensitivity). The range of accessible reflections can be increased by using X-ray of higher energy.

The reciprocal vectors Q_x and Q_y were calculated using the equations through those

[3]X'Pert Data Collector is the central data acquisition toolbox for PANalytical's multipurpose XRD instruments.

Figure 3.7: *Schematic representation of the DSH1100 interconnections [146].*

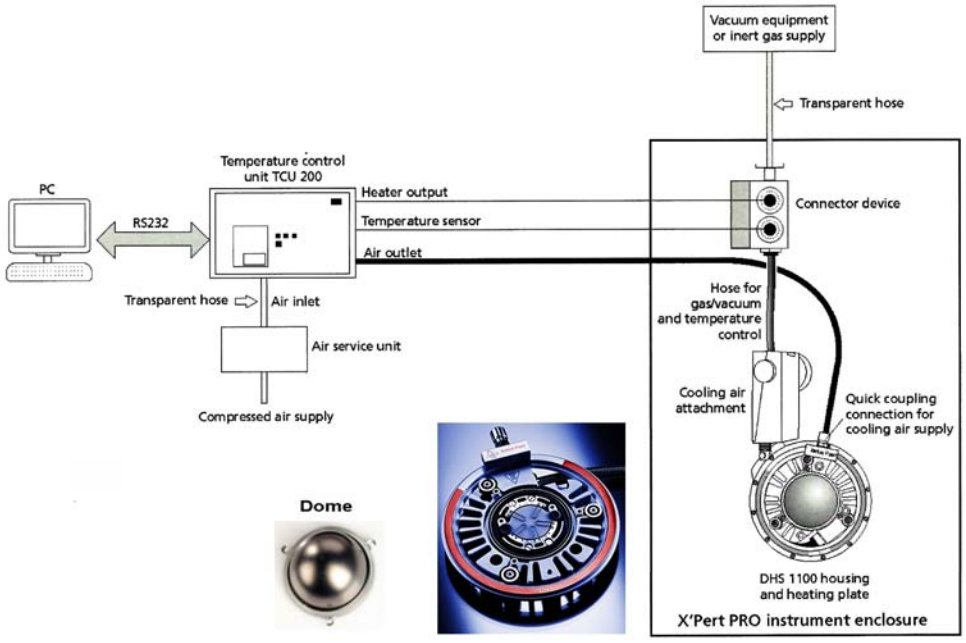

series of 2θ and ω values (see Fig. 3.5a):

$$Q_x = \sin\theta \sin(\theta - \omega) \tag{3.2}$$

$$Q_y = \sin\theta \cos(\theta - \omega) \tag{3.3}$$

2θ is the detector position at which the reflection from reciprocal lattice points hkl can be observed and ω is the angle made by the incident X-ray beam with the sample surface. The *in-plane* (normally a or b axis) and *out-of-plane* (normally c-axis) cell parameters,can then be determined by the following equations:

$$a(or\ b) = \frac{\lambda h}{2Q_y} = \frac{\lambda h}{2\sin\theta \sin(\theta - \omega)} \tag{3.4}$$

$$c = \frac{\lambda h}{2Q_x} = \frac{\lambda l}{2\sin\theta \cos(\theta - \omega)} \tag{3.5}$$

where $\lambda = 1.541874$Å and h and l are Miller reflection indexes from the selected reflection plane. The RMS measurements will be discussed in the chapter 4

3.1.1.3 XRD in atmosphere controlled at different temperatures

DHS 1100 graphite dome from Anton Paar can be coupled on the X'Pert PRO MRD goniometer (see Fig. 3.7). DHS110 is a unique compact high-temperature device allowing tilt and rotation of the sample with respect to the X-ray beam for advanced thin film

applications. The optimized heater design guarantees high temperature uniformity and accurate temperature measurement and control ($25 - 1100°$, internal volume $52cm^3$, plus 19 cm^3 gas tubing) [146]. The X-ray-transparent half-circle dome enables a large field of view when working with 2D or linear detectors. For easy handling of air-sensitive samples a gas flow ring enabling a flow of gas is placed around the sample insert port. We carried out two types of measures as a function of temperature.

1. The first one consists to carry out RSM at specific temperatures, from the RSM information, the evolution of the lattice parameter with temperature is obtained. Before each measurement, a reasonable time is waited until the sample is in thermal equilibrium and a sample realignment is carry out to correct any effects due to thermal expansion of the system, these experiments were performed in a controlled air atmosphere.

2. We developed a method to study the oxygen surface exchange kinetics in oxide materials in the form of epitaxial thin films by analyzing subtle cell parameter variations induced by changes in the oxygen stoichiometry of the material. The method consists of continuously analyzing the X-ray diffraction pattern of particular film reflections with a linear X-ray fast detector in a static position, while exposing the sample to sudden changes in the P_{O_2} of the atmosphere at elevated temperatures [147]. Next we will describe some relevant aspects of the method used:
   Our diffractometer has a fast linear solid-state PIXcel detector. This multichannel solid-state detector allows the simultaneous measurement of a 2θ range of 2.51° (255 channels with a 2θ resolution of about 0.01° in static mode) for the 320 mm goniometer radius. In a typical XRD measurement on polycrystalline nontextured samples, ω and 2θ goniometer angles are fixed to the initial values of a particular symmetric hkl reflection (incidence ω angle is half the value of 2θ diffracted beam angle in reflection geometry). The measurement of the diffracted intensity over a linear detector in static mode (without any variation in the goniometer angles) provides information of a 2θ angle range (2.51° for the present detector type and goniometer radius), and the variation in the peak angles is directly correlated with the average cell parameters through Bragg's law. This is depicted in Fig. 3.8a, where the detector is tangent to the Ewald sphere construction. A small variation of the cell parameters of a polycrystalline material is equivalent to a variation of the radius of the corresponding Laue circle for that hkl reflection. The blue short line corresponds to the equivalent position of a linear detector. The intersection between the detector position and the Laue circle indicates that Bragg condition is satisfied,

Figure 3.8: *Reciprocal space projection along with Ewald sphere construction to evidence diffraction conditions for (a) a polycrystalline film, (b) symmetric reflection for epitaxial film, and (c) largely asymmetric reflection for epitaxial film. The filled spots for the epitaxial films and the continuous circle for the polycrystalline film represent the equilibrium film structure, while the empty spots and the dashed line correspond to the compressed cell structure [147].*

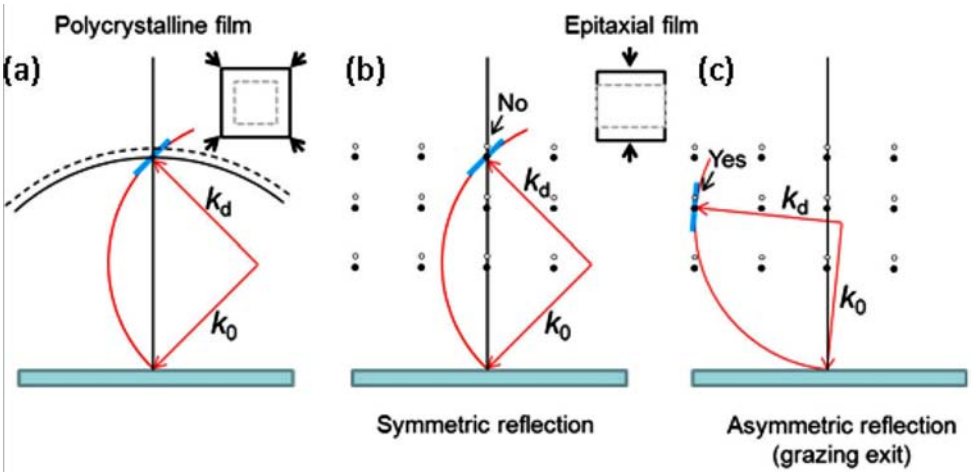

and therefore the shift in the 2θ angle is measured by the detector. However, for epitaxial films a similar static measurement over a symmetric $00l$ reflection will follow a trajectory over the reciprocal space as depicted in Fig. 3.8b. Therefore, a reduction of the out-of-plane parameter (expansion in the reciprocal lattice) causes the $00l$ reflection to lie out from the detector and deviate from Bragg conditions. In epitaxial films one may consider that coherent growth with a substrate causes the in-plane parameter to match that of the substrate (at least below a certain critical thickness from what progressive strain relaxation is expected). Therefore, any variation in film cell volume due to changes in oxygen stoichiometry (or changes in the temperature) will be limited to variations in the film out-of-plane parameter. This corresponds to a vertical axis in the reciprocal space representation. The only measuring conditions where a 2θ scan follows an almost vertical line in the reciprocal space are those of asymmetric reflections ($\omega \neq \theta$) with the grazing exit angle, which corresponds to $\omega \approx 2\theta$, as depicted in Fig. 3.8c. The selection of the proper hkl reflection for monitoring the out-of-plane parameter variations depend on the availability of sufficiently intense reflections at high 2θ angles in the grazing exit angle geometry. For instance, in epitaxial c-axis oriented GBCO films on STO(001) substrates, a suitable choice of hkl reflections will correspond to the reflections in Table 3.1. We return to this type of measure later in the results section.

	STO	NGO Orthorhombic	NGO Pseudocubic	$GdBaCo2O_{5.5}$
Reflection	$\bar{3}03$	$33\bar{6}$	$\bar{3}03$	$\bar{3}06$
ω (deg)	101.8144	102.8061	102.8189	103.166
2θ (deg)	113.6288	114.9647	115.7714	117.4782
ϕ (deg)	0	270	0	0
F(hkl)			0	117.2
Reflection	033	$3\bar{3}6$	033	066
ω (deg)	101.8144	102.8861	102.8189	101.8138
2θ (deg)	113.6288	114.9647	115.7714	115.8245
ϕ (deg)	270	90 ($\psi = 88.96$)	270	270
F(hkl)			0	

Table 3.1: *Angular Positions of Different hkl Film and Substrate Reflections*

3.1.1.4 Reflectometry

Reflectometry can generally be considered to refer to the measurement and analysis of scans taken when ω and 2θ are both close to zero. For the case where ω is always precisely equal to $2\theta/2$ the resulting scan is a Specular Reflectivity scan. When omega is not equal to $2\theta/2$, the measurement or analysis is said to be "off-specular". In the off-specular region the scattered intensity from specular reflectivity is extremely low. In this region it is possible to study the much weaker Diffuse Scatter. Diffuse scatter can occur at all angles in reflectometry however it can only be studied in regions well away from the high intensity specular scattering.

In Specular Reflectivity (The technique is also called Grazing Incidence X-ray Reflectivity (GIXR), or simply, X-ray reflectivity (XRR)), the surface layer characteristics, such as thickness, roughness and density, can be determined from the reflectivity curve of a material. A reflectivity profile shows the response of a material during specular reflection, this scattering effect is dependent upon the change of the average electron density across an interface and not upon the periodic nature of the electron density as described by the crystal structure. It is a response that occurs for non-crystalline and crystalline materials alike, and in this respect is quite different from X-ray diffraction. A reflectivity curve is a plot of the intensity of specularly reflected X-rays (Y axis) versus the angle of incidence with respect to the surface (X axis). It is assumed that the angle of incidence is equal to the angle of detection with respect to the surface. During reflectometry these angles are scanned synchronously (a coupled $\omega/2\theta$ scan) from an angle close to zero up to a few degrees. From zero up to the critical angle θ_c for total external reflection the wave barely penetrates into the material, this means that very little intensity is absorbed. θ_c for total

external reflection is dependent upon the electron density of the surface layer. Above the θ_c the wave penetrates into the material. The penetration depth increases rapidly with angle, there is increased absorption, and the proportion of specularly reflected radiation decreases. This results in a rapid drop in intensity in the reflectivity curve. For most materials the θ_c is lower than 0.3°. At every interface where the electron density changes, a part of the X-ray beam is reflected. Due to the interference between the X-ray beams scattered from the different interfaces one is able to record a scan consisting of so-called thickness fringes, *i.e.*, intensity maxima corresponding to constructive interference and minima due to destructive interference. The period of the interference fringes and the fall in the intensity are related to the thickness and the roughness of the layer (layers in case of multilayers), respectively. The reflection can be analyzed using Fresnel's classical theory [144]. The interference maximum of order m, for a path difference $\Delta = m\lambda$, is found for:

$$m\lambda = \Delta \approx 2t\sqrt{\theta_m^2 - \theta_c^2} \tag{3.6}$$

from where the thickness t can be directly calculated as:

$$t^2 \approx \frac{\lambda^2 m^2}{2(\theta_m^2 - \theta_c^2)} \tag{3.7}$$

The typical range for measurements are between 0 and 5° in θ and the diffractometer used for the reflectometry measurements was the X'pert MRD. The curves were analyzed with Reflectivity software of PANalytical, this package allow display, simulate and fit X-ray reflectometry data for analyze off-specular (diffuse) scattering data of arbitrary multi-layer structures. Layer thickness, density and roughness of thin-layered samples are easily and quickly quantified.

3.1.1.5 Transmission Electron Microscopy (TEM)

Transmission Electron Microscopy (TEM) is a good complementary technique to XRD for evaluating the crystallography of materials, and it is conventionally applied to obtain microstructure of materials using a high-energy electron beam ($\gtrsim$ 200 keV). TEM uses the electrons transmitted through a specimen illuminated with a focused beam of electrons to form an image, which is magnified and directed to appear either on a fluorescent screen or layer of photographic film, or to be detected by a sensor such as a charged-coupled device (CCD camera). The electrons are generated by thermoionic or field emission, accelerated by an electrical field and focused onto the sample using electrical and magnetics fields. A crystalline material interacts with the electron beam mostly by diffraction rather than absorption, although the intensity of the transmitted beam is still affected by the volume

and density of the material through which it passes. The specially prepared sample is a very thin (less than 100 nm) slice of material. The electrons pass through the sample and the diffraction pattern and image are formed at the back focus plane and image plane of the objective lens. If we take the back focus plane as the objective plane of the intermediate lens and projector lens, we will obtain the diffraction pattern on the screen. It is said that the TEM works in diffraction mode. If we take the image plane of the objective lens as the objective plane of the intermediate lens and projector lens, we will form image on the screen. It is the image mode.
The resolution of the TEM technique is usually 0.3 nm. In the most powerful diffraction contrast TEM instruments, crystal structure can also be investigated by High Resolution Transmission Electron Microscopy (HRTEM), also known as phase contrast imaging as the images are formed due to differences in phase of electron waves scattered through a thin specimen. In HRTEM images, contrast is not intuitively interpretable as the image is influenced by strong aberrations of the imaging lenses in the microscope. Resolutions as high as 0.5Å has been obtained with HRTEM [148–150].

The microstructure of some layers of GBCO were studied by TEM in collaboration with Dr. Monica Burriel. These samples were prepared using a standard TEM cross-section technique. HRTEM images were recorded on a JEOL 4000EX (located in the Electron Microscopy for Materials Science (EMAT) in Antwerp) operating at 400 keV and having a point resolution of 0.17 nm. Image simulations were carried out with the Mac Tempas software. HAADF STEM was performed using a JEOL 3000F microscope operating at 300 kV and a FEI Technai G2 microscope operating at 200 kV. They have a point resolution of 0.136 and 0.2 nm, respectively. STEM-EELS was performed using a JEOL 3000F microscope equipped with a Gatan GIF2000 1K Phosphor spectrometer system used at an energy dispersion of 0.5 eV/ channel and an approximate energy resolution of 1 eV. Electron energy loss spectroscopy (EELS) scans in STEM mode were performed across the layer interfaces with a collection angle of 28.6 mrad and a convergence angle of 10.4 mrad. EELS spectra were analyzed using the EELSMODEL software [115, 151].

The other set of GBCO samples were measured in the Advanced Microscopy Laboratory (LMA) of Zaragoza in colaboration with Dr. Myriam Aguirre. Basically three types of microscopes were used:

1. *Tecnai F30*: The F30 (FEI company) is a versatile high resolution Transmission Electron Microscope. It can work in TEM or STEM (Scanning-Transmission) modes. The working voltages in this microscope are 200 and 300 kV. The field emission gun (FEG) TEM is fitted with a SuperTwin lens allowing a point resolution of 1.9 Å. For

Z-contrast imaging in STEM mode, it is fitted with a High-Angle Annular Dark Field (HAADF) detector. This TEM is equipped for spectroscopy experiments performed either in EDS (X-Ray Microanalysis) or in Electron Energy Loss spectroscopy (EELS). For the latter, it is fitted with the "Tridiem" Gatan Energy Filter (GIF). This EELS set-up allows Energy Filtered TEM (EFTEM) images to be recorded as well as line spectra or spectrum imaging experiments to be performed. A 2k × 2k Ultrascan CCD camera (Gatan) is located before the GIF for TEM imaging.

2. *Titan High-base for High Resolution Imaging: FEI TITAN*^{3}: This microscope works at voltages between 60 and 300 kV. It is located in a "box" (cube) to avoid mechanical and thermal perturbations. It has a normal FEG (Shottky emitter) and a Gatan 2k × 2k CCD camera for HRTEM images acquisition (0.09 nm resolution). The main working modes in this microscope are:
HREM: In this case, the SuperTwin objective lens and a CETCOR Cs-objective corrector from CEOS Company allowing a point to point resolution of 0.09 nm.
STEM: This Titan^3 is equipped with the basic STEM facilities (BF, DF detectors) for STEM imaging at medium resolution.
EELS: A Gatan Energy Filter Tridiem 863 allows Titan^3 to perform EELS experiments in a standard and routine way (energy resolution of 0.7 eV). ***Lorentz and holography:*** The Titan^3 is fitted with a Lorentz lens and an electrostatic biprism allowing Lorentz and medium resolution electron holography experiments to be carried on.

3. *Analytical Titan Low-base: FEI TITAN Low-base*: This Scanning Transmission Electron Microscope works either in TEM or in STEM modes at voltages between 60 and 300 kV. It can be used at low voltage to analyse electron irradiation sensitive materials. It is fitted with the last generation of a high brightness Schotky emitter developed by FEI (the so called "X-FEG" gun), a monochromator, and a Gatan 2k × 2k CCD camera. The main working modes in this microscope are:
STEM: The microscope is equipped with a CESCOR Cs-probe corrector from CEOS Company allowing for the formation of an electron probe of 0.09 nm mean size. The TEM is equipped with all the STEM facilities (BF, DF, ADF and HAADF detectors) and 0.09 nm spatial resolution has indeed been achieved in STEM-HAADF mode.
EELS and EDS: For EELS experiments, the microscope is fitted with a Gatan Energy Filter Tridiem 866 ERS and a monochromator. An energy resolution of 0.14 eV can be achieved with this setup. In addition, an EDS (EDAX) detector allows performing EDX experiments in scanning mode with a spatial resolution of about

$\sim$0.2 nm.

Lorentz and holography: In addition to the above described analytical capabilities, the Titan STEM corrected microscope is fitted with a Lorentz lens and an electrostatic biprism allowing Lorentz and medium resolution electron holography experiments to be carried out in a field-free environment (as needed for magnetic materials studies).

Tomography: a tomography set-up with a $+/-$ 70° single tilt stage permits to perform 3D reconstructions either in TEM or STEM modes.

The results and discussion of these measures will be presented later in their respective chapters.

3.1.2 Surface Morphology and Compositional Characterization

A surface, by definition, is an interface, a marked discontinuity from one material to another. Because no change in nature is ever instantaneous, any real surface has a finite depth, and in characterizing a surface one must at some point consider just what this depth is. Almost all surfaces of bulk substrate materials that are prepared by mechanical techniques contain defects resulting from plastic deformation, fracture, heating, and contamination. Even cleavage faces are rarely defect free. Mechanically abraded, polished, ground, or machined metal, polymer, and ceramic surfaces are extremely rough on an atomic scale, and crystalline structure is distorted. All surfaces contain irregularities, or hills and valleys, which are called surface texture and surface topography. Even in cleaved surfaces of single-crystal materials there are cleavage steps. Surface topography is a permanent record of the deformation and fracture process and provides a materials engineer or scientist with valuable information on the surface properties of materials and coatings. To understand the benefits that surface modifications provide, and ultimately to devise better ones, it is necessary to study the physical, mechanical, and chemical changes they cause. This section summarizes important aspects of the techniques used to study the morphology of layers grown by PLD.

3.1.2.1 Atomic Force Microscopy (AFM)

Atomic Force Microscopy (AFM) was utilised to characterise the surface roughness and topography of thin-films. An AFM can measure the force of interaction between a specimen surface and a sharp probe tip. The tip, a couple of micrometers long and often less than 10 nm in diameter, is located at the free end of a cantilever 100 to 200 mm long. When the tip comes within a few angstroms of the specimen surface, repulsive van der Waals forces between the atoms on the tip and those on the specimen cause

the cantilever to deflect, or bend. A detector, such as the position-sensitive photodetector measures the cantilever deflection as the tip is scanned over the specimen or the specimen is scanned under the tip. As a piezoelectric scanner gently traces the tip across the specimen (or the specimen under the tip), the contact force causes the cantilever to bend to accommodate changes in topography. The measured cantilever deflections allow a computer to generate a map of surface topography (see Fig. 3.9). AFM can be typically operated in three different modes: contact, intermittent and non-contact modes, for topographic measurements. The lateral resolution is around 1 nm and particularly the vertical resolution is less than 0.1 nm [152].

The AFM analyses were performed in the Catalan Institute of Nanoscience and Nanotechnology (ICN2) using MFP-3D AFM from Asylum Research. Most AFM images presented in this thesis were obtained by tapping mode and the surface analyzed with the open user interface of Asylum (based on IGOR Pro) and the open software Gwyddion for SPM (scanning probe microscopy) data visualization and analysis.

Figure 3.9: *Schematic ilustration of an atomic force microscope. Adapted from MyScope-training for advanced research.*

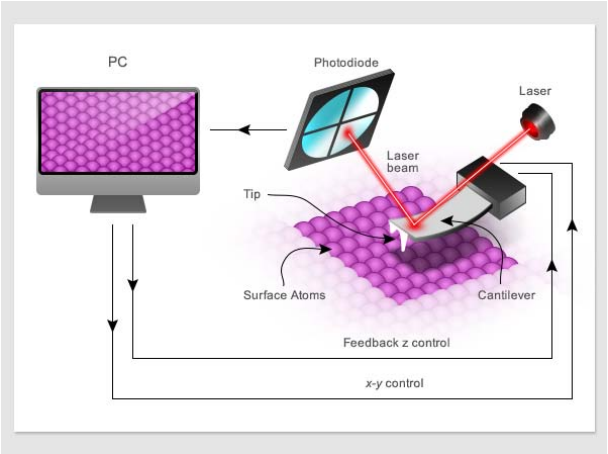

3.1.2.2 Scanning Electron Microscope (SEM)

A scanning electron microscope (SEM) is a type of electron microscope that produces images of a sample by scanning it with a focused beam of electrons (typically $0.2 \sim 40$ keV). When the electron beam hits a sample it interacts with the atoms in that sample, some electrons are bounced back out of the sample (backscattered electrons (BSE)), others knock into atoms and displace electrons that, in turn, come out of the sample (secondary electrons (SE)); alternatively X-rays, and light or heat (in the sample) can be the result of these interactions (generally heat is how most of the energy is dispersed). These signals can be used to obtain information about the surface topography and composition. The SEM technique is mainly used to detect SE and BE for the formation of images, while if it is fitted with Energy Dispersive X-ray Spectrometer (EDX) or Wavelength-Dispersive X-Ray Spectroscopy (WDS), characteristic X-rays can be detected for the compositional analysis of specimens. Specimens can be observed in high vacuum, in low vacuum, in wet conditions (in environmental SEM), and at a wide range of cryogenic or elevated

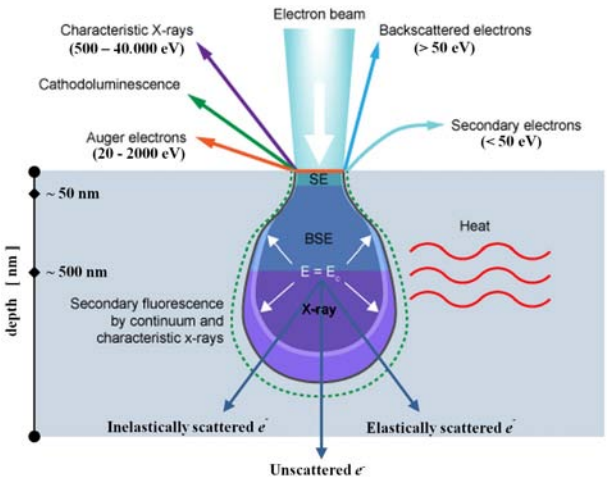

Figure 3.10: *Electron-matter interactions can be divided into two classes: Elastic scattering – the electron trajectory within the specimen changes, but its kinetic energy and velocity remains essentially constant. The result is generation of BSE. Inelastic scattering – the incident electron trajectory is only slightly perturbed, but energy is lost through the transfer of energy to the specimen. The result is the generation of: phonon exitation (heating); cathodoluminescence (visible light fluorescence); continuum radiation (bremsstrahlung); characteristic x-ray radiation; plasmon production (secondary electrons); auger electrons (ejection of outer shell electrons).*

temperatures. The volumes involved in the production of SE, BSE and X-rays, form into a shape that ranges from a tear-drop to a semi circle within the specimen. This shape is called an interaction volume and its depth and diameter depends on the kV as well as the density of the specimen. Approximately the top 15nm of the volume comprises the zone from which SE can be collected, the top 40% is the region from which BSE can be collected and X rays can be collected from the entire region [153] (see Fig. 3.10). The maximum resolution obtained in an SEM depends on multiple factors, like the electron spot size and interaction volume of the electron beam with the sample. While it cannot provide atomic resolution, some SEMs can achieve resolution below 1 nm. Typically, modern full-sized SEMs provide resolution between 1-20 nm whereas desktop systems can provide a resolution of 20 nm or more. The SEM images presented in this thesis were obtained using the FEI Quanta 650F Environmental SEM located in the Catalan Institute of Nanoscience and Nanotechnology (ICN2).

3.1.2.3 Electron Probe Micro-Analysis (EPMA)

EPMA is an analytical technique that is used to establish the composition of small areas on specimens. EMPA is one of several particle-beam techniques. A beam of accelerated electrons (typical energy = 5-30 keV) is focused on the surface of a specimen using a series of electromagnetic lenses, and these energetic electrons produce characteristic X-rays within a small volume (typically 1 to 9 cubic microns) of the specimen. The characteristic X-rays are detected at particular wavelengths, and their intensities are measured to determine concentrations. All elements (except H, He, and Li) can be detected because each element has a specific set of X-rays that it emits. This analytical technique has a high spatial resolution and sensitivity, and individual analyses are reasonably short, requiring

only a minute or two in most cases. Additionally, the electron microprobe can function like a scanning electron microscope (SEM) and obtain highly magnified secondary- and backscattered-electron images of a sample. The sample composition can be easily identified by recording WDS spectra (Wavelength Dispersive Spectroscopy). WDS spectrometers are based on the Bragg's law. The wavelength-dispersive spectrometers are "tuned" to the characteristic X-ray of interest for analysis. The "tuning" is done by scattering of X-rays from a crystal positioned between a sample and the detector. By changing the angle of incidence of the X-rays, the crystal will constructively diffract X-rays of specific wavelengths. As a result, both the crystal and the detector move to accommodate the different incident angles. Different analyzer crystals are used to cover the entire X-ray spectrum: lithium fluoride (LIF), pentaerythritol (PET), thallium acid pthalate (TAP), and artificial layered dispersive element (LDE) crystals are the most commonly used. WDS analysis results in a spectral resolution and sensitivity an order of magnitude better than is possible with EDS analysis; the detection limits of WDS ordinarily varies between 300 and 30 parts per million (ppm). Also, in comparison to EDS, WDS offers more accurate quantitative analyses, particularly for light elements, and better resolution of overlapping X-rays peaks for improved element identification and quantification[154]. For the composition analysis of the films, we used the electron microprobe CAMECA SX-50 at the CCiT in the university of Barcelona (with four crystal analyzers for WDS + 1 EDS). The typical voltages used were 12, 15, and 20 keV. A thin film analysis program (STRATAGem) was used to determine the exact composition and thickness of the thin films without interference of the substrate composition.

3.1.2.4 Isotope Exchange Depth Profililing (IEDP) Technique Using Secondary Ion Mass Spectrometry (SIMS)

The determination of the mass transport kinetics of oxide materials for use in electrochemical systems such as fuel cells, sensors and oxygen separators is a significant challenge. The ionic transport properties of an oxide ion conductor are characterized basically by two parameters – oxygen diffusion (D^*) and surface exchange (k^*) coefficients. Several techniques have been proposed to derive these data experimentally with only the oxygen isotope exchange depth profile (IEDP) technique coupled with secondary ion mass spectrometry (SIMS) providing a direct measure of these kinetic parameters. This method developed by Kilner et al. since 1984 [108, 116, 155], has been successfully used for the characterization of thin epitaxial films of different cathode materials like $La_2NiO_{4+\delta}$ [109], $Ba_{0.5}Sr_{0.5}Co_{0.8}Fe_{0.2}O_{3-\delta}$ [110], $La_{0.7}Sr_{0.3}MnO_3$ [111] as well as $La_{1-x}Sr_xCoO_{3-\delta}$ [112]. In this thesis, k^* and D^* were determined by IEDP technique (isotopic exchange of ^{18}O for ^{16}O) using SIMS in GBCO films in transverse and longitudinal configurations (per-

pendicular and parallel to the film surface, respectively (see Fig. 3.11)). The method consists of four stages: sample preparation, isotope exchange, determination of the resulting ^{18}O distribution by SIMS, and data processing to extract k^* and D^* from the obtained diffusion profile. Each of these steps will be briefly described in the following, but more comprehensive information with respect to the procedure can be found in, for example, references [108, 109].

Figure 3.11: *Configuration for Isotopic Exchage. (a) Transverse configuration (isotopic exchage perpendicular to the surface). (b) Longitudinal configuration (isotopic exchage paralell to the thin film surface)*

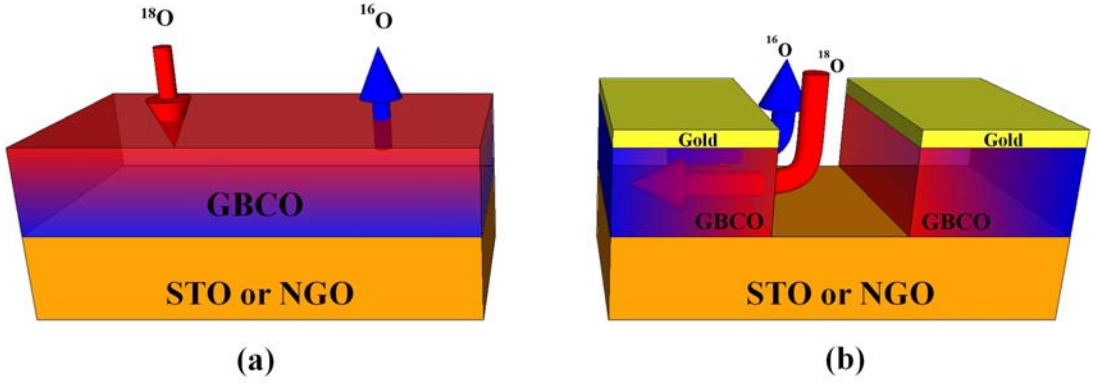

1. *Sample preparation:* Prior to the isotope exchange annealing, the film samples are ultrasonically cleaned with isopropanol and deionized water for 10 minutes for each solvent and dried with a N_2 gas gun in order to remove contamination on the sample surface. Selected samples to study the diffusion profiles in the transverse direction does not need any extra treatment, but in order to determine the oxygen transport along the film plane (longitudinal configuration), a dense and uniform Au thin film of approximately 160 nm was sputtered to cover the GBCO epitaxial film and prevent oxygen exchange from the top surface. A trench was opened at the lateral edge of the film, allowing the exchange with the ^{18}O enriched exchange gas phase and thus ensuring the diffusion of the ^{18}O species only along the direction parallel to the film plane.

2. *Isotopic exchange of ^{18}O for ^{16}O:* Before to the isotopic exchange annealing and in order to establish thermodynamic and chemical equilibrium at the exchange conditions, a pre-annealing is necessary. The samples were placed in a silica tube and evacuated to $\sim 2 \times 10^{-7}$ mbar by a turbomolecular pump backed by a rotary pump. The furnace was moved to heat the samples and these were then subjected to annealing in pure oxygen (research grade 99.9995%) of natural isotopic abundance for a period of time approximately one order of magnitude greater than the ^{18}O

tracer annealing time and at the same temperature as the exchange which took place afterwards. The samples were then cooled to room temperature, the natural oxygen gas was removed, an ^{18}O enriched gas (27.8 %) was introduced (200 mbar, similar P_{O_2} to air), and the samples were then heated to different temperatures ranging from 300 to 600°. The heating and cooling rates of the samples could be achieved either by means of predefined ramps of the furnace, or by rapidly heating the sample by rolling the furnace over the sample holder. A constant temperature was maintained for the required duration of the annealing step (10 - 60 min), and finally the sample was quenched by rolling the furnace off the sample holder. The effective ^{18}O exchange time was calculated taking into account the finite increase/decrease in the sample temperature using the method described by Killoran [156]. In the case of the transverse profiles, the reported surface exchange values were used in the exchanged time correction, since this is the rate-limiting step for oxygen transport in the thin films, while in the case of longitudinal profiles, the corresponding oxygen diffusion values were used. Once the sample had cooled the ^{18}O was cryogenically recovered. The schematic experimental setup for the exchange anneal is shown in Fig. 3.12.

3. *Determination of the resulting ^{18}O distribution by SIMS:* SIMS is a sophisticated analytical technique for determining the elements present in materials, and especially on surfaces, with trace level sensitivity and high spatial resolution. Samples are bombarded with primary ions (tipically Cs^+, O_2^+, Ar^+, Xe^+ and Ga^+) at typical energies of 10–40 keV. Secondary particles are released in a so-called sputtering process from surface-near layers (see Fig. 3.13). Besides electrons, these secondary particles are atoms and molecules, which are in part (approximately 1%) positively or negatively charged. The secondary atomic and molecular ions are extracted with electric fields and then separated and detected in a mass analyzer. Depending on the type of mass analyzer, one discerns between either conventional SIMS, with magnetic or quadrupole mass spectrometers, or TOF-SIMS, with time-of-flight mass spectrometers. Detailed descriptions of the working principles of SIMS are beyond the scope of this thesis; the interested reader is referred to the extensive literature [158–160] . Only a simple discussion of the working principle of a ToF-SIMS will be given here.

   All the exchanged samples were measured by ToF-SIMS. This analyzer allows to measure all secondary ions with one polarity quasi-simultaneously. The sample is bombarded in TOF-SIMS with a short-time primary ion pulse with typical lengths between several hundred picoseconds and a few nanoseconds. This is repeated every few hundred microseconds, resulting in a duty cycle of typically 10^{-5}. All secondary

Figure 3.12: *Exchange anneal apparatus used for the $^{18}O/^{16}O$ isotope exchange. The sample is held on the alumina boat throughout the experiment, the oxygen isotopes can be separately introduced by different reservoirs and the required temperature of the anneal is achieved with the help of a roll on/roll off furnace.[157]*

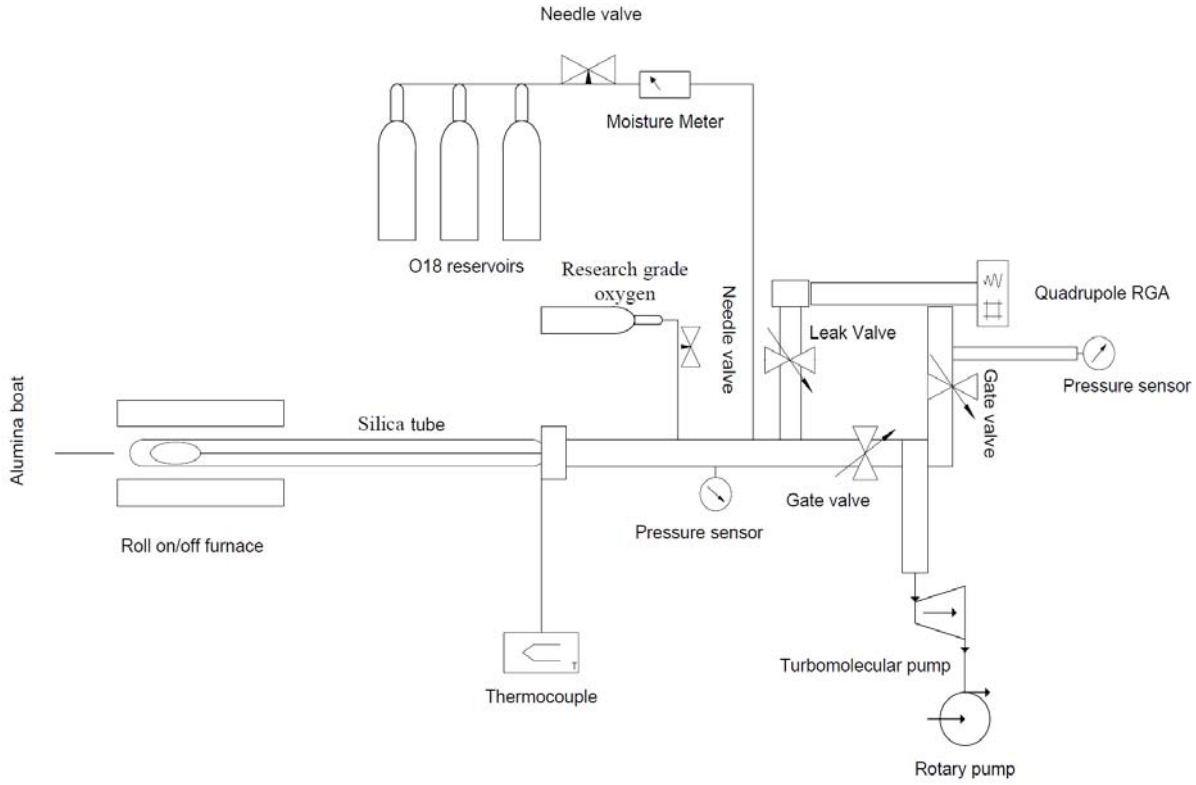

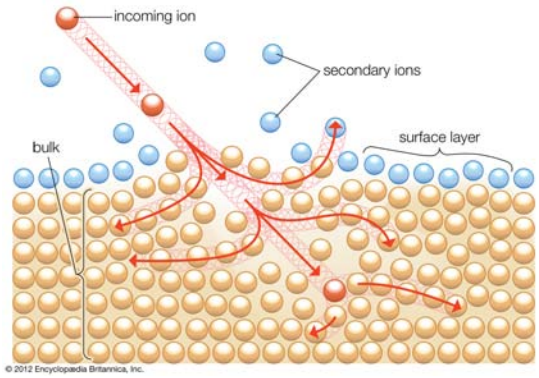

Figure 3.13: *Schematic diagram of the SIMS process. An incoming primary ion interacts with the surface layer of a material (in a collision cascade). Ion implantation or backscattering may occur. A third alternative, for thin samples only, is forward scattering. Atoms from the target material can leave the sample after several collisions as secondary particles (backward sputtering) and are then analysed by a mass spectrometer.*

ions with one polarity are accelerated in an electric field with potential U and mass m separated in a field-free drift tube. Particles with different mass-to-charge ratios m/q reach the detector after the time-of-flight t: $\frac{m}{q} = \frac{2eU}{s^2}t^2$, Here, s is the effective flight path, corresponding to the length of the drift tube[108, 161]. The x, y, z coordinates and mass of every secondary ion reaching the detector are stored. The software can reconstruct spectra from any coordinate or group of coordinates, images from any section, vertical or horizontal, depth profiles from any selected area and various 3D views as required. There are three different modes of analysis in TOF-SIMS; *1)*

Figure 3.14: *Sketch of the functional principle of a ToF-SIMS instrument and options for surface and bulk analysis of materials by (i) imaging of the lateral distribution of secondary ions, (ii) mass spectrometric analysis of surface borne secondary ions, and (iii) sputter depth profiling.*

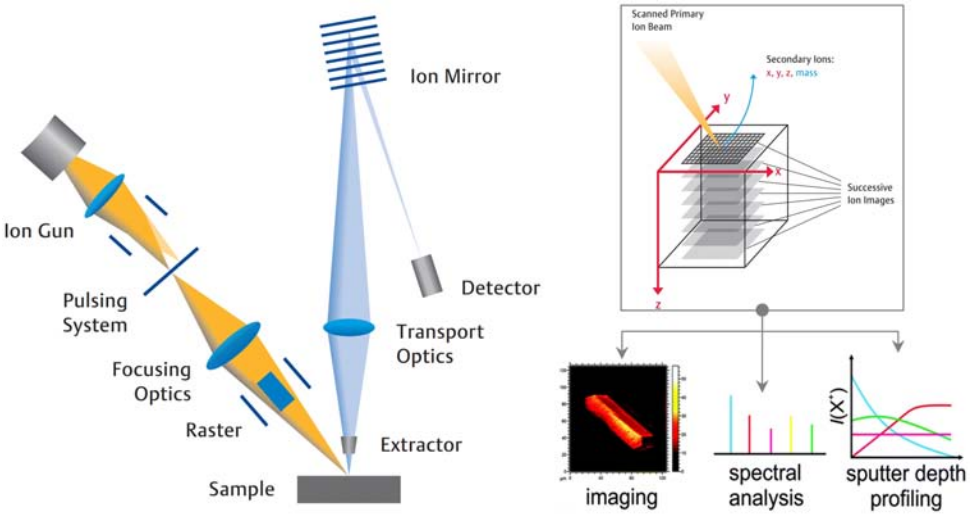

mass spectra are acquired to determine the elemental and molecular species on a surface; *2)* images are acquired to visualize the distribution of individual species on the surface; and *3)* depth profiles are used to determine the distribution of different chemical species as a function of depth from the surface (Fig. 3.14). In our case, we use the depth profile analysis, which uses two ion beams operate in the Dual Beam Mode. The two different ion sources are alternated during depth profiling measurement to decouple the analysis and sample erosion aspects. The instrument used for the IEDP technique is Tof.SIMS^5 (ION-TOF GmbH, Münster, Germany) equipped with a bismuth liquid metal ion gun LMIG (pulsed) incident at 45°. A 25 keV Bi^++ primary ion beam was used to generate the secondary ions using the low mass resolution or burst alignment mode (eight pulses) for analysis and a Cs^+ beam (2 keV) incident also at 45° for sputtering. For the longitudinal configuration secondary ion images for selected areas of the GBCO film, including the edge of the opened trench, were acquired. For the transverse configuration (perpendicular to the

film plane) tracer oxygen depth profiles were measured from the exchanged surface penetrating down to the substrate by sputter depth profiling.

4. *Data processing.* Once a sample has been isotopically exchanged and the determination of the oxygen concentration in the films has been obtained by ToF-SIMS technique, there are two potential methods for the subsequent SIMS data analysis: depth profiling and line scanning. Each of these techniques has advantages and are typically used in cases with very different diffusion kinetics in order to extract k^* and D^* from the obtained diffusion profile. Mathematically, we have to solve the diffusion equation for the concentration $c_{18}(x,t)$ of the isotope ^{18}O. However, instead of the isotope concentration, c_{18}, we can use the isotope fraction $c^* = c_{18}/(c_{18}+c_{16})$, the quantity which is directly measured by Tof-SIMS. The mathematical details and a more detailed discussion of the data processing will be described later in chapter 5. For further detailed information on the diffusion measurements by the IEDP-SIMS method, several reviews and the references therein are recommended [107, 108, 162].

The depths of sputtered craters obtained from SIMS measurements were estimated using a white-light optical interferometer (Zygo NewView 200 Profilometer). This technique measures and maps the topography of the crater in three dimensions through the constructive and destructive interference of light when the light reflects from the sample surface, forming the light and dark fringes.
All the IEDP and ToF-SIMS measurements and data processing reported in this thesis were conducted in the Department of Materials, Imperial College London in collaboration with Dr M. Burriel and the technical support of Dr Richard Chater.

3.1.3 Transport Properties

Solid state devices (fuel cells, gas sensors, oxygen pumps, etc) are based on the combination of transport phenomena in the solid electrolyte (both volume and grain boundary) and reactions at the electrolyte/electrode interface (gas diffusion, adsorption/dissociation and charge transfer). To properly understand a system of such complexity, should be possible to split it into simpler parts associated with each phenomenon that occurs. Considering the existence of a characteristic time for each process, the electrochemical impedance spectroscopy (EIS) is presented as a valuable technique for the study of complex systems type electrode/electrolyte/electrode because it allows us to separate the different system contributions based on the domain frequency. Moreover, the electrical conductivity relaxation allows us to study the evolution of the transport properties over time. In this section we briefly describe important aspects of these two techniques.

3.1.3.1 Electrochemical Impedance Spectroscopy (EIS)

EIS methods have seen a tremendous increase in popularity in recent years in the characterization of electrode processes and complex interfaces. This method studies the system response to the application of a periodic small-amplitude alternate current (AC) signal. The measurements are carried out at different AC frequencies and analysis of the system response contains information about the interface, its structure, and the reactions taking place there. EIS is now described in the general and specific books on electrochemistry [163–165], and numerous articles and reviews [166–169]. Here we only mention relevant aspects for our measures.

Almost everyone knows about the concept of electrical resistance. It is the ability of a circuit element to resist the flow of electrical current. Ohm's law (Eq. 3.8) defines resistance in terms of the ratio between voltage E and current I.

$$R = \frac{E}{I} \tag{3.8}$$

While this is a well known relationship, its use is limited to only one circuit element (the ideal resistor[4]), the real world contains circuit elements that exhibit much more complex behavior. These elements force us to abandon the simple concept of resistance. In its place we use impedance, which is a more general circuit parameter. Like resistance, Impedance (Z) is generally defined as the total opposition a device or circuit offers to the flow of an alternating current (AC) at a given frequency.

Applying an AC sinusoidal potential to an electrochemical cell and measuring the current through the cell, the response is also an AC current signal. This current signal can be analyzed as a sum of sinusoidal functions (a Fourier series). Electrochemical Impedance is normally measured using a small excitation signal. This is done so that the cell's response is pseudo-linear. In a linear (or pseudolinear) system[5], the current response to a sinusoidal potential will be a sinusoid at the same frequency but shifted in phase. The excitation signal, expressed as a function of time, has the form

$$E(t) = E_0 \sin(\omega t) \tag{3.9}$$

$E(t)$ is the potential at time t, E_0 is the amplitude of the signal, and ω is the radial frequency (expressed in radians/second). The relationship between ω and frequency f

[4] An ideal resistor has several simplifying properties: - It follows Ohm's Law at all current and voltage levels. - Its resistance value is independent of frequency. - AC current and voltage signals though a resistor are in phase with each other.

[5] A linear system is one that possesses the important property of superposition: If the input consists of the weighted sum of several signals, then the output is simply the superposition, that is, the weighted sum, of the responses of the system to each of the signals [170].

(expressed in hertz) is: $\omega = 2\pi f$. In a linear system, the response signal, $I(t)$, is shifted in phase (ϕ) and has a amplitude, I_0.

$$I(t) = I_0 \sin(\omega t - \phi) \tag{3.10}$$

An expression analogous to Ohm's Law allows us to calculate the impedance of the system as:

$$Z(t) = \frac{E(t)}{I(t)} = \frac{E_0 \sin(\omega t)}{I_0 \sin(\omega t + \phi)} = Z_0 \frac{\sin(\omega t)}{\sin(\omega t - \phi)} \tag{3.11}$$

The impedance is therefore expressed in terms of a magnitude, Z_0, and a phase shift, ϕ. If we plot the applied sinusoidal signal $E(t)$ on the X-axis of a graph and the sinusoidal response signal I(t) on the Y-axis, the result is an oval. See Fig. 3.15.a. This oval is known as a "Lissajous Figure". Analysis of Lissajous figures on oscilloscope screens was the accepted method of impedance measurement prior to the availability of modern EIS instrumentation. Using the Eulers relationship, $e^{j\theta} = \cos\theta + j\sin\theta$, it is possible to express the impedance (Eq. 3.11) as a complex function.

$$Z(\omega) = \frac{E(\omega)}{I(\omega)} = Z_0 e^{j\phi} \tag{3.12}$$

Figure 3.15: *(a). Origin of Lissajous Figures. (b). Simple Equivalent Circuit with One Time Constant. (c). Nyquist Plot with Impedance Vector. (d). Bode Plot with One Time Constant*

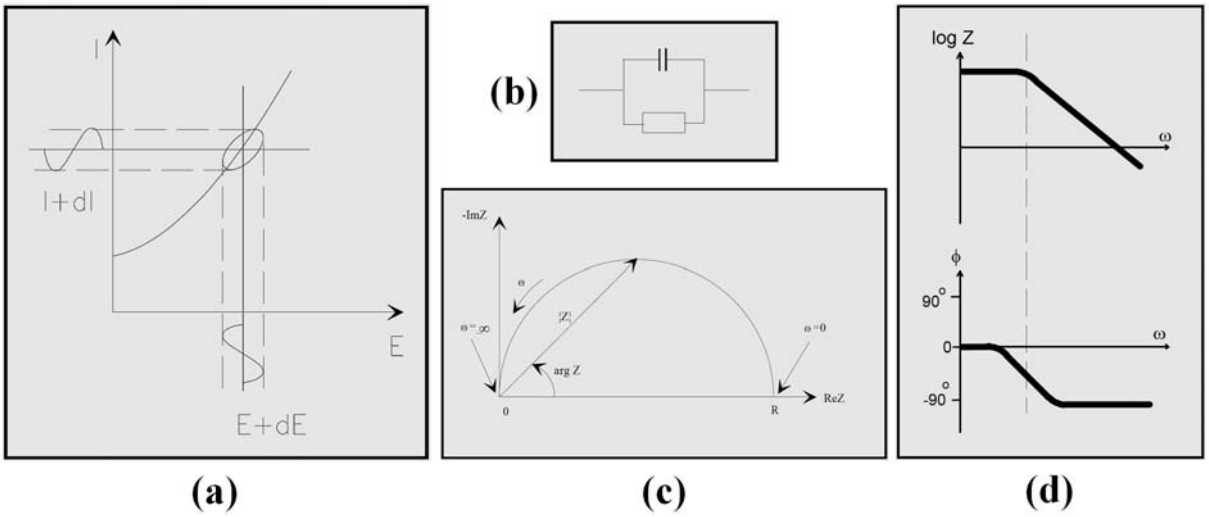

The expression for $Z(\omega)$ is composed of a real (resistance, R) and an imaginary part (reactance, X). If the real part is plotted on the X-axis and the imaginary part is plotted on the Y-axis of a chart, we get a "Nyquist Plot". See Fig. 3.15.c. Notice that in this

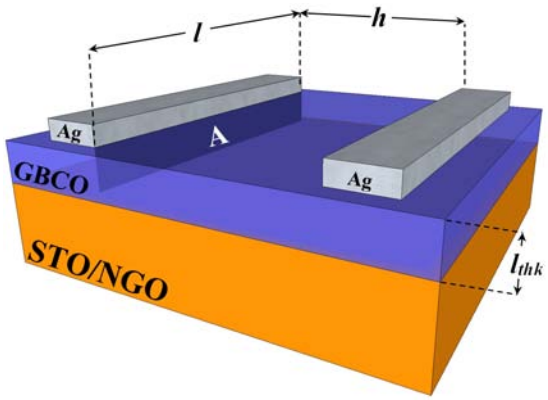

Figure 3.16: *Scheme of the conductivity measurements of a GBCO film on a STO/NGO substrate. The thickness of the thin film is grossly exaggerated when compared to the thickness of the substrate.*

plot the Y-axis is negative and that each point on the Nyquist Plot is the impedance at one frequency. Fig. 3.15.c has been annotated to show that low frequency data are on the right side of the plot and higher frequencies are on the left. On the Nyquist Plot the impedance can be represented as a vector (arrow) of length $|Z|$. The angle between this vector and the X-axis, commonly called the "phase angle", is ϕ $(= argZ)$. Nyquist Plots have one major shortcoming. When you look at any data point on the plot, you cannot tell what frequency was used to record that point. The Nyquist Plot in Fig. 3.15.c results from the electrical circuit of Fig. 3.15.b. The semicircle is characteristic of a single "time constant". Electrochemical Impedance plots often contain several semicircles. Often only a portion of a semicircle is seen.

Another popular presentation method is the Bode Plot. The impedance is plotted with log frequency on the X-axis and both the absolute values of the impedance ($|Z| = Z_0$) and the phase-shift on the Y-axis. The Bode Plot for the electric circuit of Fig. 3.15.b is shown in Fig. 3.15.d. Unlike the Nyquist Plot, the Bode Plot does show frequency information.

The resistance of a MIEC depends of the geometry of the area in which current is carried. In a bounded area with area A and length h carrying a uniform current, the resistance is defined as,

$$R = \rho \frac{h}{A} \tag{3.13}$$

ρ is the cell resistivity. The conductivity σ (the reciprocal of ρ) is more commonly used. For the conductivity measurements of our films, two parallel Ag contacts were painted on the surface of the samples (See Fig. 3.16), then, the area A is determined for the film thickness (l_{thk}) and the length contacts (l) (the substrate resistance is much higher than that of the film, so the current can be considered to be flowing entirely through the film).

$$\sigma = \frac{h}{RA} = \frac{h}{R \cdot l \cdot l_{thk}} \tag{3.14}$$

Once the film resistance through the measures of EIS is obtained, its conductivity is

calculated using Eq. 3.14 and considering that the current is flowing homogeneously across the thickness of the film, which is a valid approximation given the large ratio between the distance between parallel contacts and the thickness of the films ($h \approx 3mm$, for a film of $l_{thk} = 100nm \Longrightarrow \dfrac{h}{l_{thk}} = 3 \times 10^4$). Now, in a pure ionic conductor, its conductivity is thermally activated and follows the Arrhenius law expressed by the Eq. 1.11. From Eq. 3.14 and Eq. 1.11 we can extract the value of the activation energy using the plot slope of the $\log(\sigma T)$ vs $1/T$.

$$\log(\sigma T) = \frac{-E_a \cdot \log e}{k_B} \cdot \frac{1}{T} + \log \sigma_0 \tag{3.15}$$

To study the electrical properties of the layers, a measuring station was assembled, taking into account the demanding conditions to which would work (high temperature, highly reducing and/or oxidizing atmospheres). A more detailed description of the assembly is in the **??**. The planar resistance of the films was measured using that station applying an AC voltage at a fixed low frequency of $1kHz$. At this frequency it was proved that there is no capacitive contribution to the total impedance (using bode plots at different temperatures). AC frequency was used instead of DC in order to avoid possible problems of charge polarization and accumulation in the electrodes, which could affect the measurement. The contact resistance was checked by a four point measurement and it was estimated to be low enough not to be taken into account. The sample is located inside a tubular furnace, which temperature can be varied from room temperature to 1000 $°C$ and in which different gases can be introduced (see **??**). Electrical properties have been measured under oxygen and nitrogen flow and under mixtures of these two gases (specially to obtain a gas mixture with a concentration similar to air). The oxygen partial pressure in the nitrogen flow is estimated to be about 250 ppm.

3.1.3.2 Electrical Conductivity Relaxation (ECR)

The oxygen transport in a MIEC is determined by the oxygen exchange over the gas-solid interface and diffusion of both oxide ions and electrons/holes in the material. The oxygen transport is generally limited by the surface exchange process or by the bulk diffusion, depending on membrane thickness because the electronic charge carrier density and mobility is large when compared to those of the oxide ion. The ratio of the oxygen chemical diffusion, D^δ, to the chemical exchange coefficient, k^δ, defines a characteristic length, L_c,

$$L_c = \frac{D^\delta}{k^\delta} \tag{3.16}$$

This is the sample thickness for which diffusion and surface exchange both determine the transport rate. When L_c is much smaller than the sample thickness, l_{thk}, the transport rate will be limited by diffusion and for L_c values much larger than the sample thickness, surface exchange limitation will dominate [171, 172]. The ECR technique is widely used to study oxygen diffusion and surface exchange in thin films MIECs [173, 174]. When an abrupt change in oxygen partial pressure occurs at constant temperature, oxygen begins to diffuse into or out of the MIEC, resulting in a change in the oxygen vacancy concentration. Measuring the related change in electrical conductivity can monitor the change in oxygen vacancy concentration (change in the charge carrier concentration). For a thin film with thickness $l_{thk} < L_c$ on a non-conducting substrate, the ambient oxygen pressure is changed stepwise from $P^1_{O_2}$ to $P^2_{O_2}$ at time $t = 0$ and the time dependence of the change in the vacancy concentration, Δc_v, is monitored by the change in the electrical conductivity (σ) of the film. Assuming that the departure from equilibrium is small [175], then $c_v(t)$ is given by:

$$\frac{dc_v(t)}{dt} = -\frac{A}{V} \cdot k^{\delta} \cdot \Delta c_v \tag{3.17}$$

where A is the area of the gas solid interface and V is the volume of the sample.
For a small oxygen concentration change, the normalized change in the film electrical conductivity δ with time, $g(t)$ is proportional to the change in oxygen vacancy concentration [18]. The labels 1 and 2 refer to the initial and final values of the conductivity (σ) and vacancy concentration (c_v):

$$g(t) = \frac{\sigma(t) - \sigma_1}{\sigma_2 - \sigma_1} = \frac{c_v(t) - c_{v1}}{c_{v2} - c_{v1}} \tag{3.18}$$

Combining and integrating gives:

$$g(t) = 1 - e^{-k^{\delta} t / l_{thk}} \tag{3.19}$$

where l_{thk} is the film thickness (equals V/A). By fitting the measured electrical conductivity relaxation curve $g(t)$, with Eq. 3.19, k^{δ} can be obtained [173].

All the ERC measurements and data processing reported in this thesis were conducted in the Department of Fuel Cells and Solid State Chemistry, Risø National Laboratory for Sustainable Energy, Roskilde, Denmark in collaboration with Dr Martin Søgaard. The conductivity relaxation measurements were made on a $10 \times 5\ mm^2$ sample grown on NGO(100) and YSZ(100) substrates with thickness of 160 nm and 210 nm respectively in the temperature range $300 - 500\ ^{\circ}C$. The sample was placed inside a 30 cm long closed-end quartz tube with a diameter of 2.5 cm. The oxygen partial pressure in the quartz tube

can be controlled by varying the flow rates of different gases. In the present study, flows of oxygen and nitrogen were used for preparing oxygen partial pressures in the range of 1-0.003 atm. The oxygen partial pressure steps were targeted such that $P^2_{O_2}/P^1_{O_2} \leq 2$ where $P^2_{O_2}$ and $P^1_{O_2}$ are the final and initial oxygen partial pressures, respectively. A zirconia-based electrochemical cell was used for measuring the oxygen partial pressure in the carrier gas mixture (O_2/N_2). The quartz tube creates an empty reactor volume of $\sim$ 147 mL. To minimize the total volume of the glass reactor, a ceramic tube and a thermocouple was brought inside the reactor. In this situation, the characteristic time constant for the reactor is $\tau = (T_0/T)(V/Q_0)$, where Q_0 (250 mL/min) is the total flow rate measured at standard temperature and pressure (room temperature T_0 and 1 atm pressure). In all cases, the time constant for changing the oxygen pressure in the reactor is several orders of magnitude lower than the relaxation time of the sample investigated in this study.

Two parallel platinum wires were fixed on the surface, and platinum paste was applied to ensure sufficient current collection. A constant current of 0.35 mA was used, and the voltage across the sample was measured with a voltmeter every few seconds. As the substrate resistance is significantly higher than that of the film, the current is assumed to only flow through the film.

A more detailed description of the theory and experimental setup is given in Mosleh *et.al.* paper [172]. Results and discussion of the measures obtained are discussed in the following chapters.

Part II

Discussion and Results

CHAPTER 4

Preparation and Characterization of $GdBaCo_2O_{5+\delta}$ Thin Films

As mentioned in section 2.1, during PLD, many experimental parameters can be changed, which then have a strong influence on film properties. First, the laser parameters such as laser fluence, pulse duration and repetition rate can be altered. Second, the preparation conditions, including target composition, target-to-substrate distance, substrate temperature, background gas and pressure, may be varied, which all influence the film growth. We begin studying the phases present in the target used in the films preparation and then we will focus on the effects of the deposition parameters variation on the composition, structure and morphology of the films.

4.1 Characterization of GBCO Targets

The synthesis process used to produce the GBCO targets used in this project has been introduced in 2.1.2. Appropriate GBCO target with 1" of diameter was achieved via conventional solid-state reaction method. The phases present in the target were studied using X-ray diffraction. In the Fig. 4.1 we can observe the diffraction pattern of the targets after final sintering process for a ratio stoichiometric in the initial powder mixture (stoichometric target Fig. 4.1(a)) and for target with cobalt excess (Fig. 4.1(a))[1]. Target with cobalt excess was necessary in order to compensate deficiencies of Co in the thin films [115, 132]. The obtained patterns were compared with ICSD (Inorganic Crystal Structure Database), provided by the CDS (Chemical Database Service): We used the GBCO structure reported by Frontera *et. al.* corresponding to ICSD Collection Code 154018 [90] (orthorhombic with $a = 3.862$, $b/2 = 3.934$ and $c/2 = 3.786$Å cell parameters). The theoretical pattern exported from ICSD database is included in the graphs. For

[1]Targets with cobalt excess were obtained increasing by 5% the required weight of Co_3O_4 in the initial stoichiometric mixture

stoichometric target we used PANalytical X'Pert Pro MPD with Cu radiation, there is no evidence of secondary phases under the measurement conditions used. In the case of the Co-excess target we used MPD with Co radiation in order to obtain a lower background and higher intensity in cobalt species. The target presents a major GBCO phase and minor traces of cobalt oxides Co_3O_4 (indicated by the symbol $*$) and CoO (indicated by the symbol $\bigtriangledown$). The minor phases were identified using X'pert Highscore software with JCPDS-ICDD[2] database, with the codes PDF# 00-043-1003 and PDF# 01-071-1178 for Co_3O_4 and CoO respectively.

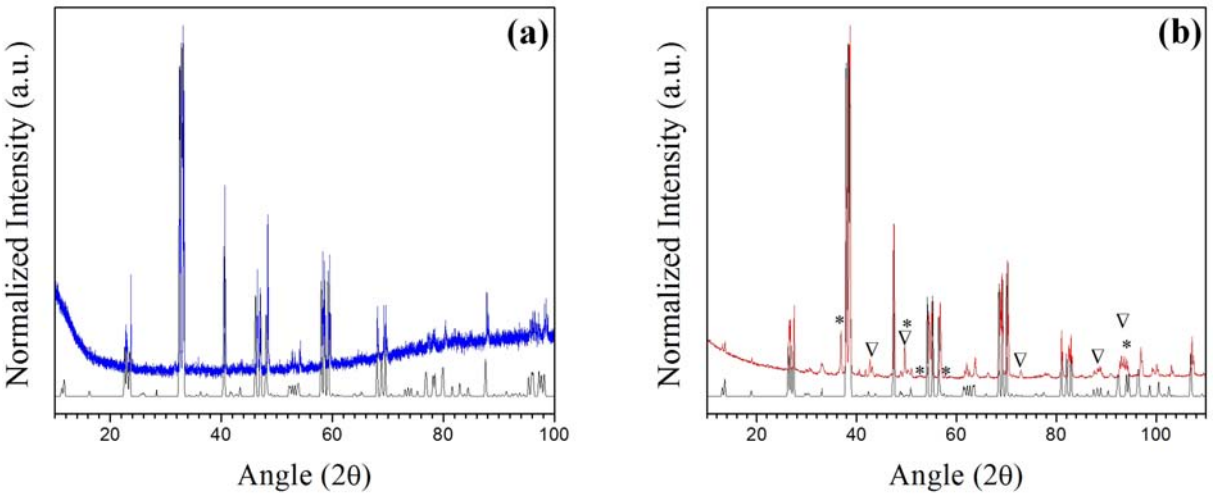

Figure 4.1: *XRD patterns of (a) GBCO with a ratio stoichiometric (using Cu radiation) and (b) GBCO with Co-excess (using Co radiation) targets show the near pure-phase of these materials with a minority traces of Co_3O_4 (indicated by $*$) and CoO (indicated by $\bigtriangledown$)*

4.2 Growth of GBCO Thin Films on STO substrates Using Stoichometric Target

[3] As mentioned in the introductory section, epitaxial films obtained by PLD of different ordered "112" cobaltite perovskites have already been reported [89, 96, 176, 177], However, to the best of our knowledge, there were no previous reports in the deposition of GBCO epitaxial films. Initially, the influence of deposition temperature on film growth was investigated. The GBCO thin films were obtained by PLD on STO (100) substrates at 10 Hz pulse repetition and at a laser fluence of around 2 J/cm^2. The target used was a stoichiometric GBCO ceramic pellet, and its distance to the substrate was fixed at 50

[2]JCPDS-ICDD: Joint Committee on Powder Diffraction Standards - International Centre of Diffraction Data, Newtown Square, USA; PDF:powder diffraction file

[3]Part of this section is summarized on the paper *Influence of the Microstructure on the High-Temperature Transport Properties of $GdBaCo_2O_{5+\delta}$ Epitaxial Films. [115]*

mm. The deposition was carried out in a high vacuum chamber, in a pure O_2 atmosphere. The substrate temperatures were varied between 800 and 900 $°C$ at a fixed pressure of 100 mTorr. The phase composition and orientation of the films was analyzed by X-ray diffraction using a Rigaku diffractometer with Cu radiation. Figure 4.2 shows the $\theta/2\theta$ XRD scans of these samples series. The films have approximately 100 nm thickness (which

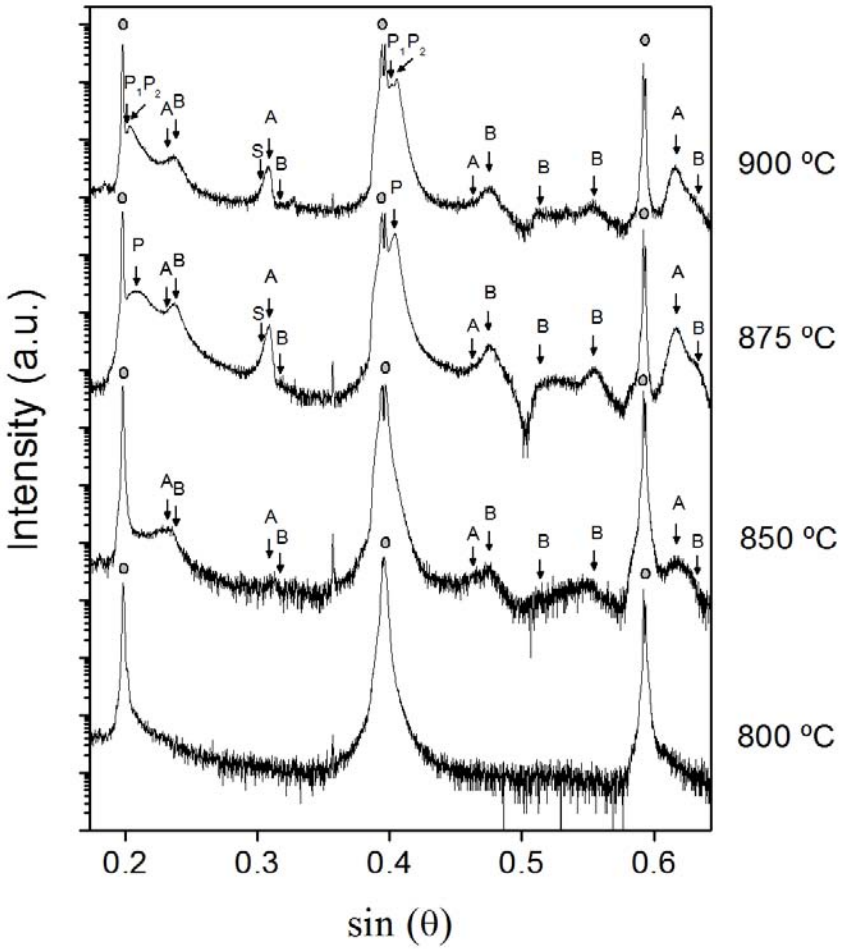

Figure 4.2: *XRD patterns of GBCO films deposited on STO at different temperatures. The positions for substrate peaks (grey circles), for the 00l peaks corresponding to the GBCO perovskite phase (P, P1 and P2) and for the peaks corresponding to a phase with a unit cell periodicity of 20.0 Å (A) and 19.5 Å (B) are indicated [115].*

correspond to 2000 ablation pulses)[4]. At the lowest temperature (800 $°C$), only the peaks of the STO substrate can be distinguished (gray circles) in a normal $\theta/2\theta$ scan. This indicates that the GBCO film shows a perovskite cell parameter so close to that of the substrate that it cannot be distinguished with the resolution of the experimental setup, as will be shown in the reciprocal space map (Fig. 4.3). No other peaks corresponding to

[4]The film thickness was determined by X-ray reflectometry for the thinner films, estimated by WDS for the thicker films, and additionally confirmed by the TEM images.

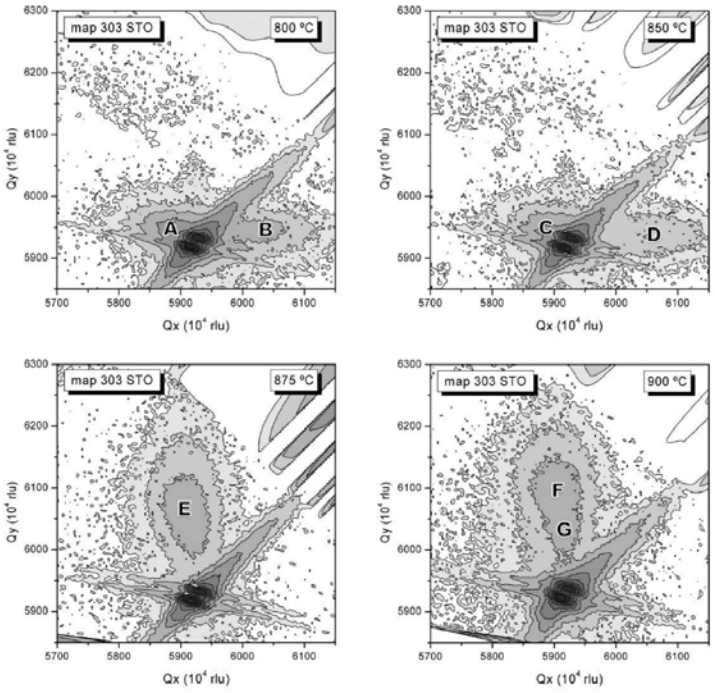

Figure 4.3: *Reciprocal space maps around the 303 STO reflection with the main contributions of the GBCO films marked in the graph. The films deposited at different temperatures have the following (in-plane, out-ofplane) cell parameters:* ***A*** *(3.92, 3.87 Å) and* ***B*** *(3.84, 3.87 Å) at 800 °C,* ***C*** *(3.92, 3.89 Å) and* ***D*** *(3.82, 3.89 Å) at 850 °C,* ***E*** *(3.91, 3.82 Å) at 875 °C and* ***F*** *(3.92, 3.80 Å) and G (3.91, 3.84 Å) at 900 °C. [115].*

other phases or orientations appear under these deposition conditions. As the temperature increases, peaks corresponding to different phases of the GBCO film appear. The peaks seem to correspond to different families of planes, which have been marked as **A**, **B**, **P**, and **S**. The family of planes marked as **P** (**P1** and **P2**) corresponds to a perovskite phase (3.80-3.84 Å), and those marked as **A** and **B** correspond to a unit cell periodicity of 20.0 and 19.5 Å, respectively. Additionally, the expected position for the reflection which would correspond to the superstructure of the perovskite coming from double cell parameter is marked as **S**. At 850 $°C$, apart from the peaks of the substrate, some additional weak peaks (from the **A** and **B** families) are observed as corresponding to a secondary phase, which was not identified at this stage. At higher temperatures (875 and 900 $°C$) the main intensity (**P**) corresponding to the perovskite phase film reflections lies in a region very close to the (00l) reflections of the substrate. On a closer inspection of that region it is possible to identify a peak corresponding to a mean out-of-plane cell parameter of 3.82 Å for the film deposited at 875 $°C$ and two peaks (**P1** and **P2**) with out-of-plane cell parameters of 3.84 and 3.80 Å for the film deposited at 900 $°C$. The presence of the superstructure peak **S** at these high temperatures cannot be ruled out, as it might overlap with the peaks of the other secondary phases. In addition, the intensity of the **A** and **B** families of peaks is larger at the higher temperatures ($875 - 900$ $°C$) than at the lower ones ($800 - 850$ $°C$).

In Fig. 4.3 reciprocal space maps around the 303 STO reflection are plotted in **Qx**, **Qy** coordinates (x and y correspond to [100]* and [001]* directions, respectively) for

films deposited at the four different temperatures[5]. The 303 STO substrate reflection clearly appears with two intense components, $K_{\alpha 1}$ and $K_{\alpha 2}$, whereas the GBCO peak presents a different shape and position depending on the deposition temperature. At lower temperatures there are two clear contributions (marked as **A** and **B** for the 800 $°C$ film and as **C** and **D** for the 850 $°C$ film) with a common out-of-plane parameter (3.87 Å for the 800 $°C$ film and 3.89 Å for the 850 $°C$ film), but two distinct in-plane parameters (3.84 and 3.92 Å for the 800 $°C$ film and 3.82 and 3.92 Å for the 850 $°C$ film). The lattice parameters extracted from the reciprocal space maps in Fig. 4.3 for the films deposited at various temperatures are summarized in Table 4.1. The reciprocal space maps for the films deposited at higher temperatures show the presence of one (at 875 $°C$, marked as **E**) and two (at 900 $°C$, marked as **F** and **G**) main contributions of the film with out-of-plane parameters (3.80-3.84 Å), consistent with previous XRD $\theta/2\theta$ patterns observations, and in-plane parameters of 3.91 Å at 875 $°C$ and of 3.92 and 3.91 Å at 900 $°C$, respectively, closely matching that of STO substrate (3.905 Å). This indicates that this part of the film is very likely to grow coherently with the substrate. A direct comparison with bulk values $a = 3.862$, $b/2 = 3.934$ and $c/2 = 3.786$ Å of the *Pmmm* phase [90] and assuming that the shorter parameter in the film corresponds also to the c-axis, establishes, as first approximation, that the films mainly correspond to either $c_{\parallel}$ (c-axis parallel to the film plane) for the films deposited at 800 and 850 $°C$ or $c_{\perp}$ (c-axis perpendicular to the substrate plane) for the films deposited at 875 and 900 $°C$. It should be noticed that it is possible for both the low- and high-temperature GBCO films to have some regions in which both the in- and out-of-plane cell parameters are quite close to those of the STO substrate (3.905 Å). These regions would be indistinguishable by XRD, as the peaks corresponding to the perovskite film and to the substrate would overlap in both the $\theta/2\theta$ scans and in the reciprocal space maps.

As we will show later in the High Resolution Transmission Electron Microscopy discussion, there is a general trend for GBCO films deposited at different temperatures. The first GBCO cells directly on the STO substrate always seem to grow preferentially $c_{\perp}$, *i.e.*, with the doubleperovskite superstructure perpendicular to the STO surface. This behavior is to be expected, as the first unit cells will grow strained, with the in-plane cell parameter matching that of the substrate (3.905 Å), and therefore with ordering and a correspondingly shorter cell parameter out-of-plane. But after about 20 nm, as a relaxation mechanism, the first defects appear in the structure. As a consequence the GBCO cells that grow on top are not restricted to the in-plane cell parameter of the substrate (3.905 Å), and a mixture of orientations can appear.

[5]The in- and out-of-plane lattice parameters were accurately determined performing area scans of asymmetric reflections of the layers using a Bruker D8 DISCOVER with a four-angle goniometer and GADDS detector.

Deposition Temperature [°C]	Main Contributions	In-plane cell Parameter [Å]	Out-plane cell Parameter [Å]
800	A	3.92	3.87
	B	3.84	3.87
850	C	3.92	3.89
	D	3.82	3.89
875	E	3.91	3.82
900	F	3.92	3.80
	G	3.91	3.84

Table 4.1: *Lattice Parameters Extracted from the Reciprocal Space Maps (Fig. 4.3) for the Films Deposited at Various Temperatures [115].*

The ideal composition of GBCO compound is (Gd:Ba:Co = 1:1:2) and through WDS microprobe analysis we can get information about the average cationic composition of the films. We used a Cameca SX-50 Microprobe (with four crystal analyzers for WDS). The typical voltages used were 12, 15, and 20 keV. A thin film analysis program (STRATAGem) was used to determine the exact composition and thickness of the thin films without interference of the substrate composition. All the samples deposited at $P_{O_2} = 100$ mTorr showed a composition ratio between the different cations of [Gd]/[Ba] = 1.1-1.2 and ([Gd]+[Ba])/[Co] = 1.2-1.4 as measured by WDS, and depicted in the ternary phase diagram representation in Fig. 4.4. The origin of the observed cation composition deviation from the stoichiometric target might come from different sources. Either the elevated deposition temperatures could induce the desorption of more volatile Co-containing species *(i)*, or the solid angle of the evaporated Co-containing species is very different to those containing Gd or Ba, *i.e.*, their different crosssections induce larger scattering in the plume, so the effective composition in the center of the plume where the sample is located might deviate from the target composition *(ii)*, or the ablation process of the target material is not congruent, so some species show larger evaporation yield *(iii)*. This last argument is possible during the first shots on the fresh surface of the target, thus causing a deficiency of a particular element in the target surface. However, after a number of shots, a stationary ablation with stoichiometric composition is generally reached with the excess evaporation compensated by the deficient target surface composition. in our experiments, we always performed a preablation step with a sufficient number of shots to rule out this problem. In addition, even though the high temperature (first argument) could be a possible cause for the deviation in stoichiometry, we do not seem to observe an increment in the deviation with the deposition temperature within the measured range (800-900 °C).

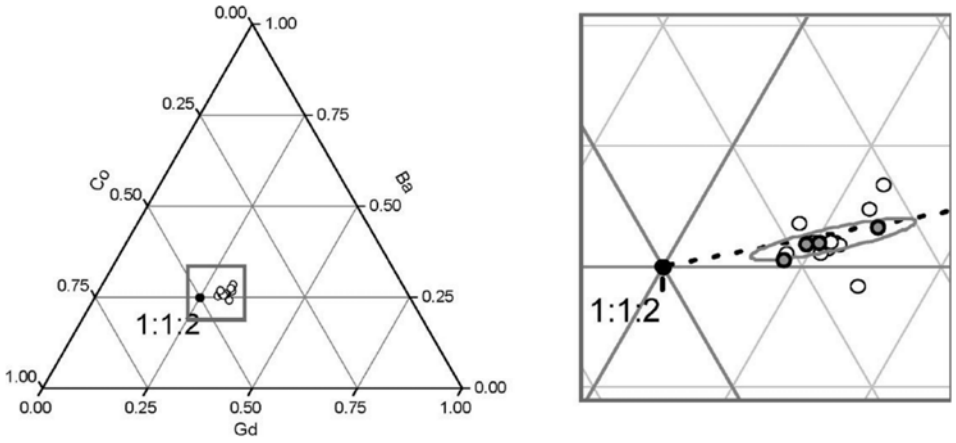

Figure 4.4: *Ternary phase diagram representation of the Gd:Ba:Co cation composition measured in the films by WDS. The image on the right is an enlargement of the region close to the $GdBaCo_2O_{5+\delta}$ (1:1:2) stoichiometric composition. The encircled area indicates a region with a constant [Gd]/[Ba] ratio of 1.2 and varying ([Gd]+[Ba])/[Co] ratio, where the set of films selected for comparison are located (full circles) [115].*

4.2.1 Study of the effects of deposition conditions on GBCO thin films

Based on these initial results, we performed a systematic study of the effects of deposition conditions on the structure and orientation of GBCO thin films obtained using a stoichiometric GBCO target. We choose 875 $°C$ as initial starting point because according to the RSM (Fig. 4.3), this deposition temperature favors the growth of the layers with predominantly c-axis out-of-plane ($c_\perp$). We study the effect of P_{O_2} variations during deposition process into the chamber, laser fluence, target-substrate distance, substrate position on the holder and finally in temperature again. Next, a summary of X-ray diffraction, RSM and WDS microprobe results are presented.

1. *Variation with the Working Pressure*

   Figure 4.5(a) shows XRD patterns obtained for three GBCO films deposited on STO (100) substrate at different working pressure. When the deposition temperature of 875 $°C$ is reaching, oxygen pressure is manipulated to achieve the desired value. A laser fluence of $\sim 2.8\ J/cm^2$ was adopted, 4000 pulses of ablation at 10Hz were carried out corresponding to 105, 138 and 81 nm of thickness for 11, 60 and 110 mTorrr deposition pressures respectively (thickness of the films were determined by WDS). After deposition, the sample was cooled down to room temperature (RT) with a rate of $10°C/min$ under the same pressure deposition.

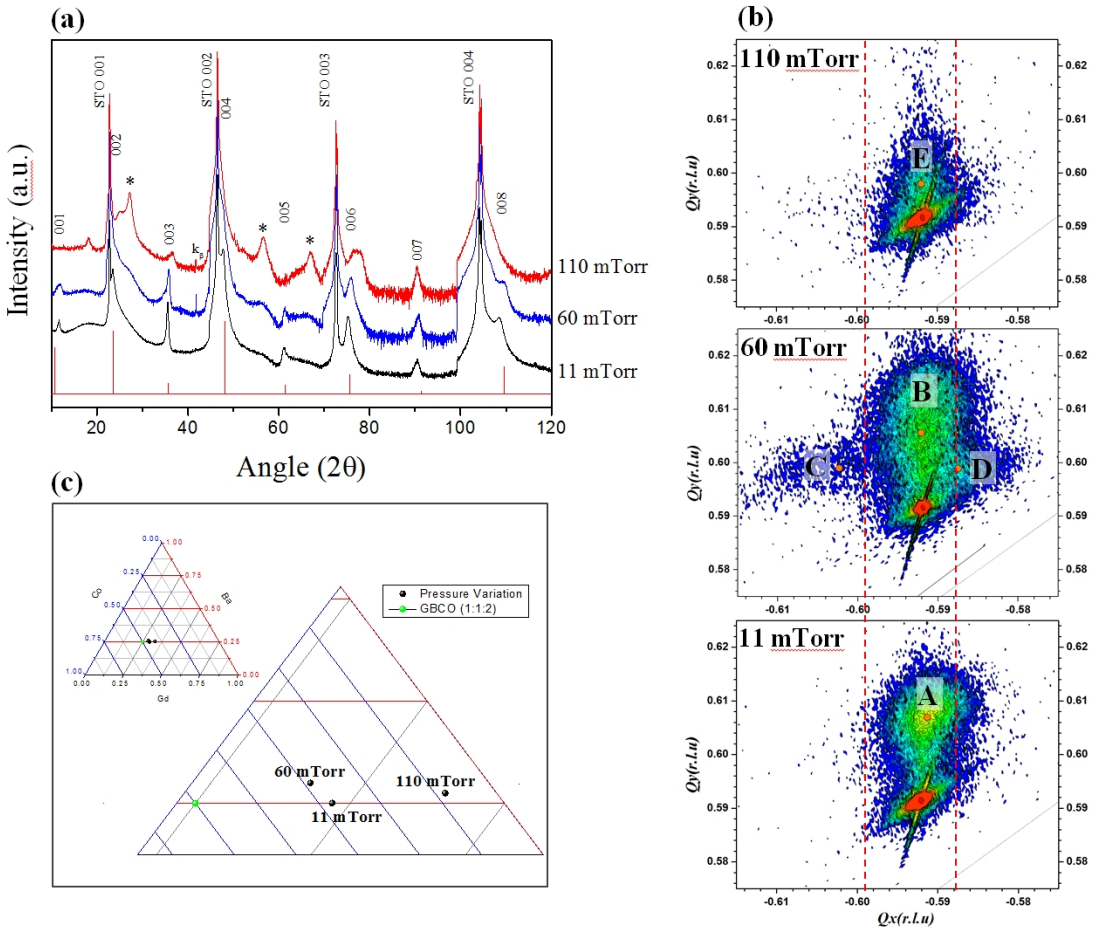

Figure 4.5: *(a) XRD patterns, (b) RSM and (c) WDS of GBCO films grown on STO (001) single crystal substrate by 875 °C, ∼ 2.8 J/cm², 50 mm target-substrate distance and 4000 laser pulses (10 Hz) with differents oxygen pressure of 11, 60 and 110 mTorr. In (a), the STO substrate peaks (00l) are indicated, the c-axis oriented GBCO film peaks are indexed by (00l), the theoretical scan of GBCO film with pure c-axis out-of-plane orientation (line red) is included and the extra peaks are designated by (∗)*

Peaks of the STO substrate can be distinguished in the $\theta/2\theta$ scan. The patterns show one set of *00l* GBCO reflections and the presence of intense reflections in the intermediate positions between the main substrate reflection (indexed as l = odd) is also characteristic of the GBCO double perovskite superstructure arising from the Gd/Ba sequential A-site arrangement in the [001] direction (we have added the theoretical scan of GBCO film with pure c-axis out-of-plane orientation, line red in the bottom of Fig. 4.5(a)). Samples deposited at 11 and 60 mTorr show similar spectra, but the layer growth at 11 mTorr has *00l* GBCO peaks family more defined and intense. On the other hand, the GBCO deposited at higher pressure (110 mTorr) presents a spectrum where additional weak peaks (marked with (∗)) are observed as corresponding probably to the formation of secondary phase deteriorating

the crystalline quality. In Fig. 4.5(b) reciprocal space maps around the $\bar{3}03$ STO reflection are plotted in **Qx**, **Qy** r.l.u. (reciprocal lattice units) coordinates. At all three pressure deposition the GBCO show a spot (labeled A, B and E in the maps) with a common in-plane cell parameter close to STO parameter (indicating that part of the films is very likely to grow coherently with the substrate) and an out-of-plane parameter (corresponding to c-axis oriented film) that increase from 3.81(1) Å to 3.86(2) Å consistent with the degradation of the superstructure peaks observed by X-rays. At intermediate pressure (60 mTorr) there are also two clear contributions (marked as C and D) with a similar out-of-plane parameter 3.87(1) Å associated to a-axis out-of-plane. It is apparent that two different orientations, corresponding to c-axis oriented and a-axis oriented grains, exist in the film. Table 4.2 collects the cell parameters measured on the STO substrate. Although the films show a much better crystalline quality than those shown in the Fig. 4.2, the results of WDS microprobe show there is still a deviation from the ideal composition ratio ([Gd]+[Ba])/[Co] between the different cations Fig. 4.5(c)).

P_{O_2} $[mTorr]$	Thickness [nm]	$\frac{Gb+Ba}{Co}$	Peak	In-plane cell Parameter [Å]	Out-plane cell Parameter [Å]
11	106	1.19	A	3.91(1)	3.81(1)
60	140	1.18	B	3.91(2)	3.82(2)
			C	3.83(2)	3.87(2)
			D	3.95(2)	3.87(1)
110	82	1.40	E	3.91(2)	3.86(2)

Table 4.2: *Out-of-plane and in-plane parameters extracted from the RSMs (Fig. 4.5(b)) for films deposited at various working pressures*

Oxygen incorporation appears to be an important role for the crystallographic reorientation behavior as a function of oxygen partial pressure. Varying oxygen partial pressure during deposition can strongly influence the oxidation state of Co (*i.e.* Co^{3+} to Co^{4+} when the pressure increase) and the oxygen vacancy in the GBCO. The pressure inside chamber also has effect on scattering in the plume, so the effective composition in the center of the plume might change by varying the pressure.

2. *Variation with the Laser Fluence*

A series of films were deposited as a function of laser fluence ($1.71 - 4.02\ J/cm^2$). As mentioned in the section 2.1, a high laser fluence can provide a large amount of ablated material from the target, consequently a high degree of supersaturation (dense plasma) and a large nucleation density on the substrate surface, these factors

can lead to a favorable 2D growth (layer-by-layer) to fabricate the films [140]. Should keep in mind that as we increase the fluence, layers of greater thickness are obtained for an equal number of pulses (4000 pulses in our case) and the film may tend to relax the stress resulting in phenomena of reorientation.

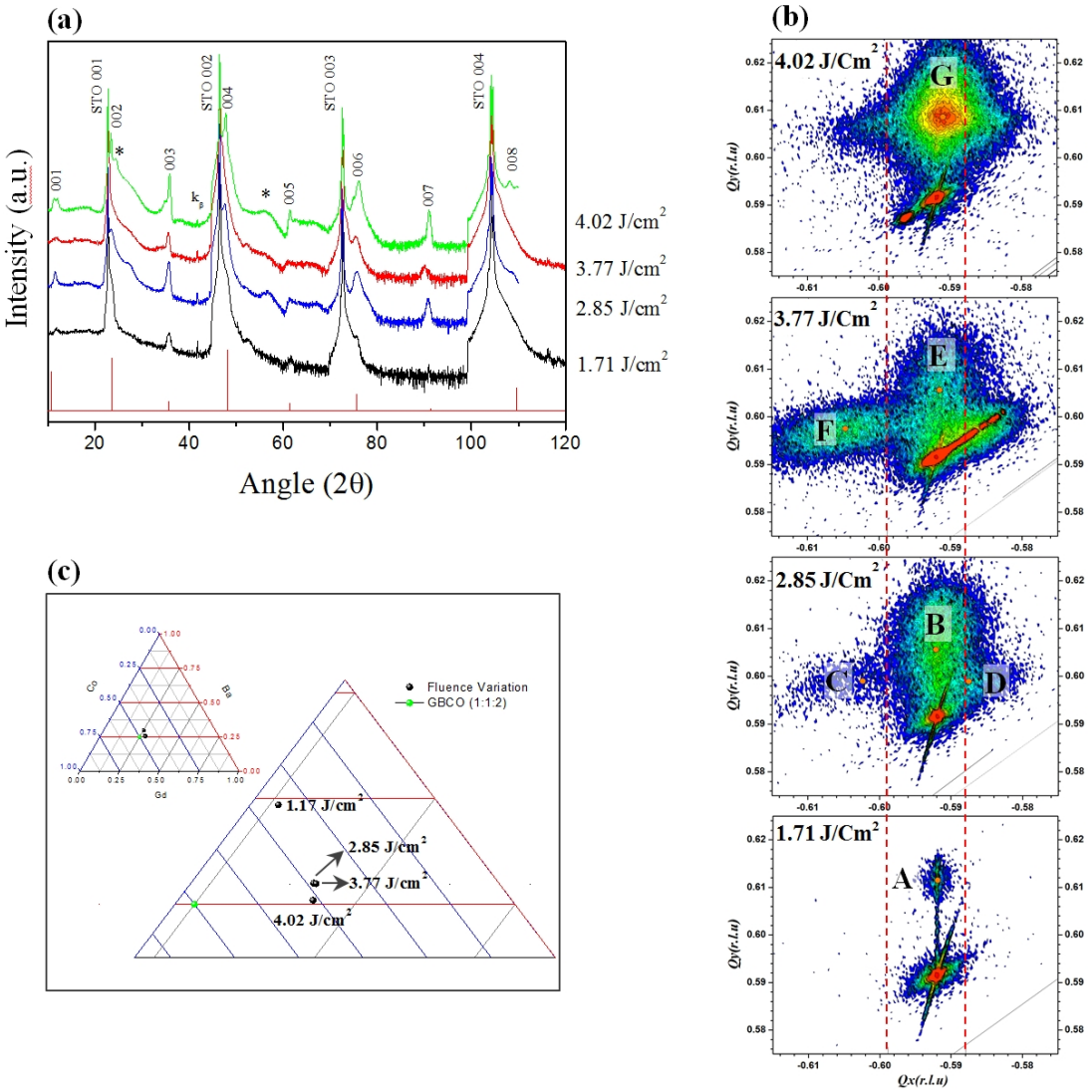

Figure 4.6: *(a) XRD patterns, (b)RSM and (c) WDS of GBCO films grown on STO (001) single crystal substrate by 875 °C, 60 mTorr, 50 mm target-substrate distance and 4000 laser pulses (10 Hz) with various laser fluences of 1.71, 2.85, 377 and 4.02 J/cm^2. In (a), the STO substrate peaks (00l) are indicated, the c-axis oriented GBCO film peaks are indexed by (00l), and the extra peaks are designated by (∗)*

The obtained X-ray diffraction patters of the films grown on STO substrates are shown in Fig. 4.6(a). All films deposited at different fluence show the *00l* GBCO reflections indicating a predominant orientation with c-axis out-of-plane, but as the fluence increases, the appearance of new phases (or structural defects as discussed in the HR-TEM results) is favored and the GBCO peak shape broaden. The

intensity of these peaks also increases, but this could be attributed to have thicker layers. Figure 4.6(b) show the RSMs around the $\bar{3}03$ STO reflection with the main contributions of the GBCO films marked in the graph. Contributions marked as A, B, E, G can be attributed to the family of planes with c-axis out-of-plane according to the results of X-ray. At fluences of 2.85 and 3.77 J/cm^2 appear new contributions (Marked as C, D and F) related to family of planes with a-axis out-of-plane. Also, looking at the peaks associated to STO for layers deposited at 3.77 and 4.02 J/cm^2 fluence, they suggest the presence of twins in the substrate. The cell parameters measured using RSMs are contained in Table 4.3. The results of WDS microprobe continue show there is still a deviation from the ideal composition ratio ([Gd]+[Ba])/[Co] between the different cations Fig. 4.6(c)).

Fluence $[J/cm^2]$	Thickness [nm]	$\frac{Gb+Ba}{Co}$	Peak	In-plane cell Parameter [Å]	Out-plane cell Parameter [Å]
1.71	12	1.22	A	3.90(1)	3.78(1)
2.85	140	1.18	B	3.91(2)	3.82(2)
			C	3.83(2)	3.87(2)
			D	3.95(2)	3.87(1)
3.77	219	1.19	E	3.91(2)	3.82(2)
			F	3.82(2)	3.87(2)
4.02	267	1.16	G	3.91(1)	3.80(1)

Table 4.3: *Out-of-plane and in-plane parameters extracted from the RSMs (Fig. 4.6(b) for films deposited at various laser fluence*

3. *Variation with Target-Substrate Distance*

Figure 4.7(a) shows XRD patterns obtained for three GBCO films deposited on STO (100) substrate at different target-substrate distance (50mm, 55mm and 60 mm respectively). A oxygen partial pressure P_{O_2} of 60 mTorr was set during the deposition and cooling down processes, a laser fluence around 2.9 J/cm^2 was adopted, 4000 pulses of ablation at 10Hz and a temperature deposition of 875 $°C$ were used.

STO substrate peaks can be distinguished in the $\theta/2\theta$ scan. The patterns show one set of *00l* GBCO reflections and the superstructure reflections arising from the Gd/Ba sequential A-site arrangement in the [001] direction. The intensity of (*00l*) reflections of GBCO gradually increased with a target-substrate distance from 50 mm to 60 mm, but some additional weak peaks (marked with (∗)) are observed as corresponding probably to the formation of secondary phase. In Fig. 4.7(b) reciprocal space maps around the $\bar{3}03$ STO reflection are plotted. At target-substrate distance

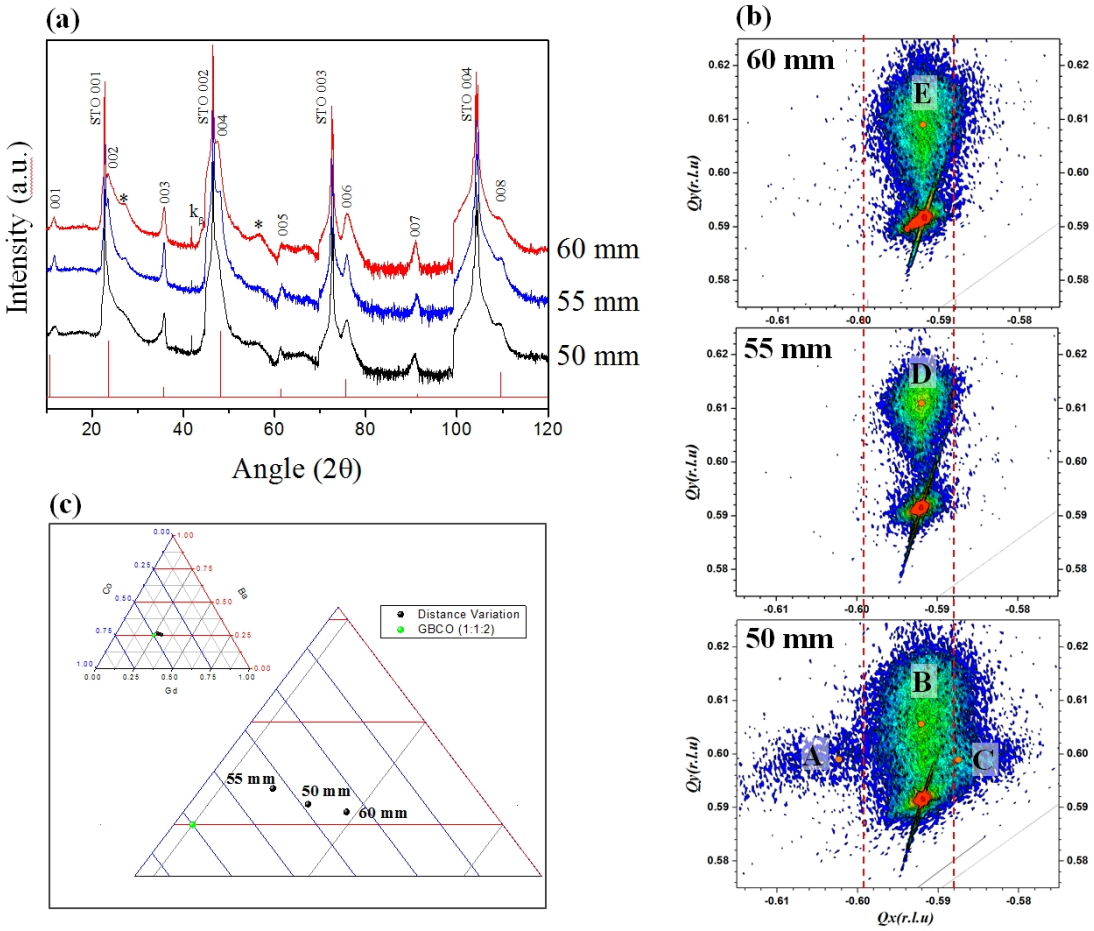

Figure 4.7: *(a) XRD patterns, (b)RSM and (c) WDS of GBCO films grown on STO (001) single crystal substrate by 875 °C, 60 mTorr, laser fluence of ∼ 2.9 J/cm^2 and 4000 laser pulses (10 Hz) with different target-substrate distance. In (a), the STO substrate peaks (00l) are indicated, the c-axis oriented GBCO film peaks are indexed by (00l), and the extra peaks are designated by (∗)*

of 50 mm there are two different orientations, corresponding to c-axis oriented and a-axis oriented grains. The peaks marked as A and C have a common out-of-plane parameter 3.87(1) Å associated to a-axis out-of-plane while the peaks labeled as B, D, and E have a parameter around 3.82 Å associated to c-axis out of plane (see Table 4.4). WDS microprobe results show once again cationic deviation from the ideal composition ratio ([Gd]+[Ba])/[Co](Fig. 4.7(c)).

4. *Variation with Deposition Temperature*

Previous experiments give us an idea about the appropriate parameter to grow GBCO films with relatively good crystalline quality. However, all the samples present a deviation in the stoichiometry from the ideal. This deficiency in cobalt can be reflected in the appearance of new phases or structural defects (*i.e.* supplementary GdO planes) in the layers as will be discussed in the HR-TEM results. Taking all

Target-Substrate Distance [mm]	Thickness [nm]	$\frac{Gb+Ba}{Co}$	Peak	In-plane cell Parameter [Å]	Out-plane cell Parameter [Å]
50	140	1.18	A	3.83(2)	3.87(2)
			B	3.91(2)	3.82(2)
			C	3.95(2)	3.87(1)
55	52	1.15	D	3.91(1)	3.76(1)
60	96	1.24	E	3.91(1)	3.76(1)

Table 4.4: *Out-of-plane and in-plane parameters extracted from RSMs (Fig. 4.7(b)) for the films deposited at various target-substrate distance*

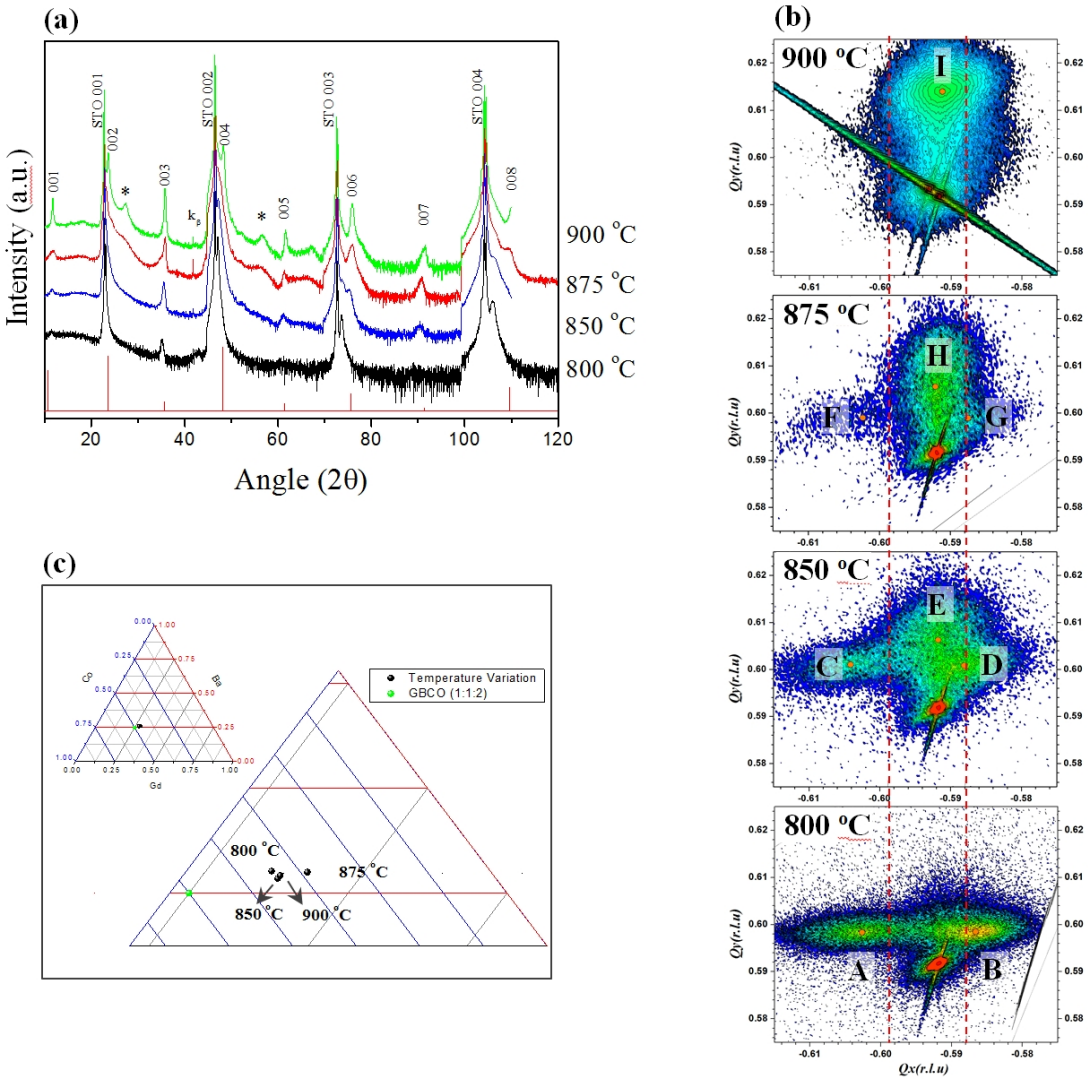

Figure 4.8: *(a) XRD patterns, (b)RSM and (c) WDS of GBCO films grown on STO (001) single crystal substrate at 60 mTorr, laser fluence of* $\sim 2.9\ J/cm^2$*, target-substrate distance of 50mm and 4000 laser pulses (10 Hz) with various deposition temperatures. In (a), the STO substrate peaks (00l) are indicated, the c-axis oriented GBCO film peaks are indexed by (00l), and the extra peaks are designated by (∗)*

this into account, we prepared a final set of samples at different temperatures of deposition, by selecting the parameters that provided a stoichiometric ratio closer to the ideal in order to compare it with the initial results shown in XRD (Fig. 4.2) and RSM (Fig. 4.3). We set a pressure of of 60 mTorr, a laser fluence around 2.9 J/cm^2, target-substrate distance of 50mm and 4000 pulses of ablation at 10Hz (corresponding to $\sim$ 160 nm of thickness).

Figure 4.8(a) shows XRD patterns obtained for GBCO films deposited on STO (100) substrate at temperatures between 800 and 900 $°C$. At the lowest temperature (800 $°C$), GBCO film shows a perovskite cell parameter very close to the substrate and some low intensity reflections corresponding to perovskite superstructure. These superstructure peaks become more intense when increase the deposition temperature. A closer inspection of pattern sample deposited at 900 $°C$ allows us to obtain (using the *00l* reflections) an out-of-plane cell parameter of 7.53Å (c/2=3.77Å). In the pattern besides we observed reflections (marked with $*$) associated with structural defects or possible formation of new phases. In Fig. 4.8(b) reciprocal space maps

Deposition Temperature [$°C$]	Thickness [nm]	$\frac{Gb+Ba}{Co}$	Peak	In-plane cell Parameter [Å]	Out-plane cell Parameter [Å]
800	157	1.13	A	3.84(2)	3.87(2)
			B	3.94(1)	3.87(1)
850	166	1.13	C	3.82(2)	3.85(2)
			D	3.93(2)	3.85(2)
			E	3.90(2)	3.82(1)
875	140	1.18	F	3.83(2)	3.87(2)
			G	3.95(2)	3.87(2)
			H	3.91(2)	3.82(1)
900	97	1.14	I	3.91(1)	3.83(1)

Table 4.5: *Out-of-plane and in-plane parameters extracted from the RSMs (Fig. 4.8(b)) for the films deposited at various STO substrate temperatures*

around the $\bar{3}03$ STO reflection are plotted. We can see clearly the same tendency observed in the x-rays patterns. At 800 $°C$ the layer has a predominant a-axis out-of-plane orientation (reflections A and B in RSM, indistinguishable by XRD). As temperature increases, the intensity of reflection associated to the c-axis out-of-plane orientation increases (reflections E, H, I) and the contribution of a-axis out-of-plane decreases. At the higher temperature (900 $°C$) the layer exhibits predominantly an orientation with the c-axis out-of-plane. Figure 4.8(c) show ternary phase diagram representation of the Gd:Ba:Co cation composition measured in the films by WDS, as in previous experiments, a deviation from the ideal composition is observed. The cell parameters obtained from the RSMs and composition ratio ([Gd]+[Ba])/[Co])

are summarized in the Table 4.5.

We can summarize the results of previous experiments in basically two points.

(i) Epitaxial thin films of GBCO grown by PLD using a stoichiometric target have been studied as a function of deposition conditions. The epitaxial GBCO films mainly consist of single- and double-perovskite regions that are oriented in different directions depending on the deposition parameters (It should be noticed that it is possible for GBCO films to have some regions in which both the in- and out-of-plane cell parameters are quite close to those of the STO substrate (3.905 Å). These regions would be indistinguishable by XRD, as the peaks corresponding to the perovskite film and to the substrate would overlap in both the $\theta/2\theta$ scans and in the reciprocal space maps). Films with a unique orientation c out-of-plane are susceptible to show new phases or structural defects.

(ii) In the range in which the growth parameters of the films were varied, it was not possible to obtain films with an ratio stoichiometric "ideal". The nature of the ablation process from stoichiometric GBCO targets generates a deviation in the composition of the films which basically consists in a Co depletion, with ([Gd]+[Ba])/[Co] ratio from 1.13 to 1.40 which deviates from 1:1:2 ([Gd]+[Ba])/[Co] = 1. This composition deviation induces the appearance of characteristic stacking faults with supplementary GdO planes as will be discussed in the next section. So, to obtain stoichiometric films, it might be necessary to change the target composition to a Co excess to compensate their deficiency in the film stoichiometry. The Fig. 4.9 shows an overview of stoichiometric deviation of the experiments listed above.

4.3 Morphological and Microstuctural Characterization of GBCO Thin Films on STO

The SEM images presented in Fig. 4.10 depict the evolution of surface morphological change of the GBCO films deposited on STO(100) with the deposition temperature. The image obtained from the films deposited at 800, 850 and 875 $°C$ displays a uniform and continuous surface and they were rather flat. The sample deposited at 800 $°C$ showed small droplets at the surface, at 850 and 875 $°C$ these droplets disappear but the surface become more granular. At 900 $°C$ a drastic change can be seen in the surface morphology, the grain size has increased and the surface looks more porous. In comparison with the

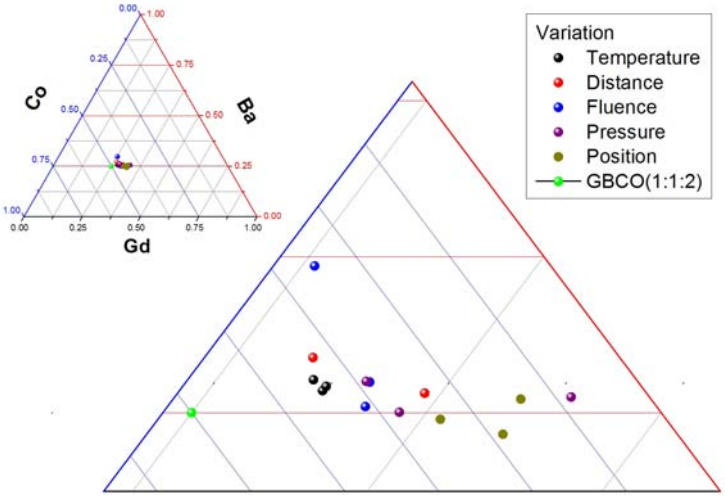

Figure 4.9: *Ternary phase diagram representation of the Gd:Ba:Co cation composition measured in the films by WDS. The image on the right is an enlargement of the region close to the $GdBaCo_2O_{5+\delta}$ (1:1:2) stoichiometric composition (green dot).*

XRD patterns and RSMs (Fig. 4.8), the formation of grains shown in Fig. 4.10(c) could be speculated to be a result of the c-axis orientation of GBCO films, a change in the possible thin-film growth mode or finally the formation of new phases in the layer.

The microstructure of these first set of GBCO films (Fig. 4.2) were studied by TEM/HR-TEM in collaboration with Dr. Monica Burriel and Dr. Montse Casas-Cabanas [115]. The experimental details and the setup used were introduced in 3.1.1.5. Microstructure observations by HRTEM of the GBCO films demonstrate the high quality epitaxial growth of the perovskite structure from the STO substrate interface to the film surface, as shown in Fig. 4.11 for a sample deposited at 900 $°C$, in which three different regions with their corresponding FFT (Fast Fourier Transform) are indicated. In region **I** a doubling of the primitive perovskite unit cell is detected from the appearance of brighter spots one cell out of two. The corresponding FFT confirms the doubling of the primitive cell, showing weak superstructure reflections between the main perovskite reflections. Region **II** corresponds to the boundary region between two 90°C oriented nanodomains (90°C rotated along parallel and perpendicular directions) in which the doubling of the primitive perovskite unit cell is maintained as observed in the corresponding FFT. These domains coexist with other perovskite domains with primitive cell (region **III**) whose Fourier transforms did not show the superstructure reflections. Cell parameters measured directly from the images, taking the STO substrate as a reference for calibration, correspond to 3.80 and 3.91 Å in the directions parallel and perpendicular to the doubling direction, respectively. In the region without double-perovskite superstructure, the cell parameters correspond to 3.94 and 3.91 Å. These values are fully consistent with those measured by XRD. Therefore, the direction of the observed superstructure, due to Ba and Gd ordering and possibly due to oxygen vacancy ordering as well, corresponds to the c-axis of GBCO $Pmmm$ structure.

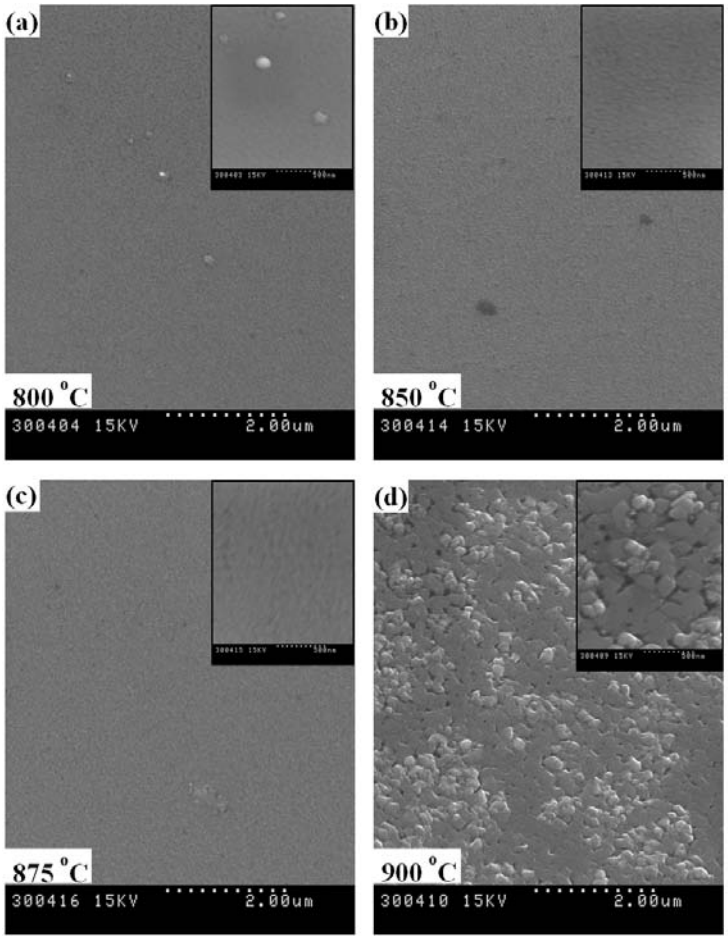

Figure 4.10: *SEM surface images of GBCO films grown on STO by 60 mTorr, 4000 laser pulses and fluence of* $\sim 2.9\ J/cm^2$ *with various deposition temperatures of* 800 °*C (a),* 850 °*C (b),* 875 °*C (c) and* 900 °*C.*

An enlargement of the **I** region is shown in Fig. 4.12, where the contrast in alternating horizontal lines of bright dots can be clearly seen. A good agreement is observed between the experimental and simulated image shown in the inset corresponding to the ideal GBCO structure. The line with brighter dots is consistent with the positions of Ba cations in the structure. Whether the observed double-perovskite superstructure in the HRTEM images is related only to the Gd/Ba ordering or also to an associated oxygen arrangement cannot be ascertained. However, the doubling of the cell along the b-axis associated with oxygen/vacancy ordering has not been observed in the electron diffraction patterns of the few areas where the b-direction was identified.

A general trend observed from HRTEM images taken for films deposited at different temperatures is that the first GBCO cells directly on the STO substrate always seem to grow preferentially $c_\perp$, *i.e.*, with the double-perovskite superstructure perpendicular to the STO surface. This behavior is to be expected, as the first unit cells will grow strained, with the in-plane cell parameter matching that of the substrate (3.905 Å), and therefore with

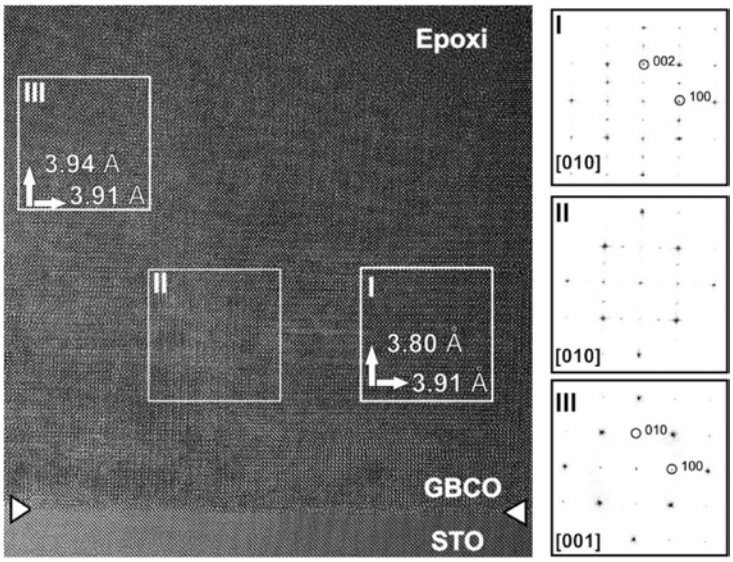

Figure 4.11: *HRTEM image of the film deposited at 900 °C with three different domains and their corresponding FFT.* ***I*** *and* ***III*** *regions correspond to different-orientations with c and b axes perpendicular to the substrate, respectively, whereas the* ***II*** *region corresponds to a 90° twin boundary between two* ***I*** *type regions. The STO/GBCO interface is indicated by white arrowheads. The values corresponding to the measured cell parameters of* ***I*** *and III regions are also indicated [115].*

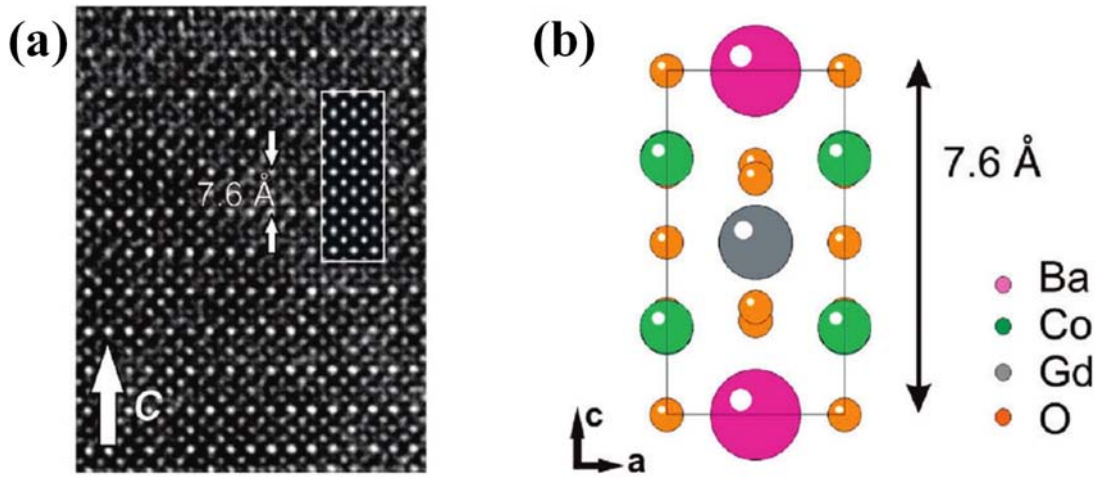

Figure 4.12: *(a) Enlarged image of the film deposited at 900 °C along the [010] direction. A calculated image corresponding to the ideal structure for a defocus value $\Delta f = -70.5$ nm and a thickness $t = 2.6$ nm is shown as an inset. (b) Schematic representation of the $GdBaCo_2O_{5+\delta}$ ideal structure [115].*

ordering and a correspondingly shorter cell parameter out-of-plane. But after about 20 nm, as a relaxation mechanism, the first defects appear in the structure. As a consequence the GBCO cells that grow on top are not restricted to the in-plane cell parameter of the substrate (3.905 Å), and a mixture of orientations can appear. Even though all the observed films present a mixture of different orientations, as previously shown in Fig. 4.11,

the predominant one depends on the deposition temperature, as shown in Fig. 4.13. At low temperatures (850 °), the GBCO film grows mainly $c_{\parallel}$, presenting bright and dark vertical lines, which correspond to rows of ordered Gd and Ba atoms (Fig. 4.13(a)). By contrast, at 900 $°C$ (Fig. 4.13(b)), the high temperature favors a $c_{\perp}$ growth, with alternating horizontal lines. These observations are in perfect agreement with the in- and out-of-plane cell parameters measured by XRD, and confirm the relationship between a small perovskite cell parameter (3.80-3.84 Å) and the existence of cation ordering in the structure along that direction.

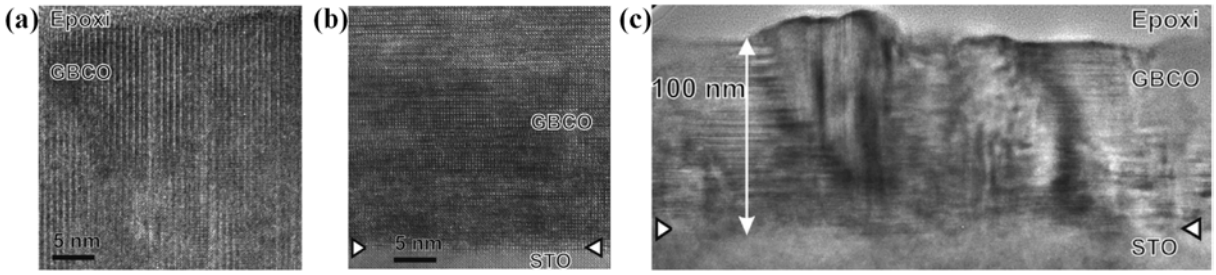

Figure 4.13: *HRTEM images of the films deposited at (a) 850 °C and (b) 900 °C. The images show that at lower temperature the GBCO film grows mainly $c_{\parallel}$, whereas the high temperature favors a $c_{\perp}$-oriented growth. (c) Low-magnification TEM image of the cross-section of the film deposited at 900 °C [115].*

A low-magnification TEM image of the film deposited at 900 $°C$ is shown in Fig. 4.13(c) in which different domains of the double perovskite with $c_{\perp}$-orientation and $c_{\parallel}$-orientation can be observed (although this film mainly exhibits $c_{\perp}$-orientation as determined by XRD). Additionally, in the $c_{\perp}$-orientation domain, the presence of a high density of horizontal lines that very likely correspond to planar defects can be seen. Similarly vertical lines are observed in the $c_{\parallel}$ domain. Domains with $c_{\perp}$ start to form directly from the substrate interface extending all across the film thickness, whereas $c_{\parallel}$ domains seem to nucleate after a film thickness of about 20 nm is reached and from these points progressively grow in the lateral direction often forming large triangular domains. To ascertain the nature of the observed planar defects also observed in Fig. 4.13 for both samples, we show in Fig. 4.14(a) a high-resolution HAADF-STEM image of the film deposited at 900 $°C$, which indicates that a $c_{\perp}$ domain grows directly from the substrate interface up to 10 nm thickness, above which the strain is relaxed and the crystal direction changes to $c_{\parallel}$. The c parameter for the double perovskite structure is 0.76 nm, which corresponds to the TEM result in Fig. 4.12. In Fig. 4.14(b,c), corresponding to the film deposited at 850 $°C$, regions which do not have an alternative Gd/Ba layer are observed with a pseudocubic structure (region B) and an epitaxial relation with the doubling structure (region A). Figure 4.14(c) shows a grain boundary between a nucleated domain and the rest of the film. In the nucleated domain (region C), another defect structure can be observed with a periodicity of about

2 nm along the c-axis. It contains two double brighter layers in one unit cell, which are indicated by two pairs of arrows. Because the STEM contrast is related to the atomic number of the element, these brighter layers are rich in heavy atoms, which could be Gd or Ba atoms. The c-axis of the domain is perpendicular to the c-axis of the neighboring double perovskite structure, which is at the $c_{\|}$-direction. The boundary between this domain and the rest of the film also crystallizes with an epitaxial relation. In another region, we also observed that the c-axis of this defect structure is parallel to the doubling structure, as will be shown later.

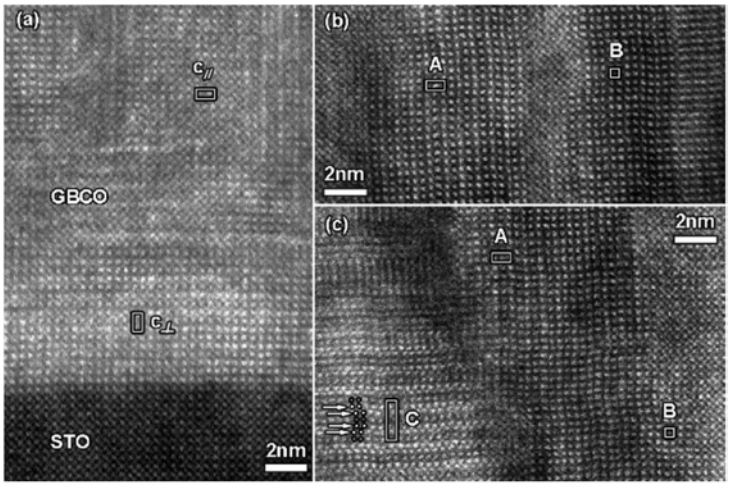

Figure 4.14: *High-resolution HAADF-STEM images of the film deposited at (a) 900 °C and of the film deposited at (b, c) 850 °C. (a) Crystal orientation change of 90° after around 10 nm growth from the substrate. (b) Epitaxial relation between the pseudocubic structure of the basic structure (region B) and the doubling structure with alternative Gd and Ba planes (region A). (c) New structure as a nucleate in region C. It has a periodicity of 2 nm along the c-direction and contains 2 double bright layers (heavy atoms) in a unit cell, which are indicated by two pairs of arrows. The heavy atoms are superimposed for clarity [115].*

To distinguish whether those defects correspond to Gd or Ba atoms, we performed 1D Scanning EELS in HAADF STEM mode at a similar area with an analytic probe. Figure 4.15(a) shows the STEM image and the region where the EELS spectra were acquired, which is indexedby a series of bright spots. The bright lines in this figure correspond to the heavy element rich double layers. Their periodicity is 1 nm at the left region which is the same as the planar periodicity of the defect structure in region C of Fig. 4.14(c). A 2 s acquisition time is applied to avoid beam damage and contamination. The fine structure of the $O-K$ edge, $Ba-M_{45}$ edge, $Co-L_{23}$ edge, and $Gd-M_{45}$ edge at the bright-layer region and at the dark-layer region are shown in panels b and c in Fig. 4.15. Note that $Co-L_{23}$ edge (779 and 794 eV) and $Ba-M_{45}$ edge (781 and 796 eV) completely overlap, which makes it impossible to quantify them separately. The relative intensity is scaled according to the $O-K$ edge. Their background is removed using a

power law fitting and the thickness changes are corrected by deconvolution with the low loss spectra acquired from the same position. The $O-K$ edge from the dark region is found to shift around 0.5 eV to higher energy loss as compared to the bright region. The $O-K$ edge from the dark region also has a slightly different fine structure than that of the bright region (indicated by a red arrow), which could indicate a slight change in the crystal field between the two structures. The atomic ratio of Gd/O, (Co+Ba)/O and Gd/(Co+Ba) is quantified by EELSMODEL [151] and the results are shown in Fig. 4.15(d) to allow direct comparison with the image position. At the bright-layer region, the Gd/O ratio is generally higher than in the dark-layer region, whereas the corresponding (Co+Ba)/O ratio is lower there. The Gd/(Co+Ba) ratio shows a consistent trend to the contrast of the STEM image. The Gd/O ratio arrives at its minimum of 0.16 at the large dark region and reaches its maximum of 0.31 at the left large bright region. This supports the assumption that the dark region consist of the doubling structure of GBCO, which has a Gd/O ratio of 0.18. It should be noted that the overlap of the Co and Ba peak makes the quantification difficult as well as the limited signal-to-noise ratio, but nevertheless the relative quantification gives reasonable values and the trend is clear.

This is independent proof of the heavy-atom enrichment as obtained from the HAADF STEM images with the added information that this must correspond to an enrichment with Gd (not Ba). This trend can also been seen visually from the EELS spectra c and d in Fig. 4.15, which are obtained by summing all spectra in the dark and bright layers separately. These spectra clearly show the enrichment of Gd and the depletion of Co and Ba in the bright layers.

Figure 4.16(a) shows a HRTEM image of a small area where these extra Gd-rich layers can be observed. The periodicity is exactly the same as in region C in Fig. 4.14(c). Combining all information from HRTEM, HAADF and EELS the local structure of these planar defects has been determined. The proposed structure consists of double GdO layers forming rocksalt-type blocks alternating with single BaO layers, both sandwiched between perovskitetype blocks, as in the Rudlesdden-Popper structure. Figure 4.16(b) shows the schematic crystal structure of the interface between the ideal GBCO structure and these planar defects. The image simulation corresponding to the planar defects (inset in Fig. 4.16(a)) shows a good fit with the experimental image, where the stacking defects are arranged in the vertical direction and are observed as double layers with a slight diffuse intensity along the planes. It should be pointed out that, although these are the defects most often encountered, other periodicities corresponding to different amounts of perovskite blocks alternated with single GdO layers have also been observed.

The new periodicity, corresponding to the $Gd_2BaCo_2O_7$ structure, has been measured in different regions, giving values from 19.5 to 20 Å, which is consistent with that observed

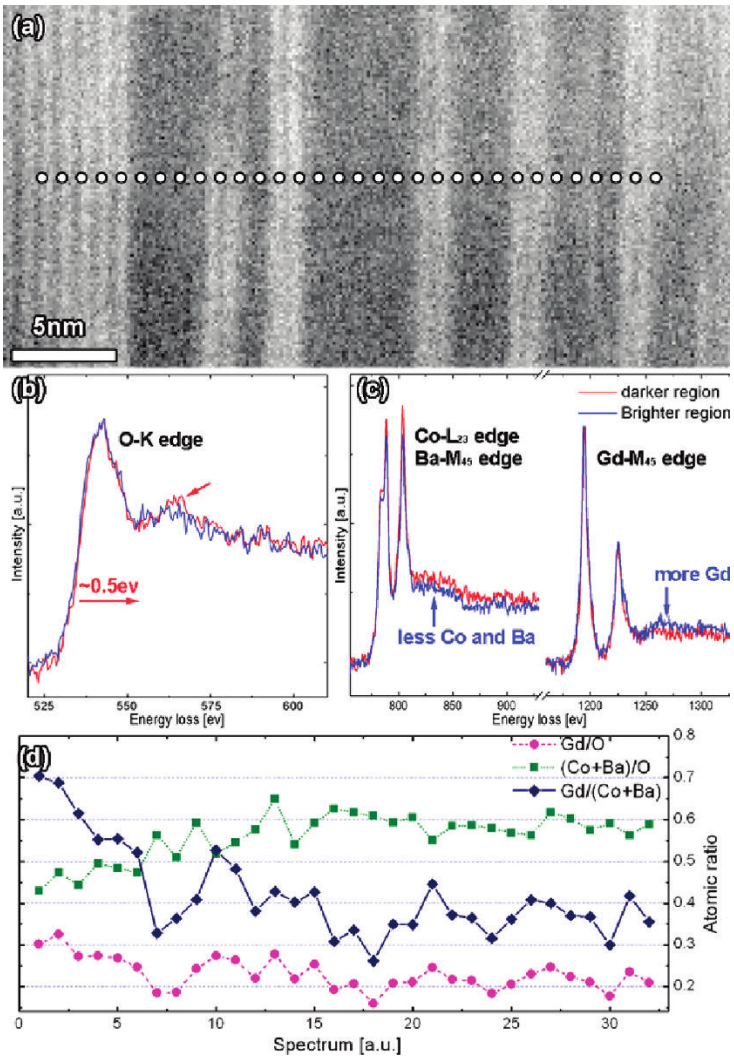

Figure 4.15: *STEM-EELS of a corresponding region of the defect region C in Fig. 4.14(c) of the film deposited at 850 °C. (a) HAADF STEM image to show the image contrast and the position where the EEL spectra were acquired. The periodicity of the bright layers at the left side is 1 nm which corresponds to the structure in region C of Fig. 4.14(c). (b, c) EELS spectra obtained by summing all spectra in the dark region (red) and bright region (blue) corresponding to image (a). All spectra are scaled to the area under the O K-edge. (d) EELS quantification shows that the bright layers are Gd-rich and Ba- and Co-poor [115].*

for A and B XRD reflections in Fig. 4.2. These highly defective regions correspond to a Gd:Ba:Co composition of 2:1:2 ([Gd]+[Ba])/[Co] = 1.5), which deviates from 1:1:2 ([Gd]+[Ba])/[Co] = 1) of the GBCO compound. The nominal Gd/O atomic ratio is 0.28, which is close to what was obtained by EELS in the bright region in Fig. 4.15(a).

As discussed at the end of the previous section 4.2, within the range in which the growth parameters of the films were varied, it was not possible to obtain films with an ratio stoichiometric "ideal" (Fig. 4.4 and Fig. 4.9). The nature of the ablation process from stoichiometric GBCO targets generates a deviation in the composition of the films

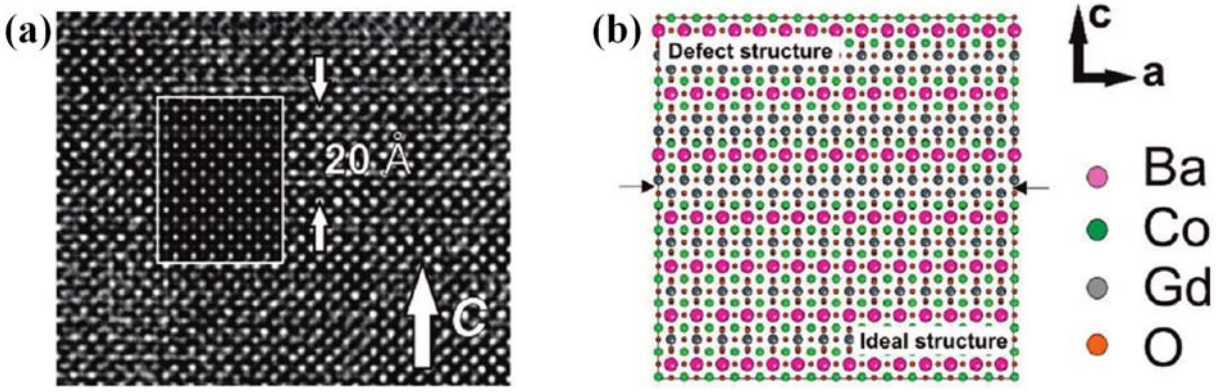

Figure 4.16: *(a) HRTEM image of the film deposited at 900 °C along [010] direction. A simulated image ($\Delta f = -66.0$ nm and a thickness $t = 2.0$ nm) of the defect structure is shown as an inset. (b) Schematic representation of the interface between $GdBaCo_2O_{5+\delta}$ ideal structure and the defect mode [115].*

which basically consists in a Co depletion, with ([Gd]+[Ba])/[Co] ratio from 1.13 to 1.40 which deviates from 1:1:2 ([Gd]+[Ba])/[Co] = 1. This composition deviation induces the appearance of characteristic stacking faults with supplementary GdO planes without affecting the overall epitaxial arrangement of the films. Despite the observed changes in the film orientation from $c_{\parallel}$ to $c_{\perp}$ upon deposition temperature increase, it will be shown in the next chapter that the film electronic conductivities seem to be mainly correlated with the cation composition. So, the larger the deviation from stoichiometric composition (Gd:Ba:Co = 1:1:2), the lower the conductivity. This effect has been mainly ascribed to the role of defects in impeding the achievement of a long-range order of the highly conducting *Pmmm* structure in the films.

4.4 Growth of GBCO Thin Films on STO and NGO substrates Using Co-Excess Target

In order to obtain stoichiometric films, it was necessary to prepare a target with Co-excess to compensate the deficits observed. The synthesis process used has been introduced in section 2.1.2 and the phases present in the pellet were studied using X-ray diffraction (Fig. 4.1(b)) and discussed earlier this chapter (section 4.1).

We prepared a new set of samples at different temperatures of deposition using the same deposition conditions as those used with the stoichiometric target and thus have a direct comparison (60 mTorr of P_{O_2}, laser fluence ~ 2.9 J/cm^2, target-substrate distance of 50mm and 4000 pulses of ablation at 10Hz). Figure 4.17(a) shows XRD patterns obtained. Peaks due to STO and GBCO perovskite and superstructure (corresponding to an orientation $c_{\perp}$) are clearly observed. The intensity of superstructure peak is much

higher than in samples grown with stoichiometric target at same deposition conditions. They are also much more symmetrical, narrow and defined and not exhibit the "shoulder" on the right side associated with defects planar (extra planes gadolinium oxide). The Fig. 4.17(b) show a comparison of two layers grown at 900 $°C$ with different target under identical deposition conditions. Very clearly, thin films grown with Co-excess target have a better crystal quality. However, all films show a family of planes (labeled with $\bigtriangledown$) for 42.98° ($d_1 = 2.11$Å) and 93.78° ($d_2 = 1.05$Å $\sim d_1/2$) 2θ angles. At the lowest temperature (800 $°C$), GBCO film shows extra peaks (marked with A) at 40.62° ($d_1 = 2.2$Å) and 87.84° ($d_2 = 1.11$Å $\sim d_1/2$) 2θ angles which could be related to (122) and (144) GBCO reflections. These peaks are quite common in perovskites because in this structure the families of planes (*111*) present intense reflections and is very usual that reduction in temperature generate growth with less epitaxy and promote the formation of such orientations. The weak peaks marked with $*$ are related to experimental artifacts since using other optics they disappear.

In Fig. 4.17(c) reciprocal space maps around the $\bar{3}03$ STO reflection are plotted. The maps shows that the Q_y component of GBCO films remains substantially unchanged ($\approx$ 0.612 *r.l.u*) with variations in the deposition temperature indicating a similar $c_\perp$ parameter for all them (corresponding to 3.78(1)Å). This in good agreement with the observed in the $\theta/2\theta$ scans. If we assume $a \times 2a \times 2a$ GBCO structure, the reflections observed in RSMs would be the combination of $(\bar{3}06)/(0\bar{6}6)$. The elongated shape of the peak in the horizontal direction (Q_x) can be attributed to the incipient a/b differentiation of the orthorhombic phase (or a distribution of the rotation of a/b plane relative to c-axis. In these cases we would see a structure centered on an average value with a very elongated distribution Q_x). This can be seen more clearly in the film deposited at 800 $°C$; the peaks labeled with A and B in the map have in-plane parameter values of 3.90(1)Å and 3.92(1)Å respectively. These values are slightly larger and shorter than the corresponding a $a = 3.862$Å and $b/2 = 3.934$Å, reported for the bulk phase [90] and are therefore assigned to these crystallographic directions indicating a certain degree of biaxial in-plane strain, tensile along the a-axis and compressive along the b-axis.

The average cationic composition measured by WDS microprobe analysis of the films deposited on STO (001) from the Co-enriched (5%) and stoichiometric target at various temperatures are shown in ternary phase diagram representation (Fig. 4.17(d)) and summarized in the Table 4.6. Clearly, the layers deposited using the Co-excess target correct the deficiencies observed in films deposited by PLD from stoichiometric 1:1:2 (([Gd] + [Ba])/[Co]=1) targets which was the most likely cause of induced the formation of a large density of planar defects.

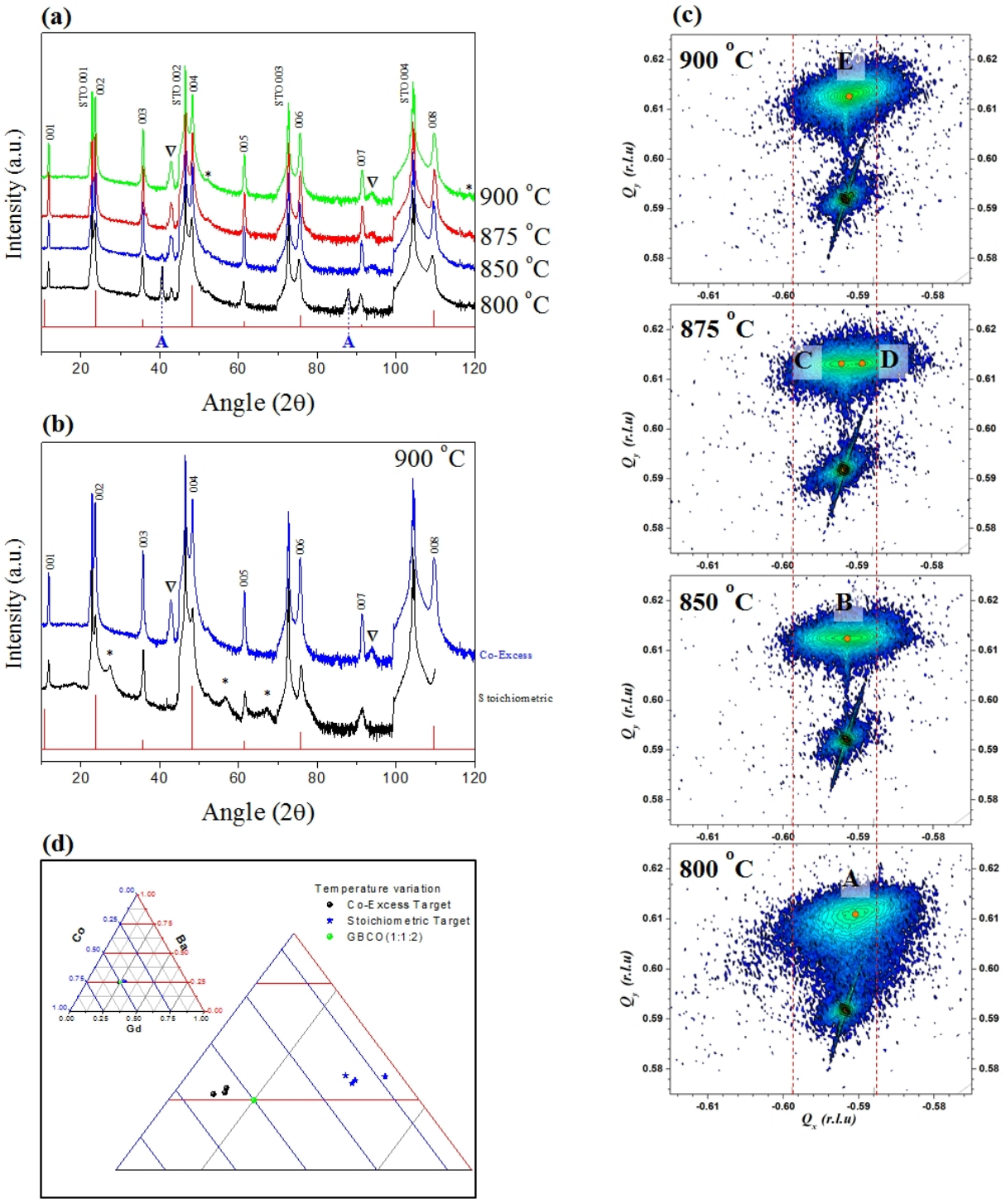

Figure 4.17: *(a) XRD patterns, (c)RSM and (d) WDS of GBCO films grown on STO (001) single crystal substrate at 60 mTorr, laser fluence of* $\sim 2.9\ J/cm^2$*, target-substrate distance of 50mm and 4000 laser pulses (10 Hz) with various deposition temperatures using Co-Excess Target. In (a), the STO substrate peaks (00l) are indicated, the c-axis oriented GBCO film peaks are indexed by (00l), and the extra peaks are designated by A and* $\bigtriangledown$*. (b) show a comparison of two layers deposited with different target at* $900\ ^{\circ}C$ *under identical conditions.*

Deposition Temperature [°C]	Thickness [nm]	$\frac{Gb+Ba}{Co}$	Peak	In-plane cell Parameter [Å]	Out-plane cell Parameter [Å]
800	-o-	-o-	A	3.92(1)	3.78(1)
850	184	0,97	B	3.91(1)	3.78(1)
875	226	0.98	C	3.91(1)	3.77(1)
			D	3.92(1)	3.77(1)
900	229	0.97	E	3.91(1)	3.78(1)

Table 4.6: *Out-of-plane and in-plane parameters extracted from the RSMs (Fig. 4.17(c)) for the films deposited at various STO substrate temperatures*

4.4.1 GBCO Thin Films Grown on NGO (110) substrates

The layered structure of the orthorhombic GBCO double perovskite compound, currently considered as a promising cathode material in SOFCs, is believed to induce a high degree of anisotropy in the oxygen diffusion coefficient, being maximum along the a–b plane in comparison to the diffusion along the c-axis direction [82, 90, 115]. The mechanism for the fast oxygen diffusion in this material is reported to involve mainly those oxygen vacancy sites arranged forming parallel channels along the a-axis, and is therefore expected to be highly anisotropic, as it has been inferred from molecular dynamics calculations [106]. In order to study this potential anisotropy, GBCO films were grown on $NdGaO_3$ (110) substrates which was selected due to their low lattice mismatch with the bc-plane in the GBCO (see section 2.1.3.1 and Table 2.3).

Figure 4.18(a) show typical X-ray diffraction patterns obtained for GBCO films grown at various deposition temperatures with a fixed oxygen partial pressure P_{O_2} of 60 mTorr, laser fluence $\sim 3\ J/cm^2$, target-substrate distance of 50mm and 4000 pulses of ablation at 10Hz (identical conditions to those used previously to obtain c-oriented films on STO (100) substrates). Normally, we use silver paint for fixing the substrate to the sample-holder. In this case, the substrate remained attached to sample-holder using a mechanical gripper system instead of silver paint, so the actual deposition temperature is slightly lower than the temperature recorded by sample-holder thermocouple (this was done in order to maintain the films clean of silver paint to be used in possible electrical measures). c-parameter in pseudo-cubic NGO has a value very close to a-parameter in GBCO (3.863 and 3.862 respectively), so we could have regions where the peaks corresponding to the film and substrate overlap in both $\theta/2\theta$ exploration and reciprocal space maps. In the patterns, a family of reflections labeled with $\bigtriangledown$ very close to 110 substrate peak is observed. It is difficult to associate this family of planes to GBCO a-parameter only from XRD information, but can be seen as increasing the temperature this family of planes tends to have a parameter closest to NGO substrate. The sample deposited at higher temperature

($900°C$) shows a series of weak reflections (labeled with $*$), using X'Pert HighScore we could speculate a possible presence of gadolinium oxide (Gd_2O_3, a precursor oxides used in the sintering of the target) or possible additional GBCO reflections.

Typical RSM diagrams in Q_x, Q_y coordinates of GBCO films are shown in Figure 4.18(b). In the maps, it is apparent that the $(33\bar{6})$ spot of the NGO substrate displays a sharp and intense peak with a unique component $k_{\alpha 1}$ due to the optics used, as expected in a low-defect single crystal (equivalent to the $\bar{3}03$ reflection for the primitive cubic cell). In films deposited at lower temperature (600 and $700°C$), a spot with Q_x component very close to the Q_x substrate component is observed (labeled with A and C respectively) with an in-plane parameter of 3.86(1) Å. If we consider only this reflection, we can say that the layer has a tetragonal structure and could be a-oriented (with b and c in almost perfect fit with the substrate), c-oriented (with the c parameter perfectly stressed - but this is less likely since superstructure peaks of Gd/Ba contrast planes are not observed in X-rays) or b-oriented planes (in this case the superstructure coming from ordering of oxygen vacancies might be too weak to be observable). As the deposition temperature increased, the intensity of this reflection decreases until practically disappear. At the same time, the presence of two distinct contributions at common Q_y becoming evident. This corresponds to an out-of-plane parameter of ~ 3.90 Å, close to the a-axis parameter of the bulk phase again. The coincidence of this value with that of the NGO substrate explains why the GBCO peaks are not observed in the standard patterns since they perfectly overlap with the NGO peaks. The corresponding in-plane parameter values for D,F,H and E,G,I is ~ 3.81 Å and ~ 3.92 Å respectively, these values being slightly longer (and shorter) than those corresponding to c/2 (and b/2) of the bulk GBCO phase. This indicates pure a-axis orientation perpendicular to the film for deposition temperatures of 800 and $900°C$, and the coexisting c- and b-axis parallel to the main in-plane [100]/[010] crystallographic orientations of the substrate primitive cell. As in the case of c-axis oriented films on STO, a-axis oriented flms on NGO show a certain degree of biaxial strain. The cell parameters obtained from the RSMs and composition ratio ([Gd]+[Ba])/[Co]) measured by WDS are summarized in the Table 4.7. The average cationic composition of the films deposited on NGO(110) from the Co-enriched (5%) target show a Co-deficient again (closer to samples grown on STO from stoichiometric target - red dot in Fig. 4.18(c)). This is difficult to understand, since it implies that the composition in the films depends on the type of substrate and the type of growth, and then the Co-deficit observed in films from the stoichiometric target was rather due to the substrate. Subsequent experiments indicate the possibility that different type of substrate cause a slight variation in the estimation of the composition by electron microprobe.

Obtaining a dense and continuous film is one of the main goals in order to study the

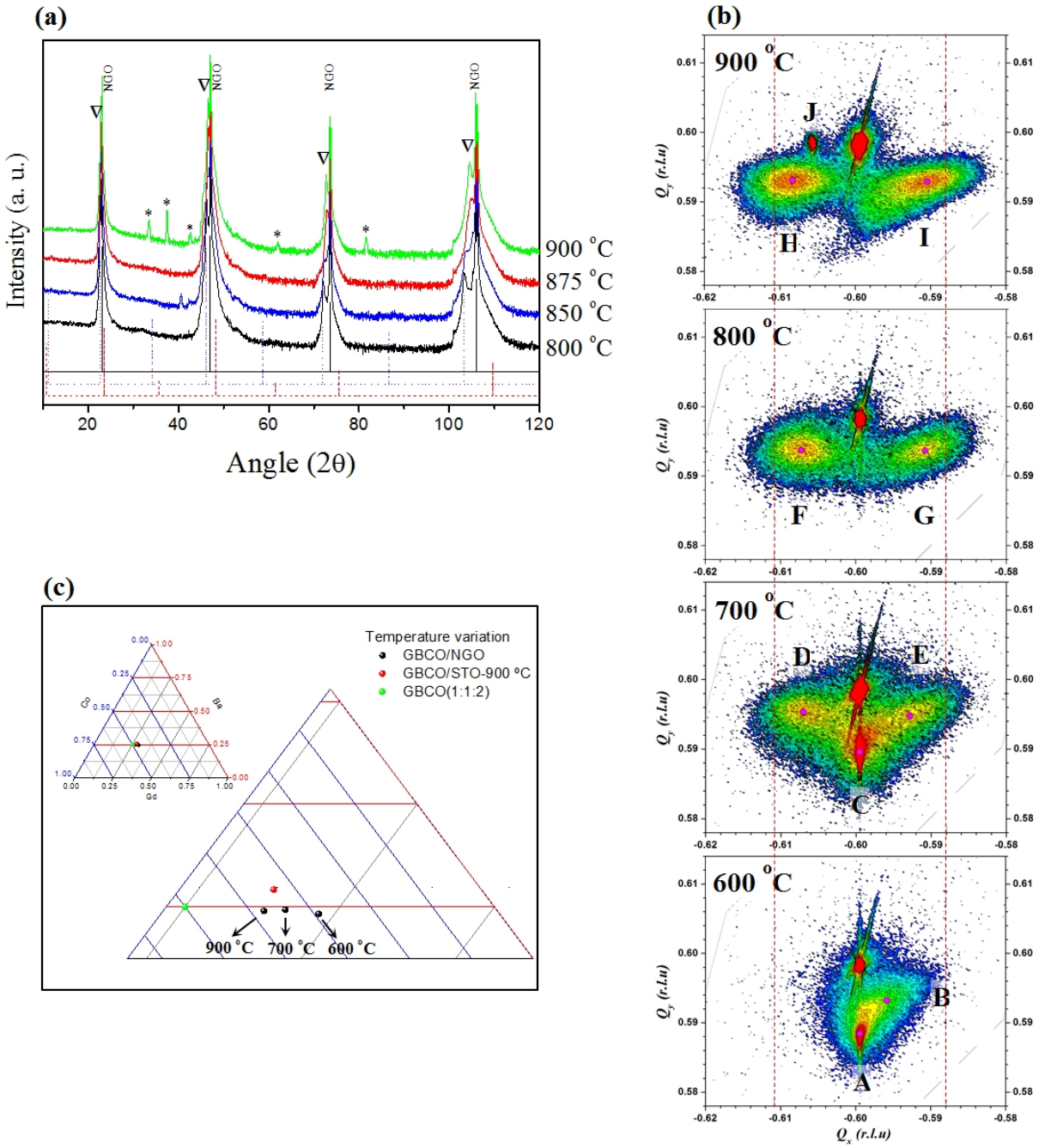

Figure 4.18: *(a) XRD patterns, (c)RSM and (d) WDS of GBCO films grown on NGO (110) single crystal substrate at 60 mTorr, laser fluence of* $\sim$ *2.9* J/cm^2*, target-substrate distance of 50mm and 4000 laser pulses (10 Hz) with various deposition temperatures using Co-Excess Target. In (a), the NGO substrate peaks (corresponding to 110 family) are indicated. The family of reflections labeled with* $\bigtriangledown$ *could be related with GBCO a-parameter. (b) show the evolution in temperature of GBCO around the* $(33\bar{6})$ *spot of NGO substrate. (c) show a Co-deficient similar to samples grown on STO from stoichiometric target*

GBCO anisotropy. To confirm the density of the obtained film, as an example, a FIB-SEM (Focused Ion Beam Scanning Electron Microscopes) image of the a-axis oriented GBCO

Deposition Temperature [°C]	Thickness [nm]	$\frac{Gb+Ba}{Co}$	Peak	In-plane cell Parameter [Å]	Out-plane cell Parameter [Å]
600	176	1.18	A	3.86(1)	3.93(1)
			B	3.88(2)	3.90(2)
700	204	1.14	C	3.86(1)	3.92(1)
			D	3.81(1)	3.88(1)
			E	3.90(1)	3.89(1)
800	∼ 200	- 0 -	F	3.81(1)	3.90(1)
			G	3.92(1)	3.90(1)
900	209	1.10	H	3.80(1)	3.90(1)
			I	3.92(1)	3.90(1)
			J	3.82(1)	3.86(1)

Table 4.7: *Out-of-plane and in-plane parameters extracted from the RSMs (Fig. 4.18(c)) for the films deposited at various NGO substrate temperatures*

film deposited on NGO (110) substrate at 900°C is shown in Fig. 4.19. A dense and continuous layer can be observed and small agglomerates of a few nanometers in size are distributed throughout the matrix. The transverse section of the ion beam indicates a high quality of the layer, confirming its homogeneity and with a thickness of around 165 nm.

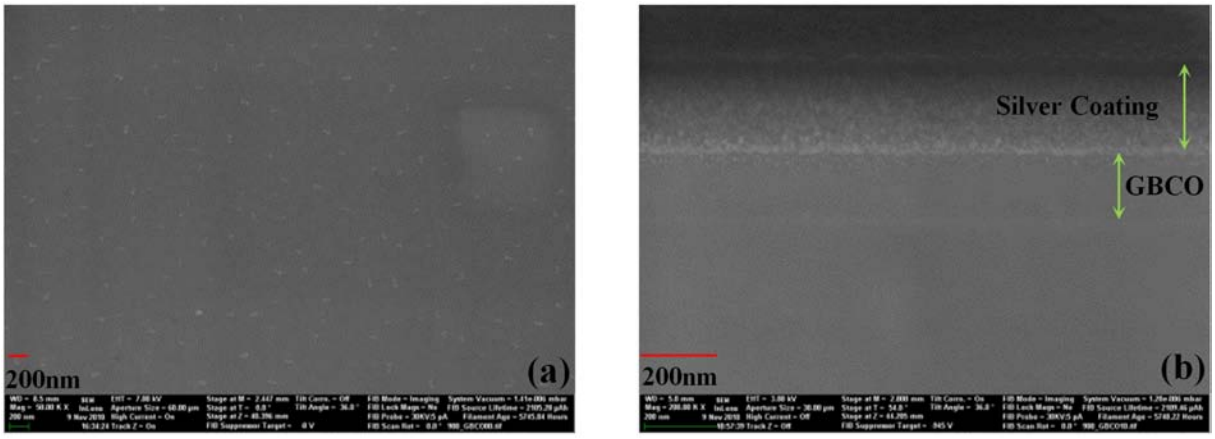

Figure 4.19: *(a) Top-view and (b) Cross-section FIB-SEM image of a-axis oriented GBCO film grown on NGO (110) substrate. Silver cap is for the protection of the film under focused ion beam (FIB) preparation process.*

4.5 Morphological and Microstuctural Characterization of GBCO Thin Films Grown on STO Using Co-Excess Target

In the section 4.2 the microstructure of layers prepared from a stoichiometric target was studied. It was found that epitaxial GBCO films mainly consist of single- and double-perovskite regions that are oriented in different directions depending on the deposition

temperature. Additionally, cobalt depletion induces the formation of a high density of stacking defects in the films, consisting of supplementary GdO planes along the c-axis of the material. Based on those initial results, we performed a systematic study of the effects of deposition conditions on the structure and orientation of GBCO thin films using a stoichiometric GBCO target in order to obtain layers with a cationic ratio closer to the ideal and prevent the formation of planar defects. The crystalline quality of the layers was significantly improved, but the results still showed unexpected values of composition ratio. It is this section, we analyze how the microstructure of the "best" layers obtained from stoichiometric target and the new layers gown from Co-excess target has improved the microstructure in order to understand the effects of planar defects on transport properties that will be described in the next chapter.

The Fig. 4.20 show the XRD and RSM of samples deposited at 850 and 900 $°C$ from stoichiometric and Co-excess targets. Both X-rays and RSM show the improvement in crystal quality and orientation of the layers obtained from the Co-excess target. More defined, intense and narrow GBCO peaks are observed in the scans and the maps show a film reflection of GBCO corresponding to an out-of-plane parameters of 3.79Å and 3.77Å at 850 y 900 $°C$ respectively and common in-plane parameter of 3.91Å. This indicates pure c-axis orientation perpendicular to the film. The sample grow at 850$°C$ from stoichiometric target show a combination of $c_{\perp}$ and $c_{\parallel}$ but an increment in the deposition temperature favors a c-axis out-of-plane growth as shown on X-rays and RSM of the layer deposited at 900 $°C$ (cell parameters of these two samples were reported in Table 4.5).

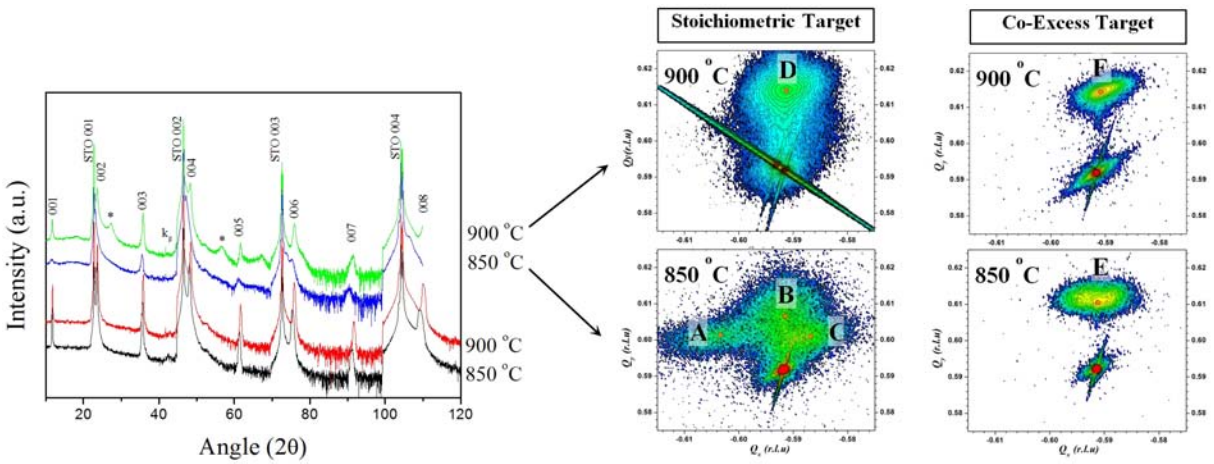

Figure 4.20: *XRD (a) and RSM (b) of samples grown from stoichiometric and Co-excess targets Top-view and at 850 and 900°C. Both X-rays and RSM show the improvement in crystal quality and orientation of the layers obtained from the Co-excess target.*

The microstructure of GBCO films were studied once again by cross-section Bright Field (BF) and high angle annular dark field (HAADF) scanning transmission electron microscopy

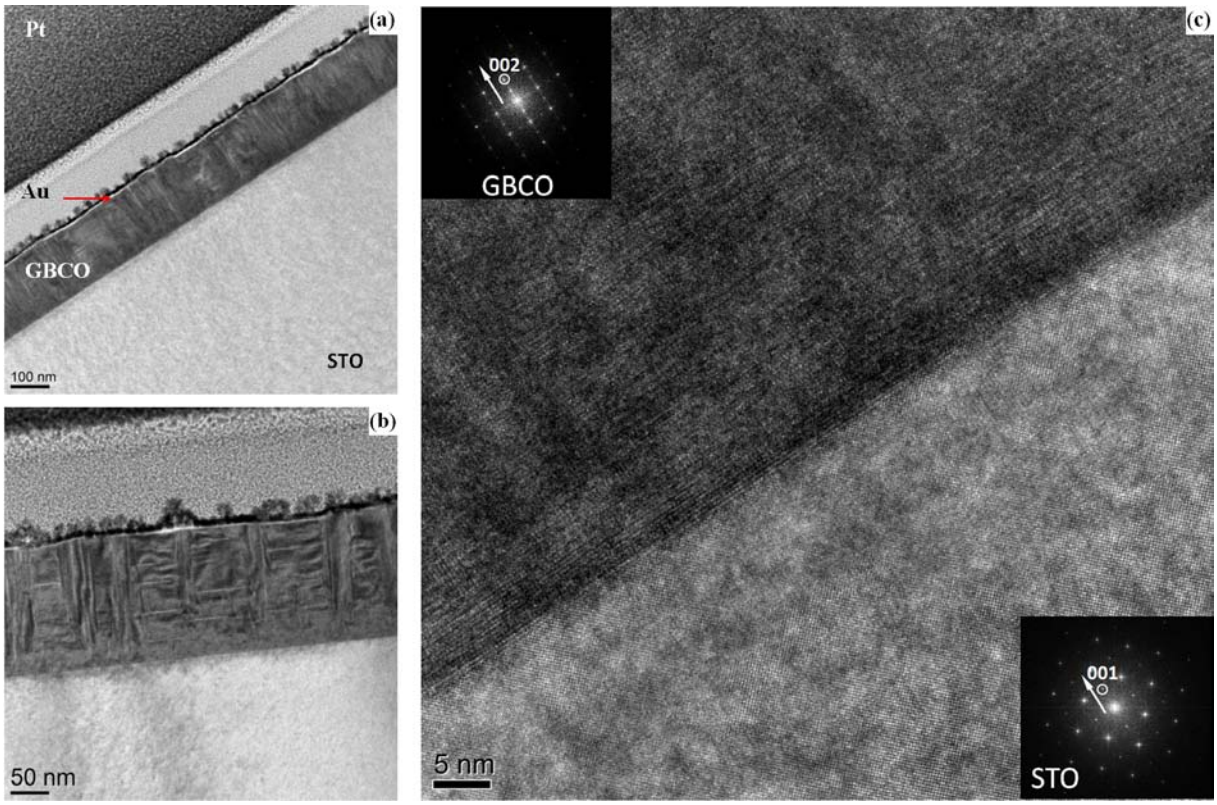

Figure 4.21: *Cross-section BF-STEM of GBCO film deposited on STO (100) at 850°C from stoichoimetric target, (a) show an overview of the exposed interfaces. In (b) can be observed light/dark contrast due to parallel and perpendicular stress along the film. (c) show the microstructure of STO and GBCO, the diffraction patterns inset in the image indicate defects in the GBCO structure. Images obtanied using Titan^3 microscope*

(STEM) images performed for high-resolution transmission electron microscopy (HR-TEM) analysis. Measurements were carried out in the Advanced Microscopy Laboratory (LMA) of Zaragoza in colaboration with Dr. Myriam Aguirre. The experimental details and the setup used were introduced in section 3.1.1.5. The samples were prepared by different methods, initially the traditional method based on focused ion beam (FIB) was used, but many amorphization problems occurred in layers due interaction with the gallium beam, so a thin layer of gold and resin was deposited in order to protect the layers. Even so, many problems due to amorphization continued to occur during sample preparation. In order to avoid this effect, some samples were initially prepared by manual polishing and finally by FIB. Unless otherwise indicated, all images were obtained with a zone axis [100]

The BF-STEM images (Fig. 4.21) shows the microstructure and planar defects observed in the GBCO film grown at 850°C from stoichiometric target obtained using a Titan^3 microscope. The overview show in Fig. 4.21(a,b) is composed of Pt, Pt-C, a small resin layer deposited by nanolithography and a thin layer of Au on top of the film. Thickness film is $\sim$ 160 nm (Consistent with the value reported by WDS microprobe in Table 4.5)

and the Au layer is between 10 and 15 nm. GBCO film presents a light/dark contrast due to parallel and perpendicular stress along the film. In Fig. 4.21(c), STO diffraction is clear without defects compared with GBCO pattern in which exhibits something of streaking and gives an idea of the failure or disorder in the stacks of planes.

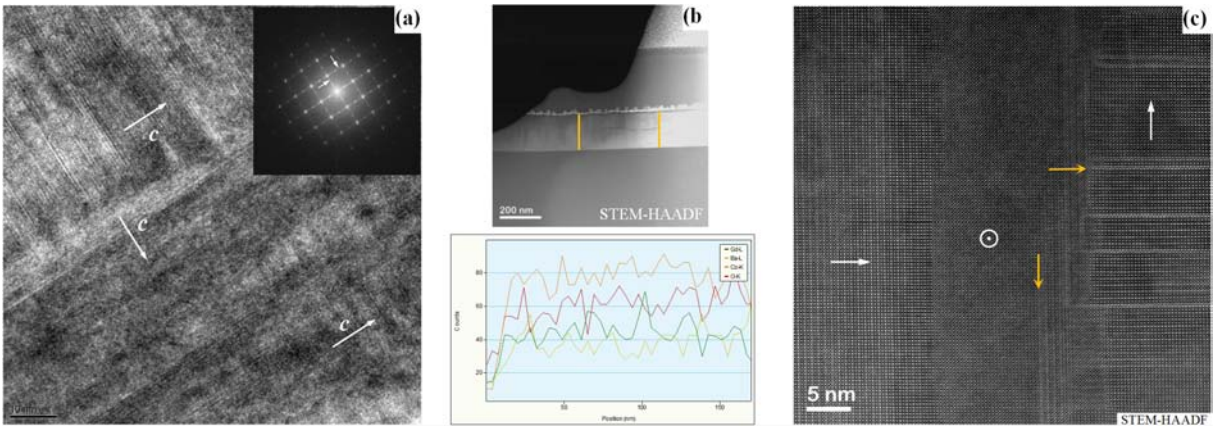

Figure 4.22: *BF-HAADF STEM images of GBCO film deposited on STO (100) at 850°C from stoichoimetric target. In (a) BF-STEM image show low magnification of domains with the c-axis oriented in different directions (indicated by white arrows). The stacking of planes is not regular, giving rise to "streaking" in the diffraction patterns (white arrows in the inset image). (b) STEM-HAADF images and EDX analysis in some regions of the layer give a cation ratio (Gd+Ba)/Co > 1 (obtained using Tecnai F30). (b) HAADF-STEM image shown a magnification of the central area of the layer with the different domains with the c-axis in the three spatial directions (obtained using Analytical Titan).*

In the image (Fig. 4.22(a)) the center of the GBCO film is shown. Twin domains are clearly observed in the image with the c-axis alternating in mutually perpendicular directions (indicated by white arrows). It is further noted that the stacking of planes is not regular, giving rise to "streaking" in the diffraction patterns observed (indicated with arrows in the inset image). The light/dark contrast and diffraction streaking observed are then due to domain boundaries where structures with an c-axis determined make the lace with the neighboring (especially at 90°) and to planar defects associated with RP planes. However, images near to STO/GBCO interface indicates that the first atomic layers grow ordered with c-axis out-of-plane, these results are consistent with those observed in less crystalline samples described in section 4.3. After a thinning of the sample, it was possible to obtain STEM-HAADF images and perform EDX analysis in some regions of the layer give a cation ratio (Gd+Ba)/Co > 1 (Fig. 4.22(b) using Tecnai F30), consistent with the results observed by WDS microprobe for this sample. The image (Fig. 4.22(c)) obtained using Analytical Titan show a magnification of the central area of the layer. It is clearly observed the different domains with the c-axis in the three spatial directions. The boundary domains often correspond to the formation "rock salt" between the rare earths (RE), these RP fail are detected by their lighter contrast (yellow arrow in the image).

Because of the lamella thickness and the detection limits of the microscope, it was not possible to determine whether the planar defects were formed by barium or gadolinium.

A first inspection of GBCO lamella obtained from the film grown at 900°C from stoichoimetric target show a thickness too thick to be analyzed by TEM, nevertheless, it allowed to observe stress contrast as in the previous sample (Fig. 4.23(a)). A second preparation of this sample allows see two regions with different contrasts (Fig. 4.23(b)); the upper zone, again due to limits attributable to "RP-faults" and the lower zone due to precipitates of cobalt oxides. However the c axis exhibits good uniformity along the layer (by Tecnai F30 - microscope without correction). In Fig. 4.23(c) both twin domains and transverse planar defects associated with RP are observed. In the case of twins domain, they have the c-axis rotated 90°. In the case of RP isolated (i.e. they do not form a precipitate, but rather isolated planes), these can be considered as stacking faults that has a visible characteristic diffraction pattern such as the "streaking" or white lines in the diffraction pattern in planes perpendicular to the fault direction (as shown in Fig. 4.24(a)). Cell parameters measured directly from the images correspond to ~ 3.87 and ~ 7.50 (2×3.75)Å in the directions parallel and perpendicular to the substrate respectively (by Titan^3). These values are shorter than those measured by RSM analysis and reported in Table 4.5.

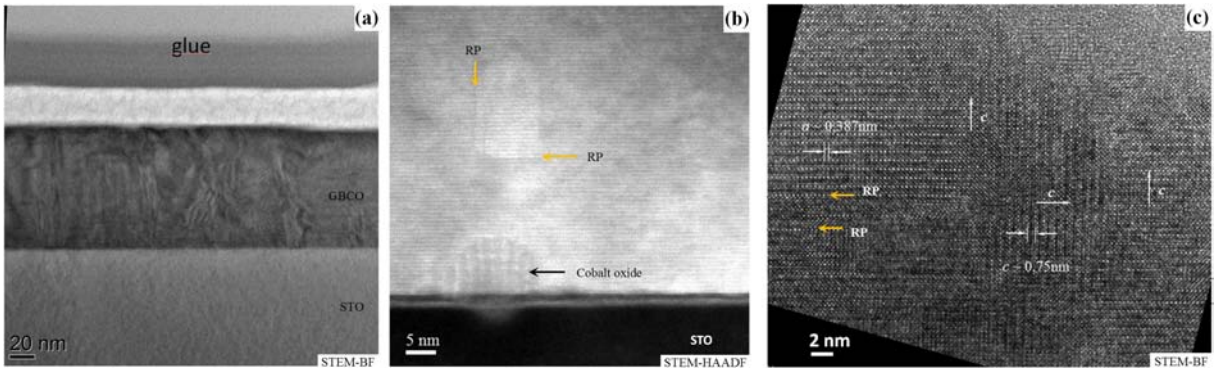

Figure 4.23: *BF-HAADF STEM images of GBCO film deposited on STO (100) at 900°C from stoichoimetric target. (a) show a STEM-BF image. In the zone corresponding to GBCO, contrast due to regions with diferents orientations, levels of stress and possible stacking faults are observed. (b) STEM-HAADF image show two regions, one with planar defects perpendicular to each other associated with RP (upper region) and the other with cobalt oxides precipitates (lower region)(by Tecnai F30 - microscope without correction). In (c), domains and transverse planar defects are observed. Cell parameters are measured directly from the images (STEM-BF obtained by Titan^3)*

The image (Fig. 4.24(a)) have two regions, in the right region can be intuited the order in the b-axis ($\sim 7.80 = 2 \times 3.90$ Å), but is quite complicated secure it because its value is too close to the c-axis value ~ 7.50Å. However, the diffraction pattern is different in the two zones and this is the reason to attribute the extra order in the b-axis

(image by Titan[3]). A thinning of the layer allows to observe parts of the sample with better detail. The observation of RP is very clear. Also, it is possible to detect the cobalt oxide precipitate (Co_2O_3)(see Fig. 4.24(b,c), images obtained using Analytical Titan with correction). Interpreting STEM-HAADF images is simpler than in STEM-BF images because in this case the contrast depends on the atomic number of the element that forms the compound. The ratio is approximately $I \sim Z^2$ being the heavier elements those appear lighter in the contrast micrograph. Then we can highlight several events in the Fig. 4.24(d). There is a clear difference between the GBCO and STO contrast. STO appears darker because the elements that comprise it are lighter. Ruddlesden Popper defects appear lighter because they are formed by rare earths and finally may be observed darker areas that can be attributed to the lack of Ba and Gd and/or a high concentration of Co.

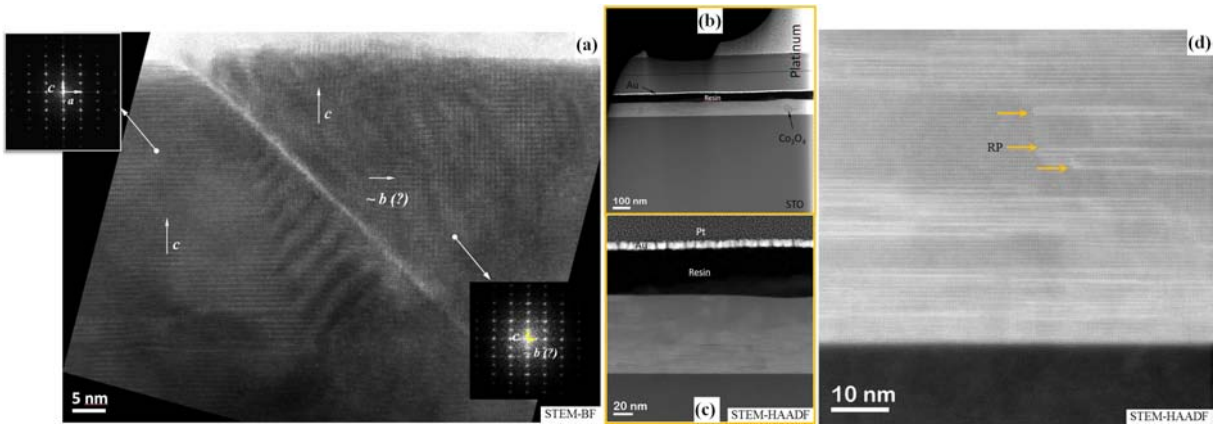

Figure 4.24: *(a). BF-STEM image show ordering in the b-axis, the diffraction pattern shows differences in the two zones with different ordering (image by Titan[3]). (b). HAADF-STEM micrograph showing an overview of the layer where a precipitate of Co_2O_3 is observed. (c). Magnification of the area shown in (a). (d). HAADF-STEM image showing evidence of planar defects formed normally by Gd-O extra layers (by Analytical Titan).*

RP defects are formed when a rock-salt layer (composed by RE-O) is introduced into the GBCO structure, in this case may be either Gd-O or Ba-O. If the introduction of this extra layer is periodic (for example every n perovskite layers) the RP structure is formed. Most defects present in these films are planar RP defects isolated, except for small areas, where maximum three or four layers are formed by Gd-O extra layers. According to the analysis of the intensities, the sample has a larger amount of RP defects formed by Gd-O extra, but also extra Ba-O planes are observed in smaller amounts. Regions with cobalt precipitates were rather isolated and not distributed through the entire layer. In contrast to the previous layer, as we move away from the STO interface, the sample becomes more homogeneous.

In the RP defects, the Gd-O extra layer is inserted into the GBCO structure by shifting half unit cell from the original as can be seen in detail in the STEM-HAADF image and

sketched in the inset (Fig. 4.25(a). The perovskite structure has a flexible crystallography therefore can tailor the RP defect coherently both horizontally and vertically, forming stairs defects (as shown in dotted line). This is because the axes a, b and c are semicoherent and/or multiples of each other. Moreover, flexibility in the oxygen position causes that the intergrowths of twins are feasible to find in this structure.

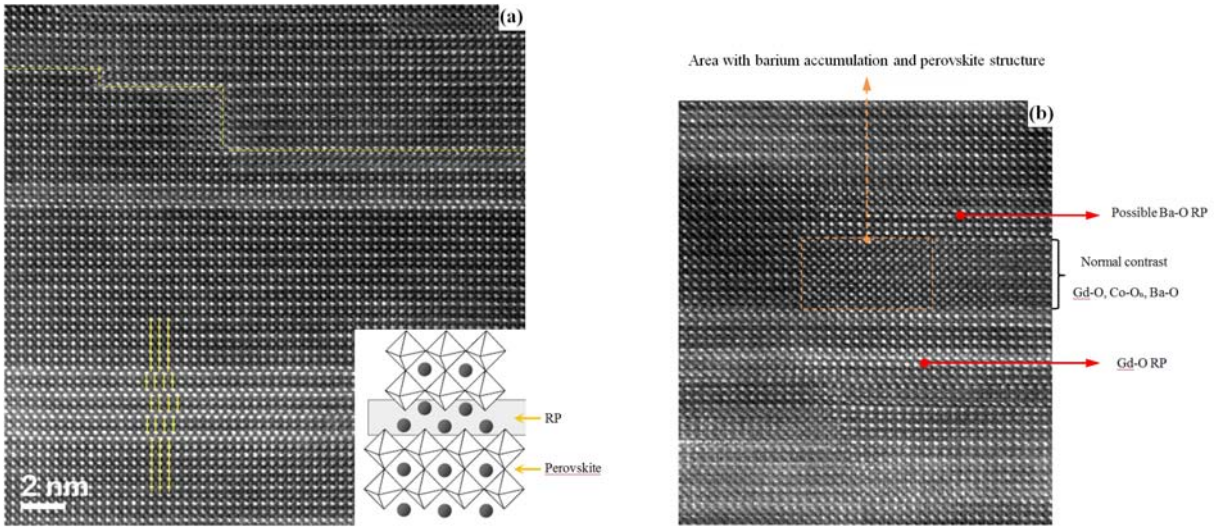

Figure 4.25: *(a). STEM-HAADF image shown the Gd-O extra layer inserted into the GBCO structure. (b). HAADF-STEM micrograph showing a magnification where differet RP defects corresponding to Gd-O and Ba-O are observed. (images by Analytical Titan)*

In a first preparation by FIB, the sample grown at 850 degrees from Co-excess target shows a coherent growth with the substrate and large domains but there was not enough transparency to carry out high resolution measures. We proceeded then to a new ion milling. Domains are watched much more defined in this case (see Fig. 4.26(a,b)), but there were many amorphization problems at domain boundaries because they are more vulnerable to the attack by argon ions. EDX measurements indicates a greater cobalt concentration near the GBCO-STO interface. As shown later, this is due to the formation of small precipitates of CoO. Quantitative analysis of the concentration profiles near the interface is complicated because the lines of Ba-L and Ti-K overlap (like the Ti-L and Ba-M). On the borders of domains where amorphization has not happened, very pronounced contrasts are observed (see Fig. 4.26(c)). This tension can be generated by a difference in the lattice parameters. One hypothesis for which these domains occur is by the appearance of alternating b- and c-axis in GBCO structure when it has the $GdBaCo_2O_{5,5}$ composition. But as these axes have values very similar to each other, it is quite difficult assert 100% ($b \sim 0.78$ nm, $c \sim 0.75$ nm).

The image (Fig. 4.27(a)) show a HAADF-STEM micrograph with a linescan crosses a precipitate rich in Co and with an accumulation of Gd (and Ba: lesser amount) in the

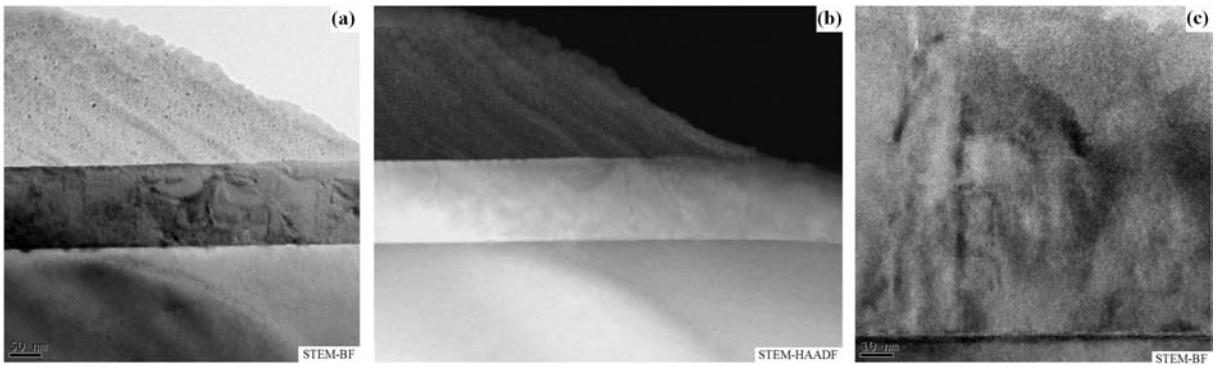

Figure 4.26: *BF-STEM (a) and HAADF (b) images of GBCO film deposited on STO (100) at 850°C from Co-excess target. (c) BF-STEM micrograph showing the borders of domains where amorphization has not happened, very pronounced contrasts are observed. (images by F30)*

grain boundary, having a microstructure type core-shell. The precipitate is located in the GBCO-STO interface. In the EDX integrated signal graph is observed as Ba-L line is added to Ti-K intensity. The layer thickness obtained by F30 microscope is ~ 130 nm.

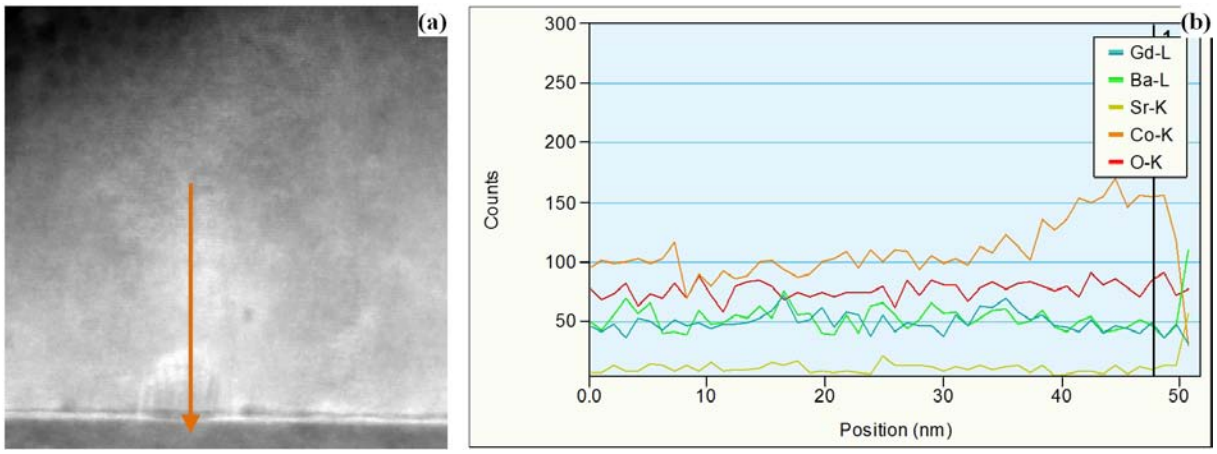

Figure 4.27: *HAADF-STEM images (a) and EDX analysis (c) of GBCO film deposited on STO (100) at 850°C from Co-excess target. The precipitate of Co has a core-shell structure with an accumulation of Gd in the grain boundary (images by F30)*

In the analysis by Titan Cube (TEM corrected objective lens) the boundary between two domains is observed (Fig. 4.28(a)). Although the two domains have the same orientation, with the c-axis perpendicular to the substrate, there is a jump discontinuity in the border. This creates disorder in the boundary zone which makes the ion beam preferentially attack there. The white dotted line indicates another domain boundary where apparently the atomic planes parallel to the substrate disappear. A FFT analysis tells us that the plans remain but with another spacing (2×3.90 Å) suggesting than in this apparently disordered area there is a mixture of b- and c-planes ($c \sim 7.50$ Å). This creates distortions in the lattice. The layer thickness by contrast using Titan cube is ~ 110 nm.

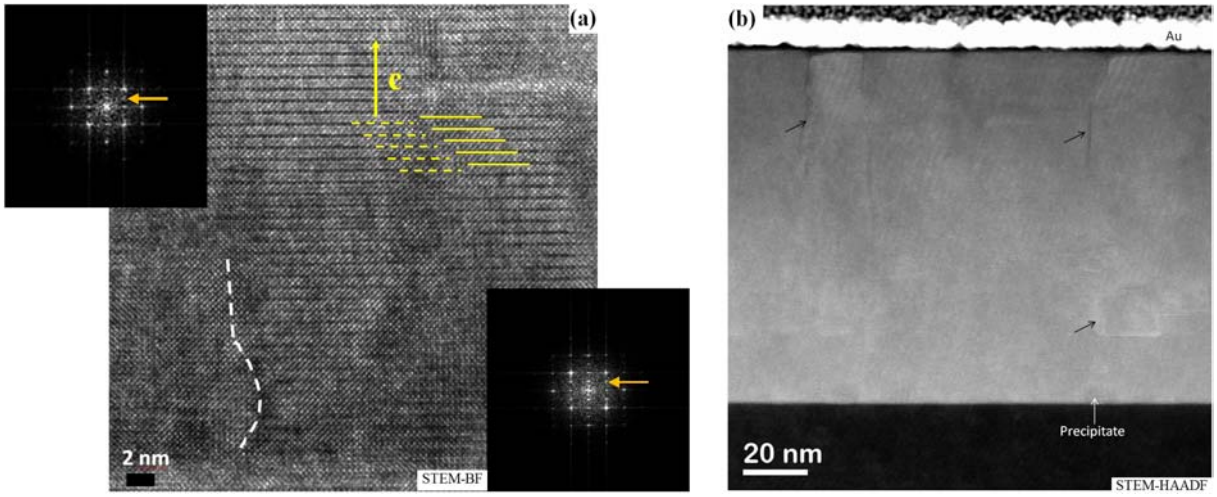

Figure 4.28: *GBCO film deposited on STO (100) at 850°C from Co-excess target. (a) show a BF-STEM image and FFT analysis in the boundary between two domains (image by Titan[3]). (b) show HAADF-STEM image with a sample general view. We can see the domain boundaries, a precipitate of Co and areas with defects between domaines (image by Titan Analytical)*

A more comprehensive analysis using analytical Titan allows us to study in more detail the domain boundaries. In the figure Fig. 4.28(b), the crystalline domains are observed with light contrasts on its border, which may be due to the concentration of heavy elements in this area as mentioned above. Also a precipitate of CoO is observed, but in general these precipitates are present in a low amount and the composition of the film is approximately constant along its thickness. The analysis of the dark regions shows a slight decrease in Ba and complementary increase in Gd. This can be explained again due to decoupling between the planes of Gd and Ba in the respective domains and the jump in the domain boundaries (Fig. 4.28(a)). These defects are used by cobalt and in these borders a higher concentration of this element appears. In Fig. 4.29(a) discontinuity in the Gd and Ba planes is seen more clearly and corroborated by EDX analysis. The composition of both atoms are complementary at both sides of the border and there is a slight difference in the composition of Co, which increases in the right domain. An analysis of STEM-HAADF intensities ($I \sim Z^2$) confirms what was found by EDX (Fig. 4.29(b)). On both sides of the defect, the Gd and Ba planes are alternated. While these domains have the same structure (with the c-axis perpendicular to STO), they have a displacement of half unit cell in the c-axis direction.

Anyway there are large regions of the sample where good crystallinity is observed. This can be seen in the Fig. 4.30, where an almost perfect interface is shown Fig. 4.30(a), a micrograph of central area free of defects (Fig. 4.30(b)) and the surface of the film with excellent finish (Fig. 4.30(c)).

The sample deposited on STO (100) at 900°C from Co-excess target has a higher

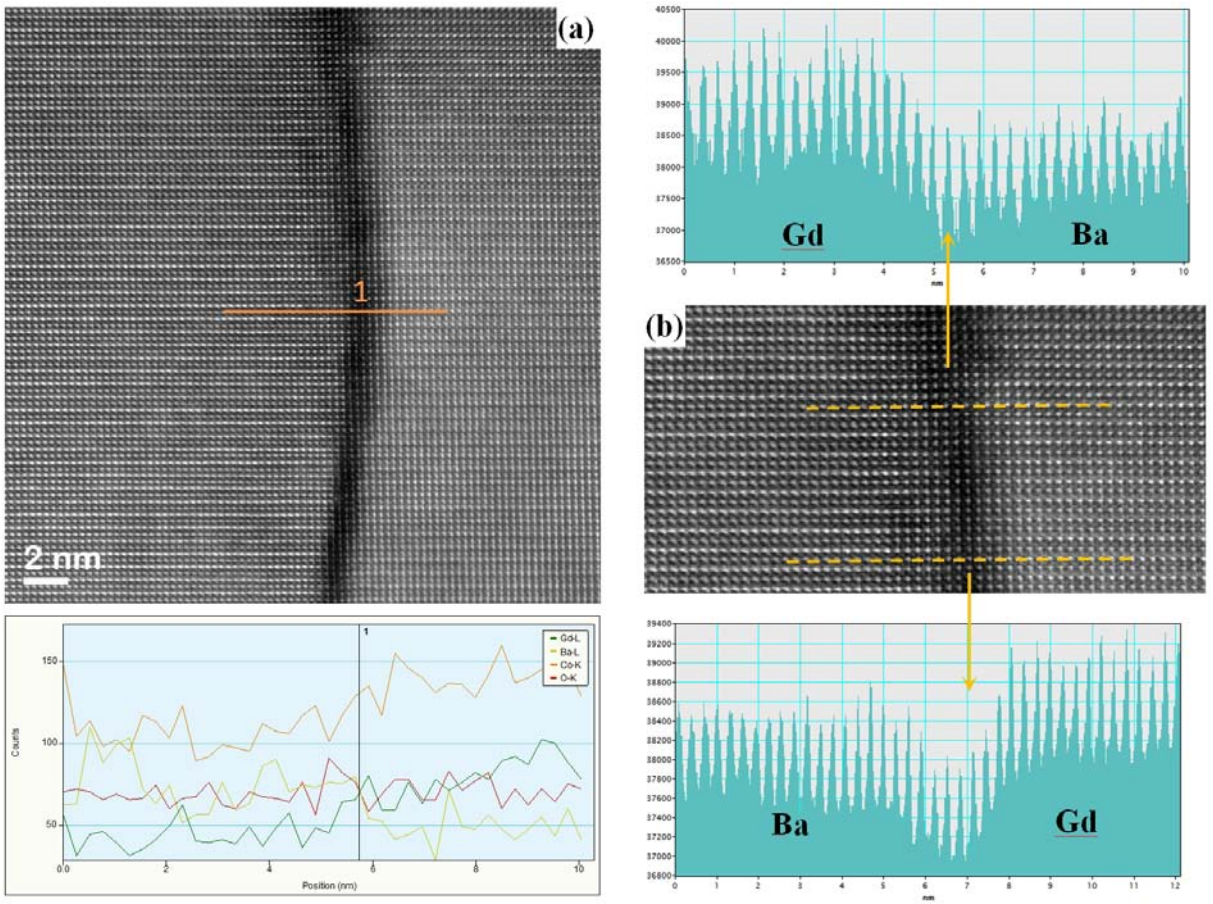

Figure 4.29: *HAADF-STEM images and EDX analysis (a), and analysis of STEM-HAADF intensities ($I \sim Z^2$) (b) of GBCO domains boundaries in film deposited on STO (100) at 850°C from Co-excess target. (images by Titan Analytical)*

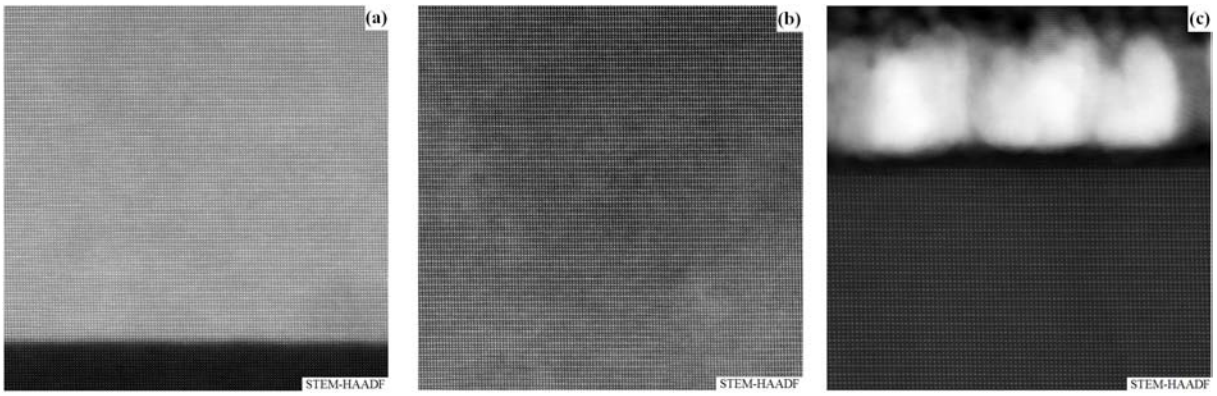

Figure 4.30: *HAADF-STEM images of GBCO-STO interface (a), central part (b) and surface (c) free of defect of GBCO film deposited on STO (100) at 850°C from Co-excess target. (images by analytical Titan)*

amount of precipitates and defects in the interface zone compared with the sample grown at 850°C. The layer has a thickness of about 130 nm and diffraction measurements show a quasi-epitaxy in zones free of defects with c-axis perpendicular to the substrate.

Crystallographic and compositional analysis by EDX indicated that the precipitates correspond to cobalt oxide. Precipitates diffraction calculated through FFT corresponds to a cubic lattice type Rock Salt of compound CoO with Fm-3m cubic structure and $a = 0.426$nm parameter (see Fig. 4.31(a)). Both reciprocal and real distances correspond to the structure of this oxide (Also Co_2O_3 structures (R-3c Trigonal) and Co_3O_4 (spinel Fd-3m, $a = 0.809$ nm) were tested but diffraction and interplanar distances do not match with the experimental results). The Fig. 4.31(b) shows the arrangement of atoms in an area without defects ([010] GBCO Zone axis).

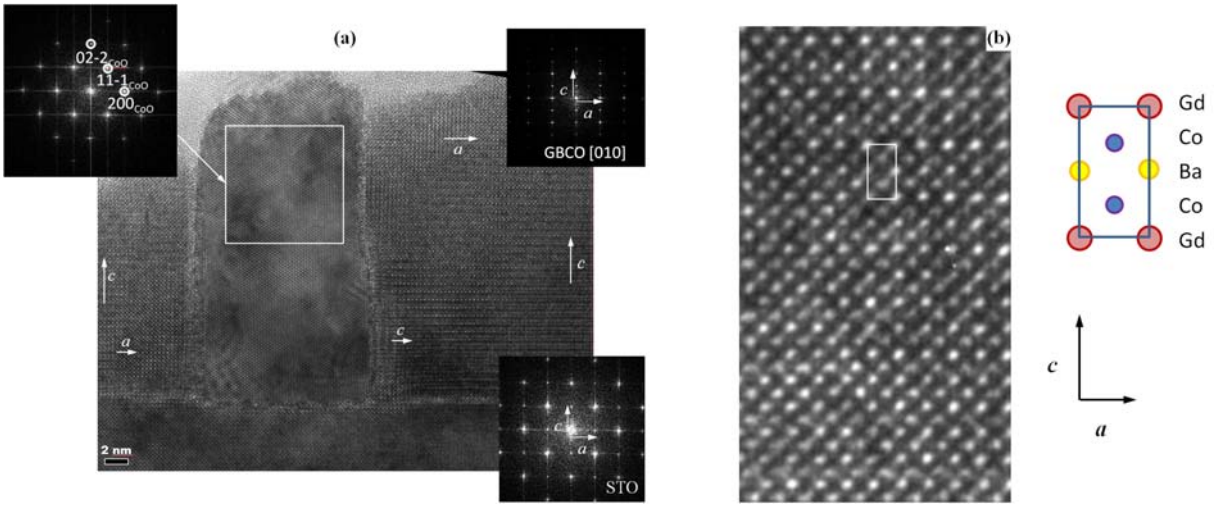

Figure 4.31: *BF-STEM images of GBCO-STO interface (a), precipitates diffraction calculated through FFT corresponds to a cubic lattice type Rock Salt of compound CoO with Fm-3m cubic structure and $a = 0.426$nm parameter. (b) shows the arrangement of atoms in an area without defects ([010] GBCO Zone axis)*

The Fig. 4.32(a) show a general overview and Co-O nanoparticle at GBCO/STO interface by STEM-HAADF. Comparison between Co-O nanoparticle and GBCO matrix composition is also shown (Fig. 4.32(b)). Out of the nanoparticle, the relation (Gd+Ba)/Co ~ 1 is preserved. There is a large increment of Co in the precipitate region, but it is still possible to detect Gd and Ba by EDX. This is because the precipitate observed is composed by an overlap of GBCO and CoO. This fact is also confirmed by the Moiré pattern in some BF-STEM images. This is the result of the sum of both structures, the CoO cubic rock salt and the GBCO Perovskite.

Around the precipitate the c-axis is alternated parallel and perpendicular to the substrate. It is interesting to note that first deposited layer seems to have the right composition (look the contrast below the precipitate in Fig. 4.33(a). As well, it is possible observe a defect close the interface with excess of Gd composition (see the rectangular region marked in orange). The parameters in-plane and out-of-plane are 0.39 nm and 0.75 nm respectively and in some regions is possible to see unit cells with b-axis parallel

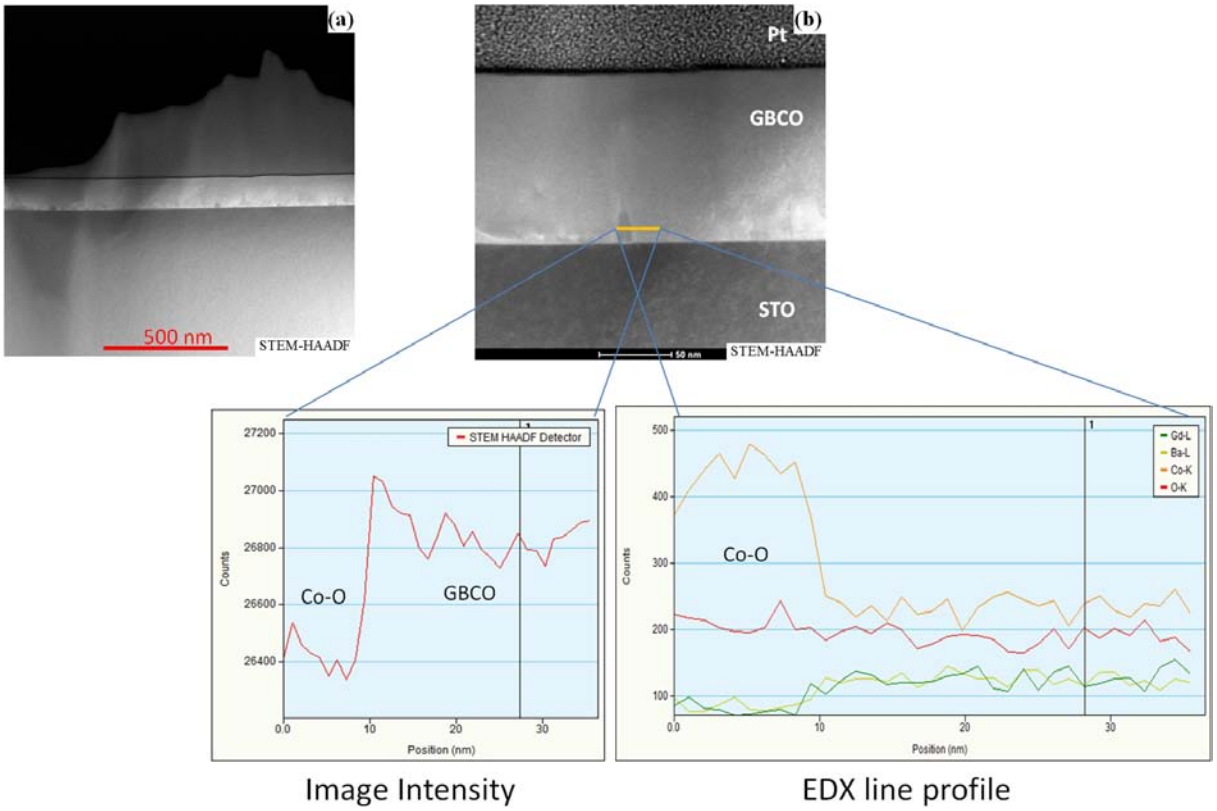

Figure 4.32: *General overview (a) and Co-O nanoparticle at interface GBCO/STO by STEM-HAADF (b). Out of the nanoparticle, the relation (Gd+Ba)/Co* ~ 1 *is preserved.*

to the substrate. Film near the surface region is quasi-perfect (Fig. 4.33(b)), the first layers most close to the Pt coating are amorphous due to the preparation . In the images contrast is possible to recognize Gd, Ba and Co.

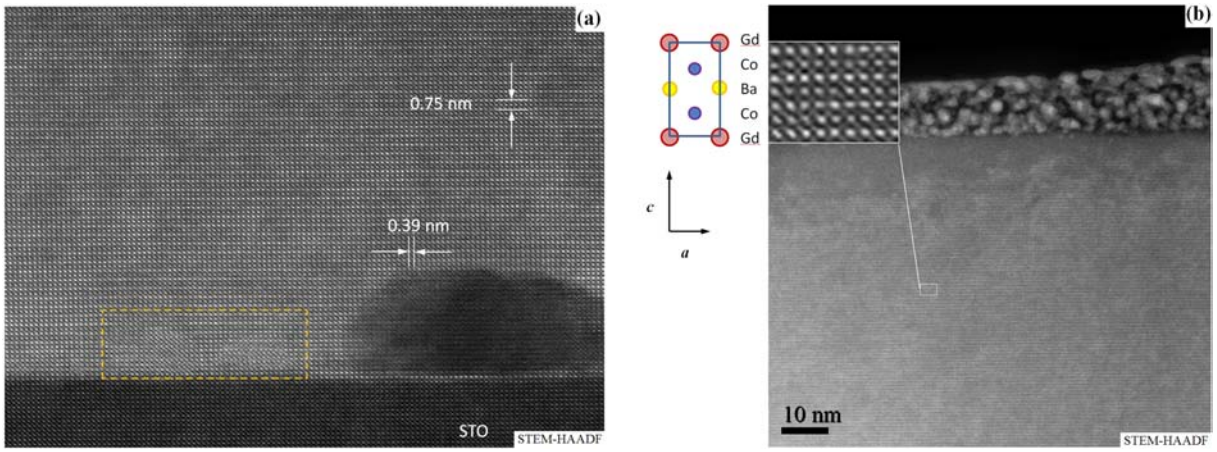

Figure 4.33: *HAADF-STEM images of GBCO-STO interface (a), aound the precipitate the c-axis is alternated parallel and perpendicular to the substrate. The parameters in-plane and out-of-plane are 0.39 nm and 0.75 nm respectively. (b) show the area near to surface, the first layers most close to the Pt coating are amorphous due to the preparation . In the images contrast is possible to recognize Gd, Ba and Co.*

We can conclude that the layers grown from the target with Co-excess have a much higher crystallographic quality and the planar defects are greatly reduced in comparison with the layers deposited from stoichiometric target. Despite this, the layers are not perfect and have precipitated CoO, perhaps due to doping of cobalt. The sample grown at $850°C$ is the one with more homogeneous regions, but in general all layers grow with a preferential orientation(with the c-axis perpendicular to the substrate). In contrast, films deposited using the stoichiometric target show a greater amount of structural defects near to surface, while the others layer have more defects close the interface zone.

4.6 Structural Evolution of GBCO Thin Films with Temperature

CHAPTER 5

Transport Properties and Oxygen Exchange in $GdBaCo_2O_{5+\delta}$ Thin Films

5.1 Conductivity Properties of GBCO Thin Films

In order to identify the role of defects in the charge transport mechanism of GBCO, conductivity measurements of nonstoichiometric films prepared under different deposition temperatures from 800 to 900°C were performed. Despite the fact that the films show changes in the film orientation in relation with the substrate temperature, as described in the previous paragraph, no clear correlation was established between orientation and film conductivity. Instead, a clear correlation against the ([Gd]+[Ba])/[Co] film composition was observed. A set of films with varying ([Gd]+[Ba])/[Co] composition ratio from 1.20 to 1.40 and the same film thickness of about 100 nm was chosen. In this set of films the [Gd]/[Ba] ratio remains almost constant at about 1.20, so the composition is explored along a straight line in the ternary Gd:Ba:Co phase diagram (as it is depicted on the right of Fig. 4.4).

Panels *(a)* and *(b)* in Fig. 5.1 show the in-plane conductivity dependencies versus the reciprocal temperature measured both at 1 atm pure O_2 and N_2, respectively, for the set of films with different compositions, along with that reported for bulk material [104]. Table 5.1 shows their measured activation energies in the range from 57 to 327°C. As a general trend all the films show a thermally activated increase in the conductivity up to about 300°C in O_2 and up to 400°C in N_2. At higher temperatures, the curves show a deviation from the linear dependence with a decrease of the conductivity associated with the loss of charge carriers, induced by the oxygen exchange with the atmosphere. This defines maximum conductivities at temperatures ranging from 330 to 550°C, depending on the composition ratio ([Gd]+[Ba])/[Co] from 1.20 to 1.45, respectively. The fact that this exchange starts at temperatures as low as 300°C (in O_2) demonstrates the enhanced oxygen surface exchange activity in this material.

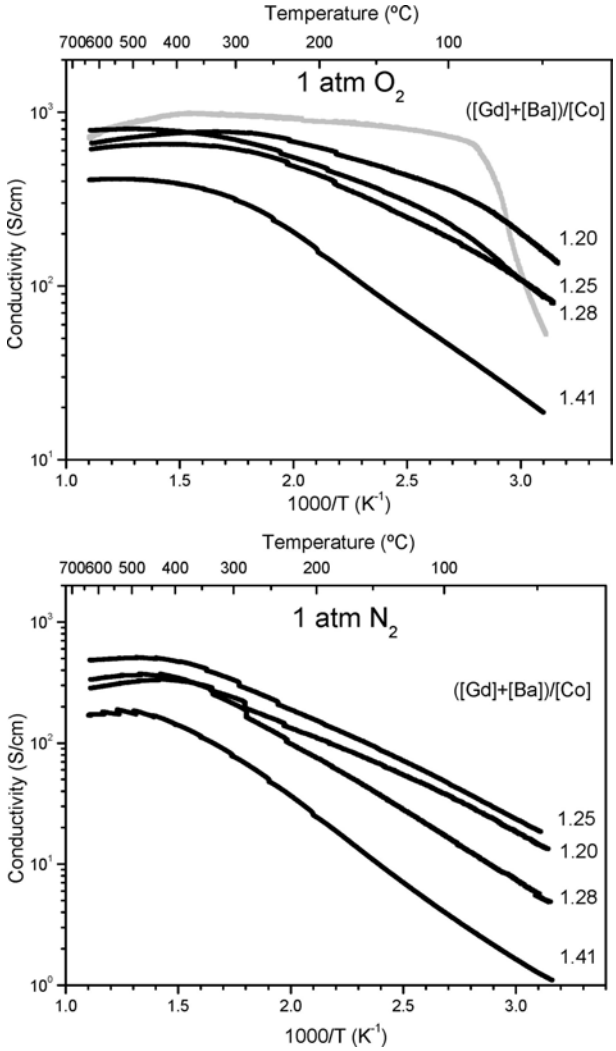

Figure 5.1: *Arrhenius plot of the GBCO film conductivities dependence with temperature for the same set of films in Fig. 4.4 with varying ([Gd]+[Ba])/[Co] composition ratio, measured under 1 atm O_2 (a) and 1 atm N_2 (b). The graph also includes reported conductivity values for bulk GBCO under O_2, from [104].*

The conductivities of the films seem to increase as their average ([Gd]+[Ba])/[Co] composition ratio gets closer to the stoichiometric value of 1, reaching a maximum value as high as 800 S/cm, somewhat below the value of about 1000 S/cm measured in bulk material under similar conditions. At the same time their activation energies increase from 0.09 to 0.18 eV for the films with ([Gd]+[Ba])/[Co] = 1.20-1.41. The same behavior is also evident in the conductivity measurements under a N_2 atmosphere with activation energies ranging from 0.19 to 0.25 eV. No evidence of the high temperature decrease in the conductivity associated with the transition from the orthorhombic to tetragonal phase, as reported for bulk material at about 400°C [104], was observed in our films. However, the films with a composition ratio close to stoichiometric (1.20 and 1.25) show a change in the slope at about 100°C under 1 atm O_2 atmosphere (in Fig. 5.1(a)), with higher activation

Sample composition $\frac{Gb+Ba}{Co}$	1 atm O_2^a	1 atm N_2^a
1.0 (bulk Sample) [92]	0.03 (0.83)^c	
1.20	0.09 (0.19)^c	0.19
1.25	0.10 (0.23)^c	0.17
1.28	0.12	0.23
1.41	0.19	0.25

Table 5.1: *Activation Energies (in eV) Measured in the Films with Different Cation Composition.* ^{a}*Temperature range from 57 to 277 °C.* ^{b}*Temperature range from 57 to 277 °C.* ^{c}*Two separated temperature ranges split at about 97 °C (lower temperature range between parentheses).*

energies of 0.19 and 0.23 eV, respectively. This is very similar to the behavior observed in bulk stoichiometric samples, which was associated with an orderdisorder transition and thought to be responsible for the high mixed ionic-electronic conductivities in the Pmmm GBCO phase [104]. However, in bulk ceramic samples, the transition seems to be more abrupt, and the difference between the activation energies at both regimes (of about 0.028 and 0.83 eV above and below the transition temperature, respectively) is more important than the one observed in the films. This is an indication that the deviation from composition, accompanied by the appearance of a higher amount of stacking defects, very likely impedes the stability of the "ordered" orthorhombic Pmmm GBCO phase, and therefore reduces the electronic conductivity. It is also very likely that the mixed orientation of the crystal domains in our films as observed by HRTEM, along with the influence of the strain induced by the epitaxial growth, might contribute to reduce the long-range ordering in the anion sublattice, thus broadening the transition temperature as well as showing intermediate values of the activation energies in comparison with those shown by bulk material.

As previously mentioned and as a general trend it seems that the cation composition, in particular the ([Gd]+ [Ba])/[Co] ratio, correlates with the observed film conductivities, as seen in Fig. 5.2, which shows the conductivities measured in 1 atm O_2 at a fixed temperature of 330°C (at this temperature there is a maximum in the sample with ([Gd]+[Ba])/[Co] = 1.20). The extrapolation of this dependence toward the stoichiometric composition, ([Gd]+[Ba])/[Co] = 1, might reach values greater than 1000 S/cm as observed in the bulk ceramic samples. It is therefore quite apparent that the presence of the observed stacking faults, associated with the ([Gd]+ [Ba])/[Co] composition ratio deviation, induce a large decrease in the conductivity of the material at a local scale. However, we cannot neglect the influence of the arrangement of those defects in the connectivity of the conduction path

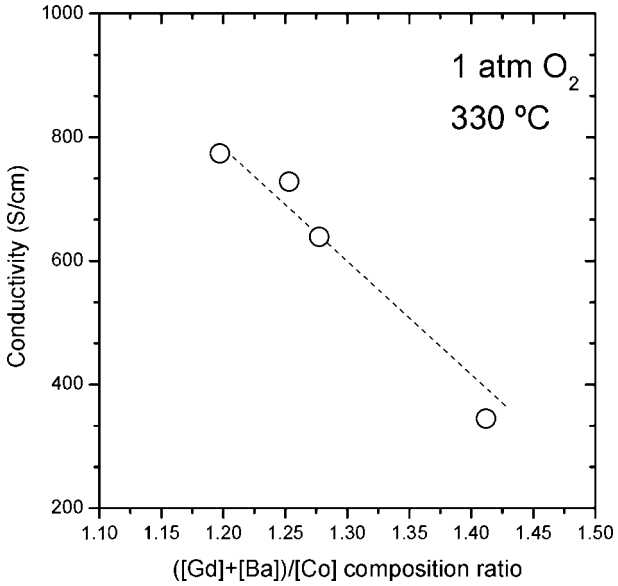

Figure 5.2: *Conductivity values measured under 1 atm O_2 at 330°C for the same set of films with different ([Gd]+[Ba])/[Co] composition ratio (see Fig. 4.4).*

in the volume of film, as well as other subtle microstructure aspects induced by deviations from the [Gd]/[Ba] composition ratio.

Fig. 5.3 shows the P_{O_2} dependence of GBCO conductivity (in a log-log plot) in one of the films with the highest conductivities (with composition ratio ([Gd]+[Ba])/[Co] = 1.25) measured at a constant temperature of 535°C. It shows a p-type power dependence associated with the electronic (hole) conductivity with exponent 0.038 (about 1/25). Measurements performed in other samples have given similar values, which are in perfect agreement with those previously reported for bulk ceramic samples7 and are related to the therein mentioned P_{O_2} dependence of the oxygen content with a power 0.075 (measured in single crystals at 550°C).5 The important deviation from the 1/4 classical power dependence as expected for a defect equilibrium established between a constant concentration of acceptor impurities and the oxygen vacancies in the system at high oxygen pressures is an indication of the complexity of the redox reactions in GBCO.

5.2 Anisotropic ^{18}O tracer diffusion in epitaxial films of $GdBaCo_2O_{5+\delta}$

Figure 5.4(a) and (b) show typical X-ray diffraction patterns obtained for GBCO films grown at a fixed oxygen partial pressure P_{O_2} of 60 mTorr and 850 °C on STO(100) and NGO(110) substrates, respectively. On STO the patterns show one set of 00l GBCO reflections with an out-of-plane parameter of about 3.775 Å, consistent with the c/2 value of the bulk GBCO material. The presence of intense reflections in the intermediate positions between the main substrate reflection (indexed as *l=odd*) is also characteristic

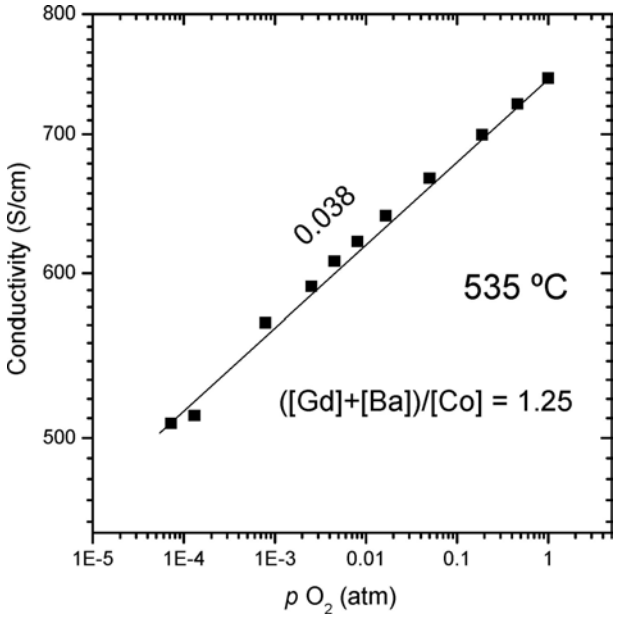

Figure 5.3: *P_{O_2} dependence of the conductivity of the film with ([Gd]+[Ba])/[Co] = 1.25 measured at constant $T = 535°C$, along with the exponent of the corresponding power law.*

of the GBCO double perovskite superstructure arising from the Gd/Ba sequential A-site arrangement in the [001] direction. No additional peaks corresponding to other phases or orientations appear under these deposition conditions. Therefore, the films on STO correspond to purely c-axis oriented GBCO. This texture was also confirmed by the reciprocal space maps around the $\bar{3}03$ STO reflection (Fig. 5.4(c)). The map shows a film reflection at *Qy = 0.6122 r.l.u.* (reciprocal lattice units) of GBCO, corresponding to an out-of-plane parameter c/2 = 3.77(1) Å, in good agreement with the value obtained from the $\theta/2\theta$ scans. The elongated shape of the peak in the horizontal direction defines two distinct maxima (labeled A and B in the map), which were attributed to the incipient a/b differentiation of the orthorhombic phase. Their corresponding in-plane parameter values are 3.89(1) Å for A and 3.92(1) Å for B. These values are slightly larger and shorter than the corresponding a = 3.862 Å and b/2 = 3.934 Å, respectively, reported for the bulk phase [90], and are therefore assigned to these crystallographic directions indicating a certain degree of biaxial in-plane strain, tensile along the a-axis and compressive along the b-axis.

Standard $\theta/2\theta$ XRD patterns of the films deposited on NGO (110), Fig. 5.4(b), do not show clearly differentiated film peaks, only a weak shoulder at the larger angle side of the 110 substrate peak (equivalent to 001 reflection for the primitive cubic cell) was observed.

Reciprocal space maps around the $33\bar{6}$ NGO reflection (equivalent to the $\bar{3}03$ reflection for the primitive cubic cell), shown in Fig. 5.4(d), evidence the presence of two clear contributions, labeled C and D, at common Qy position. This corresponds to an out-

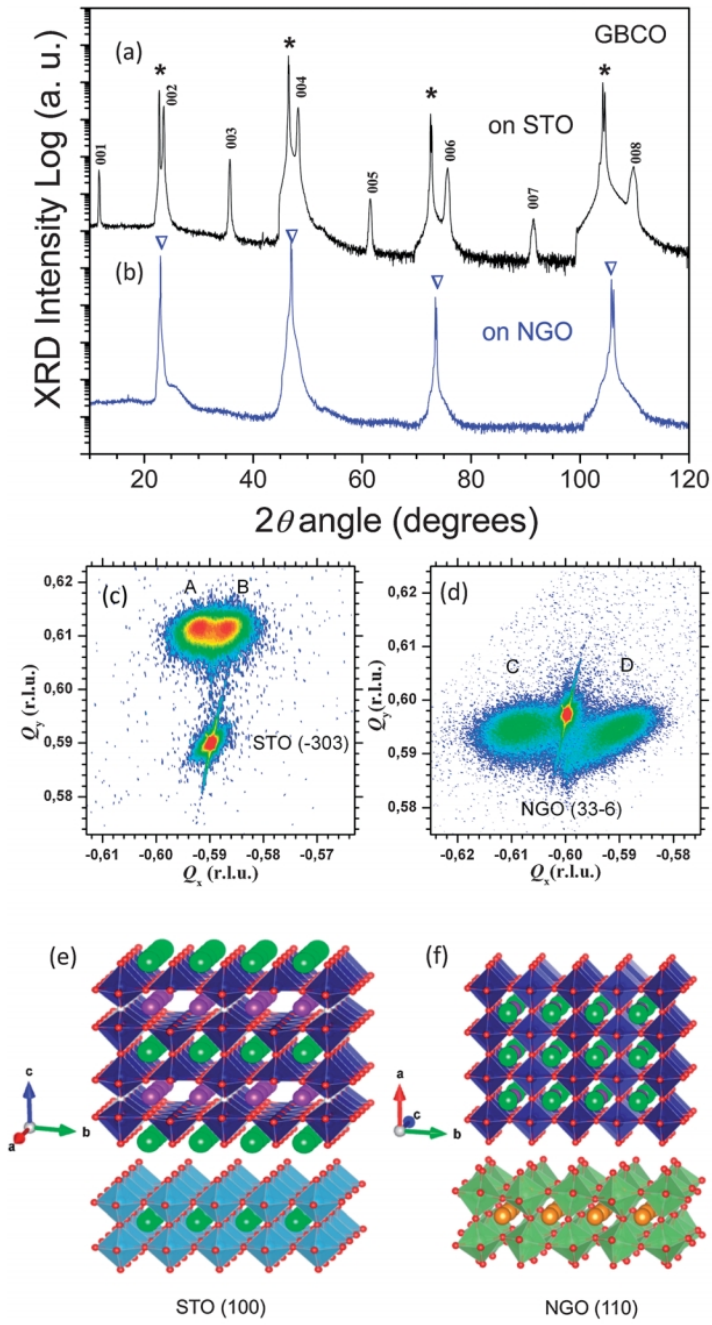

Figure 5.4: *XRD patterns of GBCO films deposited at 850 °C by PLD on STO (001) (a) and NGO (110) (b) substrates. Intense substrate peaks are labelled with asterisks (STO) and triangles (NGO). Reciprocal space maps of those films on STO (c) and NGO (d) in the area of the pseudocubic primitive* $\bar{3}03$ *reflection (*$33\bar{6}$ *for the NGO) reveal the orientation of GBCO film being c-axis oriented on STO and a-axis oriented on NGO. The schemes in (e) and (f) depict the corresponding epitaxial orientation between the film and the substrate on STO and NGO, respectively (models have been generated using Vesta software[178]. Coloured spheres in GBCO correspond to Gd, purple, and Ba, green, while Sr is green and Nd is golden in STO and NGO, respectively)*

of-plane parameter of 3.86(1) Å, very close to the a-axis parameter of the bulk phase. The coincidence of this value with that of the NGO substrate explains why the GBCO peaks are not observed in the standard patterns since they perfectly overlap with the NGO peaks. The corresponding in-plane parameter values for C and D are 3.815 Å and 3.925 Å, respectively, these values being slightly longer (and shorter) than those corresponding to c/2 (and b/2) of the bulk GBCO phase. This indicates pure a-axis orientation perpendicular to the film, and the coexisting c- and b-axis parallel to the main in-plane [100]/[010] crystallographic orientations of the substrate primitive cell. Figure 5.4(e) and (f) show the schemes of the relative orientations of film and STO and NGO substrates, respectively. As in the case of c-axis oriented films on STO, pure a-axis oriented films on NGO show a certain degree of biaxial strain. Table 5.2 collects the calculated mismatch between film and substrate cells for the different orientations as well as the measured cell parameters on both the STO and NGO substrates. Mismatch calculations involving orthorhombic structures may become confusing if one compares the linear differences between cell parameters for each crystallographic orientation (two cell parameters for each pseudocubic ⟨100⟩ orientation). Instead, a simpler approach consists of comparing the area mismatch between the corresponding rectangular sides of each primitive cell with the plane cut of the substrate. As an example, the mismatch for the GBCO a-axis oriented domains on NGO is calculated by comparing the areas of the rectangular plane cut of the substrate: $a' \times b' = 3.864 \times 3.855 = 14.896$ Å^2, and the rectangular plane formed by GBCO $b/2 \times c/2 = 3.934 \times 3.786 = 14.894$ Å^2. Their difference (Area$_{film}$ - Area$_{subs}$)/Area$_{subs}$ is -0.02% (slightly compressive), as depicted in Table 5.2 . This also helps to realize that even though the direct comparison of the separate cell parameters may induce a uniaxial strain of opposite sign along the two in-plane directions ($a' < c/2, b' > b/2$) the area mismatch is very small. Therefore it is not surprising that the corresponding GBCO out-of-plane value is not very different to the bulk value (less than +0.1% difference). By comparing the different film-substrate orientations the lower mismatch area was clearly obtained for c-axis orientation on STO and a-axis orientation on NGO, in good agreement with the experimental observation. Occasionally, in some of the films deposited on NGO substrates, a certain amount of c-axis oriented domains (very weak peaks) were observed depending on the deposition conditions. This indicates that growth of GBCO on this substrate is much more sensitive to subtle changes in the deposition parameters.

Despite some subtle differences in their strain, we may conclude that depending on the substrate type the films are purely c-axis and predominantly a-axis oriented on STO and NGO substrates, respectively. Since in the GBCO *Pmmm* structure the fast oxygen migration path would follow the crystallographic a-axis, it would be expected that

	STO Cubic [Å]	NGO Orthorhombic [Å]	NGO Pseudo-cubic [Å]	GBCO Orthorhombic[90] [Å]	PBCO Tetragonal[82] [Å]	NBCO Tetragonal[82] [Å]
a	3.905	5.463	3.863	3.862	3.9019	3.8969
b	3.905	5.563	3.863	2×(3.934)	3.9061	3.9015
c	3.905	7.708	3.854	2×(3.786)	7.6306	7.6115
STO				**ab: +0.37%** bc: +2.35% ac: +4.13%	ab: bc: ac:	ab: bc: ac:
NGO				ab: -1.99% **bc: -0.02%** ac: +1.85%	ab: bc: ac:	ab: bc: cd:

Table 5.2: *Cell parameters of STO, NGO, GBCO, PBCO and NBCO structures along with calculated mismatch for the different orientations*

depending on the film orientation the films may behave in a very distinct way. In films with c-axis orientation their corresponding crystallographic a-axis lays parallel to both the main in-plane directions, while in a-axis oriented films it is perpendicular to the film.

The average cationic composition measured by WDS microprobe analysis of the films deposited on STO (001) from the Co-enriched (5%) target corresponded to 0.96 : 1.02 : 2.02. This corrected the observed Co-deficient films observed in films deposited by PLD from stoichiometric 1 : 1 : 2 (([Gd]+[Ba])/[Co] = 1) targets which induced the formation of a large density of planar defects [115].

5.2.1 Oxygen surface exchange in transverse geometry

The oxygen transport along the transverse direction (perpendicular to the film plane) for the GBCO thin films was determined from the depth profiles obtained with the IEDP technique in combination with ToF-SIMS analysis. Figure 5.5(a) and (b) show the corresponding normalized ^{18}O isotopic oxygen fraction for the different exchange temperatures, on STO and NGO substrates, respectively. Figure 5.5(c) shows a scheme of the measuring geometry.

The calculation of the oxygen transport parameters is achieved by fitting the experimental data to the appropriate solution of the diffusion equation. We assume for this configuration the model of an infinite solid slab extending over the region of thickness $2l$ in which the initial isotope fraction is C_{bg} and the diffusion annealing takes place in a large volume of gas of constant isotope fraction C_g. The symmetrical solutions given by this plane sheet model (x being the distance from the film–substrate interface, and l being the film thickness) occupying the region $-l < x < l$, apply also to the sheet $0 < x < l$ when the face x = 0 is non-permeable. The solution to the diffusion equation given by

Crank [179] is as follows:

$$c_r(x,t) = \frac{C(x,t) - C_{bg}}{C_g - C_{bg}} = 1 - \sum_{n=1}^{\infty} \frac{2L\cos(\beta_n x/l)exp(-\beta_n^2 D*t/l^2)}{\cos\beta_n(\beta_n^2 + L^2 + L)} \quad (5.1)$$

where $C(x,t)$ is the ^{18}O isotope fraction obtained by SIMS, *i.e.* $^{18}O/(^{18}O + {}^{16}O)$, t is the time of the isotope exchange, D^* is the oxygen tracer diffusion coefficient, k^* is the surface tracer exchange coefficient and $\beta_n(n = 1, 2, .)$ are the nonnegative roots of $\beta\tan\beta = L$, and $L = lk*/D*$. The limitations of the technique are examined in detail elsewhere [107, 180–182].

The profiles are almost flat across the film thickness down to the interface with the substrate. This indicates that oxygen diffusion is too fast to be measurable for the current film thickness under the exchange conditions (T and t), so the rate limiting step in this geometry is the oxygen surface exchange. No information about diffusion was extracted for this geometry and thus only tracer exchange rates k^* were obtained. Figure 5.6 depicts an Arrhenius plot of the corresponding k^* values, obtained for the best fit of the experimental data to the diffusion equation solution, Eq. 5.1, along with those values reported in the literature at similar T. For the low temperature region, the oxygen surface exchange rates for both film orientations are about half an order of magnitude larger than those reported for the bulk material, with similar activation energies, while the bulk and thin film values are comparable at the high temperatures. The larger surface activities at low temperatures could be due to the textured films the surface of which predominantly expose particular crystallographic planes, (001) or (100) for pure c- or a-axes oriented films, respectively. This indicates greater potential for thin films with controlled surface orientation as cathodes for SOFC application at intermediate operation temperatures. The comparison between the films indicates that regardless their texture, films with c- or a-axes orientation show comparable surface activity for oxygen exchange. Either there are little differences in the surface chemical termination, or the possible differences in the surface termination plane (presumably of pure AO or $A'O$ planes for pure c-axis oriented films or mixed $AO/A'O$ in the case of pure a-axis oriented films) do not play an important role in oxygen exchange. However, the slight reduction observed at higher temperatures might be due to a surface atomic rearrangement induced by the long annealing times in a pure O_2 atmosphere needed for the annealing step prior to the ^{18}O exchange, which might cause surface segregation, as observed in Sr-substituted $LaCoO_3$ [183] as well as in $La_{0.8}Sr_{0.2}MnO_3$ perovskite [184].

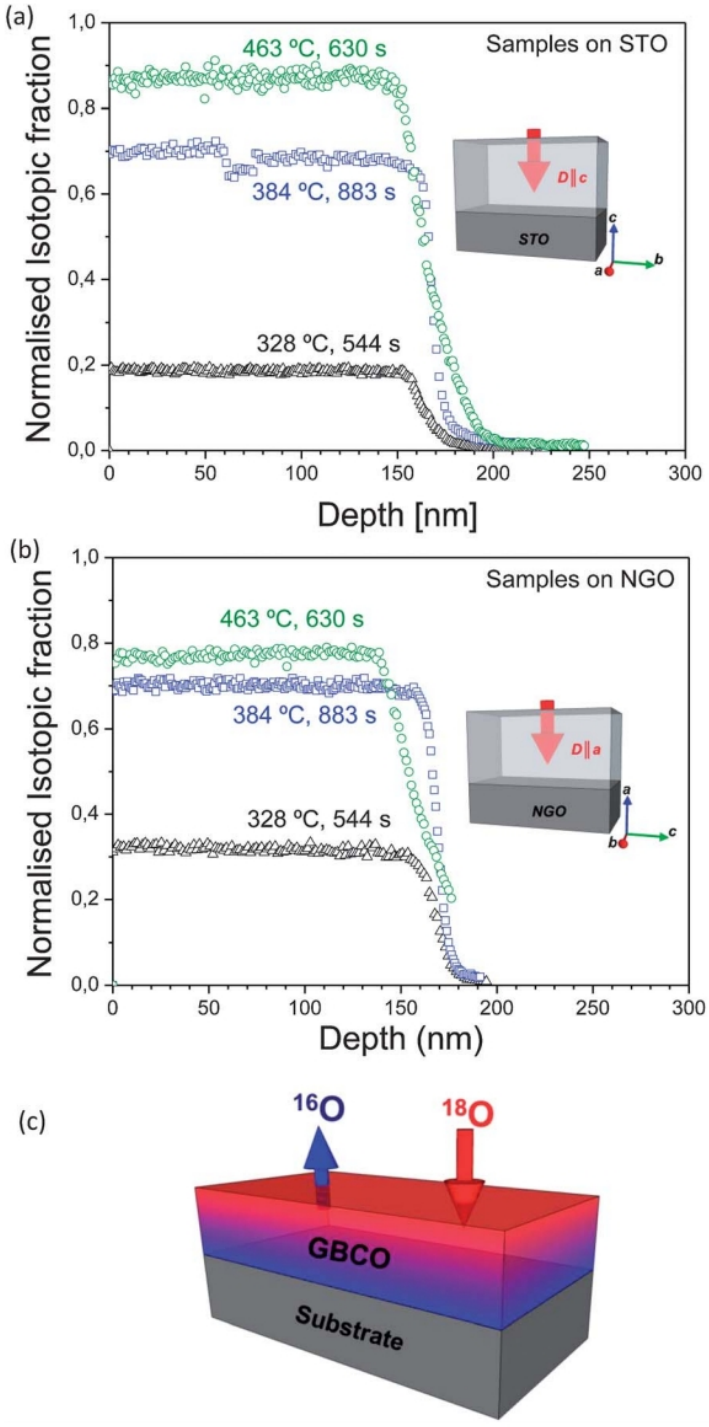

Figure 5.5: *Normalised ^{18}O isotope fraction along the transverse direction (depth profile) of GBCO films of about 160 nm thick deposited on STO (a) and NGO (b) at exchange temperatures of 328, 384 and 463°C, and times of 544, 883 and 630 s, respectively. The scheme in (c) depicts the experimental arrangement for the ^{18}O exchange directly through the top film surface.*

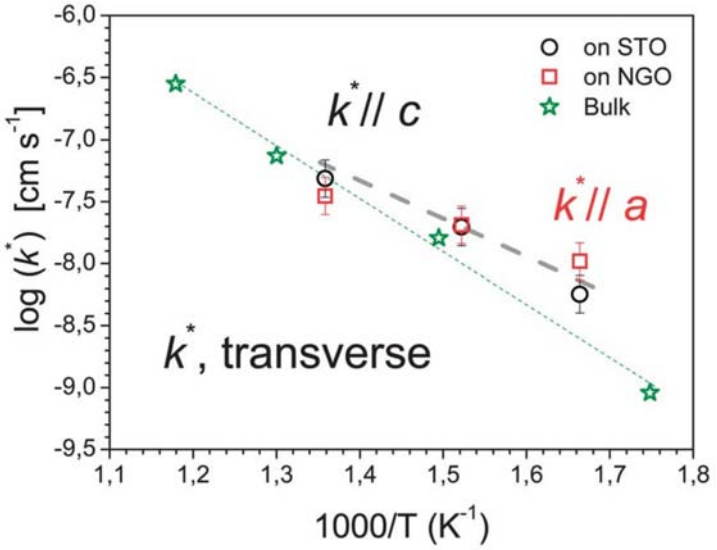

Figure 5.6: *The oxygen surface exchange rates (k*) plotted as a function of reciprocal temperature for the GBCO films with c- and a-axes orientation (deposited on STO and NGO, respectively). The graph also includes values for the bulk GBCO ceramic from the literature [92]. The dashed lines are only a guide to the eye.*

5.2.2 Oxygen surface exchange and diffusion in longitudinal geometry

Fig. 5.7(a) and (b) show longitudinal concentration profiles obtained for the films deposited on STO and NGO substrates at three different temperatures. For fitting the longitudinal concentration profiles the semi-infinite medium solution of the diffusion equation was used [179]. For this particular geometry, the analysis provides both the oxygen exchange, k^*, and diffusion coefficients, D^*, along the plane of the film, which correspond to different crystallographic orientations according to the film texture, *i.e.* along the a/b direction for c-axis oriented films on STO, and along the b/c direction for a-axis oriented films on NGO. The solution to the diffusion equation can be written in terms of dimensionless parameters and as $x' = x/\sqrt{4D*t}$ and $h' = (k*/D*)/\sqrt{4D*t}$ as

$$c_r(x,t) = \frac{C(x,t) - C_{bg}}{C_g - C_{bg}} = erfc(x') - exp(2h'x' - h'^2)erfc(x' + h') \qquad (5.2)$$

D^* and k^* values obtained for the measured regions of the exchanged samples are depicted in the Arrhenius plots in Fig. 5.8 (a) and (b). Despite the inherent variability in the measurement of k^*, the values for this longitudinal geometry follow a similar trend to the one observed in the transverse geometry. The surface exchange coefficients for films on STO and NGO (Fig. 5.8a) show values from half to one order of magnitude larger than the bulk ones, and are slightly larger than those reported for transverse geometry. This

could be related to a higher activity of the freshly cut trenches opened in this experiment in comparison with the top film surface more exposed to surface contamination and degradation in the case of transverse geometry. Besides, this longitudinal configuration may be less affected by surface segregation during the low temperature annealing because of the particular geometry and the surfaceto-volume ratio and, therefore, remain more active for oxygen reduction. Again, there are no significant differences related to film orientation, as it would be expected in this case since the exposed surfaces very likely consist of a combination of different crystallographic planes, *i.e.*:(100)/(010) for the c-axis oriented films on STO, and (001)/(010) for the a-axis oriented films on NGO.

The most remarkable differences are observed in the D^* tracer diffusion coefficient, in Fig. 5.8(b). While the D^* values obtained on c-axis oriented GBCO/STO are slightly higher than the reported bulk material in the full range of temperatures, those obtained on a-axis oriented GBCO/NGO deviate substantially, being almost one order of magnitude smaller in the low temperature range between 300 and 400 $°C$. For pure c-axis oriented films the diffusion path in the longitudinal geometry is parallel to the a/b crystallographic planes, and therefore the measured D^* values are taken as the maximum intrinsic values. On the other hand, in a pure a-axis oriented film there would be a/b planes perpendicular to the diffusion path, but also parallel due to the mixed b and c orientation within the film plane. Depending on the grain connectivity, there is little chance for a direct diffusion path along a–b planes, as in the case of c-axis oriented films. Therefore, the observed reduction of the tracer diffusion coefficient D^* is evidence of the diffusion anisotropy, as has also been proven in polycrystalline samples of $PrBaCo_2O_{5.5}$. For this material the diffusion coefficient was found to be larger in the [100]/[010] direction compared to [001][114]. At the highest temperature the a-axis oriented film shows a comparable D^* value to the c-axis oriented and bulk values. It cannot be ruled out that the presence of a small amount of c-axis orientation in predominantly a-axis oriented samples, as could be the case for this particular sample, might provide a fast diffusion path and therefore a substantial increase in the diffusion coefficient. If that was the case the anisotropy in GBCO may be even of a larger magnitude and therefore the largest anisotropy value measured (one order of magnitude) constitutes the lower bound of the measurements taking into account the possible fast diffusion paths through grain boundaries or regions with different orientation. The fact that D^* values along the fastest diffusion direction are similar to those reported for polycrystalline GBCO material (with a random distribution of domain orientations) indicates that the bulk material presents a substantial connectivity between a/b planes so the fastest diffusion path dominates, which reinforces the suitability of these ordered perovskites for MIEC cathodes.

5.3 Electrical Conductivity Relaxation Measurements with XRD

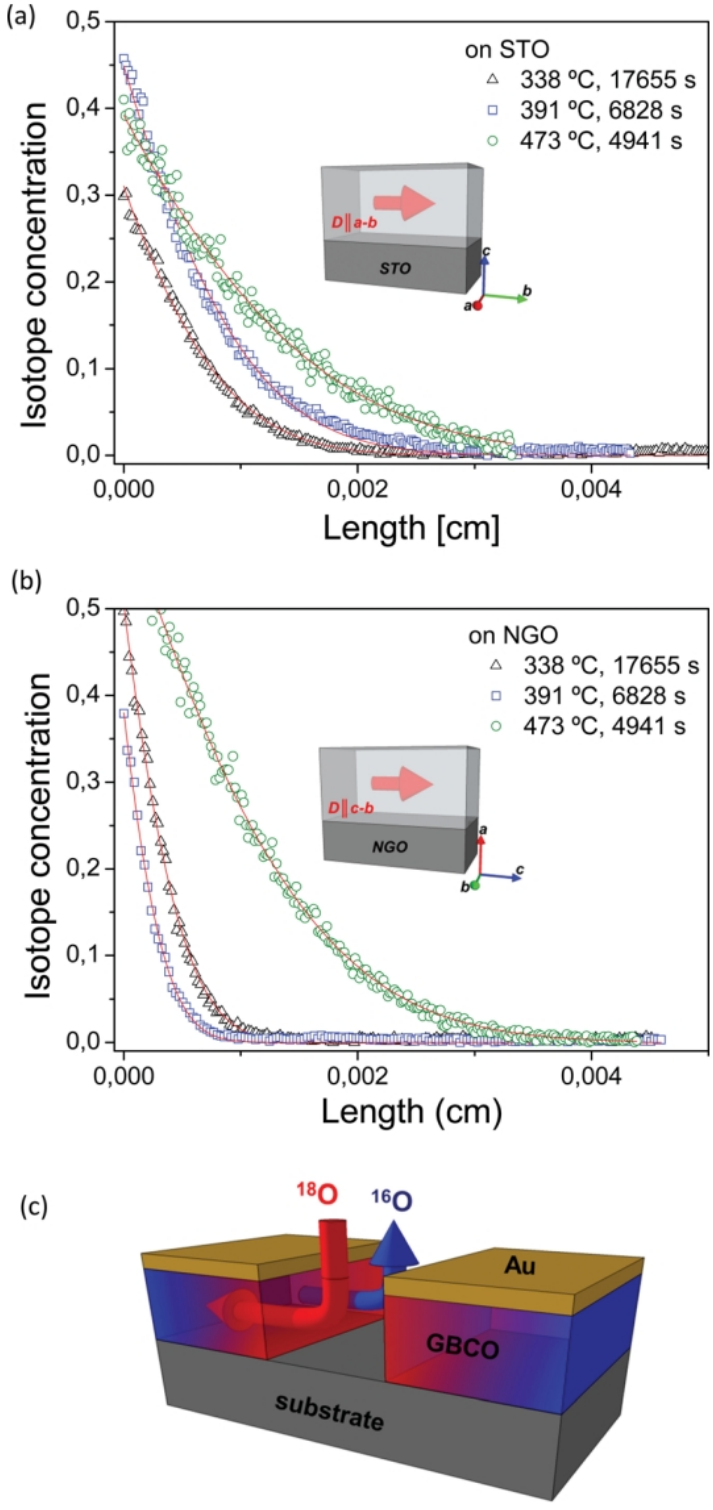

Figure 5.7: *Normalised isotopic fraction profile along the longitudinal direction of the c-axis (a) and a-axis (b) GBCO oriented films deposited on STO and NGO substrates, respectively, and exchanged at 338, 391 and 473 °C, during 17 655, 628 and 4941 s, respectively. The scheme in (c) shows the experimental arrangement for this longitudinal geometry.*

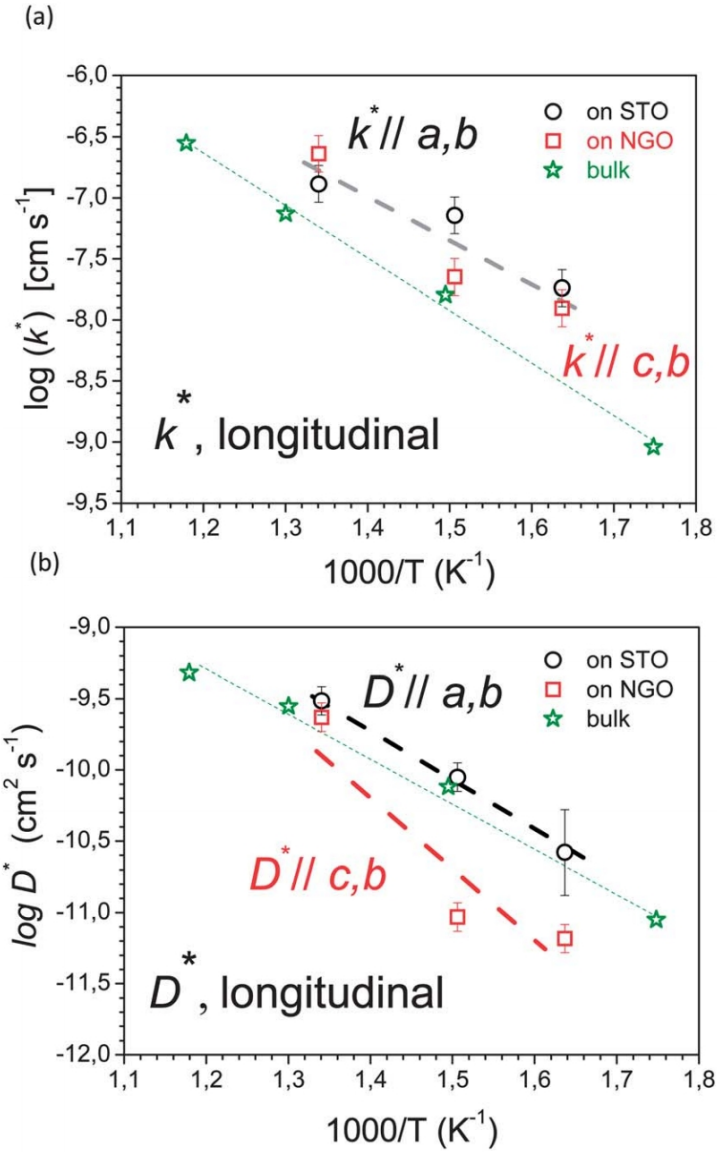

Figure 5.8: *Arrhenius plots of the tracer oxygen surface exchange rate k* (a) and oxygen tracer diffusivities D* (b) measured in the longitudinal geometry for the different GBCO film orientations. The graphs include also the values reported for the bulk material for comparison [92]. Dashed lines are only a guide to the eye.*

CHAPTER 6

Conclusion and Future Work

6.1 Conclusion

1. High-quality epitaxial GBCO films mainly consisting of single and double-perovskite regions have been obtained by pulsed laser deposition. The nature of the ablation process from stoichiometric $GdBaCo_2O_{5+\delta}$ targets generates a deviation in the composition of the films which basically consists in a Co depletion, with ([Gd]+[Ba])/[Co] ratio from 1.2 to 1.4. This composition deviation induces the appearance of characteristic stacking faults with supplementary GdO planes without affecting the overall epitaxial arrangement of the films.

2. Despite the observed changes in the film orientation from $c_{\parallel}$ to $c_{\perp}$ upon deposition temperature increase, the film electronic conductivities seem to be mainly correlated with the cation composition. So, the larger the deviation from stoichiometric composition (Gd:Ba:Co = 1:1:2), the lower the conductivity. This effect has been mainly ascribed to the role of defects in impeding the achievement of a long-range order of the highly conducting *Pmmm* structure in the films. Despite the presence of defects, the conductivities in our films, which are considered very promising for their application as cathodes in intermediate temperature SOFCs, attain values as high as 800 S/cm at temperatures between 300 and 400°C.

3. We have deposited high quality epitaxial films of the mixed ionic-electronic conducting material $GdBaCo_2O_{5+\delta}$ on different substrates, and demonstrated that the appropriate choice of substrate mismatch allows growing films with either pure c-axis or a-axis orientation. This has allowed exploration of the potential anisotropy in the oxygen transport and has proven that indeed the oxygen diffusion at low temperatures is almost one order of magnitude larger along the a-axis compared to the c-axis. This has been related to the arrangement of oxygen vacancies preferentially in the GdO planes forming channels along the a-axis, and therefore providing a path for

oxygen migration. However, no influence of the structure anisotropy was observed in the oxygen surface exchange rates, which were of similar values regardless of the film orientation or measuring geometry. The method described here provides a very powerful tool to explore intrinsic oxygen transport properties in complex anisotropic oxide materials otherwise dominated by the mixture of all orientations and grain boundary contributions in polycrystalline samples.

6.2 Future Work

Based on the fundamental research of these double perovskite $GdBaCo_2O_{5+\delta}$ materials throughout the work, a number of proposed studies would be further investigated in the future. For example, A rigorous study utilising the PLD with the in-situ reflection high-energy electron diffraction (RHEED) monitoring technique it would be possible to grow the $LnBaCo_2O_{5+\delta}$ $(Ln-BCO)$ films layer-by-layer and may further improve the film quality and help understand the phenomena observed in the $GdBaCo_2O_{5+\delta}$ layer-substrate interface.

It is of interest to investigate whether growing heteroepitaxial films of these oxides will enhance electrical and electrochemical properties in SOFC cathodes. It would be beneficial to study the correlation of strain effect with electrical conductivity, oxygen diffusion and surface exchange properties for the family $LnBaCo_2O_{5+\delta}$ $(Ln-BCO)$ epitaxial films through growing these films on different substrates. The studies on $LnBaCo_2O_{5+\delta}$ $(Ln-BCO)$ family doped with different elements are also of interest.

Bibliography

[1] *International Energy Outlook 2013 with projections to 2040*, Tech. Rep. (U.S. Energy Information Administration, 2013).

[2] B. C. H. Steele and A. Heinzel, *Materials for fuel-cell technologies*, Nature **414**, 345 (2001).

[3] EG&G Technical Services Inc. for the US Department of Energy and Office of Fossil Energy and National Energy Technology Laboratory, ed., *Fuel Cell Handbook*, 7th ed. (Morgantown, West Virginia 26507-0880, 2004).

[4] D. Shekhawat, J. Spivey, and D. Berry, eds., *Fuel Cells: Technologies for Fuel Processing*, 1st ed. (Elsevier Science, 2011) p. 568.

[5] R. O'Hayre, S.-W. Cha, W. Colella, and F. B. Prinz, *Fuel Cell Fundamentals*, 2nd ed. (John Wiley and Sons, 2009) p. 576.

[6] O. Z. Sharaf and M. F. Orhan, *An overview of fuel cell technology: Fundamentals and applications*, Renew. Sust. Energ. Rev. **32**, 810 (2014).

[7] A. B. Stambouli and E. Traversa, *Solid oxide fuel cells (SOFCs): a review of an environmentally clean and efficient source of energy*, Renew. Sust. Energ. Rev. **6**, 433 (2002).

[8] R. M. Ormerod, *Solid oxide fuel cells*, Chem. Soc. Rev. **32**, 17 (2003).

[9] J. A. Kilner and M. Burriel, *Materials for intermediate-temperature solid-oxide fuel cells*, Annu. Rev. Mater. Res. **44**, 365 (2014).

[10] F. Kröger, *The Chemistry of Imperfect Crystals*, The Chemistry of Imperfect Crystals No. v. 3 (North-Holland Publishing Company, 1974).

[11] J. Larminie and A. Dicks, *Fuel Cell Systems Explained*, 2nd ed. (John Wiley and Sons, 2003).

[12] P. J. Gellings and H. J. Bouwmeester, *The CRC Handbook of Solid State Electrochemistry* (CRC Press, 1997) p. 656.

[13] A. T. A. Appleby, M. U. (US)), and F. U. o. T. C. (Foulkes, *Fuel cell handbook* (1988).

[14] S. T. Aruna, M. Muthuraman, and K. C. Patil, *Combustion synthesis and properties of strontium substituted lanthanum manganites* $La_{1-x}Sr_xMnO_3$ $(0 \leq x \leq 0.3)$, J. Mater. Chem. **7**, 2499 (1997).

[15] S. Jiang, *A comparison of* O_2 *reduction reactions on porous* $(La, Sr)MnO_3$ *and* $(La, Sr)(Co, Fe)O_3$ *electrodes*, Solid State Ionics **146**, 1 (2002).

[16] M. L. Faro and A. Aricò, *9 - ceramic membranes for intermediate temperature solid oxide fuel cells (sofcs): state of the art and perspectives*, in *Membranes for Clean and Renewable Power Applications*, edited by A. Gugliuzza and A. Basile (Woodhead Publishing, 2014) pp. 237 – 265.

[17] J. Kilner, R. D. Souza, and I. Fullarton, *Surface exchange of oxygen in mixed conducting perovskite oxides*, Solid State Ionics **86–88, Part 2**, 703 (1996).

[18] I. Yasuda and T. Hikita, *Precise determination of the chemical diffusion coefficient of calcium-doped lanthanum chromites by means of electrical conductivity relaxation*, J. Electrochem. Soc. **141**, 1268 (1994), http://jes.ecsdl.org/content/141/5/1268.full.pdf+html .

[19] J. Mizusaki, T. Sasamoto, W. R. Cannon, and H. K. Bowen, *Electronic conductivity, seebeck coefficient, and defect structure of $La_{1-x}Sr_xFeO_3$ (x=0.l, 0.25)*, J. Am. Ceram. Soc. **66**, 247 (1983).

[20] L.-W. Tai, M. Nasrallah, H. Anderson, D. Sparlin, and S. Sehlin, *Structure and electrical properties of $Ln_{1-x}Sr_xCo_{1-y}Fe_yO_3$. part 1. the system $Ln_{0.8}Sr_{0.2}Co_{1-y}Fe_yO_3$*, Solid State Ionics **76**, 259 (1995).

[21] J. W. Stevenson, T. R. Armstrong, R. D. Carneim, L. R. Pederson, and W. J. Weber, *Electrochemical properties of mixed conducting perovskites $La_{1-x}M_xCo_{1-y}Fe_yO_{3-\delta}$ ($M = Sr, Ba, Ca$)*, J. Electrochem. Soc. **143**, 2722 (1996).

[22] M. Patrakeev, I. Leonidov, V. Kozhevnikov, and V. Kharton, *Ion-electron transport in strontium ferrites: relationships with structural features and stability*, Solid State Sciences **6**, 907 (2004).

[23] B. Wei, S. L. Zhe Lü and, Y. Liu, K. Liu, and W. Su, *Thermal and electrical properties of new cathode material $Ba_{0.5}Sr_{0.5}Co_{0.8}Fe_{0.2}O_{3-\delta}$ for SOFCs*, Electrochem. Solid State Lett. **8**, A428 (2005).

[24] J. Maier, *On the correlation of macroscopic and microscopic rate constants in solid state chemistry*, Solid State Ionics **112**, 197 (1998).

[25] P. Knauth and H. L. Tuller, *Solid-state ionics: Roots, status, and future prospects*, J. Am. Ceram. Soc. **85**, 1654 (2002).

[26] A. Aguadero, L. Fawcett, S. Taub, R. Woolley, K.-T. Wu, N. Xu, J. Kilner, and S. Skinner, *Materials development for intermediate-temperature solid oxide electrochemical devices*, J. Mater. Sci. **47**, 3925 (2012).

[27] M. Ni, N. Brandon, T. Zhao, I. Dincer, Z. Shao, C. Xia, J. Hill, L. Peter, N. Shikazono, W. Bessler, *et al.*, *Solid Oxide Fuel Cells: From Materials to System Modeling*, RSC energy and environment series (Royal Society of Chemistry, 2013).

[28] M. Sakib Khan, M. Saiful Islam, and D. R. Bates, *Cation doping and oxygen diffusion in zirconia: a combined atomistic simulation and molecular dynamics study*, J. Mater. Chem. **8**, 2299 (1998).

[29] E. Tsipis and V. Kharton, *Electrode materials and reaction mechanisms in solid oxide fuel cells: a brief review. (I. performance-determining factors)*, J. Solid State Electrochem. **12**, 1039 (2008).

[30] E. Tsipis and V. Kharton, *Electrode materials and reaction mechanisms in solid oxide fuel cells: a brief review. (II. electrochemical behavior vs. materials science aspects)*, J. Solid State Electrochem. **12**, 1367 (2008).

[31] E. Tsipis and V. Kharton, *Electrode materials and reaction mechanisms in solid oxide fuel cells: a brief review. (III. recent trends and selected methodological aspects)*, J. Solid State Electrochem. **15**, 1007 (2011).

[32] D. J. L. Brett, A. Atkinson, N. P. Brandon, and S. J. Skinner, *Intermediate temperature solid oxide fuel cells*, Chem. Soc. Rev. **37**, 1568 (2008).

[33] S. Tao and J. T. S. Irvine, *A redox-stable efficient anode for solid-oxide fuel cells*, Nat Mater **2**, 320 (2003).

[34] A. Atkinson, S. Barnett, R. J. Gorte, J. T. S. Irvine, A. J. McEvoy, M. Mogensen, S. C. Singhal, and J. Vohs, *Advanced anodes for high-temperature fuel cells*, Nat Mater **3**, 17 (2004).

[35] J. Irvine and A. Sauvet, *Improved oxidation of hydrocarbons with new electrodes in high temperature fuel cells*, Fuel Cells **1**, 205 (2001).

[36] S. Jiang and S. Chan, *A review of anode materials development in solid oxide fuel cells*, J. Mater. Sci. **39**, 4405 (2004).

[37] B. A. Boukamp, *Fuel cells: The amazing perovskite anode*, Nat Mater **2**, 294 (2003).

[38] O. Müller and R. Roy, *The major ternary structural families*, Crystal chemistry of non-metallic materials (Springer-Verlag, 1974).

[39] N. Vyshatko, V. Kharton, A. Shaula, E. Naumovich, and F. Marques, *Structural characterization of mixed conducting perovskites $La(Ga,M)O_{3+\delta}$ (M=Mn, Fe, Co, Ni)*, Materials Research Bulletin **38**, 185 (2003).

[40] J. Richter, P. Holtappels, T. Graule, T. Nakamura, and L. J. Gauckler, *Materials design for perovskite SOFC cathodes*, Monatshefte für Chemie - Chemical Monthly **140**, 985 (2009).

[41] M. Mogensen, D. Lybye, N. Bonanos, P. Hendriksen, and F. Poulsen, *Factors controlling the oxide ion conductivity of fluorite and perovskite structured oxides*, Solid State Ionics **174**, 279 (2004).

[42] I. H. Inoue, *Electrostatic carrier doping to perovskite transition-metal oxides*, Semicond. Sci. Technol. **20**, S112 (2005).

[43] C. Sun, R. Hui, and J. Roller, *Cathode materials for solid oxide fuel cells: a review*, J. Solid State Electrochem. **14**, 1125 (2010).

[44] A. McEvoy, *Activation processes, electrocatalysis and operating protocols enhance SOFC performance*, Solid State Ionics **135**, 331 (2000).

[45] S. B. Adler, *Factors governing oxygen reduction in solid oxide fuel cell cathodes*, Chem. Rev. **104**, 4791 (2004).

[46] G. Rijnders, *Oxide heterostructures: Atoms on the move*, Nat Mater **13**, 844 (2014).

[47] S. Jiang, *Development of lanthanum strontium manganite perovskite cathode materials of solid oxide fuel cells: a review*, J. Mater. Sci. **43**, 6799 (2008).

[48] V. Kharton, F. Marques, and A. Atkinson, *Transport properties of solid oxide electrolyte ceramics: a brief review*, Solid State Ionics **174**, 135 (2004).

[49] H. Hayashi, T. Saitou, N. Maruyama, H. Inaba, K. Kawamura, and M. Mori, *Thermal expansion coefficient of yttria stabilized zirconia for various yttria contents*, Solid State Ionics **176**, 613 (2005).

[50] R. D. Souza and J. Kilner, *Oxygen transport in $La_{1-x}Sr_xMn_{1-y}Co_yO_{3\pm\delta}$ perovskites - part I. oxygen tracer diffusion*, Solid State Ionics **106**, 175 (1998).

[51] R. D. Souza and J. Kilner, *Oxygen transport in $La_{1-x}Sr_xMn_{1-y}Co_yO_{3\pm\delta}$ perovskites - part II. oxygen surface exchange*, Solid State Ionics **126**, 153 (1999).

[52] M. Østergård, C. Clausen, C. Bagger, and M. Mogensen, *Manganite-zirconia composite cathodes for SOFC: Influence of structure and composition*, Electrochimica Acta **40**, 1971 (1995).

[53] T. Tsai and S. A. Barnett, *Effect of $LSM-YSZ$ cathode on thin-electrolyte solid oxide fuel cell performance*, Solid State Ionics **93**, 207 (1997).

[54] A. Chen, J. R. Smith, K. L. Duncan, R. T. DeHoff, K. S. Jones, and E. D. Wachsman, *Effect of $La_2Zr_2O_7$ on interfacial resistance in solid oxide fuel cells*, J. Electrochem. Soc. **157**, B1624 (2010).

[55] M. Suzuki, H. Sasaki, S. Otoshi, A. Kajimura, N. Sugiura, and M. Ippommatsu, *High performance solid oxide fuel cell cathode fabricated by electrochemical vapor deposition*, J. Electrochem. Soc. **141**, 1928 (1994).

[56] A. M. Saranya, D. Pla, A. Morata, A. Cavallaro, J. Canales-Vázquez, J. A. Kilner, M. Burriel, and A. Tarancón, *Thin films: Engineering mixed ionic electronic conduction in $La_{0.8}Sr_{0.2}MnO_{3+\delta}$ nanostructures through fast grain boundary oxygen diffusivity*, Adv. Energy Mater. **5** (2015), 10.1002/aenm.201570064.

[57] T. M. Huber, E. Navickas, G. Friedbacher, H. Hutter, and J. Fleig, *Apparent oxygen uphill diffusion in $La_{0.8}Sr_{0.2}MnO_3$ thin films upon cathodic polarization*, ChemElectroChem , n/a (2015).

[58] M. Ni, M. K. H. Leung, and D. Y. C. Leung, *Mathematical modelling of protonconducting solid oxide fuel cells and comparison with oxygen ion conducting counterpart*, Fuel Cells **7**, 269 (2007).

[59] M. Koyama, C. j. Wen, and K. Yamada, *$La_{0.6}Ba_{0.4}CoO_3$ as a cathode material for solid oxide fuel cells using a $BaCeO_3$ electrolyte*, J. Electrochem. Soc. **147**, 87 (2000).

[60] O. Yamamoto, Y. Takeda, R. Kanno, and M. Noda, *Perovskite-type oxides as oxygen electrodes for high temperature oxide fuel cells*, Solid State Ionics **22**, 241 (1987).

[61] N. Q. Minh, *Ceramic fuel cells*, J. Am. Ceram. Soc. **76**, 563 (1993).

[62] A. Petric, P. Huang, and F. Tietz, *Evaluation of $La-Sr-Co-Fe-O$ perovskites for solid oxide fuel cells and gas separation membranes*, Solid State Ionics **135**, 719 (2000).

[63] L.-W. Tai, M. Nasrallah, H. Anderson, D. Sparlin, and S. Sehlin, *Structure and electrical properties of $Ln_{1-x}Sr_xCo_{1-y}Fe_yO_3$. part 2. the system $Ln_{1-x}Sr_xCo_{0.2}Fe_{0.8}O_3$*, Solid State Ionics **76**, 273 (1995).

[64] Y. Teraoka, H. Zhang, K. Okamoto, and N. Yamazoe, *Mixed ionic-electronic conductivity of $La_{1-x}Sr_xCo_{1-y}Fe_yO_{3-\delta}$ perovskite-type oxides*, Materials Research Bulletin **23**, 51 (1988).

[65] L. Qiu, T. Ichikawa, A. Hirano, N. Imanishi, and Y. Takeda, *$Ln_{1-x}Sr_xCo_{1-y}Fe_yO_{3-\delta}$ (Ln=Pr, Nd, Gd; $x = 0.2, 0.3$) for the electrodes of solid oxide fuel cells*, Solid State Ionics **158**, 55 (2003).

[66] S. Simner, J. Shelton, M. Anderson, and J. Stevenson, *Interaction between $La(Sr)FeO_3SOFC$ cathode and YSZ electrolyte*, Solid State Ionics **161**, 11 (2003).

[67] W.-H. Kim, H.-S. Song, J. Moon, and H.-W. Lee, *Intermediate temperature solid oxide fuel cell using $(La, Sr)(Co, Fe)O_3$-based cathodes*, Solid State Ionics **177**, 3211 (2006).

[68] A. Mai, V. A. Haanappel, S. Uhlenbruck, F. Tietz, and D. Stöver, *Ferrite-based perovskites as cathode materials for anode-supported solid oxide fuel cells: Part I. variation of composition*, Solid State Ionics **176**, 1341 (2005).

[69] A. Tsoga, A. Gupta, A. Naoumidis, and P. Nikolopoulos, *Gadolinia-doped ceria and yttria stabilized zirconia interfaces: regarding their application for SOFC technology*, Acta Materialia **48**, 4709 (2000).

[70] Z. Shao and S. M. Haile, *A high-performance cathode for the next generation of solid-oxide fuel cells*, Nature **431**, 170 (2004).

[71] M. Zinkevich and F. Aldinger, *Thermodynamic analysis of the ternary $La-Ni-O$ system*, Journal of Alloys and Compounds **375**, 147 (2004).

[72] L. Yan, H. J. Niu, G. V. Duong, M. R. Suchomel, J. Bacsa, P. R. Chalker, J. Hadermann, G. van Tendeloo, and M. J. Rosseinsky, *Cation ordering within the perovskite block of a six-layer ruddlesden-popper oxide from layer-by-layer growth - artificial interfaces in complex unit cells*, Chem. Sci. **2**, 261 (2011).

[73] J. H. Lee, G. Luo, I. C. Tung, S. H. Chang, Z. Luo, M. Malshe, M. Gadre, A. Bhattacharya, S. M. Nakhmanson, J. A. Eastman, H. Hong, J. Jellinek, D. Morgan, D. D. Fong, and J. W. Freeland, *Dynamic layer rearrangement during growth of layered oxide films by molecular beam epitaxy*, Nat Mater **13**, 879 (2014).

[74] V. V. Kharton, A. P. Viskup, E. N. Naumovich, and F. M. B. Marques, *Oxygen ion transport in La_2NiO_4-based ceramics*, J. Mater. Chem. **9**, 2623 (1999).

[75] S. Skinner and J. Kilner, *Oxygen diffusion and surface exchange in $La_{2-x}Sr_xNiO_{4+\delta}$*, Solid State Ionics **135**, 709 (2000).

[76] P. D. Battle, M. A. Green, N. S. Laskey, J. E. Millburn, P. G. Radaelli, M. J. Rosseinsky, S. P. Sullivan, and J. F. Vente, *Crystal and magnetic structures of the colossal magnetoresistance manganates $Sr_{2-x}Nd_{1+x}Mn_2O_7$ (x=0.0, 0.1)*, Phys. Rev. B **54**, 15967 (1996).

[77] P. D. Battle, M. A. Green, N. S. Laskey, J. E. Millburn, L. Murphy, M. J. Rosseinsky, S. P. Sullivan, and J. F. Vente, *Layered ruddlesden-popper manganese oxides:synthesis and cation ordering*, Chem. Mater. **9**, 552 (1997).

[78] D. K. Finnemore, R. N. Shelton, J. R. Clem, R. W. McCallum, H. C. Ku, R. E. McCarley, S. C. Chen, P. Klavins, and V. Kogan, *Magnetization of superconducting lanthanum copper oxides*, Phys. Rev. B **35**, 5319 (1987).

[79] J. Bassat, P. Odier, A. Villesuzanne, C. Marin, and M. Pouchard, *Anisotropic ionic transport properties in $La_2NiO_{4+\delta}$ single crystals*, Solid State Ionics **167**, 341 (2004).

[80] A. Tarancón, M. Burriel, J. Santiso, S. J. Skinner, and J. A. Kilner, *Advances in layered oxide cathodes for intermediate temperature solid oxide fuel cells*, J. Mater. Chem. **20**, 3799 (2010).

[81] J. Santiso and M. Burriel, *Deposition and characterisation of epitaxial oxide thin films for $SOFCs$*, J. Solid State Electrochem. **15**, 985 (2011).

[82] A. Maignan, C. Martin, D. Pelloquin, N. Nguyen, and B. Raveau, *Structural and magnetic studies of ordered oxygen-deficient perovskites $LnBaCo_2O_{5+\delta}$, closely related to the "112" structure*, J. Solid State Chem. **142**, 247 (1999).

[83] K. Zhang, L. Ge, R. Ran, Z. Shao, and S. Liu, *Synthesis, characterization and evaluation of cation-ordered $LnBaCo_2O_{5+\delta}$ as materials of oxygen permeation membranes and cathodes of $\{SOFCs\}$*, Acta Materialia **56**, 4876 (2008).

[84] P. Anderson, C. Kirk, J. Knudsen, I. Reaney, and A. West, *Structural characterisation of $REBaCo_2O_{6-\delta}$ phases ($re = pr, nd, sm, eu, gd, tb, dy, ho$)*, Solid State Sciences **7**, 1149 (2005).

[85] J.-H. Kim and a. Manthiram, *$LnBaCo_2O_{5+\delta}$ oxides as cathodes for intermediate-temperature solid oxide fuel cells*, J. Electrochem. Soc. **155**, B385 (2008).

[86] A. Taskin, A. Lavrov, and Y. Ando, *Fast oxygen diffusion in a-site ordered perovskites*, Prog. Solid State Chem. **35**, 481 (2007), international Conference on Perovskites at EMPA, 2005.Properties and Potential Applications.

[87] A. A. Taskin, A. N. Lavrov, and Y. Ando, *Achieving fast oxygen diffusion in perovskites by cation ordering*, Appl. Phys. Lett. **86**, 091910 (2005).

[88] R. Pelosato, G. Cordaro, D. Stucchi, C. Cristiani, and G. Dotelli, *Cobalt based layered*

perovskites as cathode material for intermediate temperature solid oxide fuel cells: A brief review, Journal of Power Sources **298**, 46 (2015).

[89] G. Kim, S. Wang, A. J. Jacobson, Z. Yuan, W. Donner, C. L. Chen, L. Reimus, P. Brodersen, and C. A. Mims, *Oxygen exchange kinetics of epitaxial $PrBaCo_2O_{5+\delta}$ thin films*, Appl. Phys. Lett. **88**, 024103 (2006).

[90] C. Frontera, J. L. García-Muñoz, A. Llobet, and M. A. G. Aranda, *Selective spin-state switch and metal-insulator transition in $GdBaCo_2O_{5+\delta}$*, Phys. Rev. B **65**, 180405 (2002).

[91] A. Grimaud, K. J. May, C. E. Carlton, Y.-L. Lee, M. Risch, W. T. Hong, J. Zhou, and Y. Shao-Horn, *Double perovskites as a family of highly active catalysts for oxygen evolution in alkaline solution*, Nat Commun **4** (2013), 10.1038/ncomms3439.

[92] A. Tarancón, S. J. Skinner, R. J. Chater, F. Hernandez-Ramirez, and J. A. Kilner, *Layered perovskites as promising cathodes for intermediate temperature solid oxide fuel cells*, J. Mater. Chem. **17**, 3175 (2007).

[93] G. Kim, S. Wang, A. J. Jacobson, L. Reimus, P. Brodersen, and C. A. Mims, *Rapid oxygen ion diffusion and surface exchange kinetics in $PrBaCo_2O_{5+x}$ with a perovskite related structure and ordered a cations*, J. Mater. Chem. **17**, 2500 (2007).

[94] C. Zhu, X. Liu, C. Yi, D. Yan, and W. Su, *Electrochemical performance of $PrBaCo_2O_{5+\delta}$ layered perovskite as an intermediate-temperature solid oxide fuel cell cathode*, J. Power Sources **185**, 193 (2008).

[95] D. Chen, R. Ran, K. Zhang, J. Wang, and Z. Shao, *Intermediate-temperature electrochemical performance of a polycrystalline $PrBaCo_2O_{5+\delta}$ cathode on samarium-doped ceria electrolyte*, Journal of Power Sources **188**, 96 (2009).

[96] J. H. Kim, Y. Kim, P. A. Connor, J. T. Irvine, J. Bae, and W. Zhou, *Structural, thermal and electrochemical properties of layered perovskite $SmBaCo_2O_{5+\delta}$, a potential cathode material for intermediate-temperature solid oxide fuel cells*, Journal of Power Sources **194**, 704 (2009).

[97] X. Zhu, H. Wang, and W. Yang, *Novel cobalt-free oxygen permeable membrane*, Chem. Commun. , 1130 (2004).

[98] Z. Deng, J. Smit, H. Niu, G. Evans, M. Li, Z. Xu, J. Claridge, and M. Rosseinsky, *B cation ordered double perovskite $Ba_2CoMo_{0.5}Nb_{0.5}O_{6+\delta}$ as a potential sofc cathode*, Chem. Mater. **21**, 5154 (2009).

[99] W. Zhou, J. Sunarso, Z.-G. Chen, L. Ge, J. Motuzas, J. Zou, G. Wang, A. Julbe, and Z. Zhu, *Novel b-site ordered double perovskite ba2bi0.1sc0.2co1.7o6-x for highly efficient oxygen reduction reaction*, Energy Environ. Sci. **4**, 872 (2011).

[100] S. Streule, A. Podlesnyak, D. Sheptyakov, E. Pomjakushina, M. Stingaciu, K. Conder, M. Medarde, M. V. Patrakeev, I. A. Leonidov, V. L. Kozhevnikov, and J. Mesot, *High-temperature order-disorder transition and polaronic conductivity in $PrBaCo_2O_{5.48}$*, Phys. Rev. B **73**, 094203 (2006).

[101] S. Streule, A. Podlesnyak, E. Pomjakushina, K. Conder, D. Sheptyakov, M. Medarde, and J. Mesot, *Oxygen order–disorder phase transition in $PrBaCo_2O_{5.48}$ at high temperature*, Physica B: Condensed Matter **378–380**, 539 (2006).

[102] A. Maignan, V. Caignaert, B. Raveau, D. Khomskii, and G. Sawatzky, *Thermoelectric power of $HoBaCo_2O_{5.5}$: Possible evidence of the spin blockade in cobaltites*, Phys. Rev. Lett. **93**, 026401 (2004).

[103] C. Frontera, J. L. García-Muñoz, A. Llobet, L. M. nosa, and M. Aranda, *Selective spin-state and metal–insulator transitions in $GdBaCo_2O_{5+\delta}$*, J. Solid State Chem. **171**, 349 (2003).

[104] A. Tarancón, D. Marrero-López, J. P. na Martínez, J. Ruiz-Morales, and P. N. nez, *Effect of phase transition on high-temperature electrical properties of* $GdBaCo_2O_{5+x}$ *layered perovskite*, Solid State Ionics **179**, 611 (2008).

[105] A. Tarancón, J. Peña-Martínez, D. Marrero-López, A. Morata, J. Ruiz-Morales, and P. Núñez, *Stability, chemical compatibility and electrochemical performance of* ($GdBaCo_2O_{5+\delta}$ *layered perovskite as a cathode for intermediate temperature solid oxide fuel cells*, Solid State Ionics **179**, 2372 (2008).

[106] D. Parfitt, A. Chroneos, A. Tarancon, and J. A. Kilner, *Oxygen ion diffusion in cation ordered/disordered* ($GdBaCo_2O_{5+\delta}$, J. Mater. Chem. **21**, 2183 (2011).

[107] R. A. De Souza and M. Martin, *Probing diffusion kinetics with secondary ion mass spectrometry*, MRS Bulletin **34**, 907 (2009).

[108] J. A. Kilner, S. J. Skinner, and H. H. Brongersma, *The isotope exchange depth profilingIEDP technique using SIMS and LEIS*, J. Solid State Electrochem. **15**, 861 (2011).

[109] M. Burriel, G. Garcia, J. Santiso, J. A. Kilner, R. J. Chater, and S. J. Skinner, *Anisotropic oxygen diffusion properties in epitaxial thin films of* $La_2NiO_{4+\delta}$, J. Mater. Chem. **18**, 416 (2008).

[110] L. Wang, R. Merkle, J. Maier, T. Acartürk, and U. Starke, *Oxygen tracer diffusion in dense* $Ba_{0.5}Sr_{0.5}Co_{0.8}Fe_{0.2}O_{3-\delta}$ *films*, Appl. Phys. Lett. **94**, 071908 (2009).

[111] L. Yan and P. A. Salvador, *Substrate and thickness effects on the oxygen surface exchange of* $La_{0.7}Sr_{0.3}MnO_3$ *thin films*, ACS Applied Materials & Interfaces **4**, 2541 (2012), http://dx.doi.org/10.1021/am300194n .

[112] M. Kubicek, Z. Cai, W. Ma, B. Yildiz, H. Hutter, and J. Fleig, *Tensile lattice strain accelerates oxygen surface exchange and diffusion in* $La_{1-x}Sr_xCoO_{3-\delta}$ *thin films*, ACS Nano **7**, 3276 (2013).

[113] K. Kerman, C. Ko, and S. Ramanathan, *Orientation dependent oxygen exchange kinetics on single crystal* $SrTiO_3$ *surfaces*, Phys. Chem. Chem. Phys. **14**, 11953 (2012).

[114] M. Burriel, J. Peña-Martínez, R. J. Chater, S. Fearn, A. V. Berenov, S. J. Skinner, and J. A. Kilner, *Anisotropic oxygen ion diffusion in layered* $PrBaCo_2O_{5+\delta}$, Chemistry of Materials **24**, 613 (2012).

[115] M. Burriel, M. Casas-Cabanas, J. Zapata, H. Tan, J. Verbeeck, C. Solís, J. Roqueta, S. J. Skinner, J. A. Kilner, G. V. Tendeloo, and J. Santiso, *Influence of the microstructure on the high-temperature transport properties of* $GdBaCo_2O_{5+\delta}$ *epitaxial films*, Chem. Mater. **22**, 5512 (2010).

[116] J. Kilner, B. Steele, and L. Ilkov, *Oxygen self-diffusion studies using negative-ion secondary ion mass spectrometry SIMS*, Solid State Ionics **12**, 89 (1984).

[117] B. Raveau, M. Motin Seikh, V. Pralong, and V. Caignaert, *Ordered oxygen deficient '112' perovskites,* ($LnBaCo_2O_{5+\delta}$ *: complex magnetism and transport properties*, Bulletin of Materials Science **32**, 305 (2009).

[118] A. A. Taskin, A. N. Lavrov, and Y. Ando, *Transport and magnetic properties of* ($GdBaCo_2O_{5+\delta}$ *single crystals: A cobalt oxide with square-lattice* (CoO_2 *planes over a wide range of electron and hole doping*, Phys. Rev. B **71**, 134414 (2005).

[119] M.-B. Choi, S.-Y. Jeon, J.-S. Lee, H.-J. Hwang, and S.-J. Song, *Chemical diffusivity and ionic conductivity of* ($GdBaCo_2O_{5+\delta}$, Journal of Power Sources **195**, 1059 (2010).

[120] H. M. Smith and A. F. Turner, *Vacuum deposited thin films using a ruby laser*, Appl. Opt. **4**, 147 (1965).

[121] D. Dijkkamp, T. Venkatesan, X. D. Wu, S. A. Shaheen, N. Jisrawi, Y. H. Min Lee, W. L. McLean, and M. Croft, *Preparation of $Y-Ba-Cu$ oxide superconductor thin films using pulsed laser evaporation from high T_c bulk material*, Appl. Phys. Lett. **51**, 619 (1987).

[122] S. Jin, T. H. Tiefel, M. McCormack, R. A. Fastnacht, R. Ramesh, and L. H. Chen, *Thousandfold change in resistivity in magnetoresistive $La-Ca-Mn-O$ films*, Science **264**, 413 (1994).

[123] R. Eason, *Pulsed laser deposition of thin films: applications-led growth of functional materials* (Wiley-Interscience, 2007).

[124] D. H. Lowndes, D. B. Geohegan, A. A. Puretzky, D. P. Norton, and C. M. Rouleau, *Synthesis of novel thin-film materials by pulsed laser deposition*, Science **273**, 898 (1996).

[125] T. Lippert, M. Montenegro, M. Döbeli, A. Weidenkaff, S. Müller, P. Willmott, and A. Wokaun, *Perovskite thin films deposited by pulsed laser ablation as model systems for electrochemical applications*, Prog. Solid State Chem. **35**, 221 (2007).

[126] M. N. R. Ashfold, F. Claeyssens, G. M. Fuge, and S. J. Henley, *Pulsed laser ablation and deposition of thin films*, Chem. Soc. Rev. **33**, 23 (2004).

[127] P. Willmott, *Deposition of complex multielemental thin films*, Prog. Surf. Sci. **76**, 163 (2004).

[128] A. Ichimiya and P. Cohen, *Reflection High-Energy Electron Diffraction* (Cambridge University Press, 2004).

[129] H. M. Christen and G. Eres, *Recent advances in pulsed-laser deposition of complex oxides*, J. Phys.: Condens. Matter **20**, 264005 (2008).

[130] A. West, *Solid State Chemistry and its Applications* (Wiley, 2014).

[131] M. DUGUE, J. F. GOULLIN, P. MERENDA, and M. MOULIN, *Preparation of single crystals of iii-v compounds*, in *Preparative Methods in Solid State Chemistry*, edited by P. HAGENMULLER (Academic Press, 1972) pp. 309 – 360.

[132] J. Zapata, M. Burriel, P. Garcia, J. A. Kilner, and J. Santiso, *Anisotropic 18o tracer diffusion in epitaxial films of $GdBaCo_2O_{5+\delta}$ cathode material with different orientations*, J. Mater. Chem. A **1**, 7408 (2013).

[133] G. Hubler and J. Sprague, *Energetic particles in PVD technology: particle-surface interaction processes and energy-particle relationships in thin film deposition*, Surface and Coatings Technology **81**, 29 (1996).

[134] R. Ramesh, A. Inam, W. K. Chan, S., B. Wilkens, K. Myers, K. Remschnig, D. L. Hart, and J. M. Tarascon, *Epitaxial cuprate superconductor/ferroelectric heterostructures*, Science **252**, 944 (1991).

[135] J.-P. Locquet, J. Perret, J. Fompeyrine, E. Machler, J. W. Seo, and G. Van Tendeloo, *Doubling the critical temperature of $La_{1.9}Sr_{0.1}CuO_4$ using epitaxial strain*, Nature **394**, 453 (1998).

[136] L. Li, *Ferroelectric / superconductor heterostructures*, Mater. Sci. Eng.: R: Reports **29**, 153 (2000).

[137] G. Gao, Z. Yin, Z. Huang, S. Jin, and W. Wu, *The thickness evolution of orthorhombic lattice distortions in heteroepitaxial $La_{0.67}Ca_{0.33}MnO_3/NdGaO_3(110)_{Or}$ observed by x-ray reciprocal space mapping*, J. Phys. D: Appl. Phys. **41**, 152001 (2008).

[138] K. Oura, V. Lifshits, A. Saranin, A. Zotov, and M. Katayama, *Surface Science: An Introduction*, Advanced Texts in Physics (Springer Berlin Heidelberg, 2003).

[139] L.-C. Chen, *Particulates generated by pulsed laser ablation*, in *Pulsed Laser Deposition of*

Thin Films, A Wiley interscience publication, edited by D. Chrisey and G. Hubler (Wiley, 1994) Chap. 6, pp. 167–171.

[140] G. K. Hubler and D. B. Chrisey, *Pulsed laser deposition of thin films* (New York : J. Wiley, 1994) includes bibliographical references and index.

[141] P. P. Ewald, *Das reziproke gitter in der strukturtheorie*, Z. Kristallogr **56** (1921).

[142] B. Cullity, *Elements of X-ray Diffraction* (Addison-Wesley Publishing Company, 1956).

[143] V. Pecharsky and P. Zavalij, *Fundamentals Of Powder Diffraction And Structural Characterization Of Materials* (Springer, 2004).

[144] M. Birkholz, *Thin Film Analysis by X-Ray Scattering* (Wiley, 2006).

[145] U. Pietsch, V. Holy, and T. Baumbach, *High-Resolution X-Ray Scattering: From Thin Films to Lateral Nanostructures*, Advanced Texts in Physics (Springer New York, 2004).

[146] PANalytical, *X'Pert PRO MRD User's Guide*, par II - Chapter 11: MRD Cradle.

[147] R. Moreno, P. García, J. Zapata, J. Roqueta, J. Chaigneau, and J. Santiso, *Chemical strain kinetics induced by oxygen surface exchange in epitaxial films explored by time-resolved x-ray diffraction*, Chem. Mater. **25**, 3640 (2013).

[148] C. Kisielowski and et al, *Detection of single atoms and buried defects in three dimensions by aberration-corrected electron microscope with 0.5-Å information limit*, Microscopy and Microanalysis **14**, 469 (2008).

[149] D. Shindo and H. Kenji, *High-Resolution Electron Microscopy for Materials Science* (Springer Japan, 1998).

[150] J. Spence, *High-Resolution Electron Microscopy*, Monographs on the Physics and Chemistry of Materials (OUP Oxford, 2008).

[151] J. Verbeeck and S. V. Aert, *Model based quantification of EELS spectra*, Ultramicroscopy **101**, 207 (2004).

[152] P. Eaton and P. West, *Atomic Force Microscopy* (OUP Oxford, 2010).

[153] J. Goldstein, *Scanning Electron Microscopy and X-ray Microanalysis*, edited by T. Edition (Springer US, 2003).

[154] S. Reed, *Electron Microprobe Analysis and Scanning Electron Microscopy in Geology* (Cambridge University Press, 2005).

[155] R. Chater, S. Carter, J. Kilner, and B. Steele, *Development of a novel SIMS technique for oxygen self-diffusion and surface exchange coefficient measurements in oxides of high diffusivity*, Solid State Ionics **53**, 859 (1992).

[156] D. R. Killoran, *The effective duration of a linear slow-cool*, J. Electrochem. Soc. **109**, 170 (1962).

[157] S. Katsantonis, *Oxygen Transport in Novel Electrolyte Materials Based on Bi_2O_3*, *Thesis Ph.D.*, Department of Materials (2010), imperial College London.

[158] A. Benninghoven, F. Rüdenauer, and H. Werner, *Secondary Ion Mass Spectrometry: Basic Concepts, Instrumental Aspects, Applications, and Trends* (J. Wiley, 1987).

[159] J. Vickerman, A. Brown, and N. Reed, *Secondary ion mass spectrometry: principles and applications* (Clarendon Press, 1989).

[160] P. van der Heide, *Secondary Ion Mass Spectrometry: An Introduction to Principles and Practices* (Wiley, 2014).

[161] T. Stephan, *ToF-SIMS in cosmochemistry*, Planetary and Space Science **49**, 859 (2001).

[162] R. A. De Souza and M. Martin, *Secondary ion mass spectrometry SIMS – a powerful tool*

for studying mass transport over various length scales, physica status solidi (c) **4**, 1785 (2007).

[163] Z. Galus, R. Chalmers, and W. Bryce, *Fundamentals of electrochemical analysis*, Ellis Horwood series in analytical chemistry (Ellis Horwood, 1994).

[164] P. Gellings and H. Bouwmeester, *Handbook of Solid State Electrochemistry* (Taylor & Francis, 1997).

[165] E. Barsoukov and J. Macdonald, *Impedance Spectroscopy: Theory, Experiment, and Applications* (Wiley, 2005).

[166] B. A. Boukamp, *Electrochemical impedance spectroscopy in solid state ionics: recent advances*, Solid State Ionics **169**, 65 (2004).

[167] D. D. Macdonald, *Reflections on the history of electrochemical impedance spectroscopy*, Electrochimica Acta **51**, 1376 (2006).

[168] V. Freger and S. Bason, *Characterization of ion transport in thin films using electrochemical impedance spectroscopy: I. principles and theory*, Journal of Membrane Science **302**, 1 (2007).

[169] S. Bason, Y. Oren, and V. Freger, *Characterization of ion transport in thin films using electrochemical impedance spectroscopy: II: examination of the polyamide layer of RO membranes*, Journal of Membrane Science **302**, 10 (2007).

[170] A. Oppenheim, A. Willsky, and S. Nawab, *Signals and Systems*, Prentice-Hall signal processing series (Prentice Hall, 1997).

[171] J. ten Elshof, H. Bouwmeester, and H. Verweij, *Oxygen transport through* $La_{1-x}Sr_xFeO_{3-\delta}$ *membranes. I. permeation in air/he gradients*, Solid State Ionics **81**, 97 (1995).

[172] M. Mosleh, M. Søgaard, and P. V. Hendriksen, *Kinetics and mechanisms of oxygen surface exchange on* $La_{0.6}Sr_{0.4}FeO_{3-\delta}$ *thin films*, J. Electrochem. Soc. **156**, B441 (2009).

[173] X. Chen, S. Wang, Y. Yang, L. Smith, N. Wu, B.-I. Kim, S. Perry, A. Jacobson, and A. Ignatiev, *Electrical conductivity relaxation studies of an epitaxial* $La_{0.5}Sr_{0.5}CoO_{3-\delta}$ *thin film*, Solid State Ionics **146**, 405 (2002).

[174] M. Søgaard, P. V. Hendriksen, M. Mogensen, F. W. Poulsen, and E. Skou, *Oxygen nonstoichiometry and transport properties of strontium substituted lanthanum cobaltite*, Solid State Ionics **177**, 3285 (2006).

[175] J. E. ten Elshof, M. H. R. Lankhorst, and H. J. M. Bouwmeester, *Oxygen exchange and diffusion coefficients of strontium-doped lanthanum ferrites by electrical conductivity relaxation*, J. Electrochem. Soc. **144**, 1060 (1997).

[176] N. V. Kasper, P. Wochner, A. Vigliante, H. Dosch, G. Jakob, H. D. Carstanjen, and R. K. Kremer, *Epitaxial growth and properties of (001)-oriented* $(TbBaCo_2O_{6-\delta}$ *films*, Journal of Applied Physics **103**, 013907 (2008).

[177] J. Liu, M. Liu, G. Collins, C. Chen, X. Jiang, W. Gong, A. J. Jacobson, J. He, J. Jiang, and E. I. Meletis, *Epitaxial nature and transport properties in* $(LaBa)Co_2O_{5+\delta}$ *thin films*, Chemistry of Materials **22**, 799 (2010).

[178] K. Momma and F. Izumi, *Vesta3 for three-dimensional visualization of crystal, volumetric and morphology data*, Journal of Applied Crystallography **44**, 1272 (2011).

[179] J. Crank, *The Mathematics of Diffusion*, Oxford science publications (Clarendon Press, 1979).

[180] R. D. Souza and R. Chater, *Oxygen exchange and diffusion measurements: The importance of extracting the correct initial and boundary conditions*, Solid State Ionics **176**, 1915

(2005).

[181] E. Fischer and J. L. Hertz, *Measurability of the diffusion and surface exchange coefficients using isotope exchange with thin film and traditional samples*, Solid State Ionics **218**, 18 (2012).

[182] F. Ciucci, *A statistical perspective on oxygen diffusion and surface exchange experiments: Sensitivity analysis, parameter estimation and robust optimal experimental design*, Solid State Ionics **232**, 97 (2013).

[183] Z. Cai, M. Kubicek, J. Fleig, and B. Yildiz, *Chemical heterogeneities on $La_{0.6}Sr_{0.4}CoO_{3-\delta}$ thin films - correlations to cathode surface activity and stability*, Chemistry of Materials **24**, 1116 (2012).

[184] S. Fearn, J. Rossiny, J. Kilner, and J. Evans, *Measurement of oxygen transport in $La_{0.8}Sr_{0.2}MnO3$ perovskite grains*, Solid State Ionics **211**, 51 (2012).